IMAGE QUALITY, MODELING, AND DESIGN FOR HIGH-PERFORMANCE CONE-BEAM CT OF THE HEAD

by
Jennifer Xu

A dissertation submitted to Johns Hopkins University in conformity with the requirements for the degree of Doctor of Philosophy

Baltimore, Maryland
December, 2016

Abstract

Diagnosis and treatment of neurological and otolaryngological diseases rely heavily on visualization of fine, subtle anatomical structures in the head. In particular, high-quality head imaging at the point of care mitigates patient risk associated with transport and decreases time to diagnosis for time-sensitive diseases. Cone-beam computed tomography (CBCT) systems have found widespread adoption in diagnostic and image-guided procedures. Such systems exhibit potential for adaptation as point-of-care systems due to relatively low cost, mechanical simplicity, and inherently high spatial resolution, but are generally challenged by low contrast imaging tasks (e.g., visualization of tumors or hemorrhages). This thesis details the development and design of a CBCT imaging system with performance sufficient for high-quality imaging of the head and suitable to deployment at the point of care.

The performance of a commercially available head-and-neck CBCT scanner was assessed to determine the potential of such systems for high-quality head imaging. Results indicated low-contrast visualization was challenged by high detector noise and scatter. Photon counting x-ray detectors (PCDs) were identified as a potential technology that could improve the low-contrast visualization, and an imaging performance model was developed to quantify their imaging performance. The model revealed important implications for energy resolution, noise, and spatial resolution as a function of energy threshold and charge sharing rejection.

A new CBCT system dedicated to detection of low-contrast contrast intracranial hemorrhage was designed with guidance from an imaging chain model to optimize the system configuration (geometry, detector, x-ray source, etc.). The results indicated flat panel detectors (FPDs) were favorable due to a large field of view, but benefited from detector readout gain adjustments. Dual-gain detector readout was compared with use of bowtie filter in high-gain readout mode to investigate potential improvements to noise performance in FPDs. Finally, technical assessment of the prototype CBCT head scanner (with design based on guidance from the image quality model) indicated performance suitable for translation to clinical studies in the neurosciences critical care unit.

Readers

Jeffrey H. Siewerdsen, Ph.D. (advisor)
Professor, Department of Biomedical Engineering
Johns Hopkins University

Katsuyuki Taguchi, Ph.D.
Assistant Professor, Russell H. Morgan Department of Radiology
Johns Hopkins University

J. Webster Stayman, Ph.D.
Assistant Professor, Department of Biomedical Engineering
Johns Hopkins University

Nafi Aygun, M.D.
Associate Professor, Russell H. Morgan Department of Radiology
Johns Hopkins University

There is shadow under this red rock,
(Come in under the shadow of this red rock),
And I will show you something different from either
Your shadow at morning striding behind you
Or your shadow at evening rising to meet you…

-T.S. Eliot, The Wastelands

Acknowledgments

First, I would like to thank my advisor, Jeffrey Siewerdsen, for his seemingly tireless efforts in shaping my graduate experience. Without his lofty goals, his incredible dedication to teaching and mentoring, and the intense pressure he applies to both himself and everyone around him, I would still be a lump of coal at the bottom of the well. Additionally, a huge thanks to my mentor and bike commuting leader Wojtek for showing me how to enjoy the pursuit of scientific excellence without taking myself too seriously—and also for introducing me to the afternoon espresso break. He is truly an incredible scientist-engineer and a genuinely good person, too. To Web goes thanks for being a fount of information for all things reconstruction.

I have a tremendous amount of respect for my friends, colleagues, and role models in the iStar and AIAI labs: Saj and Sebastian—making science look good, one picture at a time; Adam, for being nice enough to tolerate all my stupid questions and for passing on the Jello lore; Alejandro, for always being the responsible adult (and also contributing the MC dose simulation code in Chapter 5); Amir, of the well-lit methods pictures, for being possibly the only person who makes more inappropriate jokes than me; Qian, Tharindu, and Hao, my tennis buddies—also, swirly frosting, cake, and bunnies; Michael Ketcha, a most dapper dresser, pun artist, and fellow foam enthusiast; Sarah, Ja, and Esme, for being strong women who know their own minds; and everybody else in the lab, for making these last few years a most enjoyable experience. Of course, these people are also extraordinary scientists and inspire me on a daily basis to push myself to even higher achievement.

The work presented in this thesis was not performed in a vacuum, and a number of collaborators contributed their time, expertise, and resources: my rotation advisor, Ken Taguchi, whose insightful comments and expertise on photon counting detectors helped inform the work in Chapter 3; Erik Fredenberg and Mats Lundqvist, whose collective expertise was invaluable in understanding the electronics and physics of silicon strip photon counting detectors; Ed Wang, Ian Yorkston, Nathan Packard, Bill Snyder, Dave Foos, and Sam Richard for their incredible hospitality while I was visiting Rochester and their tremendous support for the head scanner project; and our clinical collaborators, Doug Reh, John Carey, John Carrino, Vassillis Koliatsos, and Nafi Aygun, who help define the problems and assess our solutions in everyday practice.

For my family: my grandmother, who came all the way to America just to make sure a gangly five-year-old could survive in a completely foreign environment and my grandfather, who fostered a hunger for knowledge with his tales of exploration and discovery. A special thanks to my parents, for all the bitter medicine administered during my childhood in preparation for a brighter future, and all the sacrifice that entailed. Your lessons kept me humble, and your ambitions for the future fueled my pursuit of success. I hope I have not disappointed.

To my extended family, the Lazear-Leamon conglomerate, thank you for welcoming me into the fold as if I were one of your own, with warmth and unexpected eagerness—surely it wasn't that shocking for Justin to want to go to prom!

Finally, my husband—to whom this thesis is dedicated—has been my trailblazer through life since I first met him (even after I insisted I was smarter than he was), leading by example and lending me courage to overcome my fears and insecurities. Without his annoyingly insightful questions about my work, my understanding of science and technology would not be as complete. Without his witty repartee, my nights would be that much darker. Most of all, without him, going home at the end of the day would just not be the same.

Dedication:
For Justin.

Contents

List of Tables

List of Figures

Chapter 1: Introduction

Medical imaging focuses on non-invasive visualization of the human body for diagnosis of diseases and guidance of treatment. Since the discovery of x-ray radiation by Röntgen in the late 19th century, imaging has become a crucial component of nearly every medical discipline. X-ray imaging involves the use of high-energy (~10–100 keV) photons to cast a "shadow" of the patient's anatomical structure that can be directly interpreted as a 2-dimensional (2D) projection (radiograph) or reconstructed into a 3-dimensional (3D) representation using computed tomography (CT). The following sections first present a broad introduction of x-ray imaging physics, reconstruction algorithms, detection technologies, and imaging performance. Section IV presents the clinical motivation for a dedicated, cone-beam CT (CBCT) imaging system for high-quality head imaging and the design challenges for such systems in this application. The interested reader can find more detailed treatment of the physics, reconstruction algorithms, and electronics of these systems in texts such as *Medical Imaging Signals and Systems*,[1] *Foundations of Medical Imaging*,[2] and *The Essential Physics of Medical Imaging*.[3]

I. X-Ray Imaging Physics

I.A X-Ray Generation

X-rays are a form of bremsstrahlung radiation caused by deceleration of electrons. Relatively high-energy electrons (1–1000 keV) interact with nuclei and other bound electrons and emit photons with energy equal to the electron's lost kinetic energy. The maximum energy of emitted x-rays, $E_{\max}$, is determined by the initial energy of the electron (equivalent to an electron being completely stopped), with the continuous spectrum of emitted photons spanning 0 and $E_{\max}$.

X-ray tubes are similar to cathode ray tubes: a current is passed through a coil of tungsten filament (cathode) and an electron cloud is produced via thermionic emission. These electrons are accelerated toward the anode (a slanted piece of tungsten) by application of a voltage (30–150 kilovolts (kV) for diagnostic imaging). Bremsstrahlung radiation is emitted in the anode material, with the degree of slant (anode angle) determining the size and shape of the radiation beam that successfully passes through the anode material and x-ray tube housing to become useable x-rays.

Typical x-ray imaging protocols are controlled by 3 factors: kV, mA, and ms. The kV determines the voltage between the anode and the cathode, and therefore the energy spectrum of the generated photons. The tube current, or mA, determines the electron time-density (number of electrons/time), which is roughly proportional to the square of filament temperature.[4] The electrons generated at the filament remain in place until the kV potential is applied, typically in pulsed mode with a series of step-up transformers to achieve the large voltages necessary for generating diagnostic-energy x-ray photons. The duration of the pulse, given in ms, together with the mA, determines the total number of electrons accelerated to the anode; this quantity is indicated by the product of the mA and ms, given as mAs.

I.B X-Ray Interactions with Matter

X-ray photons interact with matter typically found in the human body under 3 mechanisms: photoelectric, Compton, and Rayleigh (coherent scatter). For a given photon energy and atom, the scatter cross-section, $\sigma(E, Z)$, can be computed for any interaction mechanism (or, more conveniently, interpolated from a reference source such as the XCOM database[5]). The units of σ are the same as that of area (cm^2 or mm^2), and the cross-section can be interpreted as the apparent "size" of an atom to a photon—the larger the apparent area, the more likely the photon will "hit" or interact. Appendix A describes the non-coherent (energy-depositing) interactions, photoelectric and Compton, and the manner in which they contribute to interactions in a silicon ($Z = 14$) detector. The probability of photoelectric interaction increases with higher atomic number (roughly proportional to Z^3–Z^4) and decreases with higher energy (inversely proportional to E^3), while the probability of Compton interaction increases with increasing energy. Coherent scatter, such as Rayleigh interactions, do not deposit energy and are a fairly small fraction of the total interactions for diagnostic imaging.

The total scatter cross-section is the sum of the photoelectric, Compton, and Rayleigh cross-sections, and generally decreases with increasing photon energy. A high energy photon is less likely to interact with matter than a low energy photon in the diagnostic imaging range (1–100 keV), except in materials with K-edges such as iodine, where the availability of K-shell electrons increases the photoelectric cross-section.

The mass attenuation, $\frac{\mu}{\rho}$, can be computed from the total scatter cross-section as $\frac{\mu}{\rho} = \frac{\sigma_{total} \cdot N_A}{m_a}$ where N_A is Avogadro's number and m_a is the atomic mass. Linear attenuation, μ, can be computed from mass attenuation by multiplying by the density and has units of inverse length (1/cm or 1/mm). This can be interpreted as the inverse of the "pathlength" of a photon, and is used in computing the expected number of photons I that successfully pass through a length l of material at energy E, given an initial number of photons I_0:

$$I(E) = I_0 e^{\int -\mu(l;E)dl} \tag{1.1}$$

This is the basic relation governing the appearance of x-ray radiographs: denser tissue (such as bones) have higher linear attenuation values, and therefore cast a darker shadow (fewer photons pass through) while soft tissues (lower density and atomic number) attenuate fewer photons and cast a lighter shadow.

I.C X-Ray Detection

Photons can only be measured or detected if they undergo an interaction. Because x-rays are much higher energy than visible light, the interaction chance (Eq. 1.1) in optical detection materials (for example, plastic film or silicon photodiodes) is low—a 40 keV photon has a 3.2% chance to interact in a 200 μm silicon wafer. Therefore, x-ray detectors use materials that are high-Z (increased photoelectric interaction), high-density, and/or increased thickness (such as the Si-strip photon counting detector in Chapter 3, which has a depth of 3.6 mm). X-ray detection mechanisms are broadly separated into two categories: indirect detection (converting x-ray interactions into low-energy secondary photons) or direct detection (directly converting x-ray interactions into electron-hole (e/h) pairs), with differing tradeoffs for cost and performance.

I.C.1 Indirect Detection: Scintillators and Phosphors

Phosphors and scintillators for x-ray imaging have a high probability of photon interaction per unit thickness (selected for high atomic number and density) and convert x-ray photon interactions into many lower-energy photons. As shown in Figure 1.1, energy-depositing interactions (Compton or photoelectric) excite valence electrons into either the exciton or the conduction band (typically 1-3 eV above the valence band for x-ray imaging scintillators), leaving behind a positively charged hole, with the number of e/h pairs proportional to the energy of interaction. Modern x-ray imaging scintillators are doped with impurities in small quantity (<4000 ppm in thallium doped cesium iodide (CsI:Tl) scintillators[6]) to create activator regions, where the majority of light emissions occur.[7] Such regions trap excited electrons and valence-band holes in the forbidden gap (energy states between the valence and conduction band) and facilitate the relatively fast radiative recombination of e/h pairs, resulting in emission of low-energy photons with energy slightly below the band gap energy, as determined by the dopant.[8] Without dopants, secondary photons are emitted only when e/h pairs recombine from the conduction and exciton bands (a slower process) and are more susceptible to recapture, where the emitted photon re-excites a valence electron instead of escaping the crystal (giving rise to afterglow).

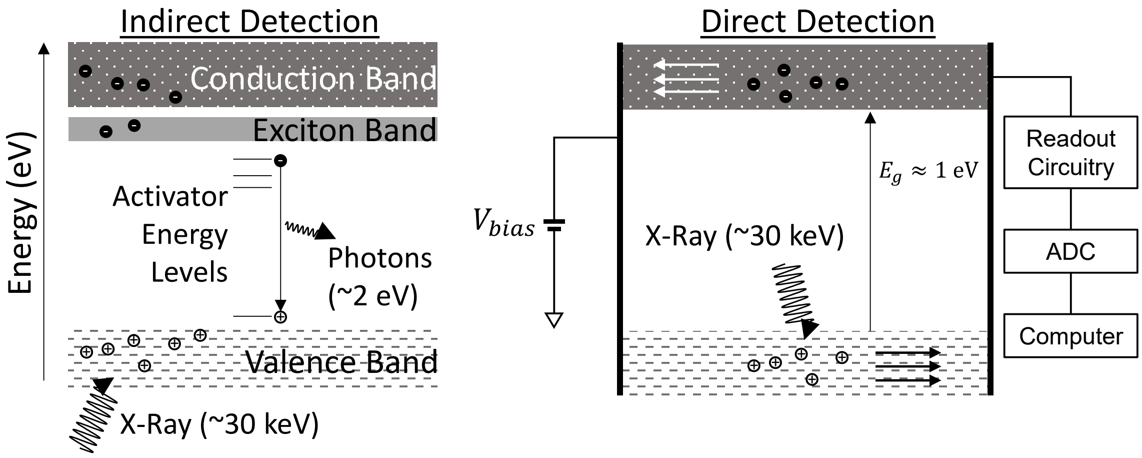

Figure 1.1. Diagram of direct and indirect x-ray detection mechanisms. In indirect x-ray detection, the emitted photons are collected in film, photodiodes, or other optical photon detectors. In direct x-ray detection, the x-ray interaction energy is directly converted to e/h pairs and detected as a current. A small band gap energy, E_g, in direct detection materials results in a large quantum gain for each x-ray interaction.

Scintillators for x-ray imaging are chosen (and doped) such that the emission energy falls within the visible light range, usually ~ 2 eV (a pale green). This facilitates incorporation of x-ray imaging with relatively mature imaging technologies from other fields, such as photography. The first radiographs were produced by sandwiching photographic film between two sheets of phosphor. As the phosphors emitted light from interaction with x-rays, the film was exposed and subsequently developed into an x-ray image using the same process for photographic imaging. After the digital revolution, scintillators or phosphor films were directly grown or deposited onto arrays of photodiodes, such as for flat panel imagers (section II.D.1). Because the secondary photons are emitted isotropically, there is a tradeoff between detector thickness (increased detection efficiency) and the spatial resolution of the resulting image (section III). Thallium doped cesium iodide scintillators can be deposited in needle-like arrays where internal reflection mitigates this spreading effect.

I.C.2 Direct Detection: X-Ray Photoconductors

Similar to x-ray interaction in scintillators, photon interactions that deposit energy in semiconductor materials excite electrons out of the valence band and into the conduction band, again leaving behind positively charged holes. The number of e/h pairs generated is equal to the interaction energy divided by the band gap energy. In semiconductor photoconductors, however, a voltage is applied across the interaction material, causing electrons in the conduction band to drift to the anode. Readout electronics measure the flow of e/h pairs as current, shown in Figure 1.2, and convert it to a digital signal proportional to the deposited interaction energy. Application of a bias voltage causes e/h clouds to diffuse quickly through the material, and the detector material can be made thicker without a large reduction in spatial resolution. For direct x-ray detectors, high detection efficiency is challenged instead by increased dark noise. Band gaps in the range of 1–2 eV are difficult to achieve with higher-Z metallic materials due to more overlapping energy levels. At small (<1 eV) band gap energies, thermal fluctuations can induce high dark currents.

I.D X-Ray Detector Technologies

I.D.1 Flat Panel Detectors

Flat-panel x-ray detectors (FPDs) typically have a large surface area, enabling digital detection of x-ray projections up to 43×43 cm^2. Indirect detection FPDs have a flat scintillator layer on the entrance surface coupled to a 2D array of photodiodes, spaced 100–250 μm apart with fill factor (active detection area) of ~80%. FPD photodiodes are composed of hydrogenated amorphous silicon and are coupled to thin-film transistors (TFTs) for readout.[9] Direct detection FPDs typically replace the scintillator and photodiode with amorphous selenium (a semiconductor material, $Z = 34$) and a charge-integrating capacitor at each pixel. Each column of transistors in the 2D array is connected to a readout amplifier and analog-to-digital signal converter (ADC) at the edge of the panel that interfaces with a frame grabber or other data port on a computer. During active matrix readout, individual "rows" are addressed sequentially by a multiplexer and every TFT in that row is read out simultaneously through the column data line.

Parasitic line capacitance is proportional to the length and width of the readout line. FPD readout lines have typically large length and close packing (small inter-line distances), resulting in high line capacitance. Power supply noise is coupled into the readout lines before the readout amplifier, contributing a fairly large component of the total additive electronics noise.[10] In fact, one of the major limitations to FPDs with smaller detector elements (finer resolution) is the increase in noise from more closely packed readout lines. Despite the relatively high electronics noise (compared to charge-coupled detectors (CCDs) and active pixel sensor detectors), the large detection area and relatively low cost per area of FPDs are advantageous for a wide range of x-ray imaging applications such as radiography, fluoroscopy, and CBCT.

I.D.2 Photon Counting Detectors

Energy integrating detectors (EIDs) such as FPDs accumulate the total charge generated by all interactions in a detector element in the signal integration window, associated with a single image frame. These systems cannot distinguish between, for example, 100 interactions each depositing 10 keV each or 50 interactions depositing 20 keV each. Photon counting x-ray detectors (PCDs) aim to record the total number of interacting photons in a detector element, with the added ability to distinguish between photons of differing energy by application of a threshold (count the photon if above threshold energy, otherwise discard). Every detector element of a PCD is coupled to a channel in an application-specific integrated chip (ASIC), composed of a readout amplifier, pulse shaper, a series of comparators, and counters. The pulse shaper is an analog band-pass filter used to temporally filter (shape) the signal from a single photon interaction. The comparator(s) determine if the pulse height is above threshold, and, if so, the counter associated with that comparator is incremented. Multiple comparators and thresholds can be implemented in a single ASIC channel, enabling multi-energy imaging (photons can be segregated into a number of energy bins). In addition to energy-resolved imaging, application of a threshold can reject additive electronics noise, discussed in further detail in Chapter 3.

In an ideal PCD, the "pulse" from a single photon would be a delta function and every interaction would be uniquely distinguishable. In reality, however, diffusion in the semiconductor material and limited sampling bandwidth on the readout imposes temporal blur on the delta function, with typical pulse widths for commercially available PCDs ranging ~0.5–10 ms.[11] When two or more photons interact in a detector element within this time window, the detector can no longer distinguish the photons, and additionally, the energy information is distorted. This phenomenon is called pulse pileup, and is a major limitation for commercial integration of PCDs into practical use. Algorithms and models accounting for pulse pileup in high-fluence x-ray transmission imaging is the subject of ongoing research,[12–14] and pileup correction algorithms show promise for PCD CT systems.[15] Additionally, as the size of detector elements decrease, high-purity synthesis techniques are developed, and readout hardware improves, pileup effects are reduced (especially for low-dose imaging), but charge sharing effects are increased, detailed in Chapter 3.

Photon counting x-ray detection presents a number of advantages, including improved contrast resolution,[16] rejection of additive electronics noise,[17] and energy thresholding for dual-energy imaging.[18, 19] The advantages and disadvantages of PCDs, as well as modern PCD designs, are discussed in Chapter 3.

I.D.3 Active Pixel Sensors

Another emerging detector technology involves use of active pixel sensors (APS), where the pre-amplifier and ADC are miniaturized such that signal amplification (and digitization) occurs before the signal is propagated through the readout lines, mitigating, for example, the high line noise of traditional FPDs.[20, 21] Such detectors leverage the same general x-ray interaction mechanism as FPDs, but replace the a:Si photodiode and TFT with complementary metal-oxide semiconductor (CMOS) transistors. Additionally, the inherent dark noise of CMOS is lower than that of TFTs, resulting in an order of magnitude decrease in per-pixel additive electronics noise when compared to FPDs.[21] Such technology requires the readout electronics to be printed on a silicon wafer, and therefore most CMOS x-ray detectors are limited in surface area by wafer size and cost. Other relative advantages and disadvantages of FPDs and CMOS detectors for use in CBCT systems are discussed in Chapter 4 and 5.

II. Computed Tomography

Section I discussed the formation and detection of images from x-rays transmitted through an object. Such static (radiographs) or moving (fluoroscopy) images are 2D projections of a 3D object, and much information along the direction of projection is lost. Computed tomography is the process by which the 3D object information is recovered from multiple 2D projections acquired at different angles.

II.A Transmission X-Ray CT Systems

Computed tomography imaging systems are composed of a source of x-rays and a detection mechanism for x-rays. The source and detector rotate about the object, and multiple images are acquired during rotation. The first generation of medical CT scanners featured a strongly collimated “pencil beam” source, which effectively only illuminated one “ray” through the body at a time. The pencil beam and detector were laterally shifted multiple times to acquire a 1D set of parallel-ray projections before rotating and repeating the shifts. The second generation systems removed the collimation in the lateral direction, and used “fan” shaped x-ray beams with multiple non-parallel rays in conjunction with multiple detector elements, arranged in a 1-dimensional (1D) array. This enabled simultaneous collection of a full set of 1D projections for each rotation angle, reducing scan time by an order of magnitude. In both the first and second generations, a full rotation would only provide data for a narrow segment of the patient, and for 3D reconstruction of the patient volume, the entire rotation had to be repeated for multiple slices in the body. The next generations of CT systems introduced spiral or helical scanning (via slip ring technology) which enabled continuous rotation of the source and detector while the patient was translated through the system, and the expansion of the fan-beam coverage in the superior-inferior direction (with multiple 1D detector arrays to match the extended illumination area).

Cone-beam CT systems operate on the same principle (rotating source and detector) as multi-detector CT systems, but the fan beam is extended in the superior-inferior direction, resulting in a large (nearly square) illuminated area per projection. In order to accommodate the large illuminated area, the multi-row detectors are replaced with a large-area detector such as a FPD, and volumetric information can be acquired with a single rotation and no patient translation. This enables a simpler mechanical configuration (no slip rings, for example) but increases artifact and noise, as discussed in section III and IV.

II.B Reconstruction and Algorithms

X-ray CT aims to reconstruct the spatial variation of linear attenuation values in the body. The first x-ray CT reconstruction algorithm was developed in conjunction with first-generation CT systems: x-ray transmission values (I/I_0) were acquired from a series of parallel rays, forming a 1D projection at angle θ. The function representing the object, $f(x, y)$, is a map of linear attenuation values. The measured projection line integrals at each angle, $p(u, \theta)$, can be represented as:

$$p(u,\theta) = -\ln\left(\frac{I(u)}{I_0}\right) = \int_{-\infty}^{\infty}\int_{-\infty}^{\infty} f(x,y)\,\delta(x\cos\theta + y\sin\theta - u)\,\mathrm{d}x\mathrm{d}y \tag{1.2}$$

Figure 1.2 shows an example object and sample projections at $\theta = 0°$ and $\theta = 90°$. A full rotational acquisition spans $\theta \in [0°, 360°]$, and the collection of these acquisitions is typically displayed in a sinogram, shown in Figure 1.2. The Fourier slice theorem states that the 1D Fourier transform of the projection at angle θ is equivalent to a 1D slice of the 2D Fourier transform of the object evaluated at that angle:

$$P(\rho, \theta) = \mathcal{F}_u\{p(u, \theta)\} = F(\rho\, cos\, \theta\, , \rho\, sin\, \theta) \tag{1.3}$$

where $F(f_x, f_y) = \mathcal{F}_{x,y}\{f(x, y)\}$, and $\rho = \sqrt{f_x^2 + f_y^2}$ is the radial spatial frequency. The interested reader may find multiple derivations of this theorem throughout the literature.[1, 22] From this theorem, the full 2D Fourier domain representation of an object can be interpolated from a series of 1D projection data, and reconstructing the original object function, $f(x, y)$, simply involves an inverse 2D Fourier transform. There are a number of disadvantages associated with this approach that limit its practical usefulness. The inverse Fourier transform requires regularly sampled Cartesian data, and small errors due to interpolation of the 1D projection slices can have a large visual impact on the final image in the spatial domain. Additionally, inverse 2D Fourier transforms are fairly computationally intensive.

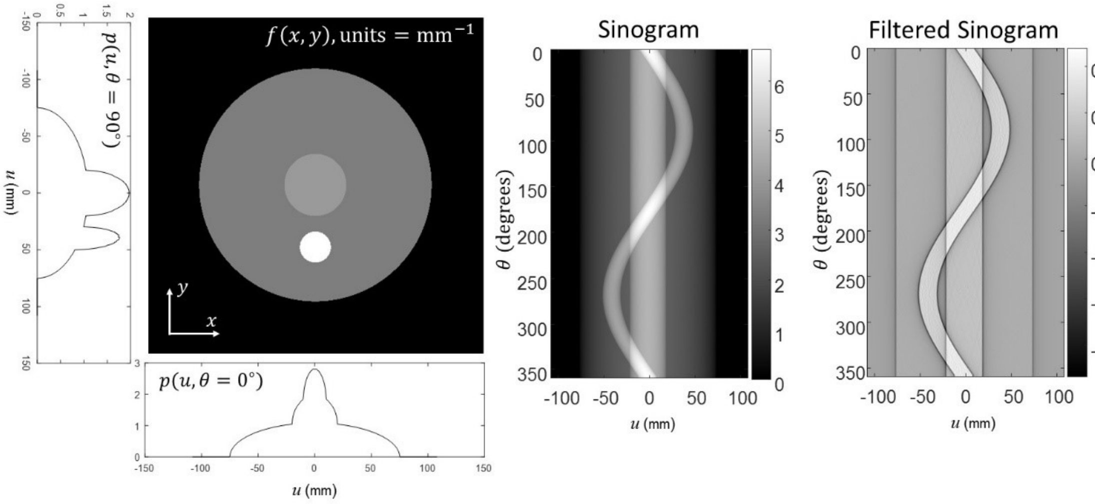

Figure 1.2. Parallel-ray geometry projections are shown for a test object at 0 and 90 degrees. The associated spatial domain sinogram and the filtered spatial domain sinogram show the sinusoidal trajectory of the dense object as the angle of projection changes.

A more practical method for CT reconstruction is the filtered backprojection algorithm, which relates the ramp-filtered projection data to the object:

$$\begin{aligned} f(x,y) &= \int_0^{2\pi}\int_0^{\infty} F(\rho\cos\theta,\rho\sin\theta)e^{2\pi j\rho(x\cos\theta+y\sin\theta)}\rho\mathrm{d}\rho\mathrm{d}\theta \\ &= \int_0^{\pi}\left[\int_{-\infty}^{\infty} P(\rho,\theta)|\rho|e^{2\pi j\rho u}\mathrm{d}\rho\right]_{u=x\cos\theta+y\sin\theta}\mathrm{d}\theta \end{aligned} \tag{1.4}$$

The inner integral is the inverse 1D Fourier transform of the (previously Fourier transformed) projection data, $P(\rho,\theta)$, multiplied with a frequency-domain ramp filter, $|\rho|$—a filtering operation. The filtered projection, $p_{\text{filt}}(u,\theta)$ (shown in Figure 1.2 as the filtered sinogram), is evaluated at $u = x\cos\theta + y\sin\theta$, which is the backprojection step converting $p_{\text{filt}}(u,\theta)$ into a 2D backprojection image. The backprojection images for each acquisition angle are summed (a fast operation on computers) to give a reconstruction of the original object.

The general filtered backprojection principle in parallel beam geometry can be applied to divergent beam data (second generation CT systems)[23] to account for changes in ray density and projection sampling. One may note, additionally, that the transform of Eq. (1.4) applies to 2D objects, and 3D reconstruction is approximated by assuming that 3D objects are stacks of 2D objects. A practical algorithm for 3D filtered backprojection by Feldkamp et al[24] extended such 2D slice reconstruction algorithms into the third dimension with additional weighting factors to account for the cone-beam geometry of the system. A modified version of this implementation was used throughout this thesis to generate 3D reconstructions from data acquired on CBCT systems.

In addition to the analytical reconstruction techniques described above, reconstruction can be performed algebraically by discretizing the object and measurements:

$$p_j = -\ln\left(\frac{I_j}{I_0}\right) = \int \mu(l;E)\,\mathrm{d}l \approx \sum_i^N \mu_i \cdot l_{ij} \tag{1.5}$$

The estimate of the object is divided into N voxels with attenuation value μ_i. Similar to Eq. (1.2), p_j is the j^{th} projection line integral measured at a discretized location on the detector, and l_{ij} is the segment length of the associated ray through the i^{th} voxel. In this framework, the values for $\vec{\mu}$ are unknown, and given a sufficiently large and well-sampled collection of measurements $\vec{p}$, the object composition can be solved directly as a system of equations. In practice, however, the size of $\vec{p}$ and $\vec{\mu}$ are large and iterative methods are typically used out of computational necessity. Additionally, instead of exactly solving the system, the problem can be formulated as an optimization problem that estimates the most likely object $\vec{\mu}$ given the set of measurements $\vec{p}$. This approach enables the inclusion of statistical models of the measurement noise, system properties, and object properties (e.g., spatial frequency content of the object), ultimately leading to a more accurate representation of the real object. Development of more complete system models,[25, 26] noise models,[27] and image regularization approaches[28, 29] is the subject of ongoing research.

III. X-Ray Imaging System Performance

Images are intended to be representations of reality, but imaging systems—like all measurement devices—impart transformations (blur, artifacts) and uncertainty (noise) in the process of image formation. For medical imaging in particular, the ability to understand and quantitatively describe how the system transforms the original information through measurement and reconstruction is a crucial component of both patient safety as well as continued development of increasingly high-performance and high-fidelity systems. This section presents the metrics governing imaging performance, tradeoffs in system design for improving specific aspects of imaging performance (discussed in detail in Chapter 4), as well as a brief treatment of deterministic effects that cause artifacts in x-ray images, particularly those associated with CBCT systems.

III.A Spatial Resolution

Spatial resolution is determined by the minimum separation between two points beyond which they are no longer distinguishable as two distinct objects. The spatial-domain metrics of resolution are characterized by: the point-spread function (PSF) using an impulse function input; the line-spread function (LSF) using a line function input; and the edge-spread function (ESF) using a step function input. The effects of the system on the input can be quantified as $g(x,y,z) = f(x,y,z) * h(x,y,z)$, where $g(x,y,z)$ is the measured output, $f(x,y,z)$ is the input function, and $h(x,y,z)$ is the impulse response function of the imaging system. For linear systems, the impulse response function h can be applied to any input (i.e., convolved with any form of $f(x,y,z)$). Therefore, the impulse response function is intrinsic to the system, and is a measure of system performance that is independent of the input. A useful metric for describing the spatial resolution of a system is the full width at half maximum (FWHM) of the LSF, which is the spatial width of the LSF at half of its maximum value. This metric simplifies much of the information imparted by the LSF (such as the overall shape or presence of edge-enhancing negative lobes, etc.), but is generally useful for comparing systems where the shape of the LSF is expected to be similar—a smaller FWHM typically indicates better spatial resolution.

An alternative metric, the modulation transfer function (MTF), is defined in the spatial frequency domain as the Fourier transform of the LSF: $\mathrm{MTF}(f) = \mathcal{F}_x\{\mathrm{LSF}(x)\}$. The physical interpretation of the MTF is the attenuation or modulation of signal amplitude at frequency *f*. For example, the frequency at which the amplitude of the MTF falls to 50% is called the f50, and an input sinusoidal wave with frequency equal to f50 will have its output amplitude reduced by 50%. Note that the actual frequency of the input signal in this case is unchanged—only the amplitude is modulated. This should not be confused with the phenomenon of signal aliasing, when the Nyquist criterion[30] is violated, and signal frequencies are aliased into a lower frequency band due to insufficient sampling.

In x-ray imaging systems, there are a number of factors that affect spatial resolution, many of which have tradeoffs with the resulting image noise, discussed in section III.B. The two major sources of resolution degradation come from source and detector blur. Source blur is a phenomenon introduced by the width of the electron beam as projected onto the tungsten anode in the x-ray source, called the focal spot size. This blur is magnified by the system magnification, implying strong tradeoffs with detector blur in the image plane (discussed in Chatper 4). Detector blur results from the spreading and subsequent collection of secondary quanta generated in the x-ray detection process. As noted in section I.C, indirect detection scintillators have generally poorer resolution than direct detection scintillators because the emission of secondary photons is isotropic and tends to diffuse (and potentially reabsorb, scatter, and re-excite, yielding even further reduction of spatial resolution) before being collected. The aperture size is determined by the size of the photodiode or active area of the anode for each detector element, and also contributes to detector blur.

III.B Noise

Image noise is the stochastic deviation of signal values from the ground truth signal value, and the magnitude of a voxel in a 3D image can be represented as an instantiation of a random variable (RV). The standard deviation of this RV is what is commonly reported as the “noise,” and can be measured by taking repeated, independent realizations of the same RV (i.e., imaging the same object repeatedly with the same parameters). Oftentimes, this process is prohibitively resource-intensive, and we leverage the ergodicity of neighboring voxels in a uniform-signal region to estimate the standard deviation from a single global realization of the image. Standard deviation in a uniform region is a convenient metric—and is reported throughout this thesis as a general indicator of the noise magnitude—but does not provide information about the noise texture or correlation. Much as the signal resolution can be modulated by the imaging system, noise correlations can be introduced, modulating the noise power at various frequency bands as well as changing the overall magnitude of the noise power spectrum (NPS). The variance (square of the standard deviation) of a voxel is equal to the integral of the NPS, and therefore two images with the same variance in a uniform area can appear dramatically different if the frequency distribution of the NPS is different. Finally, the signal-to-noise ratio (SNR) is the ratio between the expected signal and the noise (standard deviation), a useful metric to compare the relative magnitude of noise and signal.

There are two broad categories for noise sources in x-ray imaging: noise originating from fluctuations in the number of x-ray photons incident on the detector (quantum noise) and noise introduced by the detection process (detector noise). The generation of x-rays is a Poisson process and interaction of x-rays in matter is a binomial selection on the generated photons. Therefore, the number of photons interacting in the detector is a Poisson RV—as described in Eq. (1.1), the number of photons that pass through the object, I, is an expectation value representing the mean of the Poisson RV. The mean and the variance of a Poisson RV are equal, and therefore the SNR scales as the square root of the total number of photons. The number of photons per unit area in x-ray imaging scales linearly with the mAs (see Section I.A), implying tradeoffs between patient risk (radiation dose) and image quality (SNR), detailed in Chapter 2, 4, and 6. Other approaches to increase the number of detected photons per detector element is to increase the thickness of the detection material or to increase the aperture size (photodiode), both involving a reduction in spatial resolution. The propagation and introduction of noise in the system is discussed throughout this thesis, with specific consideration for design of a CBCT system for detection of low-contrast lesions.

III.C Propagation of Signal and Noise

As we described in section III.A, the imaging system can be mathematically modeled as an impulse response function or transfer function (in the spatial frequency domain) that alters the contrast and noise magnitude in different frequency bands of the input signal. The system transfer function can be divided into a cascade of individual stages in the imaging chain, composed of blur, gain and sampling stages.[31, 32] Chapter 3 details the development of a new system model for PCDs, and Chapter 4 describes the use of system imaging performance models in the optimization and design of a dedicated CBCT head scanner.

III.D Imaging Performance Metrics and Detectability

The modulated signal and NPS can be combined to derive the detective quantum efficiency (DQE) as a function of spatial frequency (Chapter 5):

$$\mathrm{DQE}(f) = \frac{\mathrm{SNR}_{\mathrm{Out}}^2}{\mathrm{SNR}_{\mathrm{In}}^2} = \frac{\bar{G} \cdot \mathrm{MTF}^2(f)}{\mathrm{NPS}(f)/\bar{q}_0} \tag{1.6}$$

where $\mathrm{SNR}_{\mathrm{Out}}$ and $\mathrm{SNR}_{\mathrm{In}}$ are the signal to noise ratio at the output and input of the system, respectively, $\bar{G}$ is the system quantum gain, $\bar{q}_0$ is the incident photon fluence, and f is the spatial frequency. For x-ray imaging systems, $\mathrm{SNR}_{\mathrm{In}}^2 = \bar{q}_0$ from Poisson statistics discussed in III.B. An ideal imaging system has DQE(f) = 1, corresponding to a system that does not transform the signal or noise at any frequency.

The product of the DQE and the incident quanta ($\mathrm{SNR}_{\mathrm{Out}}^2$) is the signal-to-noise power ratio in each frequency bin of the final image and is equivalent to the noise equivalent quanta, NEQ(f). The NEQ is defined as the number of quanta incident on an ideal detector that gives the same output SNR as the non-ideal detector being evaluated. This metric allows a dose-dependent comparison of imaging systems as well as a quantitative metric of the final image quality.

The other component of developing a task-specific imaging performance metric is defining the relevant information or detection task. The derivation and formulation of two tasks corresponding to a low-contrast lesion and a high-contrast fracture is described in Chapter 4. In each case, the task consists of a Fourier domain template of the frequencies of interest in the object scaled by the signal power of the object—high contrast objects have higher signal power per volume. The detectability index, d', is approximately the integrated SNR of the final image weighted by the task function. While such an approach is grounded in detection theory,[33] Fourier-domain metrics for detectability are used in this thesis as a guide for system design rather than as a direct prediction of observer performance, although studies have shown that such a metric can correspond fairly well with real observer performance.[34]

III.E Artifacts

Artifacts are image-degrading effects resulting from non-stochastic properties of the system. If the same object is imaged twice, the appearance of the image artifacts will not change. This section will primarily focus on a description of image artifacts in CBCT systems and their effect on low-contrast lesion detection. An example of these artifacts can be found in Figure 1.3.[a]

Scattered radiation, briefly discussed in section I.A, is caused by Compton and Rayleigh interactions in the object. When a photon scatters, its path of travel is deflected and the subsequent photon interaction in the detector is incorrectly attributed to a different ray during backprojection. Generally, the recorded scattered radiation has low spatial frequency content—described as a “fog” in film-based radiography—and therefore its effect is most severe in regions where the primary signal (unscattered radiation) is lowest. In 3D reconstructions, the approximately additive scatter fluence term in the projection domain manifests as a low-frequency shading or cupping across the image, shown in Figure 1.3b. While Chapter 4 and Appendix B show that the local detectability index is not changed by scatter correction, the cupping artifact presents challenges for visualization of low-contrast objects where the location of the stimulus is unknown. A number of scatter compensation techniques have been developed, falling into two broad categories: scatter rejection before detection,[35, 36] or scatter estimation and subtraction.[37] The two approaches have different implications for noise and signal in the reconstructed image, and as discussed in Chapter 4, design of a CBCT scanner for

---

[a] Figure reproduced from *Cone Beam Computed Tomography: Cone-Beam CT Image Quality*[233] with permission from the author.

low-contrast lesion detection considered both mechanical scatter rejection (anti-scatter grids and geometrical scatter rejection) and post-acquisition scatter subtraction (Monte Carlo scatter estimation).

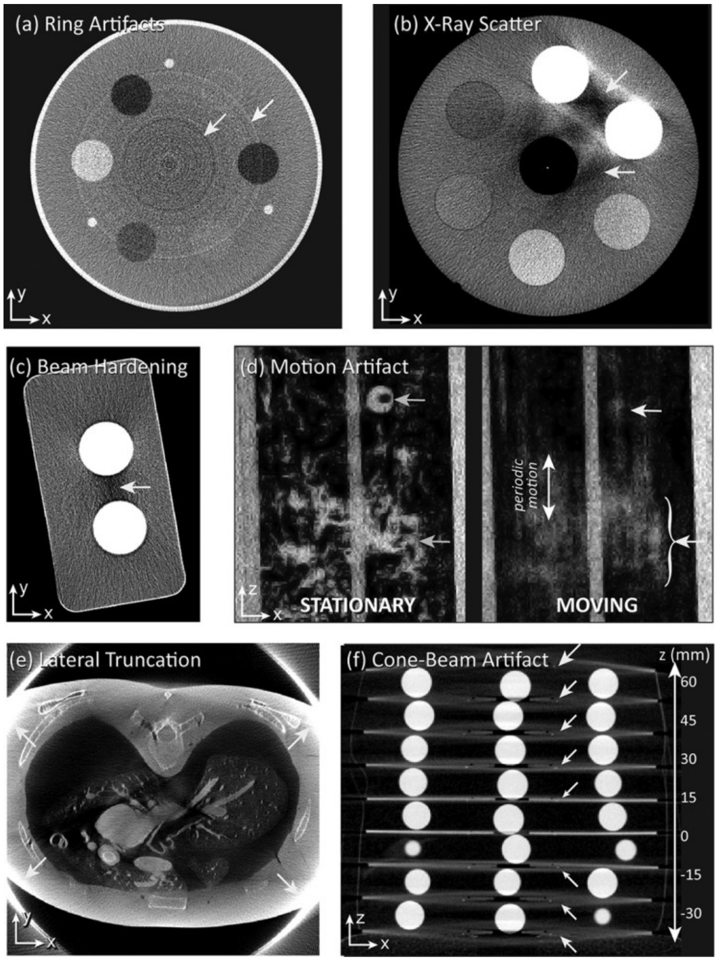

Figure 1.3. Example of CBCT artifacts such as (a) ring artifacts arising from detector signal irregularities, (b) scatter artifacts, (c) beam hardening artifacts, (d) motion artifacts, (e) truncation artifacts, and (f) cone-beam artifacts. Figure reproduced with permission from the author.

Another fairly severe artifact for low-contrast visualization in CBCT images is the cone-beam artifact, illustrated in Figure 1.3f. When CT scanners moved from fan-beam (2D slice reconstruction) to cone-beam (with 3D volume reconstruction from a single rotation), Tuy's sampling condition[38] was violated. The resulting artifact presents as a nulling of z-frequencies in a cone shape that becomes increasingly severe farther from the central slice. Especially near the top of the cranium, large shading effects from the missing frequencies can confound low-contrast lesion detection. While model-based iterative reconstruction techniques can mitigate the appearance of cone-beam artifacts using image regularization, the problem of cone-beam artifact is still fundamentally one of missing information and changes in acquisition geometry are required to eliminate this effect.[39, 40] Additional methods leverage the deterministic nature of the artifact appearance and perform a series of back- and forward-projections to estimate and subtract the appearance of cone-beam artifacts.[41]

Beam hardening artifacts arise from the polyenergetic nature of the x-ray beam. As discussed in section I.A, the energy of each photon emitted from an x-ray source is drawn from the bremsstrahlung energy spectrum. As the x-ray interacts in matter, lower energy photons have a higher chance of being absorbed, and the average energy of photons passing through the object tends to increase as the pathlength increases, causing an apparent reduction in linear attenuation for the line integral. Beam hardening artifacts are particularly severe in areas with high-attenuation tissues like bone or through large pathlengths (lateral projection through the abdomen). The appearance of beam hardening artifacts are similar to scatter artifacts in low-density regions (illustrated in Figure 1.3c). Near high-density, high-atomic-number objects (like bone) it can cause streaks or “blooming” effects that can obscure low-contrast lesions completely. Beam hardening corrections are performed on the line integral data and use a pre-generated look-up table to remap the apparent attenuation to the actual attenuation given a particular incident x-ray spectrum.

A number of other, more subtle artifacts such as temporal detector lag, detector veiling glare, off-focal radiation, ring artifacts, truncation, and patient motion during the scan can also negatively affect low-contrast lesion detection. Chapter 6 discusses compensation techniques for some of these effects.

IV. Clinical Motivation

IV.A Clinical Applications for Head Imaging with X-Ray CT

Imaging systems featuring both high spatial resolution performance and good soft tissue (low-contrast) visualization are important for diagnostic head imaging, which can be broadly divided into neurological and otolaryngological-head and neck (OHN) / maxillofacial diseases and injuries, discussed below. The short scan-times of CT systems (< 1 minute) are especially advantageous for diagnosis of time-sensitive head injuries as well as minimizing patient motion artifacts (important for high-resolution imaging). Additionally, many CBCT and MDCT systems are capable of spatial resolution approaching or exceeding 2 line pairs / mm (MTF f50) in the reconstructed image, and are particularly suitable for imaging of high-contrast fractures and fine bone anatomy.

Many diagnostic applications of OHN imaging focus on high-contrast visualization such as cholesteatoma,[42] superior semicircular canal dehiscence (SSCD),[43] laryngeal cartilaginous tumor,[44] and choanal atresia.[45] In such applications, high isotropic spatial resolution is required due to a need for planar reformatting. Semicircular canals (with each semicircle in a separate plane) have internal diameter ranging 0.7–2.1 mm,[46] and diagnosis of SSCD requires reformation of the images in the plane of the superior canal. A retrospective study found a majority of patients benefited from high-resolution, 0.5-mm beam collimation MDCT scans for proper visualization of dehiscence and surrounding structures, improving specificity and sensitivity over standard 1.0-mm collimation scanning techniques.[47] In addition to high-contrast imaging tasks, OHN cancer diagnosis and treatment planning require improved soft tissue visualization and additionally benefit from functional imaging available with combined PET/CT.[48]

Intracranial hemorrhage (ICH) is associated with a number of neurological diseases and injuries, including traumatic brain injury (TBI), hemorrhagic stroke, aneurysm, hypertensive intracerebral hemorrhage, and post-surgical hemorrhage. There are estimated to be 1.7 million visits to the emergency department annually[49] for TBI—with a 10–15% mortality rate for cases of severe TBI[50]—and ~800,000 cases of stroke annually, with about 13% of those hemorrhagic.[51] Acute ICH typically presents as a hyperattenuating lesion in non-contrast (NC) CT.[52] Common types of ICH include epidural hematoma (EDH), subdural hematoma (SDH), subarachnoid hemorrhage (SAH), and intraparenchymal hemorrhage (IPH) and exhibit an evolution in contrast that initially increases during the hyperacute and acute stages (hyperdense, ~40-80 HU contrast within ~3 days) and subsequently decreases to subacute (isodense) and chronic (hypodense, -5–20 HU contrast in ~10–20 days or longer).[53]

Non-contrast multi-detector CT (NC-MDCT) is the most prevalent front-line imaging modality for detection, diagnosis, and monitoring of ICH in its acute stage, offering speed and high sensitivity to the presence of fresh blood in the brain. MDCT also provides utility in detecting temporal bone fractures[54] and other middle ear diseases,[55] although traditionally limited in isotropic high-resolution imaging due to beam collimation and layout of multi-row detectors. For stroke imaging, NC-MDCT is widely used for exclusion of ICH,[56] with CT perfusion subsequently providing diagnosis, prognosis, and direction of therapeutic course.[57]

IV.B Benefits of a Point-of-Care CBCT Imaging System

For patients in critical care units as well as remote locations such as field hospitals, transport to the MDCT or MRI suite carries significant safety considerations. Especially in the critical care setting, patient transport is associated with alarmingly high moribidity and mortality. For example, a retrospective study indicated that adverse effects occur in up to 70% of all patient transports,[58] with 8% of such events being potentially life-threatening. A prospective study of 125 intrahospital transports of ICU patients indicated a 1 in 3 rate of adverse events, with 75% occurring while the patient was in the Radiology department.[59] Ott et al.[60] described a spectrum of contributing factors affecting patient safety in transport to Radiology, including risk of dislodging tubes and lines, movement from the patient transport bed to the scanner couch (and back), the potential need for sedation for relief of claustrophobia, and separation from their usual caregivers. Despite such risks, however, the benefits gained in diagnostic confidence and direction of proper therapy justify the significant role of imaging in managing critically ill patients. For example, 45% of cases experience a change in management based solely on radiological findings (e.g., detection of new lesions).[61]

The importance of imaging in the diagnosis and treatment of head and neck injuries combined with the risks of patient transport to the scanner suite motivates the development of point-of-care imaging for monitoring and management of patients with brain injury. A variety of commercially available portable imaging systems merit investigation for such application, including mobile C-arms for CBCT, [62, 63] CBCT systems designed specifically for head imaging,[64, 65] portable CT scanners,[66, 67] and even portable MRI.[68] Such systems exhibit varying degrees of imaging performance and logistical compatibility with the critical care environment.

IV.C Advantages and Challenges of CBCT

Cone-beam CT offers relative simplicity and flexibility in system design, with numerous embodiments emerging over the last two decades for interventional[69–77] and diagnostic[78–82] imaging applications. Such systems can offer mechanical simplicity, portability, capability for 2D radiographic / fluoroscopic as well as 3D CBCT imaging, native isotropic resolution, and relatively low cost. For image-guided interventions, CBCT image quality may be sufficient for the task of localizing known targets and adjacent vital anatomy,[71, 83] but for diagnostic head imaging, such systems tend to be limited to high-contrast imaging of bone.[84] For neuroimaging in particular, identification of natural anatomical landmarks [e.g., gray and white matter and cerebrospinal fluid (CSF)] requires contrast resolution better than ~20 HU. Such capability is primarily challenged by image noise and nonuniformity (artifacts) to which CBCT systems are particularly susceptible.[85] Achieving contrast resolution sufficient for reliable detection of ICH at the point of care requires a significant advance in CBCT imaging performance without compromising other advantageous characteristics of portability, open geometry, ease of use, and cost. This thesis will present a physics-based approach to design and optimize the imaging performance of such a system.

V. Outline for Thesis

Thesis Statement: A cone-beam computed tomography system can be developed with imaging performance sufficient for high-quality imaging of the head and suitable to deployment at the point of care, in settings such as critical care units, practitioner's offices, or field hospitals.

Chapter 2 presents an assessment of a head-and-neck CBCT system to determine the potential limitations and benefits of such systems for high-quality imaging of the head. The results were compared to literature on other such systems, and it was found that low-contrast visualization was challenging, primarily due to high detector noise and large amounts of scatter. Chapter 3 details the development of an imaging performance model for PCDs to assess the relative benefits (and limitations) of such detectors in improving noise, contrast, and dose efficiency in a CBCT system. The model revealed important implications for energy resolution, noise, and spatial resolution as a function of energy threshold and charge sharing rejection. While the low-dose performance of PCDs was found to be advantageous compared to an equivalent EID, and spatial resolution surpassed current state-of-the-art FPDs, the physical size, relatively small FOV, and count-rate limitations of such detectors suggested that alternative EID technologies may be more suitable for an initial prototype design.

The design and optimization of a new CBCT system dedicated to detection of low-contrast ICH (with consideration for high-contrast fracture) is detailed in Chapter 4. The work uses a cascaded systems model of the imaging chain to optimize the system configuration and hardware (geometry, detector, x-ray source, etc.) for detection of the low-contrast ICH task. While the prototype design was guided by these results, Chapter 4 further details hardware and logistical considerations for system design. Chapter 5 discusses FPD improvements for improved noise performance, including comparison of dual-gain detector readout to use of bowtie filter with high-gain detector readout to further improve ICH detectability. Chapter 6 presents the assessment of the prototype CBCT scanner designed in Chapter 4 as a prerequisite for clinical studies in the neurological critical care unit.

Chapter 2: Imaging Performance of a Head and Neck CBCT System

I. Introduction

X-ray CT has proliferated over the last several decades as an important medical imaging modality with widespread application in diagnosis, surgical guidance, and monitoring. Key considerations in applying this prevalent modality are knowledge of the radiation dose and imaging performance characteristics. A variety of application-specific embodiments of CBCT for the head have emerged over the last decade, including systems dedicated to dental/maxillofacial,[86–95] temporal bone,[43, 54, 96] and even soft tissue imaging,[97] with each offering the potential for isotropic, sub-millimeter spatial resolution combined with varying levels of soft-tissue contrast resolution and short scan times. Maxillofacial and temporal bone CBCT systems are of particular interest as point-of-care imaging systems due to their prevalence, low cost, and compact geometries. Such systems, however, typically involve varied system geometries, scan orbits, radiation dose profiles, and as-yet uncharacterized soft-tissue imaging performance. A quantitative technical assessment grounded in scientific methodology and imaging physics is important to rigorously quantify the performance of such systems in their early stages of development and translation. A first step toward development of a dedicated system for high-quality soft tissue imaging in the head with a point-of-care system is a rigorous technical assessment of imaging performance as demonstrated in a current state of the art CBCT scanner.

This chapter therefore describes the technical assessment of a new CBCT system (CS 9300, Carestream Health, Rochester NY) developed specifically for otolaryngology-head and neck surgery (OHNS) and maxillofacial imaging [alternatively—ear, nose, and throat (ENT) imaging]. Comparable systems that are currently commercially available include the MiniCAT (Xoran, Ann Arbor MI),[85] CB Mercuray (Hitachi, Twinsburg OH), NewTom (QR, Verona Italy), i-CAT (Imaging Sciences, Hatfield PA), Accuitomo 170 (J. Morita USA, Irvine CA), and others. The CS 9300 includes modifications of various characteristics in comparison to previous platforms (9000 series) from the same manufacturer, including: options for expanded field of view (FOV); a variety of full-scan (360°) and short-scan (~210° or greater) protocols with various FOV and scan speed; pulsed or continuous x-ray source; and enhanced acquisition and reconstruction software.

The technical assessment reported below addresses the dosimetric properties and image quality associated with manufacturer-specified technique protocols of the CS 9300 for OHNS imaging. The work was first reported in Xu et al., "Technical assessment of a cone-beam CT scanner for otolaryngology imaging: image quality, dose, and technique protocols."[65] Results are compared to reports in the scientific literature and focus on a system-specific technical assessment that was performed firstly as a basis of performance comparison with other dedicated CBCT systems for imaging of the head and neck, and secondly as an evaluation of the benefits and limitations of such systems for potential application in high-quality brain imaging at the point of care.

II. Methods and Materials

II.A. The CS 9300 and Default Protocols

According to the manufacturer, the intended use of the CS 9300 scanner is "... to produce 3D digital x-ray images of the dento-maxillo-facial and ENT regions as diagnostic support for pediatric and adult patients." The scanner capabilities and specifications are summarized in Table 2.1. The default imaging protocols deployed on the system are summarized in Table 2.2, including three sinus protocols (denoted S) and four ear (temporal bone) protocols (denoted E). All measurements involving the unilateral temporal bone protocols (E2, E3, and E4) were performed with the right ear protocol. The left ear protocols were spot-checked to be symmetric with respect to the contralateral side. The angular extent, FOV, and number of projections are all non-modifiable parameters for each imaging protocol, but the kV and mAs may be freely adjusted at the discretion of the technologist. The “short-scan” orbits are comparable to half-scan orbits (180^o + fan), with orbital extent particular to each protocol detailed separately below and in Table 2.2.

An initial technical assessment was performed (data not shown) that motivated modifications to the scan orbits (start and stop angles of the x-ray source and detector) and the technique chart (reduction in kV and mAs). All results presented below pertain to protocols and measurements *after* such modifications. The resulting protocols reduced dose by up to 30% and better situated the short-scan orbits to impart dose preferentially to the posterior of the head (and reduce anterior dose—e.g., to the eyes).

Parameter	Value
X-ray tube	CEI OPX 110
Power (max)	1.5 kW
Anode	Fixed target (W)
Focal spot size	0.7 FS
Tube voltage	60 – 90 kV (1 kV steps)
Tube current	2 – 15 mA (1 mA steps)
X-ray pulse rate	33 p/s (1 pulse per 30 ms)
Inherent filtration	2.5 mm Al equiv. (70 kV)
Added filtration	0.1 mm Cu (70 kV)
Bowtie filter	Custom (Cu)
HVL (70 kV)	4.6 mm Al
HVL (80 kV)	5.0 mm Al
HVL (85 kV)	5.4 mm Al
HVL (90 kV)	5.7 mm Al
HVL (100 kV)	6.0 mm Al
Detector type	Varian 2520
Detector readout mode	Dynamic gain
Pixel size (intrinsic)	0.127 mm
Pixel binning	
(S1, S3, S3, E1, E4)	2×2 (0.254 mm)
(E2, E3)	1×1 (0.127 mm)
X-ray converter	CsI:Tl
Antiscatter grid	None
Reconstruction filter	Not specified
Voxel Size	90 – 500 μm

Table 2.1. Summary of system parameters and specifications. The x-ray tube is the CEI OPX 110 (Trophy, Verona Italy), and the x-ray detector is Model 2520 (Varian Imaging Products, Palo Alto CA).

Protocol	kV	mA	mAs	FOV (cm^3)	Scan Time (s)	Orbital Extent	Voxel Size (mm)	Volume Size (voxels)
Sinus 1 (S1)	85	5	56	17×13.5×17	11.3	Full (360°)	0.3	567×567×450
Sinus 2 (S2)	85	5	32	17×11×17	6.4	Short (~204°)	0.5	339×339×220
Sinus 3 (S3)	85	5	51	17×11×17	10.2	Short (~204°)	0.3	567×567×367
Ear 1 (E1)	90	5	43	17×6×17	8.5	Short (~204°)	0.2	567×567×200
Ear 2 (E2)	90	6.3	126	5×5×5	20	Short (~188°)	0.2	250×250×250
Ear 3 (E3)	90	6.3	76	5×5×5	12	Short (~188°)	0.2	250×250×250
Ear 4 (E4)	90	6.3	76	8×8×8	12	Short (~192°)	0.3	267×267×267

Table 2.2. Technique chart for various protocols deployed on the scanner. Three sinus protocols include: S1 (large FOV); S2 (fast scan, small FOV); and S3 (small FOV, high quality). Four ear protocols include: E1 (bilateral FOV); E2 (unilateral (R or L), high-resolution); E3 (unilateral, fast); and E4 (unilateral, larger FOV). Each protocol entails different FOV, scan time, number of projections per scan, radiation dose, scan angle, and image quality. Voxel size (mm) is isotropic in *x*, *y*, and *z* directions.

II.B. Dose Measurement: Experimental Setup

Dose measurements were performed with methodology adapted from those outlined in AAPM Task Group Report #111.[25] As shown in Figure 2.1, three acrylic cylindrical phantoms of 16 cm diameter (CTDI phantoms) were stacked along the central cylindrical axis to simulate the "head" and a 0.6 cm^3 Farmer ionization chamber was used in conjunction with a Radcal electrometer (AccuDose, Radcal Corp., Monrovia CA) to measure the central and peripheral doses imparted for all protocols listed in Table 2.1. Dose measurements used up-to-date manufacturer calibration of the electrometer and accounted for temperature-pressure corrections at the time of measurement. Measurements were nominally performed at the level of the central axial slice of the image volume. A further measurement of dose as a function of kV and mAs was performed for the S1 protocol and the E1 protocol. The central dose (D_0) was defined as the absolute dose (mGy) at the center of the CTDI phantom for each scan for each protocol.

Peripheral dose was measured at four cardinal locations at the periphery of the CTDI phantom (at the same level as the central dose), with all other experimental factors held constant. Since several of the protocols involved short-scan orbits of the source and detector about the head, the peripheral dose varied at each of the measurement points (e.g., highest at the posterior point for short-scan orbits in which the source traverses the posterior of the head). In addition to the central absolute dose (D_0) the four peripheral dose measurements (D_{periph}) were averaged to yield a "weighted" dose value analogous to CTDI_w, specifically: ($D_\text{W} = \frac{1}{3} D_o + \frac{2}{3} \overline{D}_{\text{periph}}$). The dose-length product was defined as $DLP = D_\text{W} \cdot L$. To the limited extent that is meaningful to convert the absolute dose from such orbits to the "effective dose" (D_E, mSv) and to permit comparison to other systems for which results have been reported only in terms of effective dose (mSv), we used the tissue conversion factor for the head ($k_{\text{head}} = 0.0023$ mSv/mGy/cm) given by ICRP Publication 103[26] and computed $D_\text{E} = k_{\text{head}} \cdot DLP$. The limitation and approximation of this approach is recognized—namely, that effective dose conversion for short-scan orbits is not strictly defined. Specifically, the required tissue conversion factors were developed in the context of conversion from CTDI_w. The short-scan measurements of absolute dose (mGy) are considered to be valid, but the effective dose values (mSv) should be recognized as approximate and are only included for comparison with other systems that only report mSv.

Dose distribution "maps" were generated using a smoothed interpolation of the five measurement points (the central dose and four peripheral doses) for each protocol. The dose maps provide visualization of heterogeneous dose distribution about the lateral, posterior, and anterior aspects of the head, particularly for the various short-scan protocols. They do not pretend to account for tissue heterogeneities, though they are a valuable means of conveying dose distributions to the clinicians and manufacturer with respect to the various scan orbit pathways.

A further study was conducted with S1 and E1 protocols to characterize the out-of-field dose [$D_0(z)$] along the longitudinal axis. The absolute dose to the center of the CTDI phantom was measured as a function of z (longitudinal position) beginning at the central plane, covering the extent of the primary collimated x-ray field, and extending inferiorly beyond the field toward the "neck." The same experimental setup of three stacked CTDI phantoms was used for this assessment, with the ionization chamber position manually translated along the z-axis in ~2 cm increments.

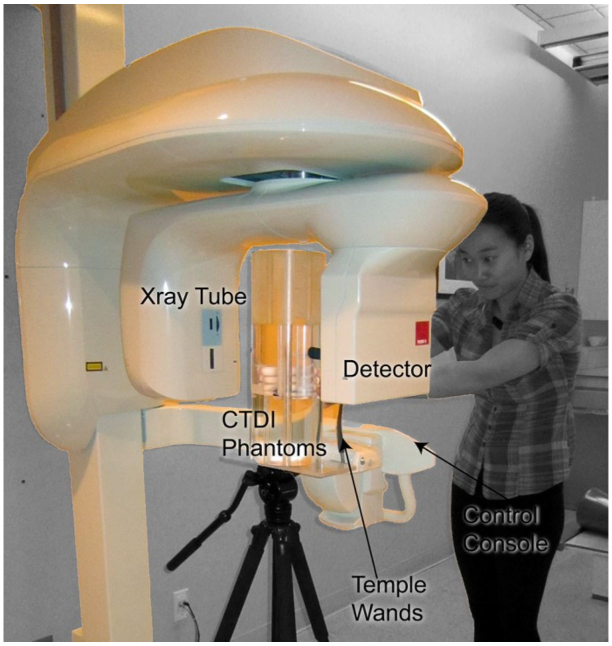

Figure 2.1. Experimental setup for dose measurements. The photograph shows the scanner with the chin rest and temple paddles removed and a stack of 16 cm diameter plastic cylinder phantoms. Variations of the phantom setup included: three 16 cm acrylic CTDI phantoms; a CATPHAN in place of the central cylinder (for SDNR measurements); a custom SolidWater^{TM} cylinder with tissue-simulating plastic inserts (Gammex RMI, Madison WI); a wire phantom (for MTF measurements); and an anthropomorphic head phantom (natural skeleton in Rando^{TM} plastic).

II.C. Imaging Performance

Performance measurements used two CatPhan modules (CTP404 and CTP528) and a custom SolidWater^{TM} cylinder with tissue-simulating plastic inserts (Gammex RMI, Madison WI). The Signal Difference to Noise Ratio (SDNR) was calculated as follows:

$$\mathrm{SDNR} = 2\frac{\left|\bar{\mu}_{\mathrm{insert}} - \bar{\mu}_{\mathrm{background}}\right|}{\sigma_{\mathrm{insert}} + \sigma_{\mathrm{background}}} \tag{2.1}$$

where $\overline{\mu}_{\text{insert}}$ is the average voxel intensity of a specified insert, $\overline{\mu}_{\text{background}}$ is the average voxel intensity of the background material adjacent to (and at the same radius as) the insert, and σ_{insert} and $\sigma_{\text{background}}$ are the standard deviations in the respective regions.

II.C.1 High Contrast SDNR

The CTP404 insert (CatPhan module, The Phantom Laboratory, Greenwich NY) containing various plastic cylindrical inserts was used to assess high-contrast SDNR. For all protocols, the SDNR was calculated between polystyrene (measured 91 HU) and background (measured -26 HU). The dose-normalized SDNR was computed by dividing by the square root of the measured absolute dose (D_0) for each protocol. Due to the presence of a significant blush and ring artifact and lateral truncation artifacts (depending on FOV), the region of interest (ROI) location for calculation of SDNR was selected to avoid such artifacts while maintaining equal radius from the center of the image for all inserts and background ROIs.

II.C.2 Low-Contrast (Soft-Tissue) SDNR

Further study of the low-contrast resolution capabilities of the scanner was performed using a SolidWater phantom with inserts that simulated soft-tissue densities. Tissue-equivalent inserts (Gammex RMI, Madison WI) included adipose (-112 HU), solid water (0 HU), brain (6 HU), and liver (87 HU). Soft-tissue SDNR was calculated in the same manner as described above.

II.C.3 HU Accuracy

The same phantoms were scanned with a MDCT scanner (Somatom Definition Flash, Siemens Healthcare, Erlangen Germany) using standard clinical “head” protocols (120 kV, 125 mAs, T80f kernel, and $0.4\times0.4\times0.4$ mm^3 voxel size), and the HU values reported by the MDCT scanner and CS 9300 scanner were compared.

II.C.4 Spatial Resolution

Spatial resolution was assessed qualitatively using a line-pair phantom (CTP528 module of the CatPhan) for all protocols. Quantitative assessment of spatial resolution for the S1 and E1 protocols was performed by measurement of the MTF from a wire phantom. The MTF was calculated as the Fourier transform of an oversampled LSF derived from Radon transform of axial images of the wire within a cylindrical phantom under tension, slightly angled to the longitudinal image axis. Radon transform, oversampling, LSF normalization, and MTF estimation followed similar procedures as previously published works.[27, 28]

II.C.5 Image Quality in an Anthropomorphic Head Phantom

An overall qualitative assessment of image quality was performed using scans of an anthropomorphic RANDO head phantom (natural human skeleton in tissue-equivalent plastic; The Phantom Laboratory, Greenwich NY). Images were qualitatively assessed by an expert, fellowship-trained rhinologist and otologist with respect to the visibility of pertinent anatomical structures and overall diagnostic quality. The potential for more quantitative observer performance assessment is recognized (e.g., ROC tests), but is beyond the scope of the technical assessment reported here. The qualitative interpretation by expert clinicians was valuable, complementary, and confirmatory of measurements of SDNR and MTF.

III. Results

These results correspond to a second technical assessment of the CS 9300 after modifications were made based upon recommendations arising from an initial technical assessment performed using the same methods and experimental setup. The initial sinus protocols (S1, S2, and S3) employed a 90 kV beam (5 kV greater than those listed in Table 2.1) and a tube current of 6.3 mA (1.3 mA higher than those listed in Table 2.1). The ear protocols (E1, E2, E3, and E4) did not change in beam energy, but the mA was reduced from 6.3 mA to 5 mA for E1 and from 8 mA to 6.3 mA for E2, E3, and E4. Several of the source-detector orbits in the initial protocols were also modified to those illustrated in Figure 2.2: The S2 protocol, for example, initially involved a longer arc beginning at the right ear, traversing the posterior of the head, and ending anterior to the left ear; similarly, the E1 protocol involved an arc beginning posterior to the right ear, traversing the posterior of the head and ending at the left anterior of the head; other scan trajectories were as shown in Figure 2.2. The adjustment of the S2 and E1 protocols to those shown in Figure 2.2 was motivated primarily to reduce the total arc length and deposit dose posteriorly [rather than to the anterior head (viz., eye lens)]. The initial assessment yielded dose values of: D_w = 9.2 mGy (S1), 5.3 mGy (S2), 8.5 mGy (S3), 6.5 mGy (E1), 7.9 mGy (E2), 5.0 mGy (E3), and 8.1 mGy (E4). Similarly, the $\mathrm{SDNR}/\sqrt{\mathrm{mGy}}$ from the original assessment for the same CatPhan module was 0.97 (S1), 1.2 (S2), 1.0 (S3), 1.2 (E1), 1.5 (E2), 1.7 (E3), and

0.75 (E4) [all units $1/\sqrt{\text{mGy}}$]. Spatial resolution assessed subjectively from the CatPhan line-pair pattern ranged between 12 lp/mm (S2) to greater than 15 lp/mm (E2-4). The reduction in kV and mAs and modification of the source-detector orbits were qualitatively assessed in anthropomorphic phantoms, with further possible modifications suggested below.

III.A. Dose

Dose measurements demonstrated that all protocols deployed on the CS 9300 scanner are similar to (or somewhat lower than) those reported for comparable CBCT scanners as well as those reported for MDCT head protocols. Table 2.3 summarizes the dose measurements, where central dose is seen to be in the range 2.9–5.7 mGy, depending on the specific protocol. For example, the lowest and highest dose protocols (E3 and S1, respectively) gave D_0 = 2.9 and 5.7 mGy, D_w = 4.7 and 8.5 mGy, DLP = 24 and 114 mGy.cm, and D_E = 0.05 and 0.26 mSv, respectively. By comparison, Ludlow et al[23] reported doses for comparable scanners to be between 0.05 mSv (NewTom) and 1 mSv (iCAT). Because other reports in the literature used thermoluminescent dosimeters (TLDs) and were aimed at patient dose characterization instead of absolute dose ("output") of the scanner itself, a comparison in terms of absolute dose (mGy) is not available. In comparison to MDCT of the head, the median value for CTDI$_W$ reported in Pantos et al[29] was approximately 52 mGy, with a range of 17-181 mGy measured over 17 studies spanning approximately two decades.

#	D_0 (mGy)	D_0/mAs (mGy/mAs)	P1 (A) (mGy)	P2 (R) (mGy)	P3 (P) (mGy)	P4 (L) (mGy)	$\bar{D}_{\text{periph}}$ (mGy)	D_w (mGy)	D_w/mAs (mGy/mAs)	DLP (mGy·cm)	D_E (mSv)
S1	5.7	0.08	6.1	6.1	6.1	6.1	6.10	5.97	80.6	1370.3	6.0
S2	3.3	0.08	1.4	4.0	4.5	4.0	3.46	3.41	37.5	637.4	3.4
S3	5.3	0.08	2.2	6.3	7.2	6.5	5.55	5.47	60.2	1023.4	5.5
E1	4.5	0.08	1.6	5.5	8.3	5.7	5.29	5.02	30.1	512.4	5.0
E2	4.8	0.03	6.4	2.5	12.1	8.2	7.30	6.46	32.3	161.5	6.5
E3	2.9	0.03	3.8	1.5	7.2	4.0	4.12	3.70	18.5	92.4	3.7
E4	3.2	0.03	5.5	2.1	6.2	5.7	4.88	4.31	34.5	275.8	4.3

Table 2.3. Summary of dose measurements for each protocol deployed on the scanner. Central dose (D_o), peripheral dose (P1-P4), and various aggregate calculated dose values are shown. Labels for peripheral positions are provided for P1-P4, where A=anterior, P=posterior, R=Right, and L=left. The protocols are in Table 2.1. The measurement locations are shown in Figure 2.2.

The measured value of D_W (an approximate analogue of CTDI$_W$ for short-scan orbits) for the CS 9300 is considerably lower than the lowest CTDI$_W$ reported for MDCT, although ongoing advances in dose reduction and improved reconstruction algorithms will likely drive MDCT to still lower values. Some of those same advances will likely apply to further dose reduction in CBCT as well.

As shown in Figure 2.2, the various scan orbits impart very different dose distributions: for a 360° orbit (S1), the dose deposition is the expected, radially symmetric dose distribution with exponential attenuation toward the center of the phantom; for the short-scan and unilateral orbits, however, the dose is deposited predominantly at the posterior of the head (S2, S3, and E1) and/or unilaterally (E2, E3, and E4). These differences in scan orbit yield variation in the peripheral dose that in turn affects the "weighted" and "effective" dose shown in Table 2.3. The dose maps in Figure 2.2 further demonstrate that the short-scan orbits achieve considerable dose sparing of the anterior region, including the eyes. Some implications with respect to dosimetry standards and further improvements in anterior dose sparing are discussed below.

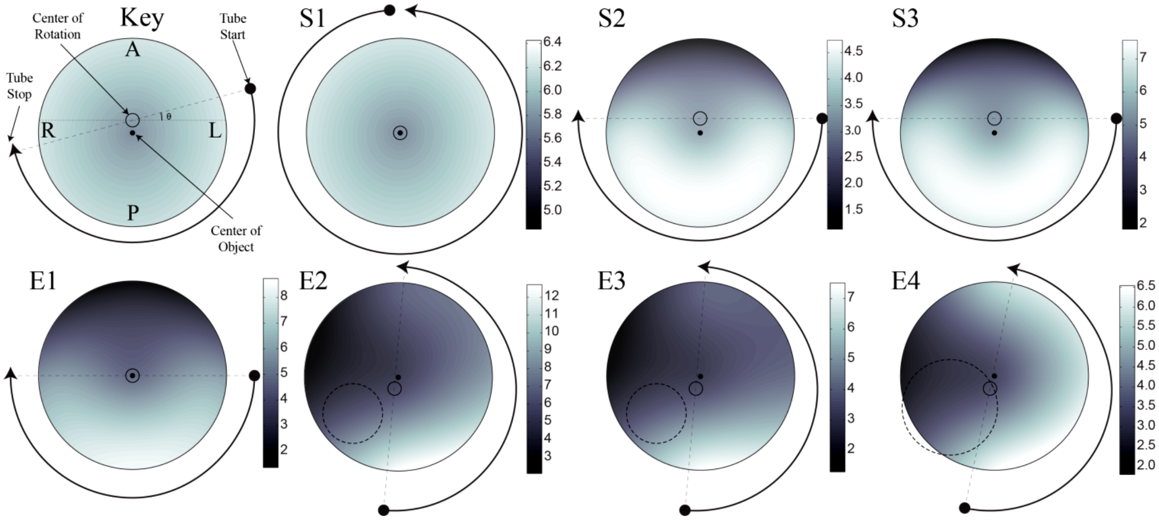

Figure 2.2. Dose distributions ("maps") in the central axial plane for various scanner orbits. The colorbars show the dose (mGy). Each protocol is labeled as in Table 2.1. The top left image "Key" shows the legend for: tube start angle, tube stop angle, center of rotation, and center of the object. The small FOV for the unilateral scan protocols are shown as dotted circles in E2, E3, and E4.

Figure 2.3 shows measurements of the longitudinal (*z*) distribution of dose within and beyond the primary beam FOV. The falloff was anticipated to be fairly gradual due to scatter in the broad volumetric beam. The longitudinal dose tails fall to ~10% of the maximum central dose at ~8 cm from the edge of the FOV and to ~1% of the maximum central dose at ~12 cm from the edge of the FOV. Assuming an approximate thyroid position at ~8 cm below the chin, the dose to the thyroid would be approximately 1.1 mGy and 0.8 mGy for the S1 and E1 protocols, respectively. Previous work[30] shows that a majority of the out-of-field dose arises from internal scatter through the patient, and a thyroid shield would not be effective in limiting dose to thyroid, since x-ray scatter originates in the head and travels "down" the neck.

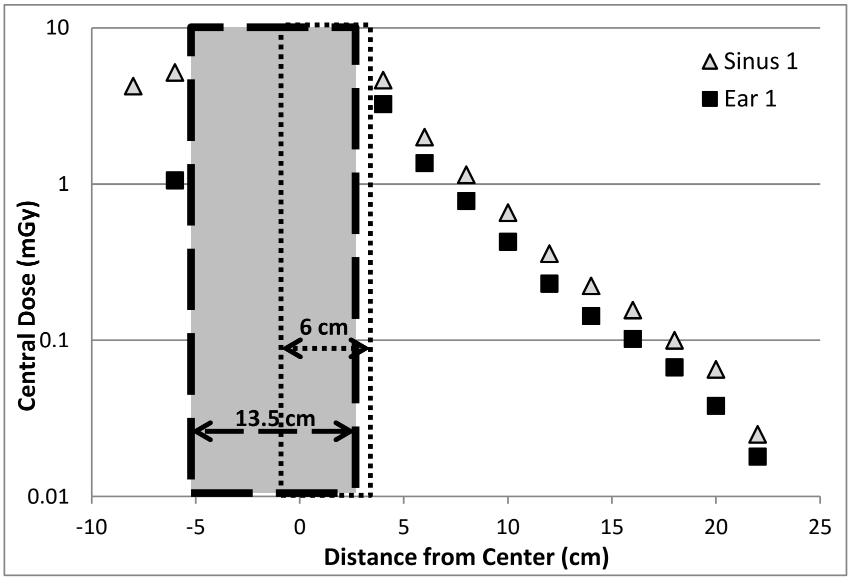

Figure 2.3. Out-of-field (longitudinal) dose profiles for the S1 and E1 protocols. The longitudinal dose tails fall off exponentially with z outside of the primary beam. The range denoted by dotted lines labeled 13.5 cm and 6 cm denote the estimated beam heights for protocol S1 and E1, respectively. These are provided as a locational reference for the out-of-field radiation.

III.B. Signal Difference to Noise Ratio and CT Number Accuracy

The SDNR was measured for all sinus and temporal bone protocols as summarized in Figure 2.4. Overall, the temporal bone protocols provided slightly improved SDNR in comparison to the sinus protocols, attributed primarily to the smaller FOV and beam width, resulting in reduced x-ray scatter. The images also illustrate the variation in FOV size and placement (shifts of the gantry as noted in Figure 2.2): S1 covers the entire phantom; S2 and S3 shift the FOV anteriorly (to cover the sinuses); E1 is intended to cover the bilateral posterior aspect of the head (temporal bones); and E2, E3, and E4 place a smaller FOV unilaterally (L or R temporal bone). For the results in Figure 2.4, the phantom was not moved in cases S1, S2, S3, and E1, but was rotated in cases E2, E3, and E4 such that the polystyrene insert (yellow arrow) remained in the FOV for purposes of comparison and SDNR analysis.

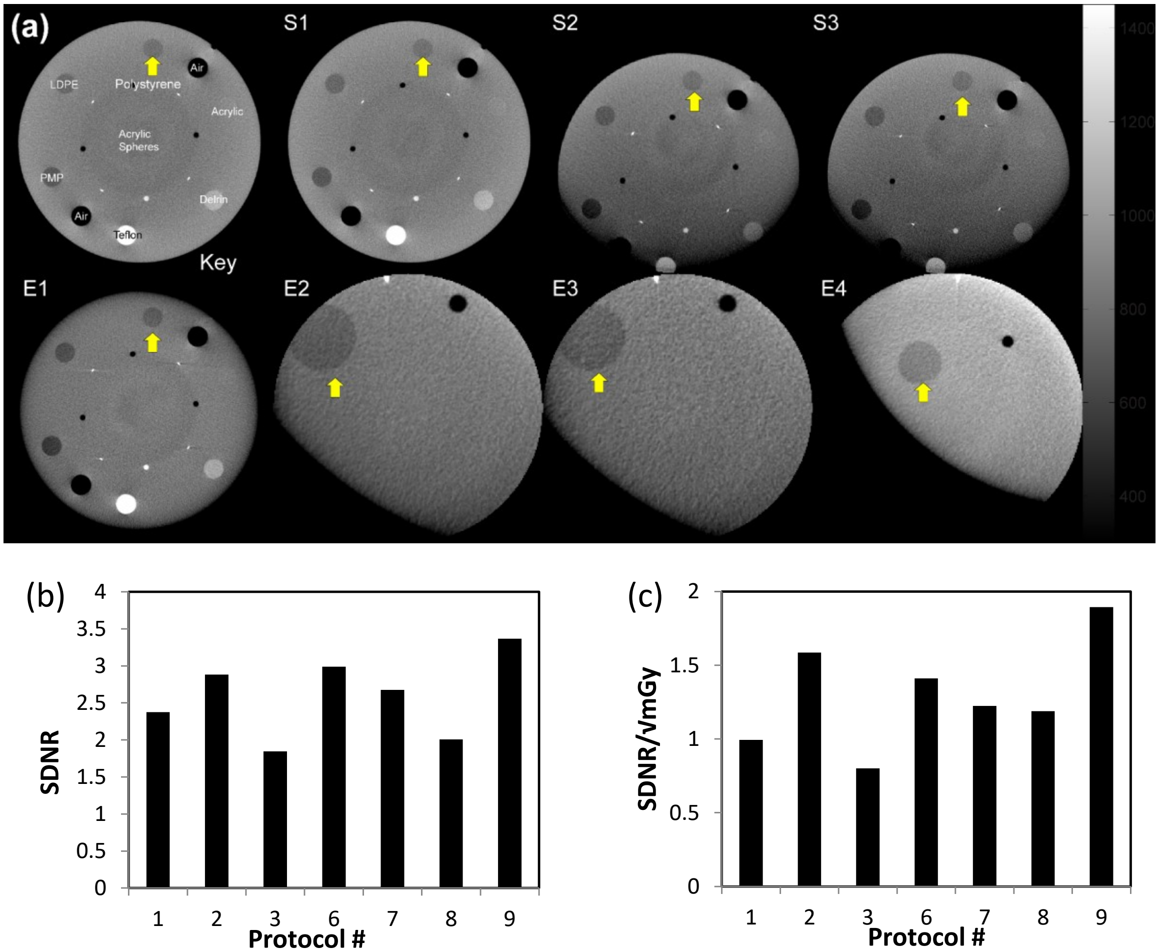

Figure 2.4. Analysis of SDNR. (a) The CatPhan Module CTP404 was scanned at all sinus and ear protocols. An equivalent window and level was set for all cases, with the intensity grayscale (native scanner voxel values) shown to the right. (b-c) SDNR calculated for the polystyrene insert (arrow).

The low-contrast imaging performance was investigated further for the S1 and E1 protocols to assess the potential for soft-tissue visualization (beyond the fairly high-contrast inserts of the CatPhan modules). Images of the 16 cm SolidWater phantom with various tissue-equivalent inserts are shown in Figure 2.5. Soft-tissue inserts include (W) solid water, (L) liver, (B) brain, and (A) adipose. Apparent differences between the two brain and liver inserts is due to variations from the manufacturer. Only the liver (+87 HU) and adipose (-112 HU) inserts demonstrated a high level of conspicuity (SDNR ~0.70 and 2.1, respectively). Soft-tissue visibility was qualitatively inferior to the same object imaged in MDCT. A dark circular blush artifact is also evident, as is a degree of spatial non-uniformity (shading near the center, likely due to x-ray scatter) that somewhat diminish overall image quality.

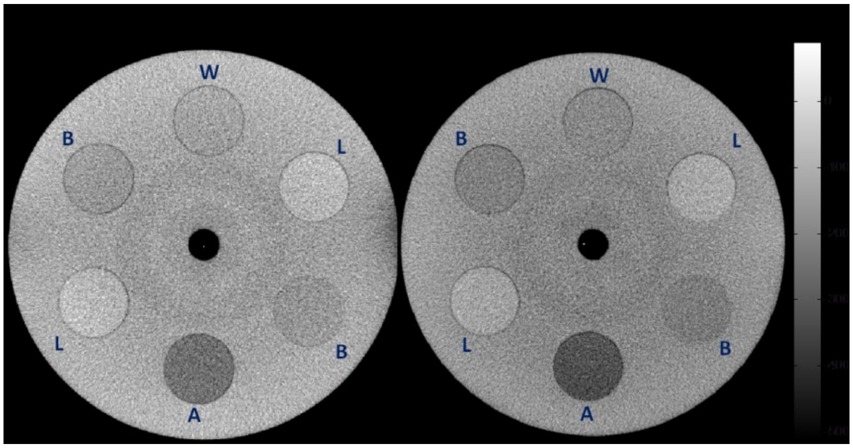

Figure 2.5. Soft-tissue phantom imaged using S1 and E1 protocols. The grayscale at right shows native voxel values reported by the scanner (not HU). Tissue-equivalent inserts are as follows: B (brain: 6 HU, $SDNR_{S1} = 0.35$, $SDNR_{E1} = 0.5$), W (water, 0 HU, $SDNR_{S1} = 0.27$, $SDNR_{E1} = 0.20$), L (liver, 87 HU, $SDNR_{S1} = 0.70$, $SDNR_{E1} = 1.2$), A (adipose, -112 HU, $SDNR_{S1} = 2.1$, $SDNR_{E1} = 2.5$), and SolidWater background (0 HU).

Figure 2.6 shows the voxel values reported by the CS 9300 plotted versus the HU reported by the MDCT scanner (standard head protocol at 120 kV, Siemens Somatom Definition Flash). Note that the manufacturer does not claim accurate HU calibration on the CS 9300. A fairly linear relationship is observed, related by slopes of 0.7 and 0.8 for the S1 and E1 protocols, respectively. The lower slope for the former is presumably associated with the larger FOV (higher x-ray scatter) and a lower imaging tube potential (85 vs 90 kV). This level of HU inaccuracy is typical for CBCT systems and presents an area for further improvement through careful calibration procedures.[31, 32]

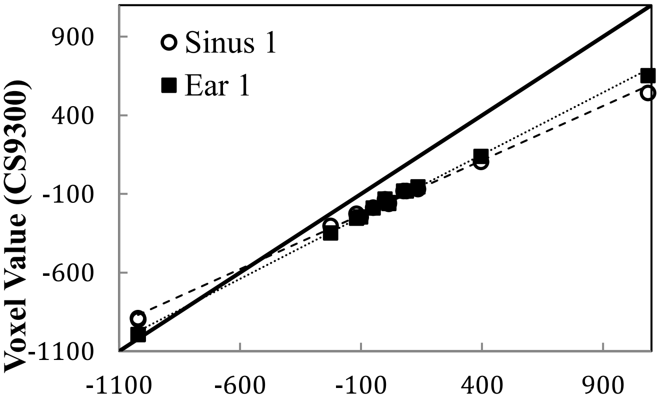

Figure 2.6. Voxel values reported by the CS 9300 in comparison to HU values measured in MDCT (standard head protocol). As is common with CBCT systems, voxel values exhibit a systematic error primarily associated with high x-ray scatter (i.e., slope less than unity and non-zero intercept). The line of identity (bold) is shown as a basis of comparison.

III.C. Spatial Resolution

As shown in Figure 2.7, all protocols exhibited spatial resolution better than 10 lp/cm in a qualitative assessment of the line-pair phantom. The unilateral temporal bone protocols (E2, E3, and E4) demonstrated the highest spatial resolution, ~13 lp/cm. The differences observed in the limiting spatial resolution among various protocols is attributed to the technique parameters shown in Table 2.1, most notably voxel size. Specifically, S1 and S3 (each with voxel size 0.3 mm) have superior spatial resolution compared to S2 (voxel size 0.5 mm). The difference in spatial resolution between S1 and S3 is more subtle and can be attributed to superior view sampling for the latter – the number of views are approximately equal for both protocols, but they are spread over a larger angle for S1 than for S3.

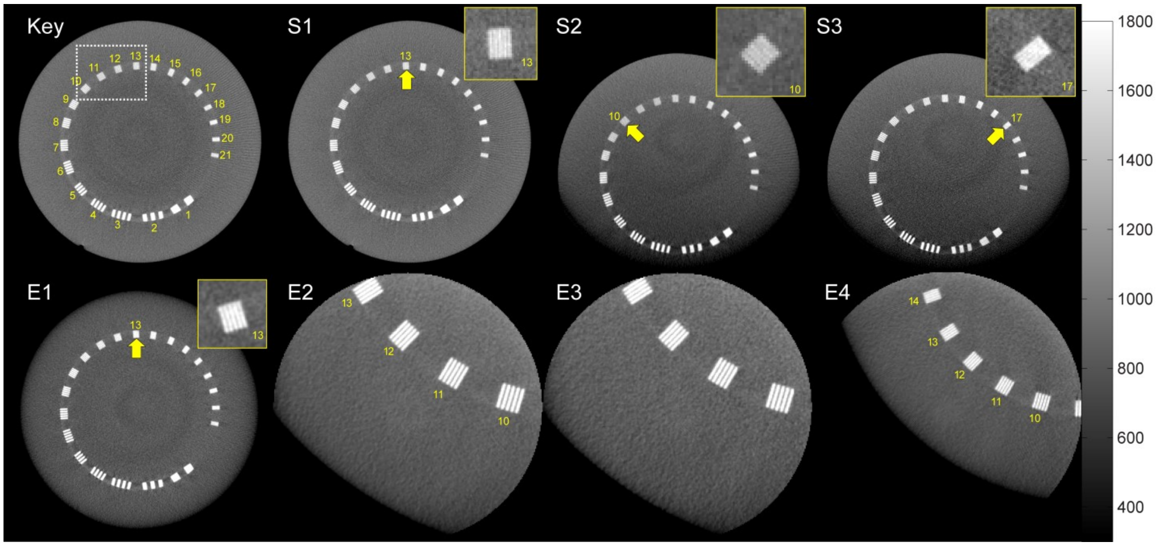

Figure 2.7. Spatial resolution qualitatively assessed in line-pair images of the CTP528 module for each scan protocol. The approximate limiting resolution is indicated by yellow arrows, and the dotted box in the key denotes the approximate FOV of the unilateral protocols (E2-E4). The unilateral ear scan protocols (E2, E3, and E4) demonstrate the highest spatial resolution.

More quantitative assessment of spatial resolution is shown in the MTF measurements of Figure 2.8, where the S1 and E1 protocols were found to give MTF exceeding 10% out to 20 lp/cm or more. The MTF is slightly improved for the E1 protocol, owing to the smaller FOV (reduced x-ray scatter and finer voxel sampling). The system interface in its current implementation does not allow adjustment of the reconstruction filter ("kernel"), and the filters associated with each protocol are not reported. It is not known if the filter varies between protocols.

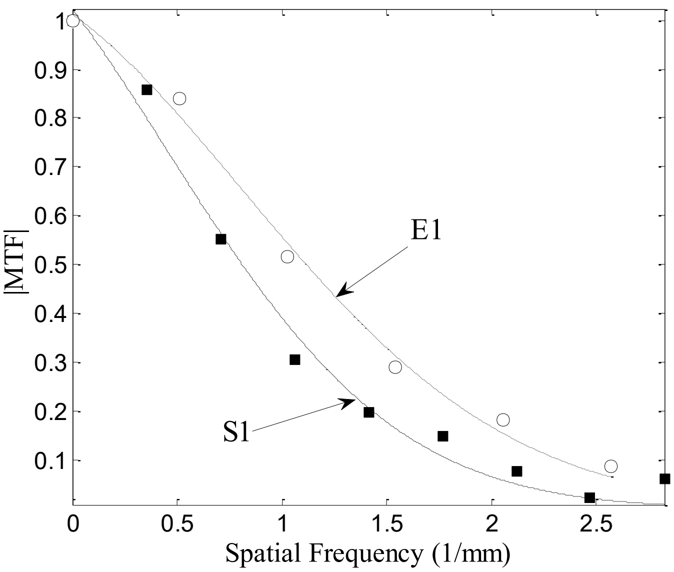

Figure 2.8. MTF for the S1 and E1 protocols. Gaussian fits to the measured data are overlaid as a guide to the eye (not as a model fit). The difference in the presampling MTF is attributed primarily to finer sampling for the latter (isotropic voxel size 0.3 mm for S1 and 0.2 mm for E1).

III.D. Image Quality Assessed in an Anthropomorphic Head Phantom

Images of the anthropomorphic head phantom in Figure 2.9 and Figure 2.10 provided qualitative assessment of the various scan protocols with respect to pertinent clinical tasks in sinus and otology imaging. As illustrated in Figure 2.9, the three sinus protocols were each assessed as generally acceptable with respect to high-contrast visualization of the frontal, ethmoid, maxillary, and sphenoid air cells, lamina papyracea, and skull base (including the carotid canals, vidian canal, and pituitary bulb). Based on qualitative assessment of sinus feature visibility combined with the quantitative assessment of dose, contrast resolution, and spatial resolution detailed above, the S3 protocol was identified as the preferred default (adult) protocol for sinus imaging. The S2 protocol was identified an alternative, lower-dose protocol to be used in situations where spatial resolution requirements were reduced, soft-tissue requirements were increased, and/or there was heightened sensitivity to radiation dose (e.g., pediatric or repeat longitudinal imaging).

As illustrated in Figure 2.9, axial, coronal and sagittal views of the sinuses demonstrated resolution of fine anatomic details and air-bone interfaces. Figure 2.10 demonstrates the image quality for all four temporal bone protocols, which were each considered acceptable for visualization of mastoid air cells, semicircular canals, and cochlea. Isotropic 3D spatial resolution was identified as a significant strength, comparable to high-resolution temporal bone protocols in MDCT and suitable for excellent visualization of sub-millimeter structures at air-bone interfaces—for example, semicircular canal dehiscence. Utility in soft-tissue visualization (e.g., cholesteatoma) was difficult to assess but (based on qualitative comparison in the same phantom) was likely inferior to MDCT. Image quality in the presence of metal (e.g., cochlear implant) was not assessed in the current work.

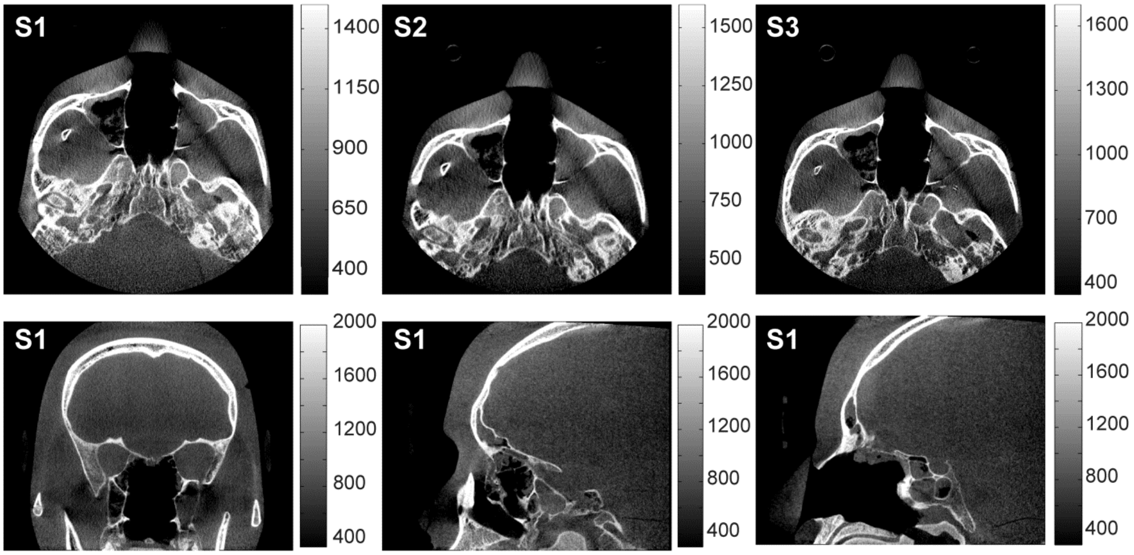

Figure 2.9. Qualitative assessment of image quality in the sinuses. (top) Axial slices from the S1, S2, and S3 protocols. (bottom) Sagittal and coronal views about structures of interest in the sinuses for the S1 protocol. Note that the anthropomorphic phantom underwent a resection of ethmoid air cells and nasal septum to allow endoscopic access to the sphenoid for other experiments (endoscopic skull base surgery). Visualization of structures associated with the ethmoid air cells is evident in fine details of residual ethmoid along the lamina papyracea. The grayscale window and level were adjusted independently to compensate for variations in voxel value scaling between various protocols.

Overall, the bilateral E1 protocol was considered generally most useful, allowing assessment of both temporal bones from a single scan and facilitating visualization of left-right symmetry. The unilateral protocols (E2, E3, and E4) require careful patient positioning and FOV placement to avoid truncation of structures of interest, and the scan orbits illustrated in Figure 2.2 were considered dosimetrically disadvantageous compared to E1 with respect to dose to the anterior head. The E2 protocol was identified as a potential alternative in situations demanding increased spatial resolution in which a unilateral view was sufficient, but requires careful attention on the part of the technologist to assure that the ROI is within the smaller FOV.

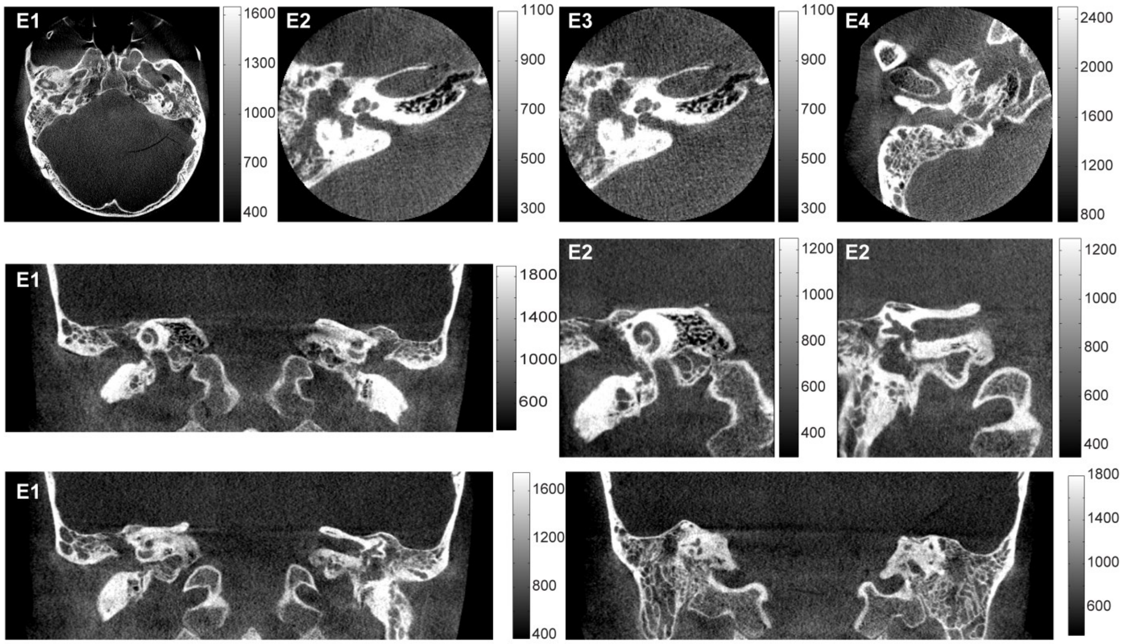

Figure 2.10. Qualitative assessment of image quality in the temporal bones. (top row) Axial slices from the E1, E2, E3, and E4 protocols. (center and bottom rows) Coronal views showing structures of interest in the temporal bones for the E1 and E2 protocols, including the cochlea, stapes footplates, and bone over the superior semicircular canal. The grayscale window and level were adjusted independently to compensate for variations in voxel value scaling between various protocols.

IV. Discussion and Conclusions

A commercially available CBCT scanner (CS 9300) for application in OHNS imaging (including maxillofacial, ENT, and otology imaging) was assessed in terms of technical performance (dose, contrast resolution, and spatial resolution) and applicability in a spectrum of clinical imaging tasks (qualitative assessment of anatomical visibility in the sinuses and temporal bones). The CS 9300 was found to provide comparable or somewhat improved radiation dose characteristics compared to those reported for similar application-specific CBCT scanners[23] as in the studies performed by Ludlow et al for other devices. Qualitatively, the results suggest that CBCT offers reduced radiation dose and comparable or somewhat superior spatial resolution in comparison to common MDCT protocols, but soft-tissue contrast resolution is still insufficient for imaging of low-contrast features such as ICH and CSF. Cost and site requirements, however, are advantageous to the simpler, application-specific CBCT systems and indicate a potential for further development with regard to improved detector hardware (reduced noise, improved temporal performance, extended FOV), reduced scatter (reduced noise, fewer artifacts), geometric calibrations, and advanced reconstruction algorithms.

A number of observations and recommendations can be appreciated in considering the dose maps of Figure 2.2. The first is the obvious challenge posed by short-scan orbits to conventional dosimetry standards: in addition to the limitations in CTDI noted by Dixon et al[33] is the fact that the central dose, D_0, alone does not differentiate between protocols that better spare the anterior of the head (e.g., S2 versus E4, each with D_0 ~3.3 mGy, but differing in anterior dose by a factor of 4). A simple variation on the "weighted" D_w was suggested to incorporate the average peripheral dose as a somewhat more useful approximation for short-scan techniques. As currently implemented by the manufacturer, the unilateral protocols (E2, E3, and E4) shift the scan orbit off-center and laterally. For imaging of the right ear (which was the case for all unilateral cases in this work), the scanner shifts laterally to the left, thereby depositing the highest dose *outside* the FOV. We hypothesized that an improvement in quantum noise and sampling characteristics would be achieved by shifting instead to the right (not the left), placing the FOV on the region receiving a higher dose (reduced quantum noise) with higher density of backprojected rays (for a short-scan orbit). We also noted that all of the short-scan orbits (specifically, E2, E3, and E4) could be better constrained as in S2, S3, and E1 such that the x-ray tube passes posterior to the head in order to spare anterior dose. These recommendations were relayed to the manufacturer to be considered in future implementations. There was no capability for mA modulation in the current implementation, although this might allow further dose reduction if properly implemented.

All of the results reported above were based on a *second* technical assessment – the first assessment highlighting a number of potential improvements that were constructively incorporated by the manufacturer. The main recommendations highlighted in the first assessment were: (*i*) a reduction in kV for each protocol by 5-10 kV to the values shown in Table 2.1; (*ii*) a reduction in mAs by ~10-30% to the values shown in Table 2.1; and (*iii*) an adjustment of the short-scan orbits such that the x-ray tube traverses the posterior of the head in the short-scan orbits (as shown in Figure 2.2 for S2, S3, and E1) and not the lateral aspect of the head (which imparted a significantly higher anterior dose). The first and second recommendations were based on quantitative assessment of dose and SDNR, recognizing that the system was primarily providing visualization of high-contrast structures (moreso than soft-tissue) and that task performance could be maintained even at the reduced dose levels. The third recommendation (posterior short-scan orbits) was adopted for the S2, S3, and E1 protocols as shown in Figure 2.2, and incorporation in all cases is being considered by the manufacturer in future implementations. These modifications demonstrate the value of rigorous technical assessment in improving the translation of technologies to clinical use. Furthermore, a number of areas of improvement were identified for potential development in application to improved soft tissue visualization: (*i*) reduction in detector noise via improved hardware implementations or novel detector technologies; (*ii*) more optimal system geometry providing improved air gap scatter rejection; (*iii*) improved artifact corrections, including scatter and beam-hardening; and (*iv*) model-based image reconstruction methods that could improve the noise-resolution tradeoffs particularly for low-contrast visualization tasks.

Chapter 3: Image Quality Modeling of Photon Counting Detectors

I. Introduction

Previous work[65, 69, 98] has shown that CBCT systems are capable of excellent high-resolution imaging of high-contrast bone anatomy, with a modest degree of soft-tissue contrast resolution (muscle to fat contrast),[83, 99] limited primarily by image noise and artifact. High-quality imaging of brain trauma requires an advance in imaging performance, including reduction in image noise. Especially for portable, point-of-care systems with low-dose imaging protocols, additive electronics noise associated with detector readout is a potentially dominant source of noise. As discussed in Chapter 1, most CBCT systems use FPD technology based on active matrix readout of hydrogenated amorphous silicon (a-Si:H) photodiodes and TFTs, which are now common in digital radiography / fluoroscopy applications. Such detectors, however, exhibit relatively high levels of electronic readout noise due to the readout line architecture and limited signal amplification. Ongoing efforts include advanced architectures featuring on-pixel amplification and reduced readout noise.[100, 101] The work reported in this chapter investigates an alternative detector technology with lower levels of electronic noise.

Photon counting x-ray detector systems are an emerging medical imaging technology with potential applications in low-dose radiography,[102, 103] mammography,[104–106] tomography,[107–109] and energy-resolved imaging.[18, 110, 111] The detection medium in PCDs includes CdZnTe[112–115] and Si strip detectors,[116, 117] micro channel plates,[118] image intensifier based systems,[119] and dual-material detectors.[120] These technologies exploit potential advantages of reduced electronic noise and the ability to discriminate the energy of detected x-ray photons, each providing the potential for improved contrast-to-noise ratio (CNR).[16] While the underlying physics of PCD systems has been studied extensively over the last decade, with investigation of spectral models,[14] detector scatter models,[121] and computer simulation,[122] there has been less work on the fundamental image quality characteristics, modeling, and analysis of Fourier metrics of spatial resolution (MTF), noise correlation (NPS), and detection efficiency (DQE).[123, 124] A cascaded systems model of signal and noise transfer characteristics, as previously developed for FPDs[32, 125, 126] and other types of EIDs[127–129] would provide a powerful tool for system development and understanding the factors that govern imaging performance, especially in the early stages of system design, development, and optimization.

Recent work[17] provides a basis for cascaded systems analysis of PCDs and highlights the distinction between previously established models of EIDs—for example, FPDs—and PCD systems involving a signal threshold stage. Specifically, a PCD model should consider the propagation of the probabilistic distribution of image quanta arising from a single x-ray interaction through each stage, rather than simply following the mean signal, MTF, and NPS. The distribution is modeled as a binomial selection process including both the magnitude (probability density) and spatial distribution at each stage, thereby enabling the application of a threshold at the appropriate point in the imaging chain. The threshold amounts to an acceptance of signal above a given energy—recorded as "counts"—and rejection of signal below that energy – potentially eliminating electronic noise, but imparting effects on mean signal and spatial resolution as well. The work reported below extends the cascaded systems framework[123] to consider the spatially dependent transfer implications of thresholding as well as charge sharing, additive noise, and count-rate-independent spectral distortion for PCD systems. The model is also validated in comparison to physical measurements with a Si strip PCD and exercised as a guide to optimizing system performance in selection of optimal threshold values and examining the effect of detector design on DQE. Finally, the model is used to highlight the fundamental advantages (and disadvantages) of photon counting in comparison to energy integration.

The work reported below was published in Xu et al., "Cascaded Systems Analysis of Photon Counting Detectors",[130] and figures with associated text are reproduced in this dissertation with permission from the publisher (AIP, Washington DC, USA). The publication was featured as "Editor's Pick" for Volume 41 of the Medical Physics journal and was awarded the 2014 Sylvia Sorkin-Greenfield Award for Best Paper in Medical Imaging.

II. A Cascaded Systems Model for Photon Counting Detectors

The PCD imaging chain is modeled as a cascade of stages, where each stage represents a physical process in which the distribution of image quanta changes in number (amplification or loss), spatial distribution (blur or integration), or is sampled at discrete locations. For PCDs, there is an additional stage (Stage 7 below) corresponding to the application of a threshold, which imparts important effects on the mean signal, charge sharing, electronic noise, false counts, and sampling effects – all with direct influence on DQE. Preliminary analysis was presented in Reference #[131] and expanded in Reference #[130] as described below to include details of the analytical model and an expanded investigation of PCD performance.

The model for signal and noise propagation in the PCD imaging chain includes a series of gain stages reflecting a binomial selection process as described by Tanguay et al[123] and extension to the spatially-varying implications of threshold-dependent gain. The serial cascade is illustrated in Figure 3.1 along with notation associated with model parameters.

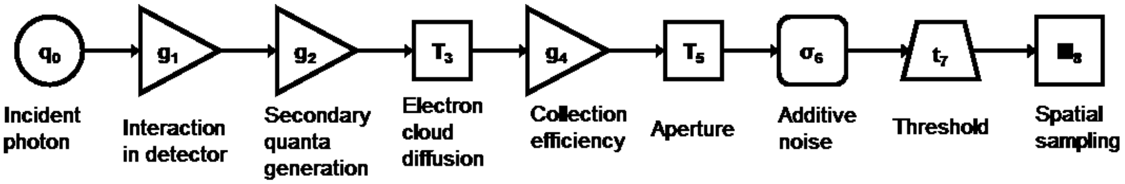

Figure 3.1. Illustration of the cascaded systems model for signal and noise propagation in a PCD with signal thresholding (Stage 7).

For the specific PCD used in this work (MicroDose Si strip detector, Philips Healthcare, Solna, Sweden) model parameters are derived below and summarized in Table 3.1. Because the system was operated well below the exposure rate at which pulse pileup effects become significant—specifically, ~6×10^3 x-rays/pixel/s (~100 x-rays/pixel for a 15 ms x-ray pulse) compared to the count rate limit of ~3×10^6 x-rays/pixel/s (~4.5×10^4 x-rays/pixel for a 15 ms x-ray pulse) as shown below and in previous work[132]—such nonlinearities were not considered in the current model.

Model Parameter:	Description	35 kV	70 kV
$\bar{q}_0 / X$	Incident fluence per exposure (X)	2.88×10^5 x-rays/mm^2/mR	6.64×10^5 x-rays/mm^2/mR
$\bar{g}_1$	Photon interaction probability	0.68	0.26
$\bar{g}_2$	Gain in secondary quanta	8000 electrons	11500 electrons
T_3	Charge cloud diffusion	$\sigma_3 = 0.015$ mm	
$\bar{g}_4$	Charge collection efficiency	0.99	
T_5	Aperture	$a_x = 0.05$ mm, $a_y = 0.55$ mm	
σ_6	Additive noise	$\sigma_6^{\text{add}} = 200$ electrons	
t_7	Threshold	1500 electrons	
III_8	Sampling function	$b_x = 0.05$ mm or 0.1 mm	

Table 3.1: Model parameters for each stage in the imaging chain, with values calculated at nominal operating conditions for the Si-strip PCD system in Figure 3.3. For the silicon strip detector, the sampling distance in the y direction, b_y, is large, and sampling in the y direction is assumed to be independent (infinitely spaced).

Stage 0: Incident x-ray spectrum. The incident x-ray spectrum was simulated using the spektr implementation[133] of TASMIP,[134] nominally 35 kV with added filtration of 2 mm Al and 4 cm water or 70 kV with added filtration of 2 mm Al and 1.2 mm Cu approximating objects in breast, extremities, or head imaging applications. As illustrated in Figure 3.2A for a 70 kV beam, the normalized spectrum, $q_0^{norm}\left(E_0\right)$ gives the probability distribution of one incident photon having energy E_0.

Stage 1: Interaction of x-ray quanta. Propagation of the distribution through Stage 1 considers energy-dependent interactions in the detector. Typical models assume a mean interaction probability ($\bar{g}_1$) derived from the total cross section of the detector material and a binomial selection process with variance in the gain given by $\bar{g}_1\left(1-\bar{g}_1\right)$. However, the distribution of energies absorbed by the detector is important in analysis of PCD systems, and photoelectric and Compton interactions impart distinct energy distributions that must be considered in the propagation of signal and noise. Appendix A to this dissertation provides a detailed description of the distinct distributions arising from photoelectric and Compton interactions similar to the analysis by Hajdok et al.[135] The resulting distribution of interactions at stage 1 is:

$$q_1\left(E\right)=\frac{\sigma_{PE}\left(E_0\right)}{\sigma_{\text{total}}\left(E_0\right)}q_{1PE}\left(E\,|\,q_0^{\text{norm}}\left(E_0\right)\right)+\frac{\sigma_C\left(E_0\right)}{\sigma_{\text{total}}\left(E_0\right)}q_{1C}\left(E\,|\,q_0^{\text{norm}}\left(E_0\right)\right) \tag{3.1}$$

where q_{1PE} represents the normalized distribution of photons undergoing a photoelectric interaction in the detector, and q_{1C} represents that undergoing a Compton interaction. The latter $\left(q_{1C}\right)$ accounts for both the scenario of scatter followed by escape [giving the low-energy peak in Figure 3.2A] and scatter followed by reabsorption (with the total energy deposited equal to the energy of the incident photon). The relative contribution of photoelectric and Compton interactions is combined according to the relative cross section at each energy ($\sigma_{PE}\left(E_0\right)$ and $\sigma_C\left(E_0\right)$, respectively), such that $\sigma_{total}\left(E_0\right)=\sigma_{PE}\left(E_0\right)+\sigma_C\left(E_0\right)$. The probability that a photon passes through the detector without interacting gives the "zero-energy" term in the distribution, $q_1\left(0\right)=1-\sum_{E>0}q_1\left(E\right)$.

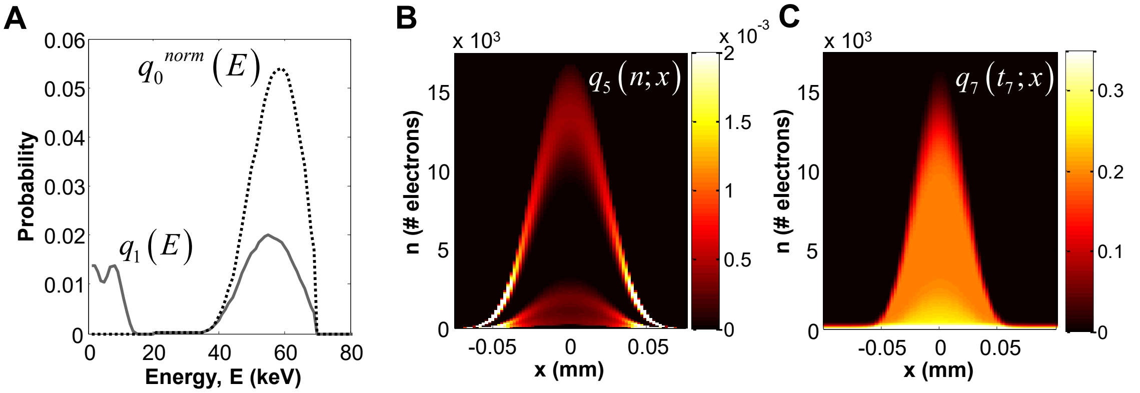

Figure 3.2. Distribution of quanta at various stages in the imaging chain. Table 3.1 provides a summary of system parameters. (A) Normalized incident photon spectrum at 70 kV (Stage 0) and spectrum of interacting photons (Stage 1). (B) Stage 5 distribution of quanta collected at a distance x from the site of interaction (taken here as $y = 0$, and aperture size $a_x = 0.05$ mm and $a_y = 0.55$ mm). (C) Distribution of quanta at Stage 7 counted at any location (x) for a given threshold (t_7) (also shown for the case $y = 0$).

Stage 2: Generation of secondary quanta. Stage 2 describes the conversion of energy to secondary quanta (e/h pairs). The distribution of the number (n) of secondary quanta is modeled as:

$$q_2(n=n_2)=\sum_{E=0}^{\infty} q_1(E)\, g_2(n=n_2 \mid E) \tag{3.2a}$$

where $g_2(n=n_2 \mid E)$ is a probability distribution function describing the generation of n e/h pairs from a single photon interaction at energy E. The mean number of e/h pairs generated at each energy $\left(\bar{g}_2(E)=E/W\right)$ is determined by W, the work function of the detector material. The distribution g_2 may be modeled as a Poisson process or by a broader distribution characterized by a Poisson excess (common in CsI scintillators), but in materials such as crystalline Si the variance is reduced according to the Fano factor ($F = 0.115$). The distribution of secondary quanta is therefore modeled as a Gaussian distribution that includes the Fano factor:

$$\hat{g}(N \mid E)=\frac{1}{\sigma_2\sqrt{2\pi}}\exp\left[-\left(N-\frac{E}{W}\right)^2 \Big/ \left(2\sigma_2^2\right)\right] \tag{3.2b}$$

$$\sigma_2^2=\frac{EF}{W} \tag{3.2c}$$

where the variance is $\sigma_2{}^2 = F\overline{g}_2$, and N is the number of quanta (continuous variable). The distribution was discretized by evaluating $\hat{g}(N \mid E)$ at positive integer values of N and normalizing so that $g_2(n \mid E) = \hat{g}_2(N = n \mid E) \Big/ \sum_i \hat{g}_2(N = i \mid E)$.

Stage 3: Spatial spreading of secondary quanta. At stage 3, secondary quanta undergo spatial redistribution (stochastic scatter) according to a PSF, $p_3(\xi,\eta)$, modeled as a Gaussian:

$$p_3(\xi,\eta) = \frac{1}{2\pi\sigma_3{}^2} \exp\left(-\frac{\xi^2 + \eta^2}{2\sigma_3{}^2} \right) \tag{3.3}$$

where σ_3 is the characteristic width of charge carrier diffusion, and (ξ, η) are spatial dimensions in x and y domains, respectively, corresponding to the relocation of a secondary quantum. For a blur stage, the probability of one quantum continuing to the next stage is $\iint p_3(\xi,\eta)\mathrm{d}\xi\mathrm{d}\eta = 1$, indicating that a spatial blurring stage propagates all quanta from the previous stage, and the number of quanta is preserved. For simplicity, we assume a normally incident x-ray photon and symmetric diffusion, though previous work[136, 137] has suggested asymmetric spread of secondary quanta for obliquely incident x-rays.

Stage 4: Collection efficiency of secondary quanta. At stage 4, the loss of secondary quanta due to effects such as e/h absorption or trapping[138] is modeled as a binomial selection with loss characterized by the factor, g_4. This quantity is assumed independent of position, which is a fair assumption for high-quality semiconductors free of defects.

Stage 5: Integration of secondary quanta. Integration of quanta by the detector aperture at stage 5 is given by the convolution in Eq. (3.5b) where x and y denote the displacement between the center of the aperture and the point of interaction in the x and y domain, and a_x and a_y are the dimensions of the aperture. This considers the effect of the relative displacement between the aperture and the center of $p_3(\xi,\eta)$, with the distribution at stage 5 given by:

$$q_5\left(n=n_5;x,y\right)=\sum_{n_2=1}^{\infty}q_2\left(n=n_2\right)\left\{\binom{n_2}{n_5}\left[p_5\left(x,\mathrm{y}\right)\right]^{n_5}\left[1-p_5\left(x,y\right)\right]^{n_2-n_5}\right\} \tag{3.5a}$$

$$p_5\left(x,y\right)=\int_{-\infty}^{\infty}\int_{-\infty}^{\infty}p_3\left(\xi,\eta\right)g_4\,\mathrm{rect}\left(\frac{x-\xi}{a_x}\right)\mathrm{rect}\left(\frac{y-\eta}{a_y}\right)\mathrm{d}\xi\mathrm{d}\eta \tag{3.5b}$$

Equation (3.5a) is a binomial distribution representing the collection of n_5 secondary quanta generated within a virtual aperture located at any point relative to the interaction. The probability of successfully collecting a single secondary quantum at (x, y) is given by $p_5\left(x,y\right)$. Equation (3.5b) assumes uniform collection sensitivity across the (rect function) aperture, though the model allows for more complex aperture models—e.g., a trapezoidal function.[139] The distribution of secondary quanta computed at all possible locations in the x domain (taking $y=0$ for simplicity) is shown in Figure 3.2C, where the probability distribution (vertical axis) is shown as an intensity map at each x location (horizontal axis) about the point of interaction. Each column in Figure 3.2B is the now familiar distribution of quanta (including, for example, the Compton peak at low n), and the distribution is modulated at increased x according to the binomial selection in Eq. (3.5a). The model thereby describes both the statistical (n) and spatial (x) distribution of quanta, with reduced probability of counts recorded at greater distance from the site of interaction (e.g., $< 5\times10^3$ electrons collected for $|x| > 0.04$ mm in Figure 3.2B).

Stage 6: Additive noise. Stage 6 models the addition of electronics noise prior to readout, modeled as a Gaussian-distributed random variable with characteristic width σ_{add}:

$$q_6\left(n=n_6;x,y\right)=q_5\left(n_5=n;x,y\right)*_n q_6^{\mathrm{add}}\left(n_6=n\right) \tag{3.6a}$$

$$q_6^{\mathrm{add}}\left(n_6\right)=\frac{1}{\sigma_{\mathrm{add}}\sqrt{2\pi}}e^{-\frac{{n_6}^2}{2{\sigma_{\mathrm{add}}}^2}} \tag{3.6b}$$

The probability distribution resulting from the addition of electronics noise is equal to the probability distribution of a sum of two random variables (namely n_5 representing the number of quanta collected in Stage 5 and n_6 representing the additive noise) and is given by the convolution of their respective individual distributions in Eq. (3.6a). Note that q_6^{add} is discretized in the same manner as the distribution of secondary quanta discussed in stage 2.

Stage 7: Threshold. At stage 7 a threshold $\left(t_7\right)$ is applied to the distribution, giving $q_7\left(t_7;x,y\right)$, the probability of collecting more than t_7 secondary quanta at location (*x*, *y*):

$$q_7\left(t_7;x,y\right)=\sum_{n_6=t_7}^{\infty} q_6\left(n=n_6;x,y\right) \tag{3.7}$$

The probability of collecting a number of secondary quanta exceeding the threshold is calculated for all possible (*x*, *y*) locations of the aperture in stage 5, implying that a single x-ray photon interaction may result in a count above threshold in multiple apertures. As detailed in Section III, depending on the characteristics of the detector system [e.g., the radius of charge carrier diffusion $\left(\sigma_3\right)$, the additive noise level $\left(\sigma_{\text{add}}\right)$, and the threshold $\left(t_7\right)$], such multiple counts ("double counts") can degrade signal fidelity by introducing false counts. Similarly, additive noise registering above threshold is a potential source of false counts. The relationship of detector threshold to false counts arising from charge sharing and/or additive noise is described in Section III.

Stage 8: Sampling. Finally, the signal is sampled at stage 8, represented by multiplication of $q_7\left(x,y;t_7\right)$ with a spatial domain comb function, $\text{III}_8\left(x,y;b_x,b_y\right)$, with the parameters $\left(b_x,b_y\right)$ equal to the sampling distance (pixel pitch) in the *x* and *y* directions and $\left(x_0,y_0\right)$ the relative displacement between the point of photon interaction and the center of the apertures:

$$q_8\left(x,y,t_7\right)=q_7\left(x,y,t_7\right)\text{III}_8\left(x-x_0,y-y_0;b_x,b_y\right) \tag{3.8}$$

Sampling corresponds to convolution in the Fourier domain between the (Fourier transform of the) presampling signal and a comb function at intervals of the sampling frequency $\left(1/b_x\right)$. While q_7 gives the likelihood of recording a count at a given threshold, the recorded signal itself is binary—0 if the signal is below threshold and 1 if the signal (including true and false counts) is above threshold.

III. Model Predictions of Imaging Performance Metrics

III.A Charge Sharing Effects on Spatial Resolution and Count Rate

As described in stage 7 of the model, a single photon can contribute counts to multiple detector elements. For example, if the spatial extent of the charge carrier cloud arising at stage 3 spans more than a single pixel, all pixels that collect charge carriers from a photon interaction have a chance to record a count, resulting in a system gain that can be greater than unity. This phenomenon, called charge sharing, causes a loss of fidelity in the recorded data. Both the true system gain, $\gamma^{\text{true}}(t)$, and the total system gain, $\gamma(t)$, can be computed from the distribution, $q_7(x,y,t)$ derived in stage 7, as an expectation value of the sampled signal, with consideration for the sampling step in stage 8 yielding an "unmodulated" signal of 1 when a count is recorded and a signal of 0 if a count is not recorded. A count coefficient, $\hat{w}_m$, can be computed to describe the likelihood that a single incident photon at threshold *t* will contribute counts to exactly *m* pixels:

$$\hat{w}_m(t) = \int \frac{1}{a_x} \text{rect}\left(\frac{x}{ma_x}\right) q_7(x;t)\,dx - \sum_{i=0}^{m-1} \hat{w}_i(t) \tag{3.9}$$

For example, *m* = 1 corresponds to a coefficient $\hat{w}_1(t)$ describing the probability of one pixel recording one count, *m* = 2 corresponds to the probability $\hat{w}_2(t)$ of two pixels recording one count each (for a total of two counts), etc. By definition, $\hat{w}_0 = 0$, since it is assumed that if a photon generates a detectable signal, then the likelihood of zero counts is zero. Note that the likelihood of interaction of the photon is included in the calculation of q_7 from stage 1.

The effects of charge sharing can be at least partially mitigated in PCD systems, such as the one in this work, by detection of temporally coincident counts in adjacent pixels. This effect can be included in the count coefficient as a modification of $\hat{w}_m$ for $m > 1$ by a coincidence rejection efficiency (CRE) coefficient, denoted r_m, as:

$$w_m(t) = \begin{cases} \hat{w}_m(t) & m = 1 \\ (1 - r_m)\hat{w}_m(t) & m > 1 \end{cases} \tag{3.10}$$

A rejection efficiency of $r_m = 1$ corresponds to perfect coincidence detection (a photon interaction contributes counts only to the pixel directly beneath it) and a rejection efficiency of 0 means nothing is rejected (e.g., a PCD without coincidence detection).

The expected mean signal resulting from a single photon interaction, $\gamma(t)$, can be computed as:

$$\gamma(t) = \left\langle q_8(t;x) \right\rangle_{x_0} = \sum_{m=1}^{\infty} m w_m(t) \tag{3.11}$$

where $\gamma(t)$ can be equivalently interpreted as the total system gain (detector counts per incident x-ray) and x_0 represents the phase difference between the sampling matrix and the photon interaction.[140] The expected true system gain is then $\gamma^{\text{true}}(t) = w_1(t)$, where $\gamma^{\text{true}}(t)$ can be equivalently interpreted as the likelihood that one incident photon will contribute one count to the detector element directly under the point of interaction.

The count coefficients, $w_m(t)$, are ideally limited simply by the quantum detection efficiency (the likelihood of the photon interacting at stage 1) and the integration of secondary quanta at stage 5 resulting in a count above threshold. However, with a sufficiently broad spread (σ_3) of secondary quanta at stage 3, a small aperture size (a_x) at stage 5, or a low threshold (t) at stage 7, the terms w_m for $m > 1$ can be nonzero, meaning that more than one pixel records a count from a single interaction. As a result, $\gamma(t)$ can in principle exceed unity due to "false" (alternatively, "double") counts. The model describes how both charge sharing and additive noise can result in such false counts, presenting a source of error that must be accounted in the propagation of signal and noise.

Furthermore, the PSF associated with a single photon counted by the detector is a rect function, since the detector records photons in a binary fashion (0 or 1) and is therefore unmodulated. However, again due to the charge sharing effect, the width of this rect function is variable in multiples of a_x – i.e., one photon can contribute counts to one pixel resulting in an aperture of width a_x, two pixels resulting in an aperture of width $2a_x$, etc. The "effective" PSF is computed as a weighted sum of such rect functions,[140] with the weights proportional to the count coefficients computed in Eq. (3.10):

$$\mathrm{PSF}(x;t)=\sum_{m=1}^{\infty}\frac{w_m^{norm}(t)}{ma_x}\mathrm{rect}\left(\frac{x}{ma_x}\right) \tag{3.12}$$

$$w_m^{norm}(t)=\frac{w_m(t)}{\sum_i w_i(t)} \tag{3.13}$$

The count coefficients w_m computed in Eq. (3.10) give the relative probability that a photon will contribute counts to exactly *m* pixels, resulting in a presampling spread of width ma_x. The effective presampling aperture is illustrated in Figure 3.6C for cases of no coincidence rejection (r_m = 0) and 35% coincidence rejection efficiency (r_m = 0.35).

III.B Additive Electronic Noise Effects on Performance and Spectral Resolution

There are two potential benefits to application of a threshold in PCDs. The first aims to achieve the highest data fidelity by optimally separating the true count distribution from the false count distribution. A second benefit is provided by the ability to distinguish incident energies. To this end, the threshold, *t* (in units of secondary quanta) can be approximately remapped to an energy threshold by $E_t(t)\approx tW$, where *W* is the average energy required to liberate a single charge carrier in the detector material, and E_t is the energy threshold equivalent. For notational convenience, the subscripts are dropped in further analysis. It is useful to cite the threshold alternatively in terms of detector threshold (*D*, units proportional to pulse height), charge carrier threshold (*t*, units of charge carriers), and energy threshold (*E*, units of energy). From Section III.A, an expected system gain can be computed for any threshold. The threshold can be converted to energy as above, and the numerical derivative can be performed to arrive at the detected energy spectrum, $\gamma^{\det}(E)=\frac{\mathrm{d}}{\mathrm{d}E}\left(\gamma\left[t(E)\right]\right)$. The detected spectrum for a PCD operating with and without coincidence rejection is shown in Figure 3.8(A-B). It is important to note that the low-energy “noise” associated with the detected spectrum in detectors without coincidence rejection or some other form of charge sharing rejection can be almost entirely attributed to false counts resulting from charge sharing. This effect is compounded by the presence of additive noise (discussed below), but can be mitigated with proper false count correction.

Additive noise contributes to the low-energy portion of the distribution in quanta and can contribute false counts if the threshold is selected at a value that is too low. Common practice is to select a threshold well above the additive noise level (i.e., t several times larger than σ_{add}), but as seen in the energy spectrum of Figure 3.8B, doing so will also set the threshold above the energy of Compton interactions, resulting in a loss of true signal as well. Reducing the threshold increases the detector signal associated with low-energy interactions, but it increases the probability that a recorded count is due to additive noise instead of a true interaction. For a given threshold, the additive noise distribution in stage 7 can be written:

$$q_7^{\mathrm{add}}\left(t_7;x\right)=\sum_{n=t_7}^{\infty}q_5\left(n=0;x\right)*q_6^{\mathrm{add}}\left(n\right) \tag{3.14}$$

a convolution of the probability of no photon interaction $\left(q_5\left(n=0;x\right)\right)$ with the additive noise term defined in stage 6. This gives the probability that a given threshold will result in a count at location x given only the additive noise and no photon interaction. The likelihood of a signal appearing above threshold due only to additive noise is derived in a similar manner as the expected gain from one incident photon in Eq. (3.9):

$$w^{add}\left(t\right)=\int\frac{1}{a_x}\mathrm{rect}\left(\frac{x}{m^{add}a_x}\right)q_7^{add}\left(x;t\right)dx \tag{3.15}$$

with the factor, m^{add}, empirically determined from measurement of additive noise recorded when no photon is incident. For the PCD system under consideration, $m^{\mathrm{add}}=3$ provided a reasonable match to measured dark field distributions, accounting for pulse shaper behavior and pulse height sampling rate. This semi-empirical approach accounts for the ratio of false-count events resulting from instances where a photon was not incident on the detector as discussed in Tanguay et al,[123] but characterization of the innate detector processes which leads to this false count ratio is outside the scope of this work.

III.C Fourier Metrics of Imaging Performance

The geometry of the Si strip detector (Figure 3.3 and Table 3.1) allows analysis of MTF, NPS, and DQE in terms of a single spatial-frequency (f_x) dimension (1D), since the aperture in the y direction (a_y = 550 μm) is much greater than the aperture width in the x direction (a_x = 50 μm) and the MTF in the y

direction is determined by the aperture of a pre-collimator (not integral to the detector and not used in this work). Additionally, the individual Si wafers are isolated by metal septa in the *y* direction, preventing electron scatter between adjacent wafers; therefore, correlation in the *y* direction is considered negligible. The model detailed above provides a general basis for the 2D MTF, NPS, and DQE, and in the following sections, each metric is shown for 2D. In Sections IV and V, analysis is shown in the 1D (f_x) domain, since the central slice is a nearly complete representation of the Fourier characteristics of the system due to the large a_y aperture.

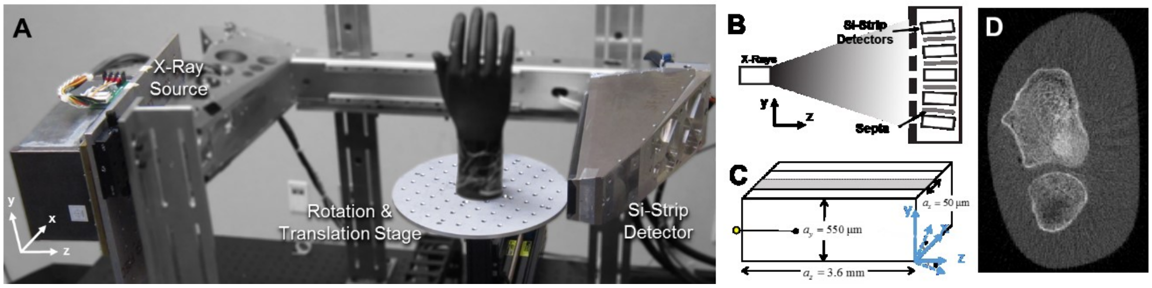

Figure 3.3. Experimental setup. (A) An imaging bench with an edge-on Si strip PCD. The detector is capable of readout at multiple detector threshold bins. The edge-on detection geometry is illustrated in (B), where photons are incident along the *z* direction, and readout is performed in the *x* direction, with bronze septa separating each Si wafer in the *y* direction. (C) Diagram of individual Si wafers (not to scale) illustrating the large detector thickness (3.6 mm) in the z direction for increased interaction probability and fine (50 µm) pixel pitch in the *x* direction. Individual wafers are aligned with the divergent beam, so the tilt angles η and ν are non-zero and different for each wafer depending on its position. (D) An example CT reconstruction of a wrist phantom obtained with the PCD detector (70 kV, 162 mAs).

III.C.1 Modulation Transfer Function

The presampling MTF is computed from the PSF(*x*,*y*) at a given threshold *t*, and taking $\mathrm{MTF}(u,v;t) = \mathcal{F}_{xy}\{\mathrm{PSF}(x,y;t)\}$, where u and v are the Fourier coordinates associated with the *x* and *y* directions, respectively. The notation *t* is interchangeable with t_7 (Stage 7, above). Theoretical calculation of the PSF and MTF is based on the distribution q_7 shown above, and measurement of the presampling MTF is described below (Sec. III.B).

III.C.2 Noise-Power Spectrum (NPS).

The NPS at a threshold, *t*, is computed as:

$$\mathrm{NPS}(u,v,t) = \left[a_x^2 a_y^2 \overline{q}_0 \gamma(t)\,\mathrm{MTF}^2(u,v,t)\right] * \mathrm{III}_8\left(u,v;\frac{1}{b_x},\frac{1}{b_y}\right) \tag{3.16}$$

where $\overline{q}_0$ is the incident x-ray fluence (photons/mm²), γ is the system gain:

$$\gamma(t) = \left\langle q_8(t;x,y) \right\rangle_{x_0,y_0} \tag{3.17}$$

and * denotes Fourier domain convolution.

III.C.3 Detective Quantum Efficiency

The system gain, MTF, and NPS are combined to yield the DQE:

$$\mathrm{DQE}(u,v,t) = \frac{a_x^2 a_y^2 \bar{q}_0 \left[\gamma^{\mathrm{true}}(t)\right]^2 \mathrm{MTF}^2(u,v,t)}{\mathrm{NPS}(u,v,t)} \tag{3.18}$$

As described in Stage 7 and section III.A, “false" counts are defined as the recording of a photon interaction when an interaction did not occur (e.g., due to electronic noise) or also resulted in a count in another detector element (e.g., due to charge sharing) and represents a source of variability in estimation of the total number of photon interactions. The analysis of DQE therefore distinguishes true counts (i.e., true system gain, $\gamma^{\mathrm{true}}(t)$, defined as the probability of one incident photon yielding exactly one count in the corresponding detector element) and total counts arising from a single incident photon [i.e., the total system gain $\gamma(t)$ in Eq. (3.9b)]. The effects of false counts on the DQE—in particular, the dependence of charge sharing and additive noise effects on detector threshold, and the potential to reduce false counts via coincidence detection—is investigated in Section V.B.

IV. Experimental Methods

IV.A Imaging Bench for Photon Counting CT

As illustrated in Figure 3.3, an imaging bench was built to test PCD imaging performance as predicted by the model and serve as a basis for the development of new PCD CT systems. The bench includes an x-ray source (XRS-125-7K-P, Source-Ray, Ronkonkoma, New York), computer-controlled translation and rotation stages (PK266-03A-P1, Velmex, Bloomfield, New York, with minimum step size 0.00635 mm and 0.0125°, respectively), and an edge-on Si strip PCD (MicroDose, Philips Healthcare, Solna, Sweden) originally developed for mammography, with 0.05×0.550 mm^2 pixel size (*x* and *y* direction) and 3.6 mm thickness (*z*-direction), as illustrated in Figure 3.3C. An example CT reconstruction of a hand phantom (natural human skeleton in tissue-equivalent plastic) is shown in Figure 3.3D, acquired on the PCD bench at 70 kV, 0.075 mAs per projection, 360 projections over 360^{o} and reconstructed using 3D filtered backprojection.

The detector features coincidence detection logic that identifies when counts are recorded by adjacent pixels within a small time window (τ_{co}). With coincidence rejection enabled, the two counts are considered to represent the same photon, and a count is assigned only to the pixel with the higher pulse height. The time window τ_{co} determines the so-called dead time extension, as two or more distinct photon interactions occurring over adjacent pixels during this time window will also be considered coincident, resulting in loss of true signal. Assuming a detector dead time of ~180 ns as specified by the manufacturer, a coincidence rejection dead time extension of τ_{co} =20 ns,[132] and fluence as reported in Table 3.1 for a 70 kV beam, only ~0.1% of all incident photons are within the dead time window even with coincidence circuitry active. These coincident counts are post-processed such that the pixel recording the larger pulse height records the "true" count, and the other count is rejected. In the nominal readout mode, coincidence detection is on by default. For measurements without coincidence detection, the system deactivates every other pixel (giving pixel pitch b_x = 0.1 mm) such that a coincident event in adjacent pixels will never be recorded. This scenario of $b_x = 2a_x$ is not intended for typical image acquisition, but is included as a testing mode for investigating the effects of charge sharing. The measurement of presampling MTF is not affected by sampling distance, so the measurements presented in Section V are not affected by sampling effects resulting from turning off coincidence rejection.

Measurements were performed at a tube voltage of 70 kV, added filtration of 2 mm Al plus 1.2 mm of Cu (approximating attenuation by 10 cm water), tube current varied from 1 to 7 mA, x-ray pulse duration of 15 ms, and detector readout at 1 frame per second. A basic calculation of tube output in spektr[133] suggests that a typical exposure (70 kV, 4 mA, 15 ms pulse, 10 cm water equivalent filtration) with a source-detector distance of 653 mm and pixel size of (0.05×0.55) mm^2 amounts to fewer than 100 photons per pixel per frame, which is well below the count rate limit of this PCD.[132]

IV.B Measurement of Detector Signal, MTF, and NPS

The performance of the Si strip PCD system (Figure 3.3) was evaluated in terms of the mean signal, MTF, NPS, and DQE. To relate the measured and predicted detector response, the threshold in secondary quanta (*t*, with units # of secondary quanta) must be converted to the detector pulse height threshold (*D,* with units of arbitrary detector threshold corresponding to pulse height in mV). A comparator determines if a count is above the voltage threshold *D*, and the pulse height monotonically increases with increased number of charge carriers. Saturation occurs when the pulse height exceeds the capacity of the pulse shaper and digitizer, resulting in a non-linear mapping of charge carrier threshold and pulse height threshold. The mapping was described by an empirical fit of the form $D = c_1 - c_2 e^{-c_3 t}$ (for $t > c_4$) and $D = c_2 c_3 e^{-c_2 c_3 t}$ (for $t \leq c_4$), where c_1 describes the maximum detector threshold, c_2 the zero-threshold offset, c_3 the saturation rolloff, and c_4 the range of linear operation. The parameters c_1–c_4 were determined by fitting the predicted mean signal $\bar{q}_0 \gamma(t)$ and the measured detector signal (at 70 kV, 4 mA, 15 ms pulse time) and were found to be consistent with previous work[132] in mammography (e.g., ~25 keV saturation energy and ~3 keV noise floor). These parameters were sufficient for testing the model and could be adjusted according to other potential applications—e.g., higher saturation energy for CT applications involving a higher-energy incident spectrum.

The mean detector signal was measured from flood field images acquired at various settings of detector threshold. Gain correction was performed to account for residual pixel-to-pixel differences after trimming the individual thresholds to adjust for varying pulse height amplification. An empirical fit of the mean signal response (Figure 3.4) with and without coincidence rejection suggested a coincidence rejection efficiency of $r_m = 0.35$. This relatively low rejection efficiency is likely due to "leakage" resulting from an inability of the circuitry to distinguish between two simultaneous pulses of similar (saturated) pulse heights at 70 kV.[132]

The MTF was measured using a 0.5 mm thick tungsten edge abutting and parallel to the face of the detector. The beam was collimated to ~1×1 cm^2 at the face of the x-ray tube to minimize off-focal radiation. An oversampled ESF was formed from 30 images of the tungsten edge in which the edge was translated in increments of 6.35 μm via the computer-controlled translation stage between each image. Data from a continuous row of pixels was analyzed for each image, and the oversampled ESF was generated by interleaving the ESF images according to the displacement of the tungsten edge. A numerical derivative of the ESF was computed, and the tails of the resulting LSF at less than 1% of the peak magnitude were smoothed by a sliding (1×7) mean filter to reduce high-frequency noise.[141, 142] The discrete Fourier transform of the area-normalized LSF was computed to arrive at the presampling MTF.

The NPS was measured from an ensemble of flood-field images at detector threshold values ranging from $D = 0$ to $D = 150$ (t range from 0 to 2.4×10^3 electrons). For each threshold, 30 flood field images were acquired (70 kV, 2 mm Al and 1.2 mm Cu added filtration, 1-7 mA, 15 ms pulse length,). Each flood field image consisted of ~100 individual edge-on Si strip detector wafers, with ~1500 pixels per wafer. The data were processed in 58 regions of interest (300 pixels each) with continuous adjacent pixels within each wafer, yielding a total of 1740 noise realizations for each setting of mA and threshold. These data were linearly detrended to account for anode heel effect, and each image was gain-corrected at each threshold. The mean signal was subtracted from each noise realization, and the squared modulus of the Fourier transform was computed and normalized by the pixel pitch and number of pixels in each realization.[143] The resulting 1740 NPS estimates were averaged to yield the ensemble NPS.

V. Results

V.A Comparison of Theory and Measurement

The predictions of mean signal, MTF, and NPS derived from cascaded system analysis were compared to measurements at nominal parameters (70 kV and without coincidence rejection) as described in Section III. As shown in Figure 3.4A, detector signal response was measured at various mA and detector threshold, with the mean signal predicted as in Section III. The mean signal decreases monotonically as detector threshold is increased, reflecting a larger number of counts rejected at higher threshold. As shown in Figure 3.4B for a fixed threshold ($D = 100$), the mean signal, $\bar{q}_0\gamma(t)$, is linear with exposure (tube current). The system gain for one incident photon, γ, does not exhibit a dependence on exposure over the range of tube currents investigated in the current system. A slight deviation from linearity is observed at tube current greater than ~7 mA, confirming that the PCD is operating at count rates well below the pileup regime. As shown in Figure 3.4C, the MTF was evaluated at low ($D = 0$) and nominal ($D = 100$) detector thresholds, showing an improvement in transfer characteristic at higher threshold. As the distance between the point of photon interaction and the center of the pixel is increased, the likelihood of collecting secondary quanta in the pixel is reduced (per Stages 5 and 7 of the model). Therefore, raising the threshold rejects signal collected far from the point of interaction and improves the effective PSF by reducing the relative contribution of adjacent apertures from multiple counts or detector crosstalk. A potential disadvantage of using a higher threshold is reduced signal, as shown in Figure 3.4A. Overall, theory and measurement were in reasonably good agreement, quantified in terms of a Pearson's correlation coefficient (R^2 value in a linear regression of measured versus theoretical values). The correlation coefficient was greater than 0.93 for all results shown in Figs. 4, 5, and 6 except where specifically noted.

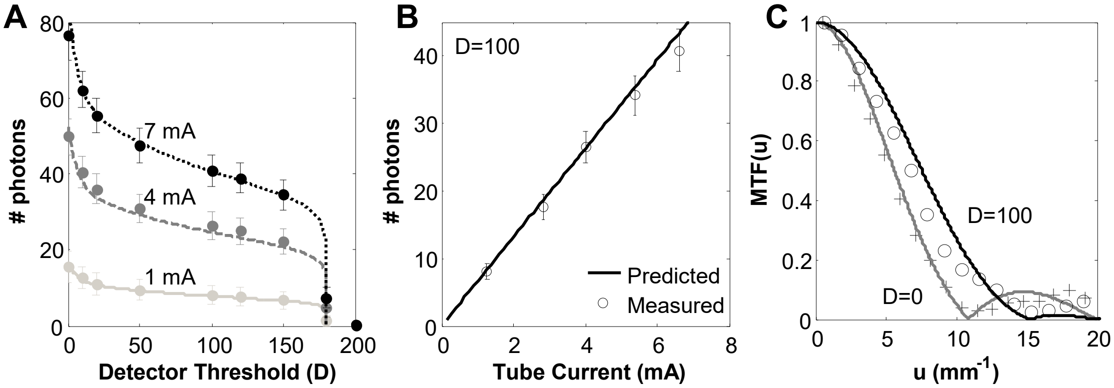

Figure 3.4. Predicted and measured mean signal response as a function of (A) detector threshold and (B) tube current. The detector response is linear over the operating range of the x-ray tube. (C) Presampling MTF at two levels of detector threshold (D = 0 and D = 100).

The spatial-frequency-dependent NPS is shown in Figure 3.5A and is found to be largely uncorrelated at all exposure levels for the nominal operating threshold despite the detector cross talk caused by charge sharing evident in the PSF. The whitening of the NPS arises from undersampling associated with doubling of the sampling distance ($b_x = 0.1$ mm) in this readout mode (see Section IV.A) without a corresponding doubling of aperture size. If the detector could be fully sampled in this readout mode (and the aliasing effect correspondingly reduced), then the broadening of the PSF would be more clearly evident in bandlimiting of the NPS.[124, 144] As shown in Figure 3.5B, individual pixel noise computed from the standard deviation of a single pixel in successive frames was seen to increase with the square root of the exposure, as expected for a Poisson RV, in good agreement with model predictions. In Figure 3.5C, the individual pixel noise is plotted as a function of threshold (with pixel noise given by the integral of the 2D NPS over the Nyquist region). The frequency dependence of the NPS (not shown) was verified in this readout mode to be white (uncorrelated) for all threshold values, $D > 20$. At the lowest threshold settings, the magnitude of the noise increases dramatically due to additive noise. This effect is predicted by the model; however, individual pixels with varying behavior in the pulse shapers and small differences in gain (detector trim differences) were found to count additive noise in varying degrees, and the error in gain calibration resulted in a slight overestimation of the noise at $D < 10$ (giving a reduced correlation coefficient of 0.81).

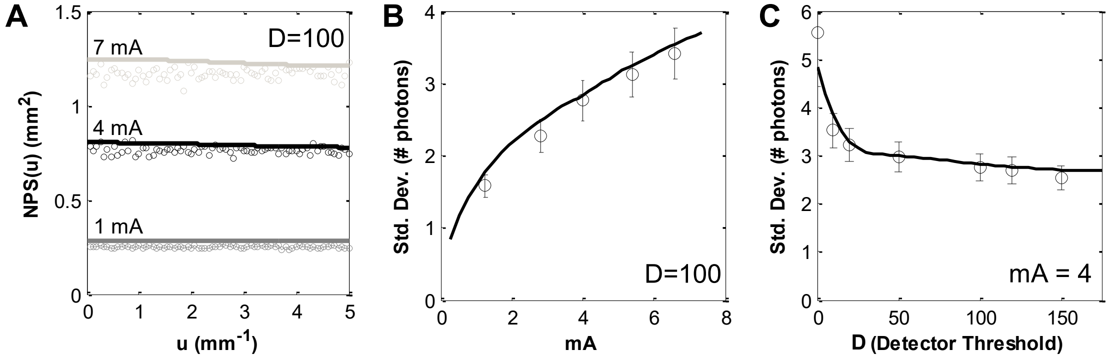

Figure 3.5. Predicted and measured NPS and pixel noise. (A) The NPS at various exposure levels for a fixed detector threshold (D = 100), showing a “white” NPS with reasonable agreement between theory and measurement. (B) The standard deviation in pixel value (noise) measured and predicted as a function of tube current. (C) Pixel noise measured and predicted as a function of threshold at a fixed exposure level (tube current 4 mA).

V.B Effect of Charge Sharing on PCD Performance.

The effects of charge sharing on PCD performance primarily involve a contribution of false counts [calculated from $q_7(x,y;t)$] from multiple adjacent pixels recording a count for the same photon interaction. As discussed in Section III, the effective PSF is a weighted combination of rect functions representing the PSF of a single count, a double count, etc. This suggests that as the threshold is reduced, the contribution from instances of multiple counting is increased, leading to a larger proportion of rect functions from multiple counting and broadening the overall PSF. The effects of charge sharing on signal response is shown in Figure 3.6A, where the predicted and measured mean signal are shown for the detector operated with anti-coincidence circuitry enabled. A discrepancy at high threshold might be expected due to channel leakage associated with high-energy charge sharing events as previously reported[132] for this detector (a reduced correlation coefficient of 0.91 and 0.93 for the case of 4 mA and 7 mA, respectively). These effects are evident in the measurement of mean signal and spatial resolution, as seen in the 7 mA measurements in Figure 3.6. Channel leakage can cause the majority of counts recorded at high threshold to be saturated, which can confound the coincidence rejection logic, resulting in a higher than expected signal. For the nominal detector threshold, however, the linearity of the signal response was preserved when the coincidence rejection circuitry was enabled, indicating that the dead time loss remained largely unchanged. In comparing the mean signal with coincidence rejection as shown in Figure 3.6A to that without coincidence rejection (Figure 3.4A), we observe little or no effect on the number of counts reported at high thresholds, since most counts at high thresholds are single counts, whereas at low threshold (D < ~50) the signal is reduced by ~10–20% due to the large proportion of double counts.

Analysis of the count coefficients, w_m (described in Section III), showed that coincidence rejection reduced the ratio of double counts (w_2) to single counts (w_1), which is reflected in Figure 3.6 as an improvement in the presampling MTF at all thresholds (e.g., comparing Figure 3.6B and Figure 3.4C). The improvement is most pronounced for low thresholds where charge sharing events are strongest, although it is still apparent to a smaller degree at the nominal threshold of $D=100$ (Figure 3.6B). The dependence of the MTF on threshold in coincidence rejection mode is less pronounced than predicted by the model (with a reduced Pearson's coefficient of 0.91 and 0.92 for $D=0$ and $D=100$, respectively), which is attributed in part to the channel leakage effect. The improved MTF (i.e., narrower PSF as shown in Figure 3.6C) indicates improved spatial resolution associated with coincidence rejection.

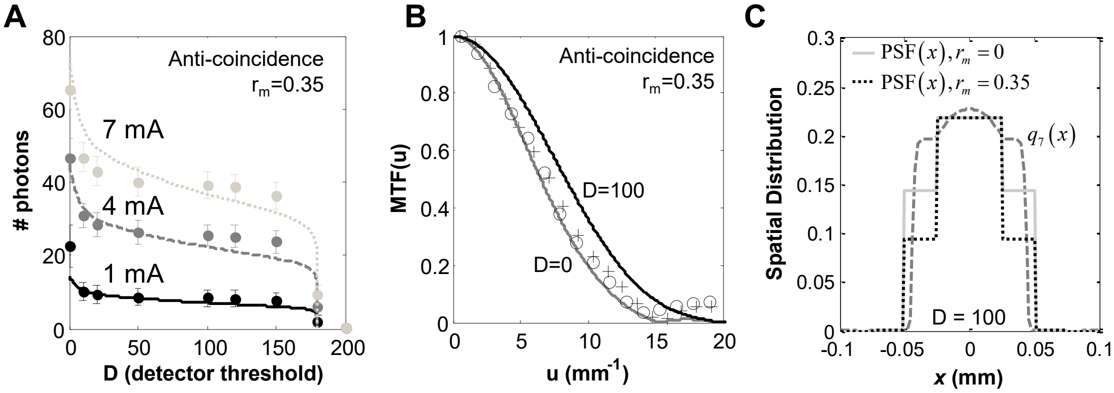

Figure 3.6. Predicted and measured signal response with the coincidence rejection circuit enabled (r_m = 0.35). (A) The mean signal as a function of detector threshold. (B) The presampling MTF shows an improvement especially at low thresholds due to rejection of counts resulting from charge sharing. (C) PSF with and without coincidence rejection, showing an improvement (narrowing of the PSF) with reduction of double counts.

The effects of charge sharing on spatial-frequency-dependent detector performance is further illustrated in Figure 3.7(A-D) as a function of exposure conditions (beam energy) and PCD parameters (threshold, charge carrier diffusion, and pixel size). As shown in Figure 3.7A, the DQE at low threshold ($D = 0$) and low energy (35 kV) suffers without coincidence rejection due to an increase in false counts. At the same energy, raising the threshold improves both high-frequency DQE and the zero-frequency DQE. A detector with perfect coincidence rejection efficiency (CRE, $r_m = 1$) was simulated, and the resulting DQE at low and high thresholds is shown as dotted lines. With perfect coincidence rejection, the threshold effect is eliminated. At higher tube voltage (70 kV, Figure 3.7B), the detector performance at low and high thresholds without coincidence rejection mirrors that at low energy, but with an overall decrease in the DQE due to a reduction in quantum detection efficiency. For a detector with perfect coincidence detection, the DQE at high threshold is worse than that at low threshold due to rejection of true low-energy counts arising from Compton interactions. See Figure 3.8(A-B) for further discussion of the contribution of low-energy Compton events to true counts.

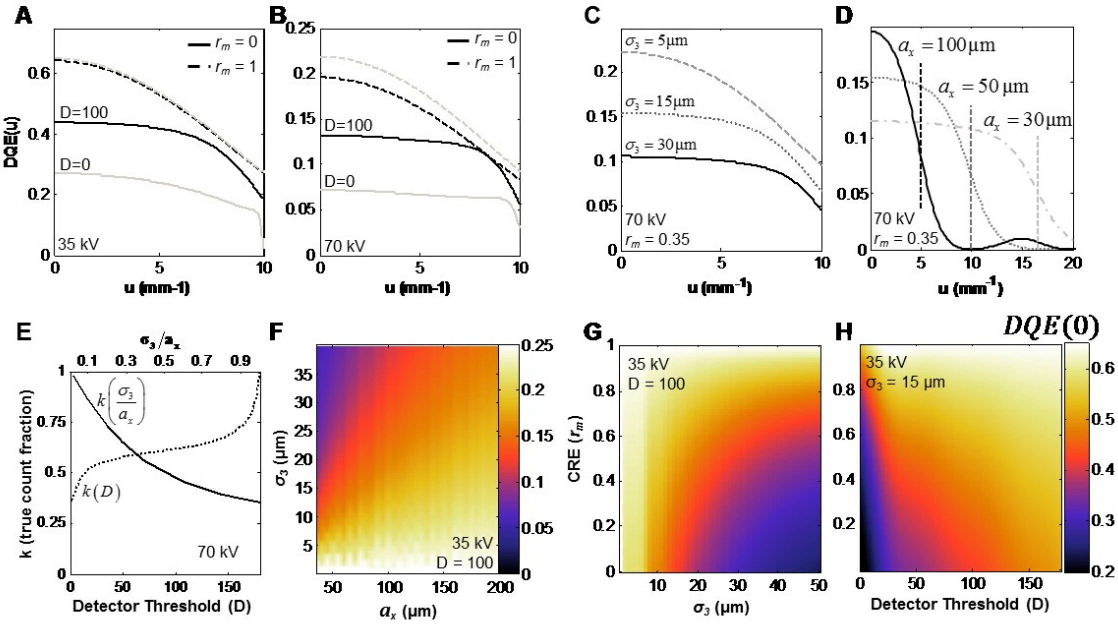

Figure 3.7. Effects of charge sharing as a function of various system parameters. The frequency-dependent DQE(u) is shown at (A) 35 kV and (B) 70 kV with 4 cm and 10 cm of water filtration. The DQE(u) is also shown for various levels of (C) charge carrier diffusion and (D) pixel size with Nyquist frequency demarked by vertical dashed lines. The reduction in DQE(0) at low coincidence rejection efficiency is due to a reduction in the true count fraction, shown in (E). In (F), the optimal detector threshold is shown at 35 and 70 kV, demonstrating a strong dependence of optimal threshold on kV. The reduction of charge sharing effects by coincidence rejection is shown to benefit DQE(0) computed as a function of (G) charge carrier diffusion radius and (H) detector threshold.

In Figure 3.7C, the effect of charge carrier diffusion is shown for three different diffusion lengths σ_3. Improving the charge carrier spread function (reducing σ_3) increases both the high frequency performance (as expected from reduced blur) and improves DQE(0) due to a reduction in false counts from charge sharing. Similarly, changing the aperture or pixel size (Figure 3.7D) reflects a tradeoff between a loss in high-frequency performance due to a reduction in the Nyquist frequency and an improvement in the low-frequency DQE from a reduction of charge sharing. It should be noted that increasing the aperture size imparts distinct implications for PCDs compared, for example, to FPDs. Increasing the aperture size does not give an appreciable improvement in the ratio of signal to additive noise, unlike in EIDs.[145] Instead, the benefit of larger apertures stems from a reduction in the chance that a single photon will contribute secondary quanta to multiple pixels—i.e., reduced probability of charge sharing.

The true count fraction, *k*, is defined as $k = \gamma^{true} / \gamma$ and shown in Figure 3.7E. The true count fraction computed as a function of threshold (dotted line) indicates that more than half of all recorded counts at low threshold ($D < 20$) are false counts (from both charge sharing and additive noise), but at high thresholds ($D > 150$), almost all counts are true. A "perfect" threshold set equal to the maximum possible number of secondary quanta generated by a photon interaction would yield unity *k*, but the system gain (γ) would be nearly zero. The solid line shows the true count fraction as a function of the ratio of diffusion radius σ_3 to aperture size (a_x). For diffusion radius much smaller than aperture size, nearly all secondary quanta generated by a photon interaction are collected by a single pixel, rendering charge sharing negligible. On the other hand, if the charge carrier diffusion radius is much greater than the aperture size, almost all photon interactions result in multiple pixels receiving some secondary quanta, increasing false counts.

Figure 3.7(F) shows the optimal detector threshold for various levels of coincidence rejection efficiency at 35 and 70 kV. The optimal threshold is that which maximizes DQE by best separating the additive noise from the signal and balancing the reduction in charge sharing versus the corresponding reduction in true signal. For a 35 kV beam, a high threshold is optimal: increasing the threshold rejects relatively few true counts (the low-energy Compton peak is small, Figure 3.8) compared to a large number of false counts resulting from charge sharing. For a 70 kV beam, there is a much larger Compton peak compared to the additive noise, and the optimal threshold balances the rejection of both additive noise and Compton signal with charge sharing rejection.

Figure 3.7(G-H) illustrates PCD performance in terms of DQE(0) for a number of pertinent parameters. The zero-frequency DQE is shown for brevity, and since the DQE(*u*) of Figure 3.7 (A-D) are nearly flat over a fairly broad range of parameters, the analysis conveys many of the pertinent ramifications of the system design parameters under consideration. Figure 3.7G shows that as charge carrier diffusion increases, coincidence rejection becomes increasingly important. Figure 3.7H shows that for low energies, the choice of detector threshold is less important. At low coincidence rejection efficiency, the detector threshold needs to be selected to balance tradeoffs among additive noise, charge sharing, and collection of true signal as discussed in relation to Figure 3.7F.

V.C Effects of Additive Noise on PCD Performance and Spectral Resolution

As detailed in section III.B, the effects of additive noise on PCD performance primarily involve a contribution of false counts at low thresholds (largely determined by the behavior of the pulse shaper and the ASIC pulse height gain) and a “blurring” effect on the detected energy spectrum. As seen in Figure 3.8A, for the PCD operating without coincidence detection, the nominal additive noise contribution to the signal is relatively small for energies greater than 1 keV. However, comparing with a PCD capable of perfect coincidence rejection (Figure 3.8B), nearly all of the signal at $E < 10$ keV (at 35 kV) and $E < 30$ keV (at 70 kV in Figure 3.8A) is due to charge sharing events registered as counts. Even with perfect coincidence rejection, however, a threshold that is high enough to reject additive noise unavoidably rejects a portion of the low-energy counts resulting from Compton interactions. This is tantamount to a reduction of the quantum detection efficiency of the detector and contributes to the different ranges of optimal detector threshold seen in Figure 3.10.

The effects of additive noise and coincidence rejection efficiency on DQE(0) are shown in Figure 3.8(C-D). In addition to the strong dependence of optimal threshold on beam energy shown in Figure 3.7F, the optimum depends on additive noise and coincidence rejection efficiency. Without coincidence rejection (Figure 3.8C), the optimal threshold exhibits a weak dependence on additive noise until the magnitude of the additive noise overcomes the charge sharing effects contributing to false counts $\left(\sigma_{\text{add}} > 1500\right)$. In Figure 3.8D, on the other hand, a detector with perfect coincidence rejection has an optimal threshold with a much stronger dependence on additive noise, since there is no contribution of false counts from charge sharing at low thresholds. The result is intuitive in that reduction of charge sharing effects allows a lower threshold (and higher signal) with reduced effect of additive noise.

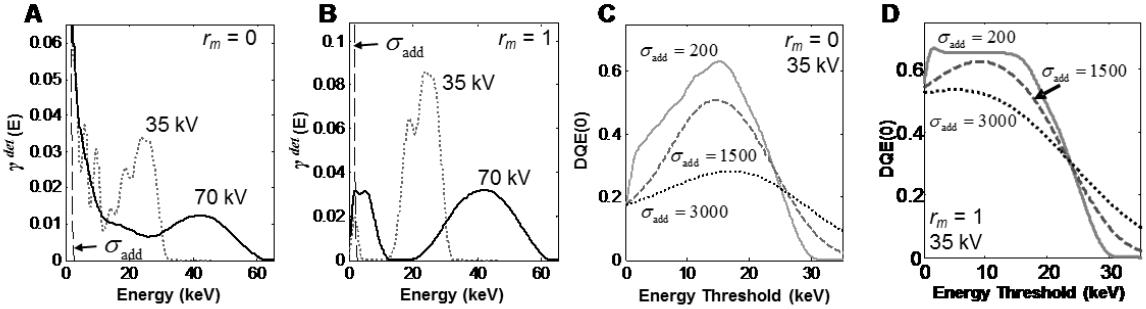

Figure 3.8. Effect of additive noise on the detected spectrum and DQE. (A) The detected spectrum without coincidence rejection. (B) The detected spectrum with perfect coincidence rejection, showing that charge sharing effects at the nominal additive noise level tend to dominate over additive noise unless coincidence rejection is employed. (C-D) Zero-frequency DQE computed as a function of energy threshold (C) without coincidence rejection and (D) with perfect coincidence rejection.

V.D Potential Advantages and Disadvantages of Photon Counting

While EIDs (for example, FPDs) have become a fairly widespread base technology for x-ray detection over the last 15 years, and PCDs have become increasingly prevalent over the last decade, the fundamental advantages and disadvantages of each has been only somewhat rigorously assessed. For PCDs, the benefit of reduced (effectively zero) electronics noise is often noted by virtue of thresholding, as is the improved energy weighting and the potential for energy discrimination and spectral imaging.[146] The latter effects are outside the scope of the current work and were not included in the analysis below. However, at least a portion of the low-energy Compton interactions are lost in selecting a threshold that rejects the entirety of the additive noise distribution [for example, as in Figure 3.8(A-B)]. To compare the fundamental advantages and disadvantages of the thresholding step, consider a hypothetical EID with the same nominal parameters as the PCD system described above (Table 3.1). For purposes of this analysis, the only difference between the PCD and the hypothetical EID is the ability of the former to threshold the detected signal at a voltage pulse height corresponding to the number of collected secondary quanta and the resulting binary nature of the recorded signal. The effects of dead time loss (pulse pileup and chance coincidence) are ignored, as discussed above. The EID therefore has equivalent quantum detection efficiency (g_1), gain and spread in secondary quanta (g_2 and T_3), aperture size (T_5), electronics noise (σ_{add}), etc. and was modeled according to well-established cascaded system analysis in previous work[147].

As shown in Figure 3.9A, a PCD system operating with perfect coincidence rejection (r_m = 1) at a typical threshold level (E = 6 keV, approximately equal to D = 100 for the system in section IV.A) selected to reject additive noise suffers from a slight reduction in DQE(0) compared to an identically parameterized EID due to the loss of low-energy Compton interactions. Reduction of the threshold (e.g., to $E = 0.5$ keV, approximately equal to $D = 5$ for the system in section IV.A) results in an improvement at lower additive noise values, but causes the PCD to suffer as additive noise is increased. Furthermore, Figure 3.9(B-C) shows that as the coincidence rejection decreases, the advantage of PCDs at all levels of additive noise and dose decreases appreciably, but still maintains regions of operation at high noise and low dose that are advantageous to that of the hypothetical EID. This analysis allows selection of an optimal threshold that balances the tradeoffs between the loss in Compton counts and the influence of additive noise. With reduced coincidence rejection efficiency, false counts from charge sharing occur at low energy thresholds (See Figure 3.7) and removes the advantage of a low threshold which does not reject the low energy Compton signal.

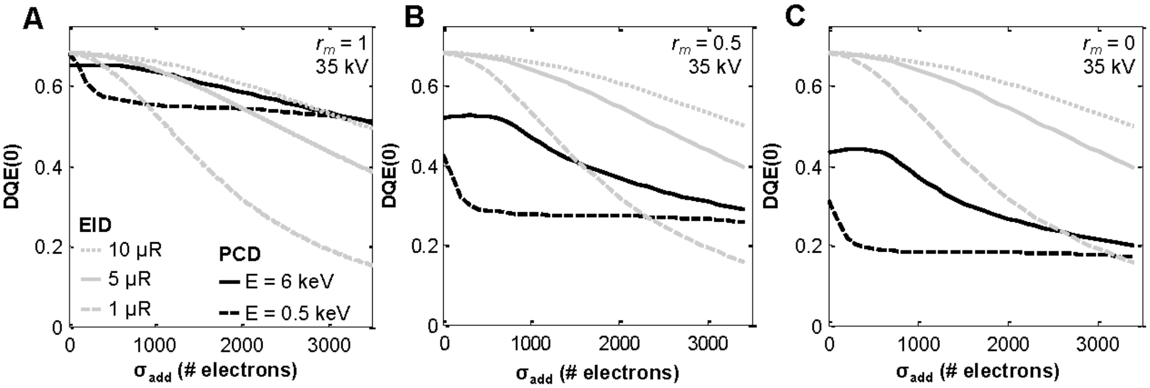

Figure 3.9. Performance of a PCD in comparison to a hypothetical EID of equivalent design (but without the ability for signal thresholding). The plot shows DQE(0) for the two systems as a function of additive noise at (A) perfect coincidence rejection efficiency ($r_m = 1$), (B) imperfect coincidence rejection efficiency ($r_m = 0.5$), and (C) no coincidence rejection ($r_m = 0$). The DQE(0) for the PCD is nearly independent of dose and was evaluated at two threshold settings [nominal 6 keV (solid black line) and a low-energy threshold of 0.5 keV (dotted black line)]. The DQE(0) for the EID is shown at three dose levels: 10 µR (dotted gray line), 5 µR (solid gray line), and 1 µR (dashed gray line).

Further comparison between the PCD and the hypothetical, identical EID is shown as a function of dose, additive noise, incident energy, threshold, and coincidence rejection efficiency in Figure 3.10. These calculations show the range of operating conditions at low-dose and/or high additive noise for which the application of a threshold in the PCD systems is beneficial in comparison to the energy-integrating system. Note, however, that the hypothetical EID features a quantum gain ($\bar{g}_2 \approx 8000$ electrons) that is much larger than for typical scintillators and less efficient semiconductors, so the performance of the hypothetical system at low dose (and higher additive noise) is greater than should be expected for a realistic EID. The point here is to illustrate the fundamental advantage (and disadvantage) of thresholding, all other factors being equal, and analysis for a realistic EID (viz., a FPD) is shown below.

Perfect coincidence rejection is assumed in Figure 3.10A for a 35 kV beam, leaving additive noise as the only contributor of false counts for the PCD. The threshold was fixed at E = 10 keV to give good separation of the additive noise ($\sigma_{\text{add}} = 0 \text{ to } 3000$ electrons) from the true signal spectrum. In the regime of low additive noise and high dose, the EID is shown to slightly outperform the PCD, because the EID is operating in close to ideal circumstances (strongly quantum limited) while the PCD suffers a small loss due to the rejection of the Compton interactions. The effect of frequency was evaluated and found to have minimal effect on the relative performance of the PCD versus the EID. In Figure 3.10B, the identical scenario is shown for a 70 kV beam. At higher incident energies, the Compton interaction cross section comprises a larger portion of the total cross section, and a threshold of E = 10 keV therefore rejects a larger portion of the interacting photons. This results in a stronger reduction in DQE(0) and a reduction in the dose range for which the PCD is advantageous in comparison to the EID.

Figure 3.10C summarizes the relative performance of EIDs and PCDs with sub-optimal coincidence rejection at a fixed dose and additive noise level as a function of coincidence rejection efficiency and detector threshold. The EID performance is independent of these parameters. For a given additive noise level, dose, and coincidence rejection efficiency, there is an optimal threshold at which PCD performance is maximized (indicated with the dashed black line). At low energy threshold and low coincidence rejection efficiency, the PCD performance suffers due to the introduction of false counts from charge sharing effects. As the threshold is increased above ~25 keV, the PCD again suffers in comparison to the EID due to the rejection of true signal (high energy Compton interactions and photoelectric interactions).

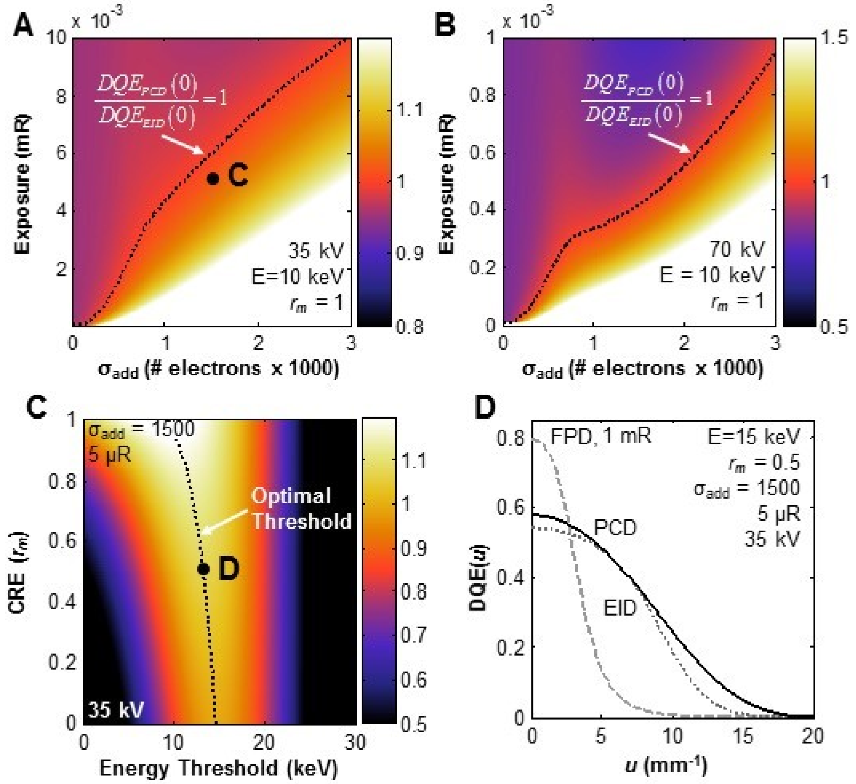

Figure 3.10. Comparison of a PCD and a hypothetical EID system with the same physical parameters. The ratio of DQE(0) for a PCD to that of an EID is plotted as a function of (A-B) dose and additive noise at 35 kV and 70 kV behind 4 cm and 10 cm of water, respectively. (C) At fixed additive noise (σ_{add} = 1500 e) and exposure (5 μR), the DQE(0) ratio is evaluated as a function of threshold and coincidence rejection efficiencies. (D) At fixed additive noise (σ_{add} = 1500 e), coincidence rejection (r_m = 0.5), exposure (5 μR), and threshold (E = 15 keV), the spatial-frequency-dependent DQE is shown for the PCD and the hypothetical EID in comparison to a FPD.

In Figure 3.10D, the spatial-frequency-dependent DQE of the PCD and hypothetical EID are shown at fixed dose, additive noise, threshold, and coincidence rejection efficiency. The PCD shows a modest improvement at low spatial frequency, and a more pronounced improvement in comparison to the EID at higher frequencies. To provide a realistic base of comparison, and because the gain at stage 2 is so high (higher than would be expected for a typical EID employing a scintillator), the performance is plotted in comparison to that of a "typical" FPD as modeled in previous work.[147–149] The FPD was modeled according to a CsI:Tl scintillator (150 mg/cm^2 thickness), $\bar{g}_2 = 900$, T$_3$ was determined by the scintillator thickness, $\bar{g}_4 = 0.99$, T$_5$ was given by a sinc function for a_x, = 0.05 mm, and $\sigma_{add} = 1000$ electrons. This more realistic representation of an energy-integrating FPD exhibits lower gain in stage 2 and a blurrier stage 3, achieving comparable performance to the PCD only down to ~1 mR. As shown in Figure 3.10D, the DQE for the FPD (gray dashed curve) is higher at low spatial frequency due to the higher atomic number of the CsI:Tl scintillator (higher g_1); however, the high-frequency performance is limited by blur in the scintillator, which greatly exceeds that of charge carrier diffusion in the silicon strip detector.

VI. Conclusions

A cascaded systems model has been developed for analysis of the imaging performance characteristics of PCD systems, building upon more than a decade of well-established modeling of signal and noise propagation in energy-integrating detectors (e.g., FPDs) and extends analysis to include effects that are unique to PCDs. The model was validated in comparison to measurements and illustrates the threshold-dependence of the MTF, extending previous work by Acciavatti et al.[124] The model also complements recent work in detector physics specifically modeling a single stage—e.g., spectral distortion effects[11,150]—to include a more complete framework for spatial-frequency-dependent signal and noise characteristics. Among the findings of the current work are: (i) illustration of numerous important factors of system performance, such as the effects of detector threshold on DQE as reported by Tanguay et al;[17] (ii) revealing the effects of charge sharing; (iii) validation of theoretical predictions in comparison to experimental measurements on a PCD benchtop across a range of exposure and detector operating conditions; (iv) formulation of a framework for system optimization; and (v) a basis for more rigorous understanding of the potential advantages (and disadvantages) of PCDs in comparison to conventional energy integrators. The model also introduces the concept of a threshold-dependent effective PSF given by a weighted combination of aperture functions and incorporates coincidence rejection in the analytical framework for PCD imaging performance.

The current model is not without limitations, as acknowledged in part in Section II. Among these is the assumption that pulse pileup—in which multiple photons are incident onto the same pixel during the dead time of the detector—and chance coincidence—in which multiple photons are incident on adjacent pixels at a nearly coincident time and blocked by the anti-coincidence logic—are negligible. As demonstrated in the experimental measurements, however, these assumptions appear to be valid for the PCD used in this work over nearly the entire range of operating techniques (kV and mA), where only a small departure from linearity was observed at the highest exposure rates. For PCD systems with larger pixel size, more compact geometry, and increased dead time compared to the Si detector considered in this work, pileup effects may degrade detector response. Extension of the analytical model to encompass both charge sharing (as shown in this work) and pileup effects (to be considered in future work) would benefit system design and optimization for such configurations.

The model was shown to demonstrate reasonable agreement with the measured signal and noise characteristics of the PCD, including spatial resolution (MTF), spectral characteristics (signal versus threshold), and stochastic noise characteristics (NPS). These aspects of detector performance are important to consider as such PCD systems begin to enter application in various areas of radiographic / mammographic and tomographic imaging. Such characteristics not only govern the fundamental low-dose performance of these systems but also the ability for energy discrimination. The model adapts equally well to a variety of PCD configurations distinct from the Si strip detector considered in this work. For example, the model allows analysis of the potential benefit of improved quantum detection efficiency of detector materials such as CdTe (higher atomic number) weighed against the tradeoffs of poor charge transport of holes (increased σ_3 and reduced $\bar{g}_4$) and K-fluorescence. In particular, K-fluorescent photons can degrade the resolution and increase charge sharing events. This can be incorporated in the model as a parallel cascade[151] representing spatial relocation at stage 2. As in previous work,[152] the distribution for photoelectric and Compton interactions would be split in stage 1, treated independently in stages 2-4 (including K-fluorescent effects) and recombined in stage 5.

Finally, the model provides a rigorous basis for understanding the fundamental performance advantages and limits of PCDs in comparison to conventional energy-integrators. Specifically, for a PCD with non-negligible internal detector scatter (contributing to the low-energy peak of the "true counts" spectrum), the "threshold" must navigate a thin line between noise reduction from rejecting additive electronics noise and quantum noise increase from rejecting true interactions. Aside from inherent contrast advantages (more favorable energy weighting) and spectral discrimination, the optimal operating point for PCDs is in regimes of very low dose (alternatively, very high additive noise). Coupled with count rate limitations (pulse pile-up effects that would tend to increase scan time), sparse sampling characteristics,[153] and a relatively small FOV in currently available PCDs, their incorporation in the design of a high quality CBCT head scanner is not well justified at this time.

Alternative EID technologies appear to offer a more promising immediate path. Considering the typical dose regime for CBCT of the head (~25-50 mGy) coupled with the large FOV requirements, the current generation of FPDs appear reasonably well suited to such application, as investigated in greater detail in subsequent chapters. Other advances, such as on-pixel gain,[100] would bolster such applicability. Moreover, electronic noise levels comparable to those shown above for PCDs can be achieved with new CMOS EID detectors. The performance of such EIDs for incorporation in the design of a high-performance head imaging system is investigated in subsequent chapters.

Chapter 4: Modeling and Design of a Cone-Beam CT System for High-Quality Imaging of the Head

I. Introduction

As discussed in Chapter 1, the front-line modality for diagnosis of acute ICH is NC-MDCT, which allows detection of fresh blood in the brain with high sensitivity as well as the diagnosis of focal contusions and fractures;[154] however, MDCT is poorly suited to point-of-care deployment. CBCT scanners are comparatively simple and can be well suited to mobile or point-of-care implementation.[71, 97, 155, 156] Such systems provide sub-millimeter spatial resolution, but soft-tissue contrast resolution is often limited by artifacts and noise.[85] The detection of small hemorrhages and subtle cranial fractures requires a system capable of low contrast visualization (40-80 HU blood-to-brain contrast),[52, 157] with low noise, minimal artifacts, and sub-millimeter spatial resolution. Recent advances in artifact correction[158] and model-based image reconstruction[159–161] demonstrate the potential for CBCT to provide soft-tissue visibility approaching that of MDCT in a portable configuration.

A quantitative approach to imaging system design with a rigorous consideration of performance tradeoffs during the early stages of development is an important step to achieving optimal image quality. Analysis of task-based imaging performance draws from methods grounded in statistical decision theory, image simulation, observer models, and/or human observer studies. Linear cascaded systems analysis of NEQ combined with Fourier domain representations of the imaging task provide a framework for analysis of detectability index that has proven valuable in the development of CBCT systems for image-guided radiotherapy,[162] image-guided surgery,[76] musculoskeletal imaging,[163] phase-contrast imaging,[164, 165] tomosynthesis,[34, 166] and breast imaging.[167, 168] Under assumptions of linearity, shift invariance, and stationarity, such models have demonstrated reasonable agreement with human observer performance for simple imaging tasks[34] and can be adapted to various geometries, imaging conditions, and detector types, including direct-detection[127, 128] or indirect-detection[9, 31] FPDs as well as PCDs,[123, 130] and model-based image reconstruction[169] for analysis of local signal and noise characteristics.

Such work has also employed methods based on spatial domain analysis of task performance. Monte Carlo (MC) simulations have been developed for various energy integrating x-ray detector types[137, 170] and energy discriminating detector types.[13, 171] Image quality model-based MC simulation has been useful in the design of dedicated breast CBCT systems, as in Boone et al.[81] and Vedual et al.,[172] as well as analysis of the performance of existing systems.[173] Optimization of breast tomosynthesis parameters have been performed with object-dependent simulations[174] and in conjunction with task-based performance of a prewhitening observer.[175] Such image simulations are also well suited to optimization based on observer models, such as the channelized Hotelling observer,[33, 176] which have been shown to correlate well with human observer performance.[177] Work by Frey et al.[178] used such analysis to optimize the parameters of 3D iterative reconstruction algorithms in emission tomography, illustrating the flexibility and robustness of these models, especially in the evaluation of nonlinear reconstruction techniques.

Analysis based on a cascaded systems model of the imaging chain elucidates the effects of individual components of the imaging system and factors of spatial resolution, contrast, and noise governing imaging performance. In the work reported below, a cascaded systems model for 3D imaging performance in CBCT is developed and applied to task-based design and optimization of a dedicated CBCT head scanner for detection of ICH. A fairly comprehensive scope of system design parameters was considered, including aspects of system geometry, x-ray source / imaging technique, and detector configuration. Model predictions were compared to experiments performed on a CBCT benchtop, and the results were considered with respect to numerous practical, logistical, and clinical considerations to guide the development of a clinical prototype. The work reported below was first published in Xu et al, “Modeling and Design of a Cone-Beam CT Head Scanner Using Task-Based Imaging Performance Optimization”[179] and figures with associated text are reproduced in this dissertation with permission from the publisher (IPEM, London, UK).

II. Theoretical Methods

II.A Model for 3D Imaging Performance

Imaging performance was modeled with a linear cascaded systems representation of the imaging chain,[32] accounting for processes of gain, blur, sampling, and additive noise for each stage. Such modeling has demonstrated close agreement with measurements of the local MTF, NPS, and NEQ[180] as well as human observer performance for simple imaging tasks.[34] A brief summary of the model and parameters describing the propagation of signal and noise is shown in Figure 4.1, with subscripts denoting stages of: (0) incident x-ray quanta; (1) absorption in the x-ray converter; (2) conversion of x-ray quanta to optical photons; (3) spread of optical photons in the scintillator; (4) coupling of optical quanta to the semiconductor detector; (5) integration of quanta by semiconductor detector; (6) additive electronics noise; (7) sampling of the 2D projection; (8) post-readout binning and resampling; (9) log normalization; (10) ramp filter; (11) reconstruction apodization filter; (12) interpolation of 2D projection data; (13) 3D backprojection; and (14–15) binning and sampling of the 3D image reconstruction.

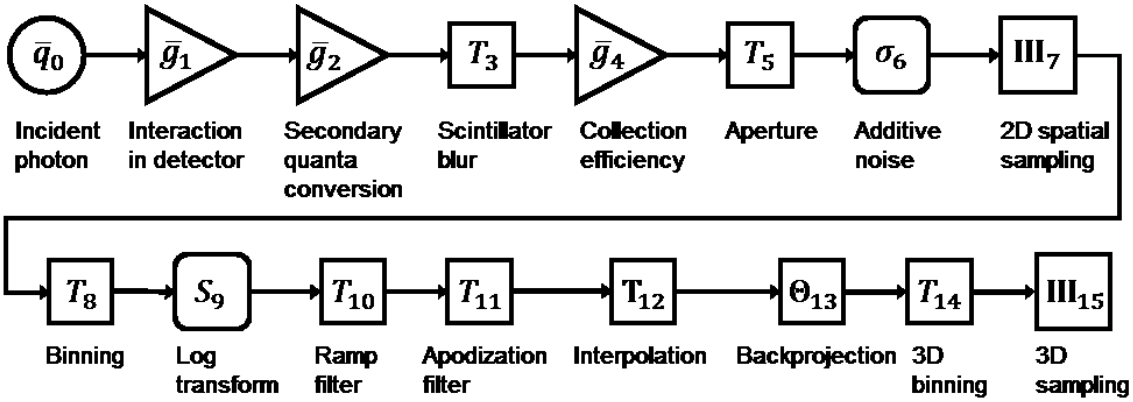

Figure 4.1. Illustration of the cascaded systems model for signal and noise propagation through the image acquisition (stages 0–7) and reconstruction (stages 8–15) process.

The analysis recognizes several important assumptions. Fourier-based metrics of resolution and noise assume a linear shift invariant system and wide-sense cyclostationary noise.[181, 182] The analysis assumes such properties to hold locally within a specific region of the image (e.g., the center of the image) and with respect to low-contrast (i.e., small signal difference) stimuli.

The spatial resolution in the 3D image reconstruction is described by the MTF,[32] given by the combination of transfer functions for each stage in the imaging chain:

$$\begin{aligned}\mathrm{MTF}(\mathbf{f}) = T_{\mathrm{spot}}(Mf_r, Mf_z)\, T_3(Mf_r, Mf_z)\, T_5(Mf_r, Mf_z) \cdot \ldots \\ T_8(Mf_r, f_z)\, T_{11}(Mf_r, Mf_z)\, T_{12}(Mf_r, Mf_z)\, T_{14}(\mathbf{f})\end{aligned} \tag{4.1}$$

where T_{spot} represents the focal spot MTF, T_3 the scintillator transfer function, T_5 the pixel aperture, T_{11} the reconstruction apodization filter, T_{12} the interpolation of projection data in the 2D projection domain, and T_{14} the voxel aperture. The 2D projection domain transfer functions are expressed as a function of the 2D projection domain frequencies (f_u, f_v) and are rescaled to the 3D image reconstruction domain [$\mathbf{f} = (f_x, f_y, f_z)$] by the system magnification (M) as $f_v = Mf_z$ and $f_u = Mf_r$, where $f_r = \sqrt{f_x^2 + f_y^2}$.

The NPS of the 3D image reconstruction[32] includes the effects of various sources of correlation (e.g., scintillator blur, the apodization filter, etc.) as well as noise associated with x-ray scatter, readout electronics (S_{add}), and 2D and 3D sampling:

$$\begin{aligned}\mathrm{NPS}(\mathbf{f}) = \frac{\pi|f_r|}{N_{\text{proj}}M^2}\left(\left[\bar{q}_0^{S+P} S_5\left(Mf_r, Mf_z\right) + S_{\text{add}}\right] ** \mathrm{III}_7\left(Mf_r, Mf_z\right)\right)\cdot \ldots \\ T_{11}^2\left(Mf_r, Mf_z\right) T_{12}^2\left(Mf_r, Mf_z\right) T_{14}(\mathbf{f}) *** \mathrm{III}_{15}(\mathbf{f})\end{aligned} \tag{4.2}$$

where S_5 represents the normalized 2D projection NPS, $|f_r|$ the reconstruction ramp filter, $\mathrm{III}_7\left(Mf_r, Mf_z\right)$ and $\mathrm{III}_{15}(\mathbf{f})$ the 2D and 3D comb functions associated with sampling in the projection and image reconstruction domain, respectively, $\bar{q}_0^{S+P}$ the total (scatter plus primary) mean photon fluence at the detector, M the object magnification, N_{proj} the number of projections, and S_{add} the additive electronics noise. The fluence and energy spectrum behind the object $\left(\bar{q}_0^{S+P}\right)$ were calculated after attenuation through 160 mm water and 1.4 mm of cortical bone (assuming a simple model of the cranium, 7 mm thick, roughly 4/5 of which is bone marrow and cancellous bone), approximating the beam quality behind the center of a head.

The spatial resolution and noise properties of the system can be combined to form the 3D NEQ:

$$\mathrm{NEQ}(\mathbf{f}) = \pi|f_r|\frac{\mathrm{MTF}^2(\mathbf{f})}{\mathrm{NPS}(\mathbf{f})} \tag{4.3}$$

This analytical form for the 3D NEQ was extended from that in previous studies[32] in two respects that warranted particular attention with respect to high-quality soft-tissue visualization (as in ICH detection).

First, the effect of x-ray scatter was incorporated, including the effect of the air gap, antiscatter grid, and post-readout scatter correction. The air gap was treated using the effective scatter point source model as in Neitzel[36] and the effect on contrast and noise as in Siewerdsen and Jaffray.[162] An antiscatter grid with primary transmission, T_P, and scatter rejection efficiency, 1-T_s, was modeled according to an analytical model,[183] with scatter and primary fluence transmission calculated behind the center of a 16 cm water cylinder. The SPR, $\bar{q}_0^P$, and $\bar{q}_0^{S+P}$ at the detector (i.e., behind the grid) were calculated for the range of grid ratios (GR) in Table 4.1.

Variable	Description	Nominal Value	Range
$\bar{q}_0^{S+P}$	Total (primary + scatter) fluence at the detector behind the object	9,250 photons/mm^2	(4 – 20)×10^3 photons/mm^2
$f = (f_x, f_y, f_z)$	Frequency domain coordinates corresponding to the (x, y, z) spatial domain of the reconstructed image	–	–
SAD	Source-to-axis distance	750 mm	350-1200 mm
SDD	Source-to-detector distance	1100 mm	500-1500 mm
M	Object magnification	1.47	1 – 2.7
kV	X-ray tube voltage	90 kV	60 – 120 kV
mAs	Current×pulse width product	0.57 mAs / pulse	0.25 – 2.5 mAs / pulse
a_{spot}	Focal spot width (assumed square)	0.6 mm	0.4 – 1.0 mm
a_{pix}	Pixel size (assumed square)	0.4 mm	0.01 – 1.00 mm
a_{vox}	Voxel size (assumed cubic)	0.7 mm	0.2 – 1 mm
h_{win}	Apodization filter parameter	0.5 (Hann)	1.0 (Ramp) or 0.5 (Hann)
S_{add}	Additive electronic noise	~7000 electrons	300 – 10,000 electrons
N_{proj}	Number of projections per scan	720	300 – 800
N	Bit depth	14	8 – 32
y_{gap}	Air gap	270 mm	70 – 500 mm
F’	Scatter fraction at the exit of the object	0.72	0.7 – 0.74
SPR	Scatter-to-primary ratio at the detector	1.06	0.9 - 1.5
y_{scat}	Distance from virtual scatter point source to object	240 mm	200 – 280 mm
GR	Anti-scatter grid ratio	8:1	6:1 – 12:1
D_0	Dose to center of CTDI phantom for one CBCT scan	20 mGy	10 – 45 mGy

Table 4.1. Glossary of terms and symbols with nominal values and ranges.

For all values of GR, the analysis assumed Pb septa of width 0.05 mm and nominal gridline spacing 40 lp / cm in computing scatter and primary transmission. Finally, previous work[158] showed the importance of x-ray scatter and beam-hardening corrections (e.g., via MC simulation) for low-contrast ICH imaging. The effect of such correction on the image signal and noise characteristics is analyzed in Appendix B of this dissertation. Analysis of scatter and primary fluence in the imaging chain shows that scatter correction improves contrast and increases image noise in a complementary manner and does not change CNR or detectability index within the assumption of local linearity, shift invariance, and stationarity stated above. Of course, scatter correction carries the benefit of improved image uniformity and HU accuracy and is still a necessary component of an advanced CBCT imaging framework. Therefore, all image-domain measurements in this paper are performed with scatter correction applied.

Second, since ICH detection carries such a strong requirement in contrast resolution, we extended the cascaded systems model of additive electronic noise. Whereas previous models treated additive electronics noise as a single parameter, we incorporate the effect of quantization noise arising from the ADC separately from other sources additive noise sources such as dark current, readout line, and amplifier noise. As detailed further in Chapter 5, we investigated the extent to which increasing bit depth beyond the typical 14- or 16-bit ADC could potentially improve ICH detection.

As in previous work,[163] a 3D non-prewhitening (NPW) observer model was used to compute the detectability index, *d'*:

$$d'^{2}_{\mathrm{NPW}} = \frac{\left[\iiint \mathrm{MTF}^2(\mathbf{f})\, \mathrm{W}^2_{\mathrm{task}}(\mathbf{f})\, \mathrm{d}\mathbf{f}\right]^2}{\iiint \mathrm{NPS}(\mathbf{f}) \cdot \mathrm{MTF}^2(\mathbf{f})\, \mathrm{W}^2_{\mathrm{task}}(\mathbf{f})\, \mathrm{d}\mathbf{f}} \tag{4.4}$$

where MTF and NPS are defined in Eqs. (4.1) and (4.2), respectively, W_{task} is the task function, and the integrals are over the 3D Fourier domain bounded by the Nyquist region of the image reconstruction. The 3D NPW observer model demonstrated reasonable agreement with human observer performance for simple imaging tasks in tomosynthesis and CBCT in previous work.[34] The model considers the full 3D frequency content of the signal and noise without assumptions on 2D slice scrolling[184] and without invoking parameters associated with anthropomorphic eye filter or internal noise. It is therefore a reasonable choice for the objective function in system design, as described below, in maximizing 3D information content pertinent to the imaging task

The primary task considered in this work is a low-contrast, mid-frequency task representing a small ICH, as illustrated in Figure 4.2. For completeness with respect to imaging of head trauma, analysis of a high-contrast, high-frequency task representing bone fracture is included in section IV.F, and the implications for accomplishing multiple tasks with a given image are discussed. For the ICH detection task, the task function is given by the product ($W_{\mathrm{task}} = C_{\mathrm{task}} F_{\mathrm{task}}$) of the contrast of the stimulus (C_{task}, units of μ or mm^{-1}) and its frequency content (F_{task}, units of mm^3). The units of W_{task} is therefore $\mu \cdot$mm^3 (where μ here represents the units of attenuation coefficient, HU or mm^{-1}) giving a dimensionless detectability index. Note that the contrast term is affected by scatter ($C_{\text{task}} = {}^{C_{\text{true}}}\!/_{1+\text{SPR}}$) and is reduced from the true contrast of the object to the background $\left(C_{\text{true}} = |\,\mu_{\text{stimulus}}\,| - |\,\mu_{\text{background}}\,|\right)$. The frequency-dependent part of the task function, F_{task}, was modeled as a difference of Gaussians to emphasize varying degrees of low-, medium-, and high-frequency content in the detection task:

$$F_{\text{task}}\left(|\mathbf{f}|\right) = A\left(\exp\left[-\frac{\left(|\mathbf{f}|-f_1\right)^2}{2s_1^2}\right] - \exp\left[-\frac{\left(|\mathbf{f}|-f_2\right)^2}{2s_2^2}\right]\right) \tag{4.5}$$

Written this way, W_{task} can be interpreted as discrimination of two Gaussian structures (of feature size $2.35/s_1$ and $2.35/s_2$ mm, respectively) or as detection of the stimulus edge (with size $(s_1+s_2)/(6s_1s_2)$ mm). The amplitude (A, units mm^3) normalizes F_{task} such that W_{task} carries the same signal power as the spatial domain object function. The task function was assumed to be isotropic (i.e., equal feature size in each direction)—a straightforward model with respect to a (spherically symmetric) ICH.

As shown in Figure 4.2, the ICH task function has low signal power (associated with the low contrast of blood-to-brain, $C_{\text{true}} \approx 8\cdot 10^{-4}$ mm^{-1} or 40 HU at 90 kV)[5] and emphasizes low and medium frequencies ($f_1 = f_2 = 0$, $s_1 = 0.35$ mm^{-1}, $s_2 = 0.25$ mm^{-1}) corresponding to a feature size of ~1.2 mm. The fracture task carries higher contrast (bone and water, $C_{\text{true}} \approx 0.021\ \text{mm}^{-1}$ or 900 HU at 90 kV) and emphasizes medium and high frequencies ($f_1 = f_2 = 2$, $s_1 = 0.4$ mm^{-1}, $s_2 = 0.2$ mm^{-1}). Analysis of *d'* for the ICH task is detailed below, and results for the fracture detection task are summarized in Section IV.F.

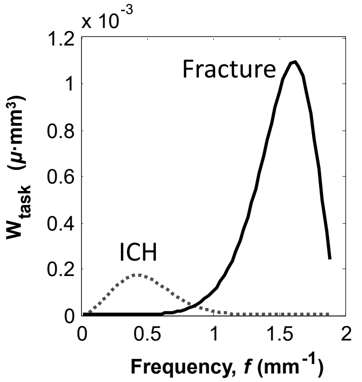

Figure 4.2. Two task functions pertinent to imaging of head injury. ICH detection carries low signal power (blood-to-brain contrast, ~40 HU) and low-to-mid–frequency content (feature size ~1.2 mm). Fracture detection carries high contrast (bone-to-water contrast, ~900 HU) and high-frequency content (feature size ~0.3 mm).

II.B Optimization of Imaging System Design

Investigation of optimal system design involved a systematic analysis of performance over a series of studies grouped generally as: (1) system geometry; (2) x-ray source and imaging technique; (3) antiscatter grid and scatter correction; and (4) detector configuration, with the aim of identifying a system design optimal to the task of ICH detection. Since each of these studies involved interdependent parameters [e.g., selection of optimal geometry in (1) depended on focal spot size in (2) and detector configuration in (4)], the analysis was repeated for each univariate (or bivariate) study holding other parameters fixed at their nominal values in Table 4.1. Recognizing that detectability increases or decreases monotonically for many of these parameters (e.g., focal spot size, additive noise, dose, etc.), a constrained multivariate optimization was performed over the remaining, non-monotonic parameters (viz., kV, SAD, and pixel size) and the global maximum matched the optima shown in the bivariate analyses illustrated below.

II.B.1 System Geometry

Selection of the system geometry included the choice of SAD and SDD and affects the magnitude of x-ray scatter and spatial resolution owing to combined effects of focal spot blur and geometric magnification. Moreover, for fixed patient dose and a given magnification, performance tends to improve with larger SDD but requires increased x-ray tube power and implies a larger scanner footprint (outer diameter). As shown in sections II.B.2-II.B.4, a nominal SDD of 1100 mm was chosen based on such considerations, and the corresponding optimal SAD was chosen based on analysis of focal spot blur, scatter rejection, etc.

II.B.2 X-ray Source and Imaging Technique

The x-ray source and imaging technique included parameters associated with the focal spot size, beam energy, and dose, which in turn pose requirements on x-ray source power. A fixed nominal dose was chosen based on the (20 – 50 mGy) dose levels reported for head CT,[185] and the optimal beam energy (i.e., the kV that maximizes *d'* for the ICH task) was determined. The x-ray tube output (mAs) in all cases was adjusted to provide a nominal dose of D_0 = 20 mGy to the center of a 16cm CTDI phantom, computed as:

$$D_0 = N_{\text{proj}} X_{\text{obj}} \left(\text{SAD}\right) e^{-\mu_{\text{obj}} \cdot r} f_{\text{water}} \left(\text{kV}\right) \text{BSF}\left(\text{kV}\right) \tag{4.6}$$

where N_{proj} is the number of projections (equally spaced over a 360° orbit), X_{obj} is the in-air exposure at isocenter (in absence of the object), f_{water} is the f-factor of water, r is the radius of the object (80 mm for the CTDI head phantom), μ_{obj} is the attenuation coefficient of the CTDI phantom, and the backscatter factor was obtained by empirical fit to dose measurements performed on the CBCT bench (as in Figure 4.3).

II.B.3 X-Ray Scatter

As stated in section II.A, MC scatter correction restores image contrast and increases image noise such that the local CNR and detectability are unaffected. For simplicity, results in Section IV assumed accurate MC scatter correction, but analysis in Appendix B of this dissertation shows that inaccurate scatter fluence estimation (or even no scatter correction at all) yields the same local detectability index. The selection of an antiscatter grid was investigated (in addition to MC scatter correction), accounting for effects of GR, T_P, and T_S according to the analytical model described in Day and Dance.[183] Grids were modeled as Pb septa with Al interspacer at 40 line pairs / cm, matching the experimental grids investigated in section III.A.

II.B.4 Detector Configuration

Investigation of detector configuration included variation of detector pixel size (a_{pd}) and additive electronics noise. The current state of commercially available detectors suggests two typical configurations: a CMOS detector with small pixel size, low readout noise, and small FOV; and a FPD with somewhat larger pixel size, relatively higher readout noise, and capable of larger FOVs. Chapter 5 details the analysis of ADC quantization noise and the effect of bit depth on system performance.

II.B.5 Additional Design Constraints

Finally, the results of the four studies described above were considered with respect to realistic physical or clinical constraints (e.g., size of the scanner) and design characteristics that can be achieved using current state of the art hardware (e.g., specific x-ray tubes and/or detectors). Other design goals, such as fast scan speed, FOV, and portability posed additional constraints on detector dynamic range, detector size, and x-ray source power. These constraints were considered with respect to the results of the optimization study to guide specification of a head scanner prototype design now being developed for clinical studies.

III. Experimental Methods and Materials

III.A X-Ray Imaging Bench and Phantoms

Imaging Bench. All images were acquired on the imaging bench shown in Figure 4.3 using an x-ray source (RAD13, Dunlee, Aurora IL), a translation and rotation stage (Compumotor 6k8, Parker Hannifin, Rohnert Park CA), and a FPD (PaxScan 4030CB, Varian, Palo Alto CA). The bench allowed variation of system geometry over a range SAD = 400–1200 mm and SDD = 700–1500 mm. In each case, system geometry was calibrated using the method described by Cho et al.[186] The x-ray beam energy was varied over a range 60–120 kV and 0.25–2.5 mAs per projection at focal spot size settings of 0.4 or 0.8 mm. A selection of antiscatter grids (each 38×46 cm^2, 40 line pairs/cm, Soyee Products, Thompson CT) was investigated, ranging in GR from 6:1 to 12:1, each with focal distance (1016–1829 mm) compatible with the nominal system geometry. The nominal CBCT scan protocol consisted of 720 projections in 0.5° angular increments at 90 kV and 0.57 mAs per projection with 2 mm Al and 0.2 mm Cu added beam filtration. Image reconstruction was performed by 3D filtered backprojection with a nominal voxel size of (0.7×0.7×0.7) mm^3 and a smooth (Hann) filter.

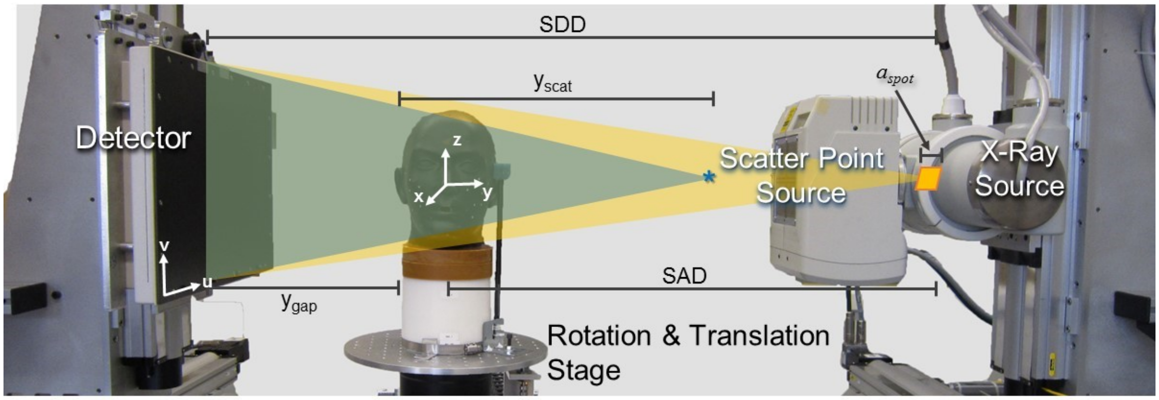

Figure 4.3. CBCT imaging bench. The bench allowed variation in SAD and SDD by repositioning the detector and x-ray source. Additional experimental variables included kV, mAs, focal spot size, GR of the antiscatter grid, number of projections, and detector pixel size (controlled through detector readout mode and binning). The illustration shows parameters related to the effect of geometry on x-ray scatter, including the position of the effective scatter point source, and various geometric parameters and coordinate systems.

Phantoms. Two head phantoms were used in image quality analysis, each illustrated in Figure 4.4. Phantom A was a custom anthropomorphic head phantom incorporating a natural skeleton in tissue-equivalent plastic (Rando, The Phantom Lab, Greenwich NY). Phantom A provided an empty cranial interior that was filled with gelatin (Knox Gelatine, Kraft, Camden NJ) mixed to ~50 HU density and a carefully arranged array of acrylic spheres (~100 HU, ranging in diameter 1.6–12.7 mm) presenting gelatin-to-acrylic (i.e., "brain-to-blood") contrast of ~50 HU. A tungsten wire (0.127 mm diameter) was also placed in the gelatin for assessment of spatial resolution. Phantom A also included CSF-equivalent wax shaped to population-average size ventricles. Phantom B was also an anthropomorphic head phantom (Atom, CIRS, Norfolk VA) featuring a synthetic skeleton in tissue-equivalent plastic. Phantom B allowed insertion of various cylindrical test objects within the cranial interior. A lighter gelatin ("brain" ~10 HU) mixture was formulated as cylindrical inserts in Phantom B in which blood-equivalent spheres (~60 HU, QRM QSA-498, ICRU 44) ranging 2–10 mm diameter were placed, again providing "blood-to-brain" contrast of ~50 HU.

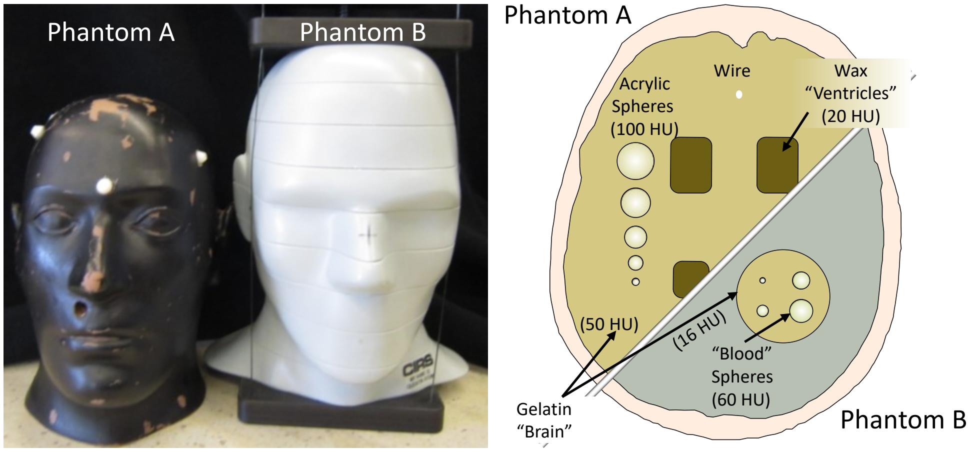

Figure 4.4. Head phantoms. Phantom A had an accessible skull cavity filled with gelatin and embedded with acrylic spheres (50 HU contrast) and a tungsten wire. Phantom B included inserts filled with brain-equivalent gelatin and blood-equivalent spheres.

III.B Comparison of Theory and Measurement

Validation of Theoretical Model. Model predictions of the 2D projection NPS and the 3D image NPS were validated over a range of imaging conditions and parameters appearing in Table 4.1. Measurements were acquired on the imaging bench of Figure 4.3 at a beam energy of 100 kV (added filtration of 8.2 mm Al + 2.1 mm Cu simulating attenuation from 16 cm of water) with dose varied over a range corresponding to 0.25–0.64 mAs per projection. 3D images were reconstructed as described above with (0.28×0.28×0.28) mm^3 voxel size. The NPS was analyzed under assumptions of weak stationarity, shown previously[187] to be a good assumption under such experimental conditions. As in Samei et al,[142] the 2D projection MTF was measured from an angled tungsten edge and fit to the product of a Lorentzian and exponential (parameterizing the scintillator MTF, T_3) and sinc function (pixel MTF, T_5). The fit for the scintillator MTF (T_3) was incorporated in Eqs. (4.1) and (4.3) for analysis of system MTF and detectability index, respectively.

Empirical Investigation and Validation of Optimal System Configuration. Images were acquired on the CBCT bench to provide qualitative visual assessment of trends in image quality in comparison to the results predicted by the theoretical framework. The effects of system geometry on imaging performance were measured using Phantom A imaged at a nominal SDD of 1100 mm, with SAD ranging 550–950 mm. For these studies, the beam energy was fixed at 90 kV, and total mAs varied from 450 (at 550 mm SAD) to 1440 (at 950 mm SAD) such that the dose at the center of a CTDI phantom centered on the axis of rotation was 20 mGy. Measurements of imaging performance as a function of kV and selection of antiscatter grid were performed using Phantom B in the nominal geometry, filtration, and dose shown in Table 4.1.

III.C Metrics of Performance

In addition to evaluation of the 2D and 3D image NPS and detectability index, imaging performance was characterized experimentally in terms of the contrast, noise, CNR, and spatial resolution measured in the phantoms of Figure 4.4. Contrast and noise were evaluated in 10×10×10 voxel ROIs in the largest diameter ICH-simulating sphere and an immediately adjacent uniform region of brain-simulating gelatin. The spatial resolution was characterized in terms of the FWHM of 2D Gaussian fits to finely sampled axial reconstructions (0.26 mm isotropic voxel size) of the tungsten wire in Phantom A. Dose values reported throughout refer to the absolute dose (mGy) to water described in Eq. (4.6) and validated by measurement with a Farmer chamber placed at the center of a 16 cm CTDI phantom at isocenter. Images of the simulated blood and brain regions in Phantoms A and B were also qualitatively assessed in terms of uniformity, artifact, and conspicuity of the simulated ICH.

IV. Results

IV.A Model Validation

The underlying cascaded systems model has been validated in previous work[32, 126] and was confirmed in the current application context as summarized in Figure 4.5. As expected (Figure 4.5a), the 2D projection NPS exhibits a low-pass characteristic governed primarily by scintillator blur and varies linearly with exposure. Similarly good agreement was demonstrated between theory and measurement at various kV, pixel binning, and other system parameters over the ranges in Table 4.1. The 3D image NPS exhibits a bandpass characteristic in the axial plane (Figure 4.5b) and low-pass characteristic in the longitudinal direction (Figure 4.5c) in good agreement with theory. It merits reiteration that the Fourier metrics of MTF and NPS analyzed herein describe the *local* transfer characteristics, which in this work corresponds to the center of the image. Since the MTF at stage 3 was taken as empirical input to the model, and the factors of fluence, quantum detection efficiency, optical gain, optical coupling efficiency, etc. that are encapsulated within the NPS demonstrated good agreement with measurement, the model therefore also provided close agreement with the measured NEQ (not shown for brevity). Such measurements confirm the modeled spatial resolution and noise components of *d'* [Eq. (4.4)], which serves as the objective function for system design and optimization detailed in the following sections.

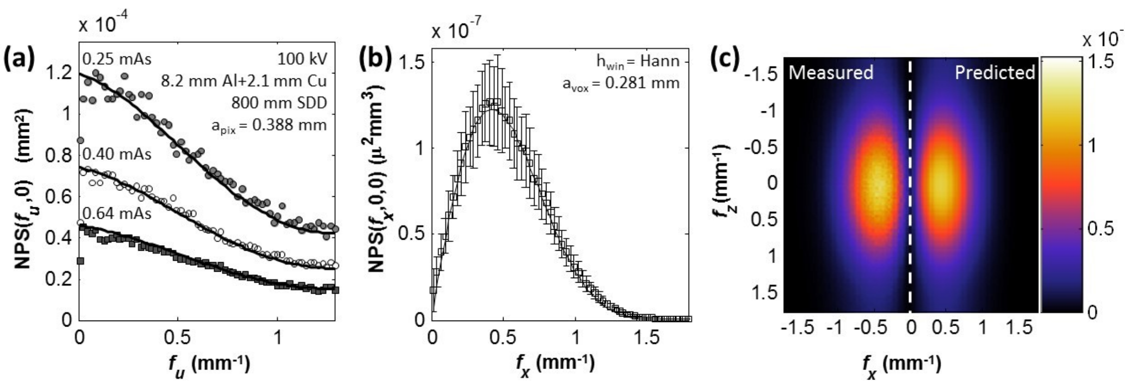

Figure 4.5. Comparison of theory and measurement. (a) The 2D projection NPS measured (symbols) and modeled (solid curves) for a range of exposure levels (mAs per projection). (b) The 3D image reconstruction NPS in the axial plane (radially averaged at $f_z = 0$). (c) The 3D image reconstruction NPS in the coronal plane ($f_y = 0$), also showing close agreement between theory and measurement.

IV.B System Geometry

Analysis and optimization of system geometry involved calculation of *d'* as a function of SAD (ranging 450–1150 mm) and SDD (ranging 750–1250 mm) assuming a centered detector and circular orbit. The effect of geometry on performance is illustrated in Figure 4.6, which shows that at each value of SDD, there exists an optimal SAD that balances the tradeoffs between focal spot blur, geometric sharpness (demagnification of pixel size in the image plane), fluence at the detector, and x-ray scatter, as described in Siewerdsen & Jaffray.[162] Since calculations were performed for a fixed dose at isocenter (20 mGy), the maximum detectability at optimal SAD increases monotonically with increasing SDD. This effect is primarily due to the inverse square law: as the SDD increases, the optimal SAD increases, and the total x-ray output (mAs) required to deliver 20 mGy of dose increases (with a concomitant increase in total fluence at the detector). For example, we considered two nominal SDDs marked by horizontal lines in Figure 4.6: a fairly compact configuration with SDD = 850 mm and a more extended geometry with SDD = 1100 mm. The compact configuration is optimized with SAD = 580 mm (M = 1.47), similar to the geometry of some commercially available head scanners[188]. The extended geometry is optimized with SAD = 750 mm (M = 1.47) and provides an ~8% increase in d' compared to the compact geometry.

Such calculations were repeated over a broad range in beam energy (50–140 kV), dose (10–20 mGy), focal spot size (0.3–2.0 mm), pixel pitch (0.01–1.0 mm), and reconstruction parameters (voxel size and smoothing filter). In this way, the analysis iterated over the multivariate space of parameters in system design and for conciseness were reduced to the bivariate analysis in Figure 4.6. The nominal parameters held fixed in Figure 4.6 were selected in a manner consistent with findings below—viz., 90 kV, 0.6 mm focal spot, 0.4 mm pixels, 0.7 mm isotropic voxels, and a smooth (Hann) reconstruction filter.

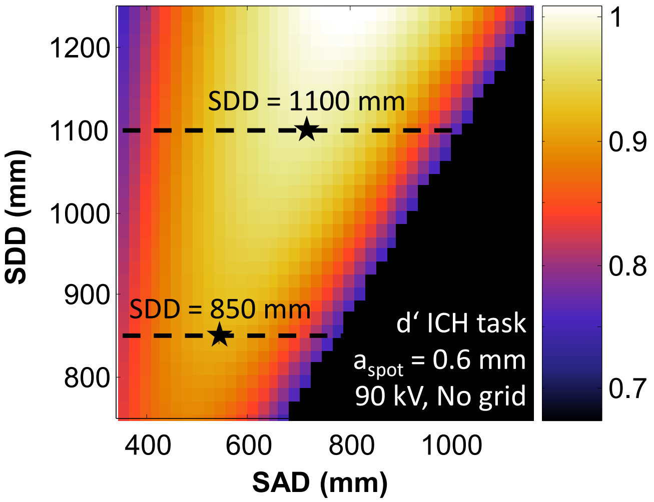

Figure 4.6. Analysis of system geometry. Detectability index was computed as a function of SAD and SDD. For any value of SDD, there exists an SAD that maximizes performance. Example "compact" and "extended" scanner geometries are marked by horizontal lines.

The results in Figure 4.7 validate quantitatively and illustrate qualitatively how system geometry affects imaging performance in terms of the CNR (simulated blood-to-brain) and PSF measured as a function of SAD (at SDD = 1100 mm and other parameters fixed as in Table 4.1). Figure 4.7a shows axial slices (without scatter correction) and zoomed insets about simulated bleeds (with MC scatter correction[158]). Figure 4.7(b-d) shows the contrast and noise, CNR, and PSF, respectively, as a function of SAD. Symbols demark measured values and curves show theoretical prediction with MC scatter correction. The images and quantitative metrics illustrate the numerous tradeoffs in the optimization of system geometry. Specifically, (for fixed SDD, dose, etc.) reducing SAD has the following effects: x-ray scatter effects (cupping and streaks) are reduced due to the larger air gap; noise increases (since D_0 is fixed, requiring lower scan mAs); contrast improves in the uncorrected image (due to reduced x-ray scatter) but is independent of SAD following MC scatter correction (as expected, with the concomitant noise increase discussed in Appendix B); CNR is accordingly reduced (with the exception of the data point at SAD = 950, where scatter outside the FOV was unaccounted in the MC simulation); and spatial resolution improves due to geometric sharpness.

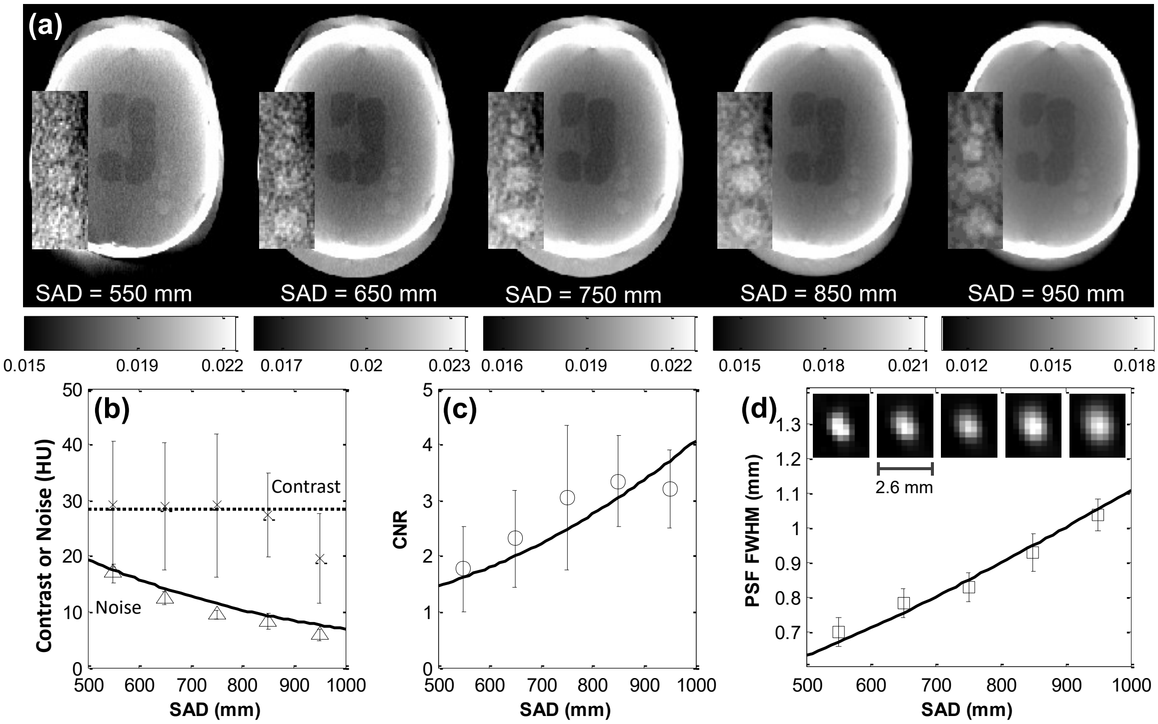

Figure 4.7. CBCT images of Phantom A and basic measures of imaging performance analyzed as a function of SAD (at fixed SDD = 1100 mm and D_0 = 20 mGy). (a) Axial slices (without scatter correction) with zoomed ICH inserts (with MC scatter correction). (b) Contrast and noise and (c) CNR measured in MC corrected images. (d) Spatial resolution (FWHM of the PSF) measured using a tungsten wire in Phantom A. In (b-d) symbols are measurements from CBCT images of Phantom A, with error bars representing the standard deviation of CNR measured in independent axial slices, and curves from the theoretical model.

Overall, for this system configuration, reduced SAD corresponds to sharper images but reduced CNR, analogous in some ways to the imaging performance evident in some commercially available head scanners[65] that show good bone detail visualization but limited soft-tissue imaging capability. Conversely, increasing SAD increases x-ray scatter effects (stronger cupping and streaks in uncorrected images), decreases noise (increased mAs with fixed dose), improves CNR, and degrades spatial resolution (reduced geometric sharpness). The combined tradeoffs between CNR and PSF are encapsulated well in the trends of Figure 4.7—e.g., consistent with an optimal SAD of ~750 mm for the task of small bleed detection.

IV.C X-Ray Source and Technique

The effect of focal spot size (a_{spot}) and beam energy (kV) on system performance are shown in Figure 4.8 in terms of both theoretical predictions and phantom measurements at SDD = 1100 mm. Although performance monotonically improves with reduced focal spot size (with power and heat limitations considered in section V.A below), performance for a low-to-mid–frequency task such as ICH detection (Figure 4.8a) has a modest dependence on a_{spot}. As shown in Figure 4.8b, beam energy exhibits a clear, broad optimum in detectability at 90–100 kV, and that optimum is insensitive to geometry. The underlying factors are illustrated in analysis of contrast and CNR (simulated blood-to-brain) in Figure 4.8c, where symbols denote measurements in Phantom A, and curves are theoretical prediction. At lower kV, contrast increases, but noise also increases due to reduced penetration. As beam energy increases, contrast reduces due to reduction in the difference in attenuation coefficients, and noise reduces due to increased penetration (i.e., increased fluence reaching the detector). The beam energy that maximizes CNR agrees with the predicted optimum of 80–100 kV (taken nominally as 90 kV) for the ICH detection task.

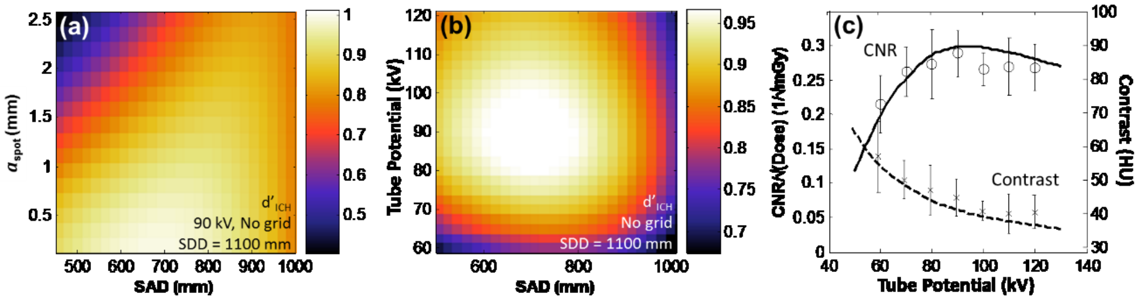

Figure 4.8. Analysis of x-ray focal spot size and beam energy. (a) Detectability index was computed as a function of a_{spot} and SAD. (b) Detectability index for the ICH detection task was computed as a function of beam energy and SAD, implying an optimum at ~90 kV that is corroborated by measurements and prediction of CNR in (c).

IV.D Scatter Correction and Anti-scatter Grid

Use of an antiscatter grid reduces the x-ray scatter fluence reaching the detector (thereby improving contrast) but also imparts a reduction in primary fluence. For a detector with non-negligible electronic noise, the relative benefit (or detriment) to imaging performance in using a grid is determined by the grid parameters (GR, T_S, and T_P) and the imaging dose. Figure 4.9a shows ICH detectability computed as a function of GR and air gap, showing an optimal GR in the range ~8-12. The optimal air gap without a grid (y_{gap} ~270 mm) corresponds to the same optimal SAD (~750 mm) shown above. Figure 4.9b shows the relative benefit (or detriment) of an optimal grid (GR = 8) by analyzing the ratio of d' with and without a grid as a function of dose, with the "break-even" line marked in white. For the optimal configuration discussed above (SAD = 750 mm, SDD = 1100 mm), use of a grid degrades performance slightly (~5–10% reduction in d') for D_0 = 10 mGy but improves performance slightly (~5–10% increase in d') at 20 mGy. The finding is corroborated by images of simulated ICH in Phantom B, as shown in Figure 4.9c, where the CNR without a grid is superior at 10 mGy dose, but CNR with a grid is superior at 20 mGy dose. Overall, the results suggest marginal (if any) improvement gained through use of a grid at the nominal dose and N_{proj}; moreover, grids can introduce added complexity in flood-field correction. With an eye toward lower-dose scan protocols (10 mGy or less), the analysis suggests a gridless system configuration that manages scatter primarily by means of optimal geometry (air gap) and MC scatter correction.

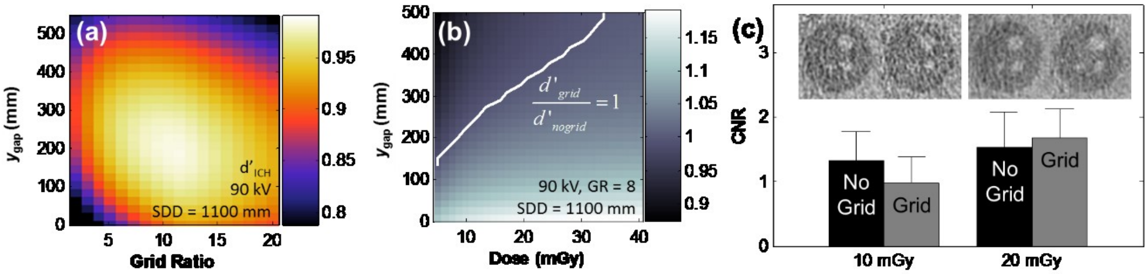

Figure 4.9. Analysis of antiscatter grid. (a) Detectability index for the ICH task computed as a function of GR and air gap. (b) The ratio of d' with and without a grid computed as a function of air gap and dose. The break-even line (ratio = 1) is superimposed in white, showing the benefit of grids at higher dose. (c) Images and measurements of simulated blood-to-brain CNR with and without a grid at 10 and 20 mGy, supporting the theoretical prediction in (b) that even an optimal grid can be detrimental at lower dose.

IV.E Detector

Two detector types were considered in the analysis below, differing mainly in their pixel size and additive noise: CMOS detectors and FPDs. Other important factors that distinguish these detectors (e.g., FOV and frame rate) are discussed among practical considerations in section V.A. Figure 4.10a shows that the optimal pixel size for ICH detection is ~0.3–0.5 mm over the entire range of dose considered: finer pixel size suffers from a reduced number of photons per pixel and an increased relative contribution of electronic noise, while larger pixels carry a loss in spatial resolution. Figure 4.10b shows the effect of electronic noise on the dose required to achieve a given level of detectability—i.e., if electronic noise increases from ~470 e to 4160 e, the dose would need to be increased 13% to maintain detectability at 20 mGy and by 33% at 10 mGy. Figure 4.10c shows the detectability index computed as a function of pixel size and additive noise, superimposing the nominal values for CMOS and FPDs in various pixel binning modes. Overall, a CMOS detector is seen to offer a potentially strong improvement in performance due to reduced electronic noise. The contribution of digitization noise (see Chapter 5) to the total electronic noise also becomes significant for the CMOS configuration, but the analysis in Figure 4.10 assumed sufficient bit depth that line noise, pixel dark noise, and amplifier noise dominated the additive electronic noise.

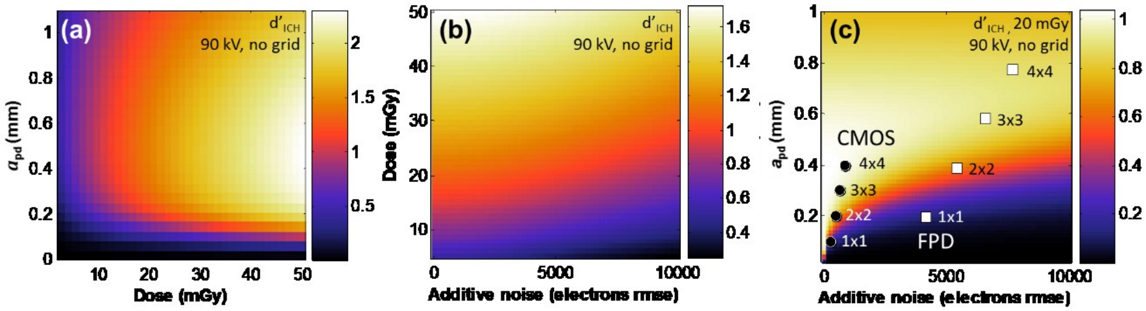

Figure 4.10. Analysis of x-ray detector configuration. (a) Detectability index computed for the ICH detection task as a function of pixel size and dose shows an optimal pixel size in the range ~0.3–0.5 mm. (b) The analysis shows the steady reduction in *d'* with increased electronic noise, or—alternatively—the dose required to maintain a given level of *d'* as electronic noise increases. (c) Detectability index computed as a function of pixel size and electronic noise, superimposed by symbols marking nominal CMOS and FPD performance in various pixel binning modes.

IV.F Fracture Detection Task

The analysis reported in sections IV.B-E focused on the task of ICH detection. In evaluating head trauma, however, the ability to visualize fractures is also pertinent to confident diagnosis. Analysis corresponding to the fracture detection task is summarized below to investigate to what extent the optimal system configuration differs from that identified for the ICH task and—perhaps more importantly for this application—that detectability for the fracture task is still high for the configuration identified above. More generally, for scenarios in which more than one imaging task is important, a weighted optimization[189] may be considered the mitigates the tradeoffs in detectability in proportion to the clinical significance of the disparate tasks.

Figure 4.11 shows the analysis of detectability index for a high-frequency, high-contrast fracture task. As shown in Figure 4.2, the fracture detection task assumes a small volume and high-contrast (~900 HU) linear or planar fracture averaged over all (equally likely) orientations. Such a task function may still be considered within the assumption of a small signal difference in that it exhibits small signal power. For example, the signal power of a fracture of feature size 0.25 mm (0.015 mm^3 volume) and contrast = 900 HU is approximately equivalent in signal power to an ICH lesion of 1.7 mm diameter (2.6 mm^3 volume, 50 HU). The small-signal power assumption is therefore valid for a subtle fracture.

Figure 4.11a shows the analysis of system geometry for the fracture detection task. The optimal magnification in both the compact and extended geometries is higher (M = 1.72 and 1.76, respectively) than for the ICH task (M = 1.47), but *d'* for the fracture task is reduced from its maximum value by just 7% (and is still 2.2 times higher than that of the ICH), suggesting that fracture is detectible even in the ICH-optimized geometry. Figure 4.11b shows detectability index computed as a function of SAD and focal spot size. Compared to the ICH task (Figure 4.8a), the fracture detection task exhibits a steeper decline in detectability as focal spot size increases. At the nominal focal spot size identified for the ICH task ($a_{\text{spot}} = 0.6$ mm), *d'* for fracture detection is similarly 2.2× the ICH task, suggesting that the fracture is detectible in the nominal geometry. Figure 4.11c shows that fracture detection is also sensitive to the choice of detector type (i.e., pixel size and additive noise). Compared to the ICH task (Figure 4.10c), detectability exhibits a steep decline as pixel size or additive noise increases, and the optimal pixel size for fracture detection is 0.2–0.4 mm for the range of additive noise achievable with CMOS and FPDs. This suggests that acquiring images with finer detector binning (e.g., 1×1 or 2×2 binning, instead of 4×4 binning discussed in relation to Figure 4.10c) may be beneficial—with a high-resolution reconstruction (e.g., sharp filter and 0.23 mm voxel size) for fracture detection and a lower-resolution reconstruction (e.g., smooth filter and 0.7 mm voxel size) for ICH detection. This approach has been implemented in other applications of CBCT—e.g., musculoskeletal imaging[80] in which data are acquired with finer detector binning followed by a high-resolution reconstruction for bone visualization and a low-resolution reconstruction for soft-tissue visualization.

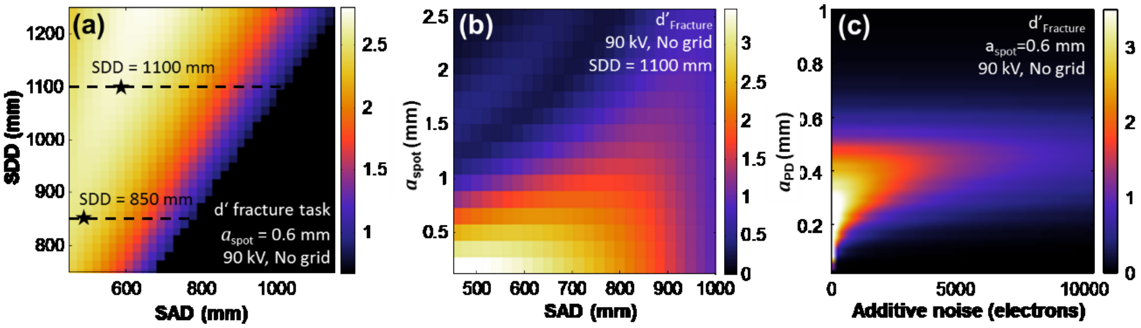

Figure 4.11. Analysis of detectability for the fracture detection task. (a) System geometry, analogous to Figure 4.6. (b) Focal spot size, analogous to Figure 4.8a. (c) Detector pixel size and additive noise, analogous to Figure 4.10c. While the fracture detection task suggests an optimal configuration that differs from the ICH detection task, fracture detectability is still high (~2× greater than ICH detectability) in the nominal configuration identified for ICH detection.

V. Prototype Design

V.A Additional Constraints and Practical Considerations for System Configuration

Following the guidance of system design obtained from the theoretical analysis detailed above, the practical implications and feasibility of various design choices were considered with respect to currently available x-ray tubes and detectors. Other practical considerations not explicit in the analysis above include the number of projections, scan time, x-ray tube power, and FOV.

The total number of projections has a direct effect on total scan time (as shown in Figure 4.12a). For example, a 30 s scan time could be achieved using 720 projections and an x-ray pulse length of 20 ms at 50% duty cycle. This requires a detector readout rate of 25 frames per second which is within the range of typical FPD operation. The total scan time in turn affects the required tube power (Figure 4.12b), indicating for example that a > 5 kW source is required to achieve a scan time less than 20 s (with 20 mGy dose and a 50% pulse duty cycle) in the extended (SAD = 750 mm, SDD = 1100 mm) geometry. Further reduction of scan time (below 20 s) would challenge commercially available FPDs and potentially requires CMOS detectors with increased frame rate, a more powerful x-ray source (higher dose per pulse), and/or a more compact geometry such as the SDD = 850 mm geometry shown in section IV.B (i.e., less power required to achieve the same detector signal).

There are two important FOV design requirements: the detector FOV must be sufficient to cover the object at SDD without truncation, and the anode angle must be sufficient to cover the object at SAD in all projections. For a 24 cm object (approximately the dimension of the head in the anterior-posterior direction) in the nominal geometry (SDD = 1100 mm and SAD = 750 mm), a detector width > 35 cm and anode angle > 9º is required. An isocentric geometry may be more mechanically favorable (e.g., SDD = 1100 mm, SAD = 550 mm), and increases the detector width to 48 cm and the required anode angle to 13º.

These practical tradeoffs impose important design constraints on the choice of x-ray source and detector. Considering the differences in power provided by high-end stationary anodes (focal spot index = 1, 15º anode, 3 kW, SR-130, SourceRay, Ronkonkoma, NY) and lightweight rotating anode sources (focal spot index = 0.6, 15º anode, 15 kW, Monobloc, IMD, Grassobbio, Italy), a greater than two-fold reduction in dose is necessary for the use of a stationary anode tube. Combined with the scan time requirements (< 30 s), the results indicate that a lightweight rotating anode x-ray source is strongly advantageous to meeting the optimal design and performance. While CMOS detectors feature low additive noise and fast readout, the largest currently commercially available CMOS detector is ~30×30 cm^2, whereas FPDs are available up to 43×43 cm^2). An offset-detector configuration (common in IGRT[190, 191]) can overcome detector FOV limitations but preclude half-scan protocols (which can spare dose to the eye lens) and potentially favorable gantry configurations (C-arm).

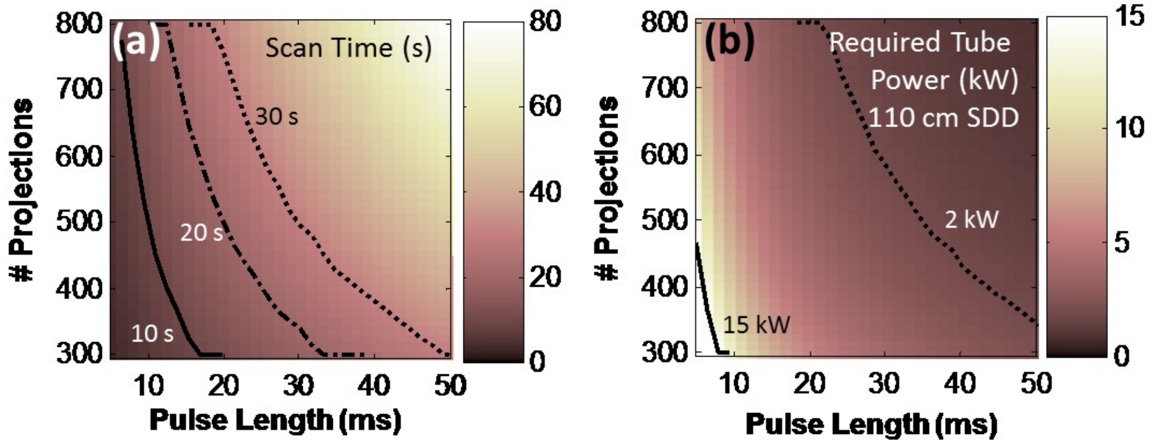

Figure 4.12. Analysis of additional practical considerations of the x-ray source power, pulse width, scan time, and FOV. (a) Total scan time computed as a function of the number of projections and x-ray pulse width, assuming 20 mGy dose and nominal system geometry. (b) X-ray tube power (giving 20 mGy dose) computed as a function of the number of projections and pulse length.

V.B Prototype Configuration

As discussed in section IV.B, two nominal scanner geometries were considered (SDD = 850 mm and 1100 mm, each at their respective optimal SAD). The more compact geometry (SDD = 850 mm) provides a smaller scanner footprint and reduced power requirements with slight (~7%) reduction in detectability. The more extended geometry (SDD = 1100 mm) may carry other advantages in terms of patient positioning and a larger interior envelope for clearance of the patient and auxiliary systems. Figure 4.13a shows a schematic of a mobile prototype CBCT generally consistent with the analysis detailed above.

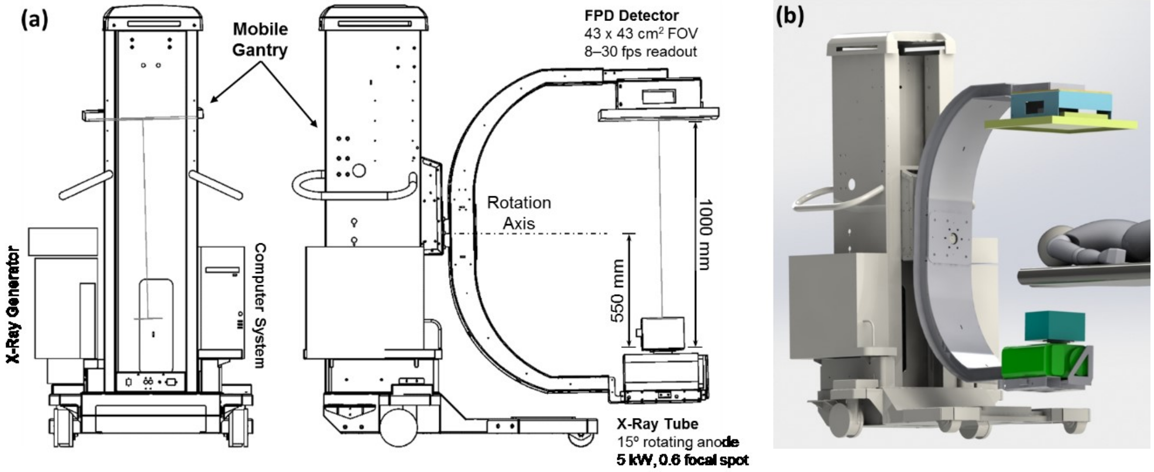

Figure 4.13. (a) Schematic of the prototype design. (b) Illustration of patient positioning in the large-bore mobile CBCT system.

The design in Figure 4.13[b] shows a slightly smaller geometry (SDD = 1000 mm, SAD = 550 mm) meeting the size and power constraints for a mobile system that is still capable of high-quality brain imaging. The SAD and SDD were reduced slightly to accommodate an open bore for ease of patient positioning and setup in a proof-of-concept prototype test environment (Figure 4.13b), with plans to re-evaluate for future iterations with potentially more compact and specialized brain imaging geometries. A small-footprint rotating anode x-ray source (HF Monobloc, IMD, Grassobbio, Italy) was chosen that has sufficient power to deliver a 30 second scan at this geometry with the optimal imaging techniques identified in section IV.C ($D_0 < 25$ mGy) while powered from a single standard North American wall socket (110 V and 2 A). A large FOV

---

[b] Mechanical drawings and graphical representation of the prototype were provided based on an academic-industry collaboration with Carestream Health. Acknowledgment goes to Ed Wang and Bill Snyder for the mechanical and component design of the mobile gantry, U-Arm, and power encoder layout.

(43×43 cm^2) FPD (4343CB, Varian, Palo Alto, CA) was selected for greater flexibility in testing both centered- and offset-detector configurations (ability to perform both full- and short-scan acquisitions) as well as for the ability to image in high-gain and dual-gain detector readout mode with potential benefits to additive noise levels.

VI. Conclusions

CBCT with soft-tissue imaging performance beyond that of existing head CBCT scanners appears feasible, and the design of a prototype offering reliable detection of ICH benefits from task-based 3D image quality modeling and optimization. Such a model-based approach weighs the numerous factors governing image quality optimization and provides a quantitative guide to selection of system geometry, x-ray source, detector, and imaging technique. Such trends, combined with the practical considerations outlined in section V.A, provided the basis for design of a high-performance scanner prototype from first principles, reducing the reliance on time-consuming and expensive hardware / mechanical design iterations and accelerating the development and translation of a system for clinical applications.

A prototype dedicated CBCT head scanner similar to the schematic shown in Figure 4.13 was developed based on the analysis in this work, and features an artifact correction framework that includes MC-based scatter correction, two-pass beam hardening correction, detector glare correction, and temporal lag deconvolution as reported in Sisniega et al.[158] Furthermore, a penalized weighted least squares model-based image reconstruction framework similar to that presented by Dang et al[161] was implemented. Chapter 6 details the characterization of the imaging performance of the prototype system as well as assessment of image quality in a human cadaver.

As identified in section IV.E, the question of detector readout noise is still a point meriting further investigation. Chapter 5 investigates the potential benefits to image quality resulting from alternative detector readout techniques, including high signal-amplification readout (with concomitant reduction in dynamic range and increase in digitization noise) as well as use of a bowtie filter.

Chapter 5: Effect of Detector Readout Gain Mode and Bowtie Filters on Imaging Performance

I. Introduction

Chapter 4 described the use of an image quality model as a basis for system design and showed that detection of small, low-contrast ICH was susceptible to electronic noise, especially at low dose (< 25 mGy) and in highly attenuating regions (at the center of the head, posterior to the skull base). Strategies to address this challenge include improved detector performance (e.g., higher gain and reduced electronic noise), modulation of the x-ray beam (e.g., using a bowtie filter or other forms of fluence-field modulation), as well as post-processing by artifact correction, MBIR, and/or noise suppression. This chapter investigates the first two of these strategies (detector and beam modulation) to identify system hardware configurations yielding higher quality projection data and potentially reduced patient dose.

Advances in detector technology offer a means to reduce the electronic noise floor, as with CMOS readout technology[21, 192] or direct detection (a-Se) with avalanche signal amplification.[193, 194] Flat-panel detectors can also leverage signal amplification to reduce the relative contribution of electronic noise via high-gain detector readout.[195] In each case, there is a tradeoff between signal amplification (increasing signal relative to electronic noise) and dynamic range (alternatively, detector "latitude") that constrains the dose per pulse below detector saturation, particularly in the bare beam at the periphery. Additionally, as the dynamic range is altered by detector gain, the digitization bit depth also becomes an important consideration—especially for soft-tissue imaging, as described in Chapter 4. Such tradeoffs pose a challenge to scenarios in which low-contrast features (e.g., ICH lesions) are to be detected throughout a highly attenuating object (e.g., the cranial vault), requiring both large dynamic range and low electronic noise and motivating the development of detectors with multiple gain modes and/or the implementation of added beam modulators—the simplest of which is a bowtie filter.

Dual-gain (DG) detector readout mode seeks to address such tradeoffs by combining low-gain (LG) and high-gain (HG) data within a single projection, effectively replacing the saturated HG pixel values with unsaturated (though higher noise) values from the LG readout. Previous work[69, 196] has shown that DG readout can improve image noise and prevent saturation artifacts, but can extend the total scan time due to increased readout time. Dynamic gain (DynaG) similarly carries the advantages of DG readout[197] without increasing the readout time through use of a comparator at the input to the readout amplifier, dynamically switching from HG to LG if the signal exceeds a threshold, and encoding a readout bit to indicate LG or HG for each pixel.

Pre-patient beam modulation (e.g., a bowtie filter) can also prevent bare-beam and skin line saturation in HG readout, preserve or enhance image quality in the center of the image, reduce dose,[198–201] and reduce x-ray scatter.[202] However, bowties may reduce image quality at the periphery of the image[203] and can introduce challenges to flood-field calibration, which may result in ring or shading artifacts. While the use of bowtie filters is standard in clinical MDCT systems, and recent advances indicate even further improvement (and challenges) through dynamic beam modulation,[204–206] the basic incorporation of bowtie filters in CBCT is still largely indeterminate and deserves rigorous analysis and optimization, particularly with respect to calibration methods. In principle, combining a bowtie filter with HG detector readout has the potential to improve the image quality and dose characteristics beyond what either could individually accomplish.

The work reported below investigates each of these challenges to dynamic range for development of a prototype head scanner for high-quality imaging of the head. We extend an analytical model of readout gain mode and digitization bit depth in its effect on electronic noise and DQE. The benefits of HG readout (along with the necessary modifications to detector calibration) are investigated for visualization of low-contrast ICH lesions. In addition, three bowtie filter designs (low, medium, and high attenuation and curvature) were assessed in terms of their effect on scatter, image noise, and dose, and a novel polyenergetic flood-field correction method was developed to reduce artifacts arising from use of a bowtie. The relative performance advantages of DG readout and/or use of a bowtie filter were factored against other considerations such as scan time and complexity of detector calibration. This work was first reported in Xu et al., “Evaluation of Detector Readout Gain Mode and Bowtie Filters for Cone-Beam CT Imaging of the Head”.[207]

II. Materials and Methods

II.A Theoretical Methods

II.A.1 Effect of Detector Readout Gain and Digitization Bit Depth on Electronic Noise and DQE

The effect of detector readout gain on the electronic noise and DQE can be modeled by consideration of the relationship between the capacitance of the integrating amplifier and the range and bit depth over which the signal is digitized. The total additive electronics noise (σ_{add}) can be modeled as a combination of pixel noise (σ_{pixel}), line noise (σ_{line}), amplifier noise (σ_{amp}), and digitization noise ($\sigma_{\mathrm{digitization}}$):[208]

$$\sigma_{\mathrm{add}}^2 = \sigma_{\mathrm{pixel}}^2 + \sigma_{\mathrm{line}}^2 + \sigma_{\mathrm{amp}}^2 + \sigma_{\mathrm{digitization}}^2 \tag{5.1}$$

The units of pixel, line, and amplifier noise are the same as that of the signal (electrons), while the digitization noise (applied after signal integration) has units of volts and can be converted to electrons as:

$$\sigma_{\mathrm{digitization}}\left(C_g\right) = \frac{C_g V_{\mathrm{ref}}}{q_e 2^N \sqrt{12}} \tag{5.2}$$

where C_{g} is the integration capacitance, V_{ref} is the analog-to-digital (ADC) reference voltage, N is the bit depth of the readout, and q_{e} is the electron charge. Typically, the readout gain is controlled by the integration capacitance (although changing V_{ref} for fixed C_g can also affect the digital gain of the readout), with larger values of C_g giving a lower readout gain and higher dynamic range.

In addition to the readout gain (controlled by the readout capacitance, C_{g}) digitization noise is also affected by the analog-to-digital converter (ADC) following the readout amplifier. The root mean square error (rmse) introduced by digitization goes as $\Delta/\sqrt{12}$, where $\Delta = V_{\mathrm{ref}}/2^N$ is the voltage associated with one digitized bit, N is the number of bits, and V_{ref} is the reference voltage of the ADC.[209, 210] The magnitude of digitization noise therefore depends on the bit depth.[179]

The DQE can be modeled as reported in Antonuk et al.[125] and Siewerdsen & Jaffray:[162]

$$\mathrm{DQE}\left(f_u, f_v\right) = \frac{\bar{G}^2\,\mathrm{MTF}^2\left(f_u, f_v\right)}{S_Q\left(f_u, f_v\right)/\bar{q}_0 + S_{\mathrm{add}}\left(f_u, f_v\right)/\bar{q}_0} \tag{5.3}$$

where $\bar{q}_0$ is the incident fluence (photons/mm^2), $\bar{G}$ is the detector gain (electrons/photon), MTF is the modulation transfer function, S_Q is the noise-power spectrum (NPS) associated with input quantum noise, and S_add is the NPS associated with the readout electronics, with the bandwidth integral of S_add equal to σ_{add}^2.

The analysis in this work assumes a pre-digitization additive noise $\sqrt{\sigma_\text{pixel}^2 + \sigma_\text{line}^2 + \sigma_\text{amp}^2}$ of ~2000 electrons for FPDs and a considerably lower typical value for CMOS detectors of ~470 electrons,[21] a reference ADC voltage of 2 V, digitization bit depth ranging 8–32 bits, and integration capacitance ranging 0.5–16 pF (corresponding to HG and extreme LG modes, respectively), consistent with previously reported values for FPDs.[195] The DQE was computed with $\bar{G}$ and S_Q as derived from an image quality model for FPDs[31] and incident fluence filtered by 16 cm of water and 1.4 cm of cortical bone (roughly equivalent to the beam quality behind the head), simulated using the spektr toolkit[133] modified to include TASMICS spectral modelling.[211]

II.A.2 Monte Carlo Dose Calculation

Bowtie filters modulate the distribution of fluence incident on the subject and, hence, the dose distribution therein. We implemented a dose calculation tool based on a fast GPU implementation of a Monte Carlo simulation engine (MC-GPU version 1.0),[212] modified to calculate dose in a voxelized volume by recording the energy deposited by each interaction (scatter or absorption) for each simulated photon.[c] The deposited energy is assumed to be released directly at the interaction site, neglecting range effects of products of the interaction. The computational performance of the MC dose estimation was enhanced with variance reduction techniques, including Woodcock tracking (already included in MC-GPU) and forced interaction.

---

[c] The MC simulation code was written and validated by Dr. Alejandro Sisniega and reported in "Evaluation of Detector Readout Gain Mode and Bowtie Filters for Cone-Beam CT Imaging of the Head."[207] For purposes of the work performed for this dissertation, the author performed the simulations reported in this chapter, with thanks to Dr. Sisniega for assistance with the code and numerous helpful discussions.

The latter approach forces all photon histories to undergo an energy-depositing interaction (i.e., Compton scattering or photoelectric absorption) and corrects according to the energy-dependent probability of such interaction.

Dose calculations were performed with a realistic system model, including: i) polyenergetic spectrum simulated with the modified spektr / TASMICS toolkit integrated into the MC engine as described in Sisniega et al;[173] and ii) a bowtie filter simulated by applying an analytically estimated weight to each generated photon, where the weight accounts for bowtie attenuation and depends on the photon energy, material of the bowtie filter, and the pathlength traversed by the photon through the bowtie as a function of the ray direction. The MC calculation did not model scatter in the bowtie. The simulation engine provides dose per mAs in each voxel, computed as:

$$D = \frac{E}{V\rho} \cdot \frac{N_{PH}}{A\Phi_0} \tag{5.4}$$

where E is the energy deposited in the voxel (J), V is the volume of the voxel (mm^3), ρ is the density of the material in the voxel (kg/mm^3), N_{PH} is the number of photons in the simulation, A is the area of the irradiated beam at the center of the FOV (mm^2), and Φ_0 is the photon fluence (number of photons / mm^2 / mAs) for a given spectrum.

Dose calculation was performed for CBCT volumes reconstructed with scatter and beam hardening correction[158] to yield accurate Hounsfield unit (HU) attenuation values for each voxel. Soft tissue and bone were identified using a threshold-based segmentation of the CBCT volume. Voxel density within each tissue class was linearly varied as a function of HU as described in previous work.[158] The dose calculations involved 10^7 tracked photons per projection and 1° angular increment between projections. The orbital extent of the source-detector trajectory was varied from a half-scan (200°) to a full circular orbit (360°). Beam parameters were matched to those in the experimental studies (below) using spektr[133] to simulate the photon fluence, Φ_0, for a given mAs, kV, added filtration, etc., and the dose was computed according to Eq. (5.4).

II.B Experimental Methods

II.B.1 Cone-Beam CT Bench

Image data were acquired on the bench shown in Figure 5.1, featuring an x-ray source (RAD13, Dunlee, Aurora IL), a translation and rotation stage (Compumotor 6k8, Parker Hannifin, Rohnert Park CA), and a FPD (PaxScan 4030CB, Varian, Palo Alto CA). All acquisitions were performed with 2×2 hardware binning (binned pixel size = 0.388 x0.388 mm^2) and 2×2 software binning (resulting in final pixel size = 0.776×0.776 mm^2) with source-axis distance (SAD) = 550 mm and source-detector distance (SDD) = 1000 mm. The x-ray beam energy was fixed at 90 kV with 0.4 mm Cu and 2 mm Al added filtration (without addition of a bowtie filter), and tube output was varied from 0.1–0.8 mAs per pulse over 720 projections in 0.5° angular increments. Filtered backprojection was used to reconstruct all images with voxel size = 0.5×0.5×0.5 mm^3 and a Hann apodization filter with cutoff frequency at 75% of the Nyquist frequency.

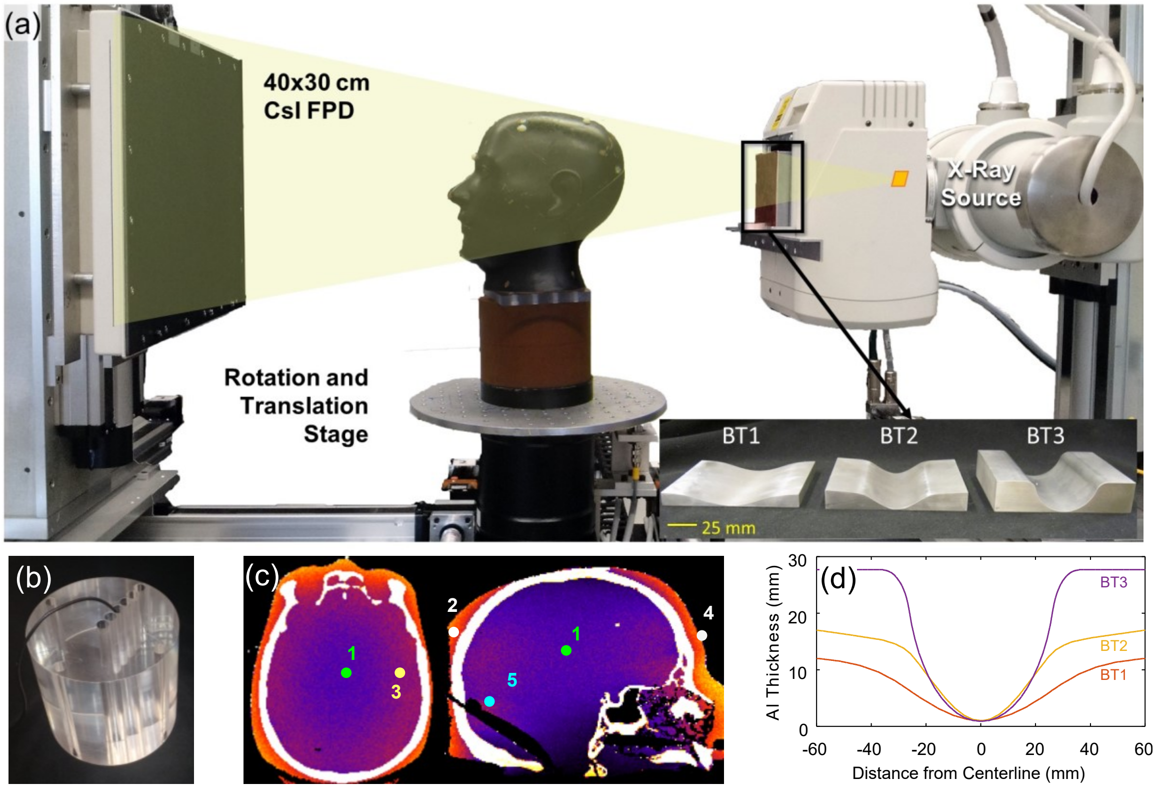

Figure 5.1. Experimental methods. (a) The CBCT bench set to the geometry of the prototype head scanner for assessment of dose and image quality in various readout gain modes and with various bowtie filter designs (inset). (b) A CTDI phantom was modified to allow Farmer chamber placement at various distances from the center. (c) Axial and sagittal views of a custom head phantom with MOSFET dosimeters placed at locations 1-5 on the cranial surface and interior. (d) Bowtie filters were designed with varying thicknesses, including a modest curvature (BT1, ranging from 1 mm at center to 12 mm at the field edge), a medium curvature (BT2, ranging 1-17 mm), and a design (BT3) matched in attenuation to a 13 cm water cylinder.

II.B.2 Readout Gain Modes

The FPD is capable of detector readout in LG (C_g = 4 pF), HG (C_g = 0.5 pF), and DG (C_g = 4 and 0.5 pF) modes. The nominal imaging parameters for HG, DG, and LG flood-field and projection data were selected to achieve a maximum 80% detector saturation in any pixel (0.1 mAs and 0.8 mAs in HG and LG, respectively). Each DG readout contained a complete set of LG and HG data, and projections were separated and processed individually with corresponding offset (dark) and gain (flood-field) scans. The LG projection data were individually normalized to a signal = 1 in the bare beam, and the associated HG projection data were normalized to have the same mean signal as the LG data in a 50×50 pixel unsaturated region. The final DG projection was formed by replacing the HG projection data with pixel values > 75% of the HG saturation value with those from the LG data.

II.B.3 Bowtie Filters

Three aluminum bowtie filters were designed and evaluated, shown in Figure 5.1a (inset): bowtie 1 (BT1) had the lowest bare-beam attenuation and smallest curvature; bowtie 2 (BT2) had a moderate bare-beam attenuation and similar central curvature to bowtie 3 (BT3); and BT3 was designed to flatten (i.e., make spatially uniform) the energy fluence transmitted by a 13 cm diameter water cylinder at SAD = 550 mm. The bowtie thickness profiles are shown in Figure 5.1c. Offset-corrected projections (p_{proj}) were acquired at a tube output of 0.2, 0.4, and 0.8 mAs per pulse for BT1, BT2, and BT3, respectively, chosen as the maximum exposure/pulse in HG mode that allowed saturation-free data in all locations. All bowties were centered in the beam at the exit face of the collimator (243 mm from the source) with 0.2 mm of the 0.4 mm total Cu filtration relocated to the exit surface of the bowtie to reduce scatter originating in the bowtie. Offset-corrected flood-field projections (p_{flood}) for all bowties were acquired at 0.1 mAs per pulse in HG mode to avoid saturation in the central region where the bowtie was thinnest.

Raw transmission (T_{raw}) values for each projection were computed as:

$$T_{\text{raw}}\left(u,v\right)=\frac{I\left(u,v\right)}{I_0}\approx\frac{p_{\text{proj}}\left(u,v\right)}{c_{\text{Air}}p_{\text{flood}}\left(u,v\right)} \tag{5.5}$$

where $I(u,v)$ is the number of photons per pixel incident at location (u,v) on the detector plane, and I_0 is the number of photons per pixel in the bare beam. The transmission value can be approximated by dividing the projection data by the flood field data (which also corrects for individual pixel differences in readout response). Because the projection and flood-field data were acquired at different exposure/pulse, a scaling factor (c_{Air}) was applied to normalize the transmission through air to 1 (i.e., a ray through the bowtie filter that never passes through the object but is recorded by the detector gives transmission = 1).

Imaging with a polyenergetic beam imparts a mismatch between the incident spectrum, $q_0(E)$, for the flood-field data obtained for calibration and the actual projection data obtained during a scan, which can artificially increase or decrease the estimated transmission value. Typical two-pass, segmentation-based beam-hardening corrections (such as the Joseph-Spital beam hardening correction[213]) can account for the detector response difference in the water and bone correction look-up-table but assume the spectrum in the flood field to be spatially invariant (aside from the heel effect). The presence of a bowtie introduces a strong spatially varying polyenergetic effect in the flood-field normalization that is not factored into such corrections and requires a renormalization to account for the detector response of a bowtie-free flood-field correction. In the proposed polyenergetic flood-field correction, the detector response ($\bar{G}$) was equalized at each location between the flood-field with and without a bowtie in the beam to estimate the true transmission values with only beam-hardening effects imparted by the object itself:

$$\begin{aligned} T(u,v) = & \frac{p_{\text{proj}}\left(u,v;q_0\left(E;\delta_{\text{obj}}(u,v),\delta_{\text{bowtie}}(u,v)\right)\right)}{c_{\text{Air}}\,p_{\text{flood}}\left(u,v;q_0\left(E;0,\delta_{\text{bowtie}}(u,v)\right)\right)}\cdot\ldots \\ & \frac{\bar{G}\left(u,v;q_0\left(E;0,\delta_{\text{bowtie}}(u,v)\right)\right)}{\bar{G}\left(u,v;q_0\left(E;0,0\right)\right)} \end{aligned} \tag{5.6}$$

where δ_{obj} and δ_{bowtie} are the pathlength through the object and bowtie filter, respectively, for a ray incident on the detector at location (*u*,*v*), and $\bar{G}$ is the detector response (electrons / incident photon) in Eq. (5.3) derived from a cascaded systems model of the detector.[126] The energy-dependent components of the detector response were isolated as the product of the quantum detection efficiency, $\bar{g}_1$, and the optical photon gain of the scintillator, $\bar{g}_2$:

$$\bar{g}_1 = \frac{\int q_0(E)\left(1-e^{\left[-\mu_{\text{detector}}(E)\cdot\delta_{\text{detector}}\right]}\right)\mathrm{d}E}{\int q_0(E)\,\mathrm{d}E} \tag{5.7}$$

$$\bar{g}_2 = \frac{\int q_1(E)\,\bar{g}_{2a}(E)\,\mathrm{d}E}{\int q_1(E)\,\mathrm{d}E} \tag{5.8}$$

where $\mu_{\text{detector}}(E)$ and δ_{detector} are the attenuation coefficient (1/mm) and thickness, respectively, of the scintillator (in this case, 600 μm CsI:Tl), $q_1(E)$ is the spectrum of interacting x-ray photons, and $\bar{g}_{2a}(E)$ represents the number of secondary photons generated for each interaction of a particular energy.

Figure 5.2a shows the detector response as a function of pathlength through the bowtie filter. In each case, the hypothetical "flat" flood-field detector response corresponds to $\delta_{\text{bowtie}} = 0$ mm. Points A and B denote the response of the detector in the center and peripheral region of the bowtie flood-field, respectively. The central rays are filtered through a small thickness of filter, so the spectrum and detector response are similar to those of a flat flood-field. At the periphery, however, the spectrum has higher average energy, and the detector response is lower for the bowtie flood-field than for a flat flood-field. Figure 5.2b shows the ratio of detector response for a bowtie flood-field to a flat flood-field, showing that the largest mismatch occurs at the periphery (4% difference), where the bowtie is thickest. The ratio map in Figure 5.2b was used as a polyenergetic correction of the transmission data for each projection angle.

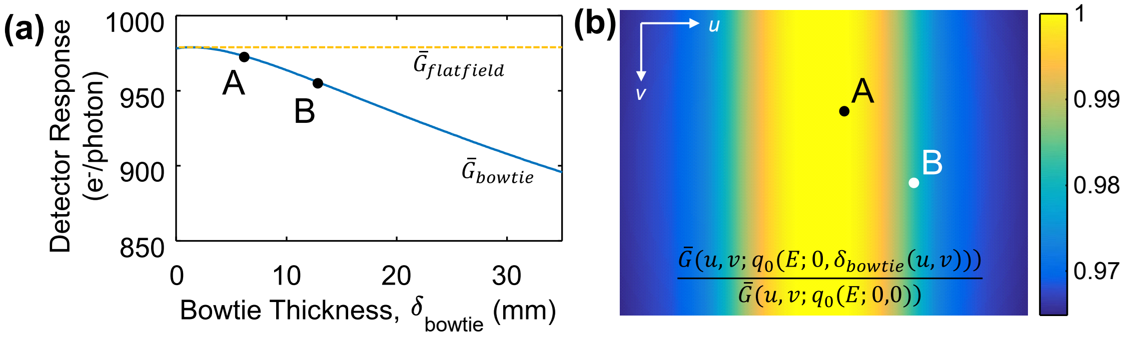

Figure 5.2. Effect of the bowtie filter on detector response. (a) Detector response ($\bar{\mathrm{G}}$) was pre-computed as a function of the spectrum filtered through varying lengths of bowtie filter. (b) The ratio of detector response in the flood-field to that in a hypothetical flat flood-field shows that the mismatch is generally higher at the periphery of the image, where the bowtie is thickest.

II.B.4 Phantoms and Measures of Imaging Performance

Two phantoms were used to evaluate dose and validate the MC dose calculation. The first was a 16 cm CTDI phantom (Figure 5.1b) modified to allow measurement of dose at locations intermediate to the center and periphery. The modified phantom included 4 additional Farmer chamber bore holes placed at 1.4 cm increments between the central and peripheral bores normally included in the CTDI phantom. Measurements were performed using a 0.6 cm^3 Farmer chamber (Accu-Dose, Radcal Corp., Monrovia CA) and MOSFET dosimeters (Mobile MOSFET, Best Medical, Ottawa ON, Canada). All holes not containing the Farmer chamber were filled with acrylic plugs during dose measurement.

To evaluate the effects of bowtie filters on the spatial distribution of x-ray scatter, a narrow strip Pb beam blocker ($3.5\times6\times160$ mm^3) was used to measure the scatter behind a uniform 16 cm diameter acrylic cylinder. The cylinder was placed at isocenter, and the beam blocker was placed at the entrance surface of the phantom between the cylinder and the source, oriented within the central axial plane (i.e., strip extending laterally at the entrance surface of phantom). The position-dependent scatter signal, $S(u)$, was measured as the (offset- and gain-corrected) detector signal behind the blocker at location u (the lateral position along the length of the strip) on the plane of the detector, and the scatter + primary signal, $(S+P)(u)$, was measured as the (offset- and gain-corrected) detector signal 2 cm above the lead blocker. The scatter-to-primary-ratio, $SPR(u)$, was calculated as $S(u)/[(S+P)(u)-S(u)]$. To relate $SPR(u)$ to the contrast degradation associated with x-ray scatter at any particular location in the reconstructed image, the $SPR(u)$ for a single projection was remapped to the object (x) such that $SPR(x) = SPR(Mu)$, where M is the system magnification. The average $SPR(x)$ over 360° was computed to yield $SPR(r)$, which is the SPR associated with the reduction in contrast [proportional to $1/(1+SPR(r))$] at any location (r) in the axial plane of the image reconstruction.

The effects of bowtie filters on the magnitude and spatial distribution of CBCT noise were assessed in images of a uniform 16 cm diameter acrylic cylinder. The cylinder was imaged at the nominal scan protocol described above with each of the three bowtie filters. Images were corrected for scatter and beam-hardening effects as in Sisniega et al.,[158] yielding uniform attenuation coefficient (within ~3%) throughout the image. A noise-only difference image was created by subtracting two CBCT images acquired in succession, and the local standard deviation (noise) was measured using a $10\times10\times10$ voxel sliding window for all locations in the reconstructed volume (accounting for a factor $\sqrt{2}$ due to image subtraction). The resulting noise map, $\sigma(x, y, z)$, was normalized by the position-dependent (square root) dose, $\sqrt{D(x, y, z)}$, to enable comparison between scans with different bowtie filters.

Imaging performance was assessed in basic terms of contrast and CNR for ICH-equivalent spheres (2-12 mm diameter, ~90 HU contrast to brain-equivalent background) within the cranial vault of a third phantom representing an anthropomorphic head. Contrast was measured as the average HU difference between a 10×10×10 voxel region inside the largest sphere and a 10×10×10 voxel region in adjacent uniform background. Noise was measured as the average standard deviation in the sphere and the background. The CNR was measured in CBCT scans acquired with each of the three bowtie filters. Spatial-frequency-dependent imaging performance measures, such as MTF and NPS, were not assessed in the current work, which focuses on the effects of readout gain mode and bowtie filters on the low-frequency transfer characteristics (viz., contrast, noise, and uniformity).

III. Results

III.A Effect of Gain Mode on Electronic Noise and DQE

Figure 5.3a shows the digitization noise and the total additive electronic noise as a function of the integrating capacitance, C_g, for a fixed bit depth ($N = 14$) and reference ADC voltage ($V_{ref} = 2$ V). For higher gain settings ($C_g < 1$ pF), digitization noise constitutes a small proportion of the total electronic noise. For lower gain settings, on the other hand, ($C_g = 2 – 5$ pF), digitization noise constitutes more than half of the total electronics noise. For even lower gain readout ($C_g > 12$ pF, which has been proposed for high dynamic range applications requiring triple-gain readout[195]), digitization noise is the dominant noise source, increasing the total additive electronics noise by a factor of ~5 compared to high gain mode. Therefore, use of such a very low-gain / large latitude mode would benefit from increased bit depth. These results are pertinent to the task of ICH imaging: previous work[179] investigated the minimum bit depth requirements, finding $N \geq 14$ bits sufficient for this imaging task; further to the point, Figure 5.3a motivates the use of HG detector readout mode – either via DG readout mode or HG in combination with bowtie filters, as detailed below.

Figure 5.3b shows the effect of detector readout gain (controlled by C_g) on zero-frequency DQE for two scenarios of dose and signal level: (i) holding mAs constant (for all values of C_g) to achieve a fixed dose (20 mGy, and ignoring detector saturation); and (ii) varying mAs to achieve a fixed pixel signal level of 80% detector saturation in the bare beam (with scan dose varying accordingly from ~4 mGy at $C_g = 0.5$ pF to ~107 mGy at $C_g = 15$ pF). At fixed dose, HG detector readout (lower C_g) benefits DQE due to the reduction in electronic noise as in Eq. (5.3), noting however, that the detector would saturate in regions of low attenuation for the low C_g end of the curve in Figure 5.3b. On the other hand, varying mAs (and dose) to give 80% saturation in the bare beam suggests an optimal detector readout gain ($C_g \sim 4$ pF, which is close to the nominal LG readout mode) that balances the tradeoffs between reduced fluence at high gain (necessary to avoid saturation) and increased digitization noise at low gain.

Figure 5.3c shows the ratio of DQE(0) between the cases of fixed dose (20 mGy) and fixed signal level (80% saturation) as a function of lateral position on the detector for a projection of a 16 cm water cylinder (with a concentric 1.4 mm thick, 14 cm diameter annulus of cortical bone simulating the skull). In HG mode ($C_g = 0.5$ pF), the DQE(0) is higher by a factor of ~2 in areas of high attenuation (behind the bulk of the cylinder and behind bone) due to reduced electronic noise, recognizing that the detector is saturated near the periphery (bolded region of the curve). As readout gain decreases, the performance of the fixed-dose and fixed-signal-level cases become more similar (roughly equal for $C_g \sim 5$ pF) and in very low-gain mode ($C_g = 12$ pF), the fixed-dose case is such that DQE(0) is reduced by half – i.e., the detector is free from saturation and has very high latitude, but electronic noise becomes the limiting factor in DQE.

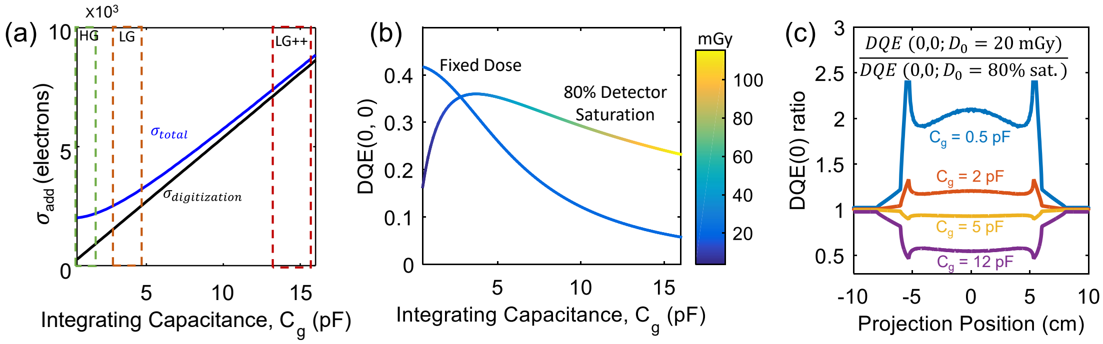

Figure 5.3. Effect of gain mode on imaging performance (a) The total electronic noise and the digitization noise are shown as a function of integrating capacitance (C_g). The high-gain (HG), low-gain (LG), and very low gain (LG++) regions are highlighted over corresponding ranges in C_g. (b) Zero-frequency DQE calculated as a function of integrating capacitance for scenarios of fixed dose (20 mGy) and fixed signal level (80% detector saturation). For the latter scenario, the colorscale along the curve denotes the corresponding CBCT scan dose. (c) Ratio of DQE(0) for fixed-dose and fixed-signal-level cases shown for various gain modes (C_g) as a function of position behind a cylindrical head phantom. Regions (at the periphery) for which the detector is saturated are marked in bold.

Considering the various readout gain options, Figure 5.3 indicates that for fixed-gain readout (i.e., LG or HG, but not DG) the nominal LG mode ($C_g = 4$ pF) at 80% detector saturation (corresponding to $D_0 \approx 25$ mGy) is optimal. Dual-gain readout, on the other hand, combines the noise benefits of HG mode in highly attenuating areas while preventing saturation artifacts in areas of low attenuation and can improve the

DQE at the center of the projection by ~20% at 20 mGy fixed dose, as shown in Figure 5.3c. This analysis quantifies the tradeoffs between noise, saturation level, and DQE in the selection of readout gain mode, and for DG, it helps guide selection of the HG capacitance (which determines the "depth" of the transition from HG to LG in the DG projection data).

Figure 5.4(a) shows the total electronic noise (σ_{add}) and the digitization noise ($\sigma_{\mathrm{digitization}}$) as a function of bit depth for two levels of additive noise typical of FPDs and CMOS detectors. We observe a strong inflection point at a bit depth below which digitization noise is the dominant component of the total electronic noise – viz., $N = 14$ bits for FPDs and $N = 17$ bits for CMOS detectors. For a FPD operating at high gain (and with total electronic noise dominated by the pixel, line, and amplifier noise), there is little to be gained by increasing bit depth beyond 14 bits (although analysis at higher spatial frequencies deserves further investigation). For a CMOS detector, however, the low electronic noise is such that digitization noise is an appreciable component, and performance is improved for bit depth increased to 16 – 18 bits. Figure 5.4(b) shows the effect of gain mode (C_g = 1, 3 and 5 pF, corresponding to high, medium, and low gain, respectively) together with digitization noise on the zero-frequency DQE at fixed pixel, line, and amplifier noise. Each curve was computed using the nominal conditions discussed in section II.A. Under conditions for which the digitization noise dominates ($N < 14$ bits and $N < 18$ bits for FPDs and CMOS detectors, respectively), systems with lower gain (i.e., larger C_g and larger dynamic range) experience an increased penalty due to amplification of the digitization noise. Therefore, detectors with low additive noise and high dynamic range, like CMOS systems, are more sensitive to digitization noise and benefit more from increased bit depth.

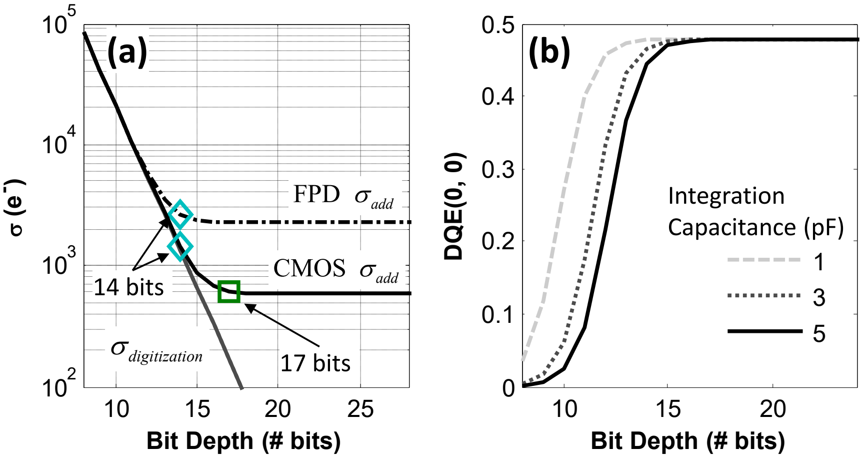

Figure 5.4. ADC digitization noise. (a) Electronic noise computed as a function of ADC bit depth. For an FPD and CMOS detector, there is steep dependence on bit depth for N = 14 and 17 bits, respectively, followed by a region for which the ADC contributes negligibly to electronic noise. (b) Zero-frequency DQE computed as a function of bit depth for various levels of readout amplifier gain (i.e., C_g = 1, 3, and pF). A system with lower gain and lower electronic noise (e.g., a CMOS detector) potentially benefits from increased bit depth.

III.B Effect of Readout Gain on Image Quality

Figure 5.5(a-d) shows axial image comparisons for various gain modes in images of an anthropomorphic head phantom with an array of ~90 HU contrast spheres within the cranial vault. Figure 5.5a shows an image for LG readout, which is free of saturation effects and provides CNR = 3.0 at 576 mAs (18.2 mGy). Imaging in HG readout at the same mAs results in saturation, clearly evident as peripheral shading artifacts in Figure 5.5b, but in the central area of the head image quality is quantifiably improved (CNR = 3.1) due to reduced electronic noise. To image without saturation in HG mode requires a reduction in dose as shown in Figure 5.5c (72 mAs, 2.3 mGy), with a corresponding increase in quantum noise that far outweighs the reduced electronic noise (CNR = 1.1). Imaging in DG mode (shown in Figure 5.5d) captures the benefits of LG near the periphery (as in Figure 5.5a) and HG in the interior (Figure 5.5b), yielding an image that is free of saturation artifacts while improving performance (CNR = 3.4) in highly attenuating regions.

Figure 5.5(e-g) shows the ratio of image noise in an axial slice between various gain modes, and Figure 5.5e shows the ratio of noise between a LG and DG image, showing ~15-30% higher image noise in LG mode compared to DG, especially near the center of the object where attenuation is highest. This agrees with the advantages of DG or HG in the center of the image indicated in Figure 5.3c. Imaging in HG generally reduces image noise compared to LG as shown in Figure 5.5f, suggesting that the small increase in CNR between Figure 5.5a and Figure 5.5b may be due to a change in contrast resulting from the saturation artifact. Finally, Figure 5.5g shows the noise in DG to be similar to that in HG, as expected.

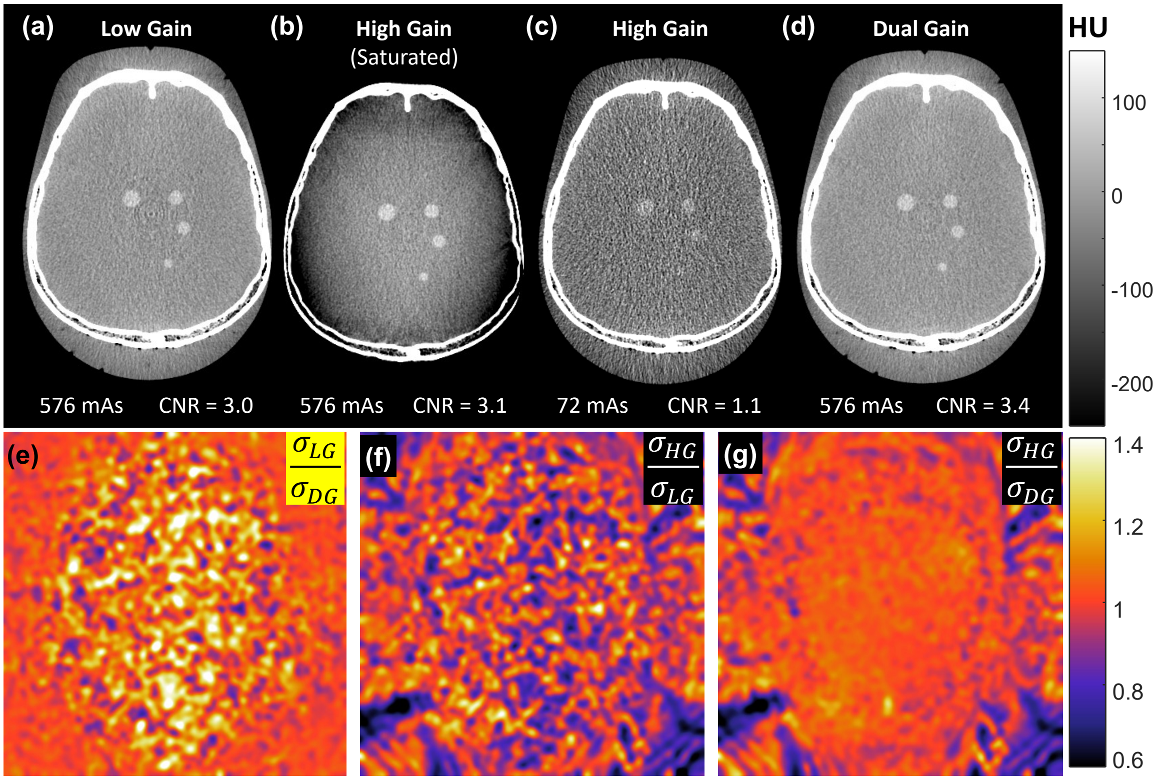

Figure 5.5. Effect of gain mode on image quality. (a) Images acquired in nominal LG, (b) HG with saturation, (c) HG without saturation, and (d) DG mode. All images except the unsaturated HG case were acquired at the same dose. Dual gain mode is found to improve CNR by ~15% over LG mode. Noise maps show the ratio of noise between various gain modes. (e) LG has higher noise in the center than DG at the same mAs, and (f) HG has the same noise as DG in the center of the image.

Analysis of the image noise in various gain modes indicates that DG detector readout reduces image noise (at higher mAs per pulse) and combines the benefits of HG (reduced additive noise) with LG (increased latitude and avoidance of saturation effects). Additionally, the images show little or no artifact associated with the HG-LG transition region and suggest that DG readout may be advantageous for clinical studies on the CBCT prototype. While DG mode provided improved overall imaging performance at the same dose as LG mode, the frame rate of the detector is reduced by a factor of 2, which doubles the scan time unless other factors are considered—e.g., reducing the number of projection views per scan. For example, the nominal scan protocol described above (720 views over a 360° orbit) implies a scan time of 28 s for LG (or HG) mode, and 90 s for DG mode. The benefits to image quality in DG mode should be factored against such considerations, including the potential for patient motion, and motivate the dynamic gain (DynaG) implementation of dual gain (DG) readout capability. An alternative approach, detailed in the following sections, implements HG mode in combination with a bowtie filter to mitigate saturation effects.

III.C Effect of Bowtie Filters on Dose and Image Quality

III.C.1 Dose Distributions for Full-Scan and Short-Scan CBCT Acquisition

The MC dose calculations were validated in comparison to MOSFET measurements. Figure 5.6a shows calculated and measured dose distribution from a single x-ray pulse (90 kV) normalized per unit mAs. The MC calculation (left) is compared to interpolation of the 8 point dose measurements (right) from MOSFETs placed in each channel of the custom CTDI phantom. Figure 5.6b shows the measured and calculated dose as a function of distance from the center of the object, showing close agreement between the MOSFET measurements and the MC simulation. Figure 5.6c shows the measured and calculated dose for a short scan (200°) in the anthropomorphic head phantom, with locations 1-5 as indicated in Figure 5.1c. Agreement between MOSFET measurement and MC calculation was within 10% at each location, and similar levels of agreement were observed for other combinations of orbital extent (short scan or full 360° scan). To further assess the accuracy of MC dose calculations in the presence of a bowtie filter, calculations were also compared to dose measurements at the center and periphery of a 16 cm CTDI phantom for all three bowtie filters (BT1, BT2, and BT3). Results are shown in Figure 5.9a (and discussed further below in section III.C.2), demonstrating agreement between calculation and measurement within 6.8% (mean error = 4.5%) at the center and within 10.2% at the periphery (mean error = 6.3%). The fairly small disagreement may be attributed to discrepancy between the true and estimated (spektr) x-ray spectrum and/or tube output (mGy/mAs) and the fact that the MC simulation does not account for x-ray scatter in the bowtie filter.

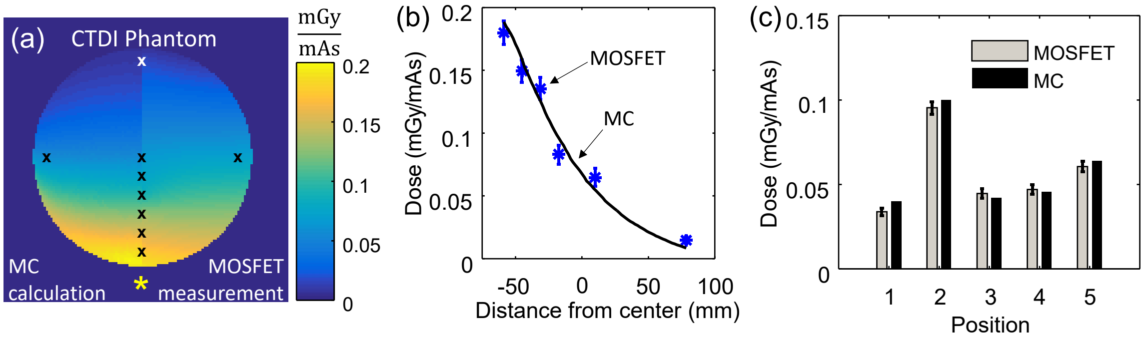

Figure 5.6. Validation of the MC dose calculation in comparison to MOSFET measurements. (a) The spatial distribution of dose from a single x-ray pulse as predicted by MC simulation (left) and interpolated from MOSFET measurements (right, with each measurement location indicated by “x”). The location of the x-ray tube is denoted with an asterisk (*). (b) Comparison of MC dose calculations and MOSFET measurements as a function of position inside the custom CTDI phantom. (c) Comparison of MC dose calculation and MOSFET measurements at various locations within the cranial vault of an anthropomorphic head phantom, showing better than 10% agreement throughout.

Figure 5.7 shows the dose distribution for various bowtie filters (Figure 5.1d) calculated in an anthropomorphic head phantom with full (360°) and short scan (200°) acquisitions. The total mAs was adjusted in each case to give a dose of 20 mGy at the center of the head (analogous to D_0 measured at the center of a CTDI phantom with a 0.6 cm^3 Farmer chamber). For the full scan cases, addition of a bowtie filter is seen to reduce the peripheral dose relative to the central dose, with stronger bowtie curvature giving greater reduction in peripheral dose. Concomitant with the reduction in peripheral dose is a reduction in image quality at the periphery, as quantified below. Use of a bowtie also reduced the total energy imparted to the imaged volume (denoted E_{tot} (mJ)) by 21% (for BT1), 33% (for BT2), and 40% (for BT3) compared to scanning without a bowtie. For fixed (20 mGy) dose to the center of the head, short scans are seen to redistribute the dose to the posterior of the head (for the source rotated under the head) and has the potential advantage of sparing dose to the eye lens. Short scans with a bowtie filter are seen to further reduce the anterior dose, with the strongest bowtie (BT3) reducing anterior dose by a factor of ~3 compared to the posterior dose and a factor of ~3.3 compared to a short scan with no bowtie (at the same D_0).

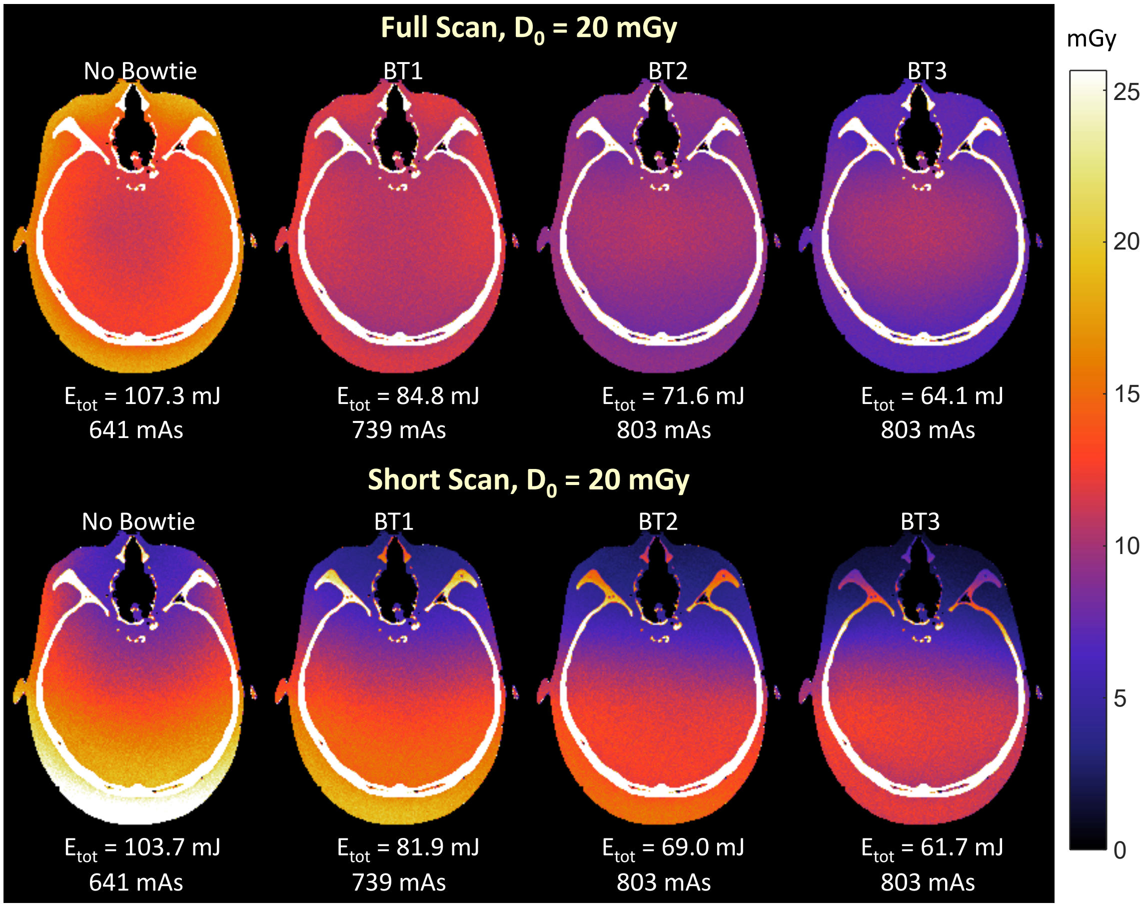

Figure 5.7. Monte carlo dose calculations for full and half scan CBCT acquisition with three bowtie designs (BT1, BT2, and BT3 as in Figure 5.1). Bowtie filters are seen to reduce peripheral dose and total energy imparted (E_{tot}). Combination with a short scan trajectory further reduces E_{tot} and, especially, the anterior dose (i.e., dose to the eye lens).

Figure 5.8 shows the dose to the eye lens (i.e., a 25 mm spherical region centered in the orbital socket of the phantom in Figure 5.7) as a function of CBCT orbital extent (from short scan ~200° to a full 360° orbit). Shorter scans and thicker bowties reduce the lens dose, and the dose reduction associated with the bowtie filters is relatively higher for lower orbital extent. This analysis shows that use of bowtie filters and short scans can yield large reduction in dose to specific areas of the patient, as expected. Moreover, use of a bowtie filter can enable an increased orbital extent (> 200°) without increase to the lens dose, which may carry advantages in image quality characteristic related to increased view sampling.[214]

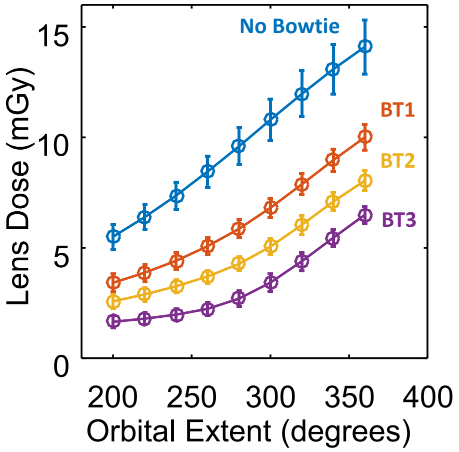

Figure 5.8. Dose to the eye lens calculated as a function of orbital extent (with fixed 20 mGy dose to the center of the head) for various bowtie configurations. Use of any bowtie is seen to reduce the lens dose, with up to 55% reduction possible with use of BT3. Shorter angular extent combined with bowtie filters reduces the lens dose even further.

III.C.2 Effect of Bowtie Filters on Image Quality

The effects of bowtie filters on dose, x-ray scatter, noise, and CNR are quantified in Figure 5.9. Figure 5.9a shows the dose (per unit mAs) as a function of position (distance from center of a CTDI phantom at isocenter) for a 360^{o} scan. Symbols mark Farmer chamber measurements at the central and peripheral positions. At equivalent mAs, a stronger bowtie filter reduces both the central and peripheral dose: the central dose is lower because of reduced scatter in the interior of the phantom, and the peripheral dose is lower due to reduced primary fluence.

Figure 5.9b shows the SPR measured as a function of position (distance from center of a CTDI phantom) for a nominal CBCT scan. Use of a bowtie is found to increase SPR at the periphery of the image while reducing the SPR at the center. This effect is understood from the fact that the primary fluence at the center is nearly unchanged by a bowtie filter (attenuated through only ~1 mm Al), and scatter originating from the center of the object is therefore minimally reduced by a bowtie filter. The angular distribution of this scatter is unchanged, of course, and it is detected at the periphery of the detector in nearly the same quantity with or without a bowtie. However, the primary fluence at the periphery is reduced by a bowtie filter, and the SPR at the detector periphery is therefore increased in the presence of a bowtie. Similarly, the incident (primary) fluence and scatter originating in the periphery of the object are much reduced by a bowtie filter. Therefore, the total detected scatter at the center of the detector is reduced due to a smaller contribution from peripheral object scatter, while the primary fluence remains nearly unchanged at the center. These trends indicate a tradeoff between central and peripheral CNR for various bowtie filters designs, with greater tradeoffs between central scatter and peripheral primary signal depending on the thickness and curvature of the bowtie filter design.

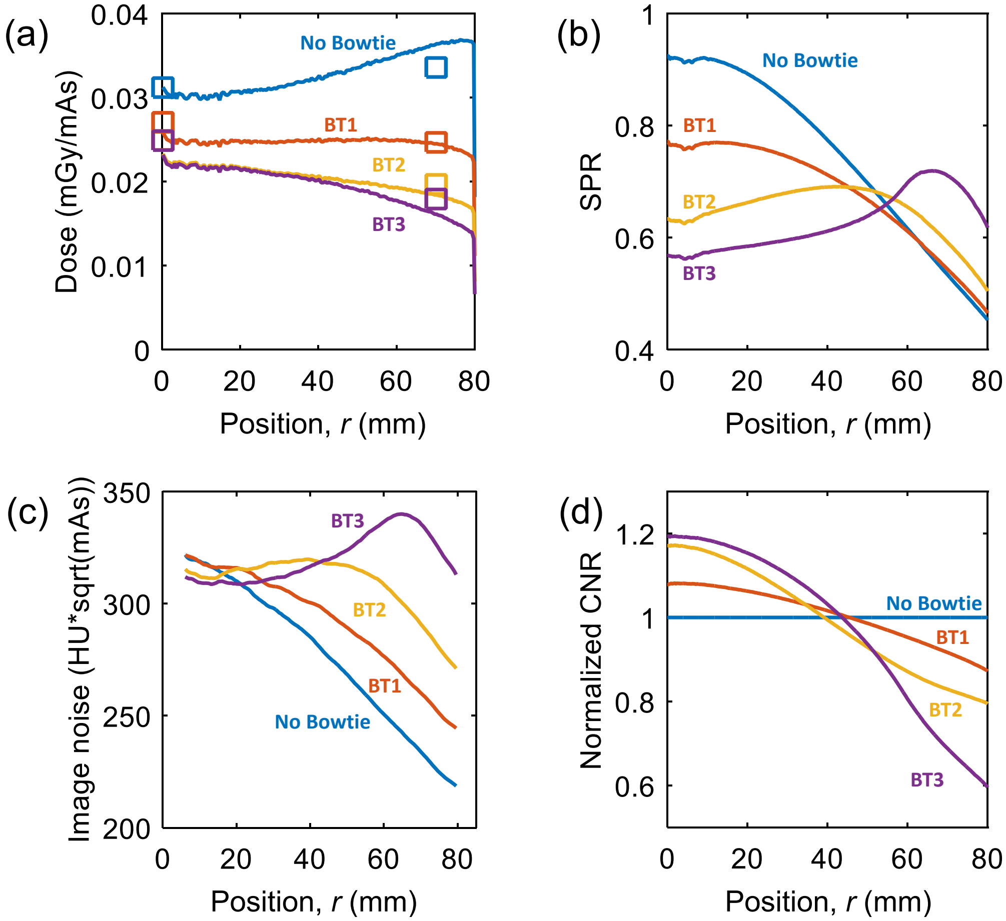

Figure 5.9. Effect of bowtie filter design on (a) dose, (b) scatter, (c) noise, and (d) CNR as a function of position from the center of a 16 cm diameter cylinder.

Figure 5.9c shows the noise in CBCT reconstructions as a function of image position in the axial plane (distance from center in a uniform 16 cm cylinder). Without a bowtie, image noise is highest in the center (where attenuation is highest) and lowest at the periphery. BT1 introduces a modest increase in noise at the periphery with little effect on the noise at the center. BT2 achieves a nearly constant noise level throughout the central region and slightly reduces the noise at the center. BT3 reduces the primary fluence at the periphery to an extent that noise at the periphery actually exceeds the noise at the center.

Figure 5.9d shows the combined effect of dose, scatter, and noise on the CNR as a function of position in the axial plane. The CNR values for each bowtie filter in Figure 5.9d are normalized by the CNR without a bowtie filter per unit square root dose (from Figure 5.9a), accounting for contrast degradation due to the spatially varying SPR (Figure 5.9b) and noise (Figure 5.9c) in the presence of a bowtie filter. The analysis reveals a strong tradeoff between image quality in the center and periphery of the image, depending on bowtie filter design: the strongest bowtie (BT3) yielded the highest CNR in the central region (~20% increase compared to no bowtie), but strongly degraded CNR near the periphery (~40% reduction in CNR); bowtie filters with reduced curvature and thickness modulated this tradeoff, with BT2 giving ~18% increase in CNR at the center and ~18% reduction in CNR at the periphery.

Figure 5.10(a-b) shows images acquired in HG and LG mode with BT2. As expected, contrast of the simulated intracranial lesion was the same in both cases (~69 HU), but noise in the LG image was 28% higher than in the HG image (due to higher electronic noise). In the HG image of Figure 5.10a, use of a bowtie filter reduced the bare-beam fluence to avoid detector saturation, yielding CNR similar to that for the DG image in Figure 5.5d (but with half the scan time). Figure 5.10(c-d) shows images obtained in HG mode with and without BT2 and equivalent $\text{CTDI}_w = 18.8$ mGy (computed from Figure 5.9a and validated by MC dose calculation). The bowtie filter reduced the noise in the center of the image by ~24%, consistent with trends in the uniform phantom, yielding CNR = 5.2 with BT2, compared to CNR = 4.2 without a bowtie. A slight residual artifact (bright circular area in the central region) can be seen in Figure 5.10c but suggests that the polyenergetic flood-field correction of Eq. (5.6) and Figure 5.2 for the bowtie image worked fairly well (much better than conventional monoenergetic flood-field correction, not shown, which resulted in a strong dome artifact).

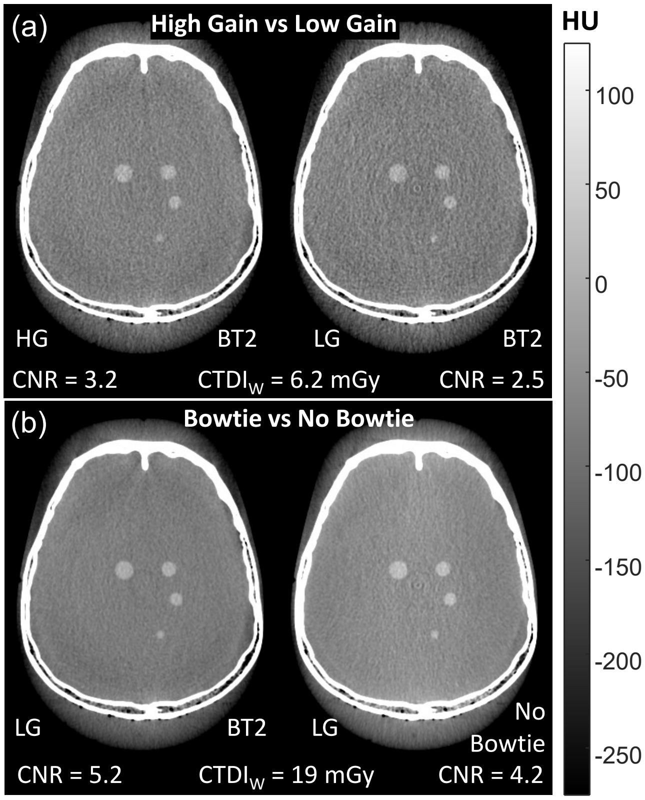

Figure 5.10. CBCT image quality using HG and a bowtie filter. (a) The HG image acquired with BT2 shows a 28% improvement in CNR compared to (b) the LG image with bowtie. (c) Dose-matched (CTDI$_W$ = 19 mGy) images with and (d) without a bowtie show a 24% improvement in CNR near the center of the head with use of a bowtie filter.

IV. Discussion and Conclusions

High-quality CBCT imaging of the head was shown to benefit from increasing dynamic range via HG detector readout in combination with a bowtie filter. Analytical modeling showed that the reduction in digitization noise resulting from increased detector readout gain can improve the DQE by ~20%, and image reconstructions of DG readout and/or bowtie filters in HG mode showed improved CNR at equivalent dose.

Similarly, DG detector readout was shown to improve CNR in highly attenuating regions of the object by ~15% at equivalent dose, by reducing digitization noise in HG projection data. However, because DG mode requires readout of each pixel value twice, the maximum detector frame rate is reduced, more than doubling the total scan time (from 28 s in LG mode to 90 s). Reduction of the number of projections, increasing the hardware binning factor (reducing number of pixels read out per frame), and/or using DynaG readout mode (which does not suffer the factor of two increase in readout time) can be used to reduce the total scan time. These solutions may carry additional challenges of artifacts arising from flood-field calibration (in DynaG mode) and sampling effects (reduced number of projection views).[214]

Bowtie filters enable imaging in HG mode without saturation and without increasing the total scan time. Additionally, the use of bowtie filters can improve image quality per unit square-root dose at the center of the image, but reduces image quality at the periphery (attributed to increased SPR—reduced contrast—as well as increased quantum noise). Therefore, the choice of bowtie filter should be governed by image quality requirements throughout the image balanced with considerations for patient dose, especially to radiosensitive organs. For example, BT1 (a very moderate bowtie) increased the dynamic range of HG mode by ~2× and reduced peripheral dose to be approximately the same as central dose. Such a bowtie could potentially find use in regions with soft tissue at the edges (extremities, abdomen) where CNR at the periphery is important. Bowtie 2 was chosen as the nominal bowtie for head imaging, yielding a reasonable dynamic range in HG readout mode, good tradeoff between central and peripheral image quality, and a large decrease in lens dose. Use of the proposed bowtie filter combined with a short scan centered about the back of the head can reduce dose to radiosensitive organs near the periphery by half while preserving image quality near the center of the image.

Either DG readout or the use of bowtie filters appears to be feasible and carries benefits of reduced electronic noise in the HG projection data. While the benefit to image quality with DG is more modest at equivalent dose (15% increase in CNR using just DG, compared to a 24% increase with HG and bowtie filter at the center of the head), DG readout is generally simpler to implement than use of a bowtie filter, and it is less susceptible to patient positioning errors and system motion during scanning. Furthermore, DG readout does not degrade image quality at the periphery. Additionally, to match the dose with use of a bowtie filter, the required tube output (mAs / pulse) is increased, placing a larger constraint on the selection of x-ray tube for a point-of-care CBCT system (and potentially exceeding the specifications of commercially available, compact x-ray tubes as discussed in Chapter 4). Slight residual artifacts can also be seen in the bowtie images, likely resulting from errors in the estimation of bowtie position during polyenergetic flood field correction. Additionally, the polyenergetic flood field correction is fairly sensitive to estimation of the spectrum, and can be susceptible to errors on systems in which the spectrum is difficult to calibrate, due to, for example, large amounts of off-focal radiation.

Taken together, the findings detailed above regarding detector readout gain mode and/or selection of a bowtie filter guided selection of the hardware configuration to be implemented on the initial scanner prototype. As detailed in the next chapter, the prototype uses DG readout (to reduce noise in high-attenuation regions) and does not incorporate a bowtie filter (at least for initial clinical studies).

Chapter 6: Imaging Performance of a Prototype Point-of-Care CBCT Head Scanner

I. Introduction

Imaging of ICH using CBCT is a challenging task, as identified in Chapter 1, requiring contrast resolution of ~20-60 HU for confident visualization. Such capability is primarily challenged by image noise and nonuniformity (artifacts) to which CBCT is particularly susceptible. Particularly for a mobile CBCT system suitable to application at the point of care, these challenges pose major limitations to imaging performance, and mobile CBCT has largely been limited to applications involving fairly high-contrast anatomy (e.g., orthopedic imaging). The work in previous chapters addressed such challenges in part via optimization of system configuration and hardware selection, guiding the design and development of a prototype mobile CBCT head scanner for reliable detection of ICH at the point of care.

Based upon the modeling, design, and optimization presented in Chapters 4 and 5, and incorporating algorithms for artifact correction[158] and model-based image reconstruction (MBIR) techniques,[215] a prototype suitable for first clinical studies has been developed. As detailed in Chapter 2, the imaging performance and radiation dose for such a system needs to be rigorously assessed in the early stages of development as a prerequisite to clinical translation. Especially in the context of nonlinear reconstruction algorithms and artifact corrections, such technical assessment is important to guiding the selection of imaging protocols. The work reported in this chapter was published in Xu et al., "Technical Assessment of a Prototype Cone-Beam CT System for Imaging of Acute Intracranial Hemorrhage."}Ref when available

II. Methods and Materials

II.A CBCT Scanner Prototype

Figure 6.1a shows the prototype CBCT system, and a summary of system characteristics is listed in Table 6.1. The main hardware components are as follows:

Mobile gantry. The system includes a mobile U-arm gantry with a maximum rotation rate of 24^{o} / s, allowing a half-scan orbit (210^{o}) in 9 seconds or a full 360° rotation in 15 seconds. Positioning controls on each side of the gantry are used to position the U-arm (raise, lower, or rotate). The entire system can be powered from a standard (110 VAC, 20 A) North American outlet.

X-ray source and generator. The x-ray source is a rotating tungsten anode x-ray tube (Monobloc, IMD, Grassobio, Italy) with 150 kJ heat capacity and 17° anode. The system has 5 kW maximum power, pulse duration ranging 2–40 ms, tube current ranging 5–40 mA, and tube potential ranging 70–120 kV at 0.6 FS focal spot size. Specified inherent filtration for the x-ray window is 1.4 mm Al equivalent at 75 kV. Based on the results discussed in Chapter 5, the initial prototype did not include a bowtie filter.

Collimator. A manual square-field collimator (R72, Ralco srl, El Dorado Hills CA, USA) is attached to the face of the x-ray source. The collimator area ranges up to 43×43 cm^2 at 1000 mm from the source. The system also features a light-field and a laser crosshair for positioning. The light field mirror specifies 1 mm Al equivalent filtration. A filter slot includes an additional 0.2 mm Cu added filtration.

Detector. The system features a FPD (Paxscan 4343CB, Varian, Palo Alto CA, USA) with a 43×43 cm^2 FOV and native 0.139×0.139 mm^2 pixel pitch, which can be hardware binned to 2×2, 3×3, and 4×4, resulting in isotropic pixel sizes of 0.278, 0.417, and 0.556 mm, respectively. The FPD readout gain mode can be varied between low gain (LG, 3–4 pF integrating capacitance), high gain (HG, 0.5 pF integrating capacitance), and dual gain (DG, 0.5 pF HG and 4 pF LG) using 2×2 or 4×4 pixel binning at 16-bit depth. The maximum frame rate of the detector in LG or HG mode is 30 frames per second (fps) for 4×4 binning, 25 fps for 3×3 binning, 15 fps for 2×2 binning, and 4 fps for 1×1 pixel binning. For DG readout, the frame rate is halved—for example, nominal 2×2 DG readout and ~8 fps. The nominal frame rate, pixel binning, and gain modes are further detailed in section II.C. Based on previous analysis,[179] the current system configuration did not include an antiscatter grid.

System geometry. The system has a source-axis distance (SAD) of 550 mm and source-detector distance (SDD) of 1000 mm. The FPD is approximately centered on the FOV, giving a 25° fan and cone angle. The resulting 3D image FOV is $23.7\times23.7\times23.7$ cm^3. Previous analysis[179] shows this geometry to be nearly optimal with respect to tradeoffs among focal spot blur, geometric magnification, air gap (x-ray scatter rejection), and detector exposure level. According to Zhuang et al.,[216] it is also sufficient to give full axial coverage of the head in 99% of the population.

Control Console. The control console and workstation are located behind a mobile shield wall. The workstation used for CBCT image acquisition in this work was a HP Z620 Workstation (Hewlett Packard, Palo Alto CA, USA). Although 3D image reconstruction (details below) can be performed on the acquisition computer, for this study, 3D images were reconstructed on a Precision T7910 (Dell, Round Rock TX, USA) offering superior GPU (GeForce GTX Titan X, NVIDIA, Santa Clara CA, USA).

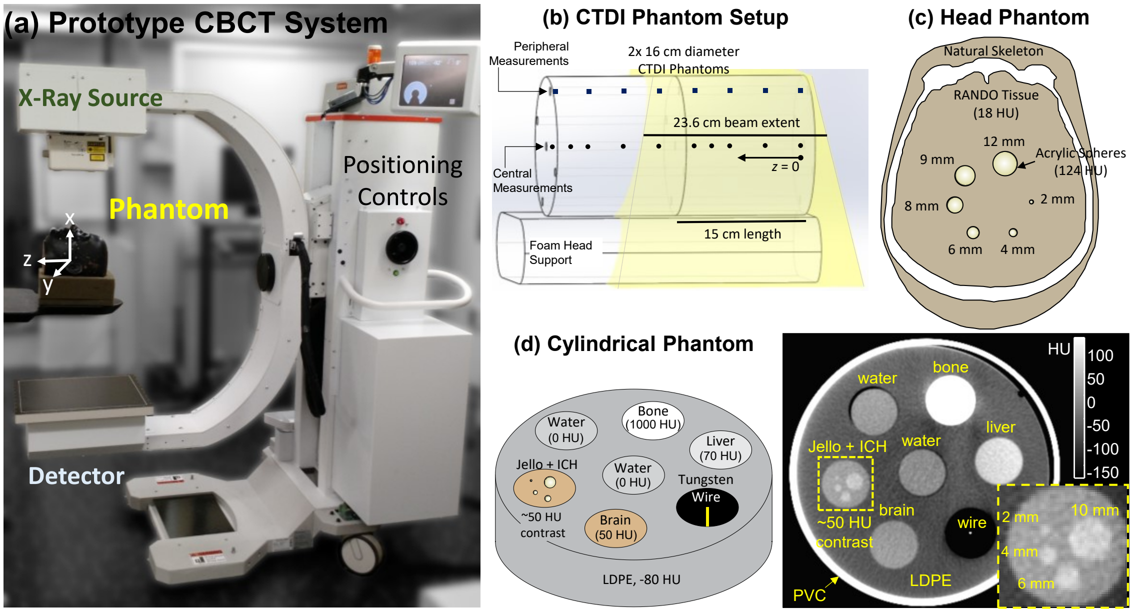

Figure 6.1. (a) Prototype CBCT system developed for ICH imaging. Dose was assessed in (b) a stack of two 16 cm diameter CTDI phantoms as a function of position. Image quality was assessed in (c) an anthropomorphic head phantom containing a natural skeleton and tissue-equivalent plastic (18 HU) embedded with spheres of varying size (2–12 mm) and attenuation (-30–900 HU) and (d) a simple cylindrical phantom as well as a cadaver (not shown).

II.B Image Acquisition

Beam Quality. Beam quality was characterized by measuring the half-value layer (HVL) using a back-shielded silicon diode (AccuDose, RadCal Corp., Monrovia CA, USA) placed at the FPD with varying thickness of Al filtration (placed at the exit face of the collimator) across a broad range of kV. The HVL was determined by exponential fit of exposure vs Al thickness and computing the thickness required to reduce exposure to 50% of the bare-beam value. These data were also used to parameterize an x-ray spectral model using the spektr 3.0[217] implementation of TASMICS.[211] The spectral model was subsequently used in correction of scatter and beam hardening artifacts (below).

Hardware Parameter	**Value**	
Power (max)	5 kW	
Focal spot size	0.6 FS	
Anode	Rotating (W) 17°	
Tube voltage	70–120 kV	
Total filtration	2.4 mm Al equiv. inh. filtration 0.2 mm Cu added filtration	
HVL (80 kV)	6.1 mm Al	
HVL (90 kV)	6.8 mm Al	
HVL (100 kV)	7.4 mm Al	
HVL (110 kV)	7.7 mm Al	
FPD pixel pitch (a_{pix})	0.139 mm	
Scintillator	0.6 mm CsI:Tl	
Gantry rotation rate (max)	24° / s	
SAD	550 mm	
SDD	1000 mm	
FOV at isocenter	23.7×23.7×23.7 cm^3	
Acquisition Parameter	**Nominal Scan Technique**	**Clinical Scan Protocol**
Orbital extent	360°	
Detector readout mode	Dual Gain (0.5 pF HG / 4 pF LG)	
kV	100	
Total mAs	216	
mAs / projection	0.3	0.48
Number of projections / scan	720	450
Scan time	90 s	30 s
Pixel binning	2×2 (hardware) 2×2 (software)	4×4 (hardware) 1×1 (software)
Frame rate	8 fps	15 fps
Central Dose, D_0	20.8 mGy	
Peripheral Dose, D_P	23.8 mGy	
Weighted Dose, D_w	22.8 mGy	
Reconstruction Parameter	**Sharp Bone Protocol**	**Smooth Soft-Tissue Protocol**
Algorithm	FBP	PWLS
Filter, Cutoff Frequency	Hann, $k_{\text{filt}} = 1$	n/a
Penalty, Regularization	n/a	Huber, $\beta_R = 10^{2.6}$, $\delta = 10^{-4}$ mm^{-1}
Voxel size	0.3×0.3×0.3 mm^3	0.5×0.5×0.5 mm^3
Slice Thickness (display)	0.3 mm	2.5 mm

Table 6.1. Summary of prototype scanner characteristics along with nominal image acquisition and reconstruction parameters.

Radiation Dose. Dose was measured using a Radcal electrometer (Accudose, Radcal Corp., Monrovia CA, USA) and a 0.6 cm^3 Farmer ionization chamber placed at the central and peripheral locations of a 16 cm diameter CTDI phantom. As shown in Figure 6.1b, two 16 cm diameter CTDI phantoms were placed end to end and centered along the axis of rotation, with one end of the stack aligned at the superior edge of the x-ray field and the other end of the stack extending 6.5 cm beyond the inferior edge of the beam, roughly approximating the extent of the head and neck and sufficient to capture the dose associated with long x-ray scatter tails. The central dose (D_0) was measured as the absolute dose (mGy) in the center of the beam in the central hole of the CTDI phantom, and the peripheral dose (D_p) was that in a peripheral hole (only one peripheral location measured for 360° source-detector orbits). The weighted dose (D_w) was calculated as $D_w = \frac{1}{3}D_0 + \frac{2}{3}D_p$. The dose was measured for tube potential ranging 70–120 kV. The dose along the superior-inferior (SI) central axis was also measured (with $z = 0$ corresponding to the superior edge of the beam) by translating the Farmer chamber along the z axis in approximately 2 cm intervals, providing a longitudinal dose profile including that outside the inferior aspect of the FOV (approximate to the location of the thyroid).

CBCT Image Acquisition Technique. Initial studies identified 3 CBCT image acquisition protocols for the system: (1) DG readout mode with 2×2 pixel binning (0.278×0.278 mm^2 pixels), 720 projections over 360° at 0.3 mAs/pulse (216 mAs/scan) with a total scan time of 90 s; (2) LG readout mode with 3×3 pixel binning, 720 projections over 360° and 0.3 mAs/pulse (216 mAs/scan) with a total scan time of 28 s; and (3) DG readout mode with 4×4 pixel binning, 450 projections over 360° and 0.48 mAs/pulse (216 mAs/scan) with a total scan time of 30 s. All protocols use 100 kV with total filtration as in Table 6.1. The standard scan protocol in studies below was protocol (1)—identified as the "nominal" protocol in Table 6.1—unless otherwise specifically mentioned. Protocol (2) was used in phantom studies to investigate the advantages of DG readout. Protocol (3) was defined following the technical assessment detailed below as part of the translation to clinical studies, providing the same dose as Protocol (1) with faster scan speed.

II.C Image Reconstruction

Data Pre-Processing. Fifty dark (offset) scans were acquired immediately before each scan. Two hundred flood-field projections were acquired in air with the gantry stationary at the 90° position shown in Figure 6.1a. Two flood-field data sets were acquired for DG correction: low mAs (0.04 mAs/pulse) for the HG channel and high mAs (0.25 mAs/pulse) for the LG channel. After acquisition, the HG and LG channels of each DG projection were separately offset- and gain-corrected, and each HG projection was normalized to the value in a 100×100 pixel region of the unsaturated region of the corresponding LG region, similar to the process described in Chapter 5. The two projection data sets were then recombined such that HG pixels > 40% of the HG signal saturation value were replaced with the corresponding LG pixel values. Pixel defects were corrected by 3×3 median filtering for isolated defective pixels (3×5 filtering for line defects) identified in a map of pixels demonstrating anomalous dark signal or gain characteristics. For soft-tissue reconstructions (below), the projection data were further binned (additional factor of 2×2, giving pixel pitch = 4× and a_{pix} = 0.556 mm).

Lag Correction. The projection data were then corrected for temporal lag as described in Sisniega et al.[158] by deconvolution with the lag kernel, $L(k)$:

$$L\left(k\right)=\sum_{n=1}^{N}\frac{b_n}{\left(1-e^{-a_n}\right)}e^{-a_n k}u\left(k\right) \tag{6.1}$$

where k represents the frame number, $u(k)$ is the unit step function, and six exponential terms (N = 6) were used to characterize the falling-edge step response function, with a_n = [1.96, 0.01, 0.07, 0.99, 3.90, 31.46] and b_n = [0.029, 0.003, 0.006, 0.02, 0.20, 0.75].

Glare Correction. Correction of low-frequency "glare" effects arising from detector veiling glare and/or off-focal radiation was applied by deconvolution of the projection data with the glare spread function, GSF(r):

$$\mathrm{GSF}\left(r\right)=\frac{c_1}{\pi c_2}\left(\frac{1}{1+r^2/c_2^2}\right) \tag{6.2}$$

where r represents radial distance (dimensionless pixel number), and c_1 and c_2 are 0.1 and 14.59, respectively (also dimensionless).

Beam-Hardening Correction. Two-pass beam hardening correction was applied according to the algorithm described by Joseph and Spital[213] and implemented in Sisniega et al.[158] Both the water and bone corrections were based on the spectral model derived in section II.A. A first-pass water correction was performed by replacing the measured attenuation values by those in a pre-generated look-up table (LUT) that matched the "ideal" (pre-hardened) attenuation values to beam-hardened attenuation values, assuming an object composed entirely of water (with varying density). A 3D image was then reconstructed, and voxels with value greater than 200 HU were segmented as "bone" and forward projected, giving a bone-only projection. A second LUT for bone attenuation was used to correct the bone-only projections, and the corrected bone-only projections were recombined with the water-corrected projections for reconstruction of a final beam-hardening corrected 3D image.

X-ray Scatter Correction. X-ray scatter correction was integrated with the beam-hardening correction as described in Sisniega et al.[158] A MC estimation of scatter fluence was computed for each projection based on the beam-hardening corrected 3D volume. The computation time of scatter fluence estimation was reduced using variance reduction,[218] GPU parallelization,[170, 219, 220] and sparse sampling in the angular domain.[221] The scatter fluence was subtracted from each projection, and all projections were individually renormalized to the bare-beam signal prior to reconstruction. Application of the beam hardening and scatter corrections was iterative, with the scatter-corrected image from iteration *i* providing input to the beam-hardening correction of iteration (*i*+1), and so on for 4 iterations.

Geometric Calibration. The system geometry was calibrated using a cylindrical phantom with tungsten BBs embedded in a spiral pattern at precisely known locations. A 360° scan of the phantom was acquired, and the center of all BBs in each projection was computed. A projection matrix describing the pose of the x-ray source and detector according to 9 degrees of freedom is computed for each view based on the projected BB locations, similar to the procedure described in Navab et al.[222] The view angle for each projection in the calibration scan was recorded from the gantry motor encoders. For subsequent imaging scans, the projection matrices were interpolated from the calibration data according to the encoder values in each view (trilinear interpolation of the 6 translational components and quaternion average of the 3 rotational components).

3D Image Reconstruction. Two reconstruction protocols were used: a sharp reconstruction based on 3D filtered backprojection (FBP)[24] for bone visualization; and a smooth reconstruction based on penalized weighted least squares (PWLS) for low-contrast soft-tissue and ICH visualization. FBP reconstructions were performed using a Hann apodization window with variable cutoff frequency, k_{filt}. Voxel size in FBP reconstructions was nominally 0.3×0.3×0.3 mm^3 (alternatively, 0.5×0.5×0.5 mm^3 for studies that compare to PWLS, below). PWLS reconstructions were performed by minimizing the objective function:

$$\hat{\mu} = \arg\min_{\mu} \left\| \mathbf{A}\mu - l \right\|_{\mathbf{W}}^{2} + \beta R(u) \tag{6.3}$$

where $\hat{\mu}$ is the image estimate, **A** is the linear projection operator, l represents the measured line integrals, and **W** are the data fidelity weighting terms optionally taken either as the data directly[223] or modified to account for artifact corrections as in Dang et al.[215] The penalty strength β was freely variable, with a nominal value of $10^{2.6}$, and the roughness penalty, $R(\mu)$, was a Huber function that penalizes the difference between a voxel at index j and its N = 6 nearest neighbors (at location k) in 3 dimensions as:

$$R(\mu)=\sum_{j}\sum_{k\in N}\begin{cases}\frac{1}{2\delta}\left(\mu_j-\mu_k\right)^2, & \left|\mu_j-\mu_k\right|\le\delta\\ \left|\mu_j-\mu_k\right|-\frac{\delta}{2}, & \left|\mu_j-\mu_k\right|>\delta\end{cases} \tag{6.4}$$

to control the transition between quadratic smoothing (for small signal differences) and linear edge preservation (for large signal differences). The δ term determines the threshold contrast (signal difference) between the quadratic and linear penalty, varying within the range (1×10^{-4} to 5×10^{-4}) mm^{-1} as in Dang et al.[215] The separable quadratic surrogates method with ordered subsets (OS-SQS) was used as in Erdogan and Fessler[224] to perform the optimization in Eq. (6.4) with precomputed curvatures using 20 subsets and 100 iterations. A separable footprint[225] forward- and back-projector was used with modifications as in Wang et al[226] using custom CUDA libraries for GPU acceleration. Voxel size in PWLS reconstructions was nominally $0.5\times0.5\times0.5$ mm^3 with option for displayed slice averaging.

II.D Image Quality Assessment

II.D.1 Artifact Corrections

The overall quality of the artifact corrections was first assessed in terms of uniformity and effect on contrast, noise, and CNR. An anthropomorphic head phantom (RANDO, The Phantom Lab, Greenwich NY, USA) was used, featuring a natural skeleton encased in tissue-equivalent plastic (~18 HU). Two arrangements of spheres were included within the cranial vault as illustrated in Figure 6.1c: the first contained 12 mm diameter spheres of varying contrast (-30–900 HU); and the second contained acrylic spheres (124 HU) of varying size (2–12 mm diameter). Image uniformity was measured in terms of the mean signal difference in a 10×10 voxel region near the interior of the skull ($\bar{\mu}_{\text{edge}}$) compared to a region near the center ($\bar{\mu}_{\text{center}}$) normalized by the signal value in the edge region:

$$t_{\text{cup}}=\frac{\bar{\mu}_{\text{edge}}-\bar{\mu}_{\text{center}}}{\bar{\mu}_{\text{edge}}} \tag{6.5}$$

Contrast was measured as the difference in mean signal between a 7×7 voxel region within the largest acrylic sphere and a 7×7 voxel region in the adjacent soft-tissue background, repeated for 9 slices about the center of a sphere. Noise was measured as the mean standard deviation in voxel values in soft-tissue background. The CNR was evaluated with and without artifact corrections for the FBP and PWLS reconstructions.

II.D.2 Contrast, Noise, and Spatial Resolution

Imaging performance was further evaluated (in FBP and PWLS reconstructions with artifact correction) in terms of contrast, noise, and spatial resolution using a 15 cm cylindrical phantom (Figure 6.1d) containing tissue-simulating inserts (Gammex, Middleton WI, USA) and a 0.127 mm diameter tungsten wire in Styrofoam. The phantom also contained a custom gelatin formulation (Knox Gelatine, Kraft, Camden NJ, USA) mixed to simulate brain (~10 HU) and containing an arrangement of ICH-simulating spheres (QRM GmbH, Moehrendorf, Germany) ranging 2–10 mm in diameter, each 57 HU (or 47 HU contrast to gelatin).

Images were acquired using the nominal protocol (1) identified during the design phase (Chapter 4) and specified in Table 6.1 (100 kV with 720 projection images). CNR was measured as a function of dose by varying 72–346 mAs (adjusted by varying 0.10–0.48 mAs / projection). Similar to Section II.D.1, contrast and noise were evaluated for the low-contrast inserts (10 mm ICH sphere) using 7×7 voxel regions of low-contrast insert and background.

For FBP reconstructions, the spatial resolution was characterized in terms of a 2D Gaussian fit to the PSF measured in 100 adjacent axial slices of the tungsten wire. Each Gaussian fit was deconvolved with a symmetric (0.127 mm diameter) circle function representing the wire cross-section, and the ensemble average FWHM was computed. As broadly appreciated, nonlinear reconstruction methods such as PWLS exhibit contrast-dependent spatial resolution characterstics;[226, 227] therefore, the spatial resolution for PWLS reconstructions was characterized with respect to the low-contrast (47 HU contrast) sphere. As previously described,[215, 226] an oversampled ESF was generated by converting voxel locations to spherical coordinates, (r, θ, ϕ), with $r = 0$ corresponding to the center of the sphere. The sphere was then separated into 12 equiangular sectors, and for each sector a cumulative 1D Gaussian function, $\mathrm{erf}(r; \mu, \sigma)$, was fit to the voxel values as a function of r for all angles in that sector. The equivalent PSF FWHM was computed from each fit, and the ensemble average was reported. The PSF FWHM was analyzed as a function of k_{filt} (for FBP) and as a function of β (for PWLS, with δ fixed to a value of 1×10^{-4} mm^{-1}). The results were further characterized in terms of the MTF by Fourier Transform (FT) of the spread functions: for FBP, the central slice of the 2D FT of the Gaussian PSF fit to the wire; and for PWLS, the 1D FT of the derivative of the erf fit to the low-contrast ESF.

II.D.3 Image Quality in Cadaver with Simulated ICH

A human cadaver was imaged 9-15 hours post-mortem without preservation agents to maintain the natural contrast of the brain as much as possible, recognizing that tissue decomposition in the brain proceeds within hours of death. Data were acquired at the nominal image acquisition technique (1) specified in Section II.B. Sharp (FBP) and smooth (PWLS) images were reconstructed as specified in Section II.C and Table 6.1. Images were first acquired with the specimen in its natural state. Then, a custom solution was prepared with contrast simulating ICH (~64 HU contrast to brain) by mixing 12% sucrose, 4% NaCl, and 0.5% gelatin powder (all by weight) in solution with water. Two injections of the simulated ICH into the right frontal lobe were performed using a cannula and trochar (Jamshidi Needle, Becton Dickinson, Franklin Lakes NJ, USA)—first, a small (2 cm^3) bolus, followed by an additional larger (6 cm^3) bolus, with images acquired after each. A diagnostic CT scan was also acquired (12 hours post-mortem, prior to the simulated ICH injection) using a standard head scan protocol (120 kV, 500 mAs, 59.4 mGy, $0.42\times0.42\times1$ mm^3 voxel size; Brilliance CT Big Bore, Philips Healthcare, Amsterdam, Netherlands).

Images were displayed on a 3D imaging workstation (VuePACS, Carestream Health, Rochester NY, USA) with diagnostic-quality monitors (MDCG-3221, Barco, Kortrijk, Belgium) and interpreted by a fellowship-trained neuroradiologist. Image features were qualitatively evaluated with respect to a variety of imaging tasks: (*i*) spatial resolution characteristics in bone with respect to visualization of cranial sutures and/or fracture; (*ii*) brain-CSF differentiation; (*iii*) ability to visualize midline shift; (*iv*) conspicuity of the ICH injection; (*v*) gray-white matter differentiation; and (*vi*) overall image uniformity (including shading and streak artifacts that may confound visualization of ICH). For each task, the neuroradiologist assessed task performance as (1) conspicuous, (2) well visualized, (3) adequately visualized, (4) challenging, or (5) unidentifiable and provided free response regarding factors of contrast, noise, spatial resolution, and artifacts.

III. Results

III.A Dose

Figure 6.2 shows the central (D_0) and peripheral (D_p) dose measured as a function of tube potential and superior-inferior position, z. The dose increased with tube potential as shown in Figure 6.2a. The longitudinal variation in dose is shown in Figure 6.2b, showing that the central and peripheral dose peak near the central slice ($z = 12$ cm) at a value of $D_w = 22.8$ mGy. The dose is reduced toward the superior and inferior edges of the FOV to values of $D_w \sim 15.5$ mGy and 8.2 mGy, respectively. The distribution is asymmetric in z, and the peripheral dose is higher than the central dose across the superior portion of the FOV (toward z=0) but lower near the inferior edge (z~23 cm) as well as outside the beam due to asymmetry in the internal attenuation of x-ray scatter—i.e., increased and decreased scatter attenuation in the superior and inferior regions, respectively. The out-of-beam central and peripheral dose were 32% and 11% of the respective maximum values, giving $D_w \sim 1.6$ mGy at $z \sim 30$ cm (approximate location of the thyroid).

Absolute dose measurements were related to effective dose (E, mSv) as often reported in the literature according to $E = D_w \cdot L \cdot k_{\text{head}}$, where $D_w = 22.8$ mGy, the length of the scan, L, was taken as 23.67 cm, and the tissue weighting factor, $k_{\text{head}} = 0.0023$ mSv/mGy/cm, was taken from ICRP publication 103[228] for the head. This yielded an effective dose of 1.2 mSv, roughly one-third the dose of a typical MDCT head scan protocol.[185]

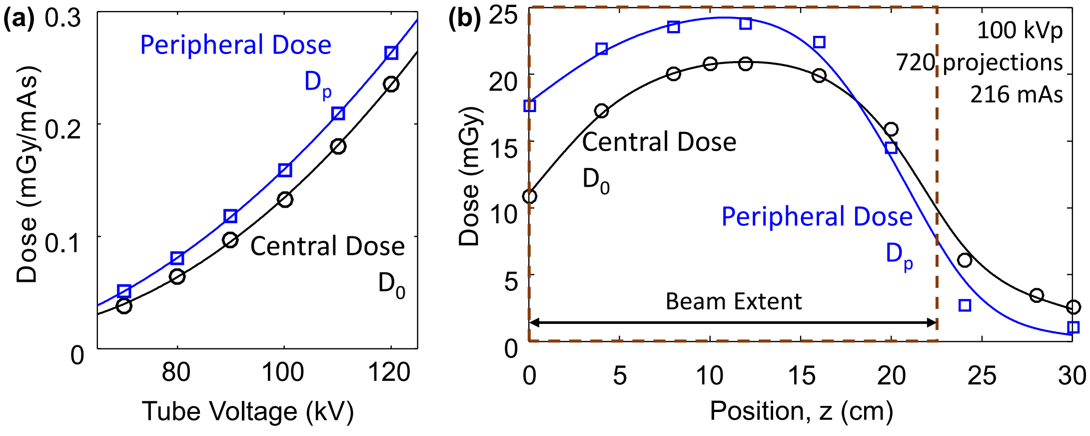

Figure 6.2. Dose measured as a function of (a) x-ray tube potential and (b) superior-inferior (z) position in a stack of CTDI phantoms. Location z = 0 cm corresponds to the crown of the skull and z = 30 cm the approximate location of the thyroid.

III.B Artifact Corrections

Figure 6.3(a-b) shows FBP reconstructions with and without artifact corrections. Prior to artifact correction, the image exhibited severe shading (t_{cup} = 13.5%), strong reduction in contrast (ΔHU = 39 HU, compared to true difference in attenuation, ~106 HU between acrylic and Rando material), and modest CNR (5.4). The artifact correction provided a strong improvement in uniformity (t_{cup} = -0.8%), boost in contrast (~92 HU) close to the true value, and an improvement in CNR (7.9) despite an increase in image noise (σ ~7 HU prior to correction, increased to ~12 HU after correction). A variety of other streak and shading artifacts were also visibly improved by the correction method—e.g., streaks attributed to beam hardening about the supraorbital ridge.

Figure 6.3c shows the same data reconstructed with PWLS after correction. The PWLS images exhibited comparable uniformity (t_{cup} = 0.4%) and contrast (~86 HU) and improved CNR (12.9) by virtue of reduced noise (σ ~7 HU), with parameters selected to match the spatial resolution with respect to the width of the acrylic sphere ESF—viz., for FPD (k_{filt} = 0.6 and a_{vox} = 0.5 mm) and for PWLS ($\beta = 10^{2.4}$, $\delta = 10^{-4}$, and a_{vox} = 0.5 mm). The results illustrate the benefit of artifact correction (which improved uniformity but somewhat amplified noise) combined with PWLS reconstruction (to mitigate the increase in noise).

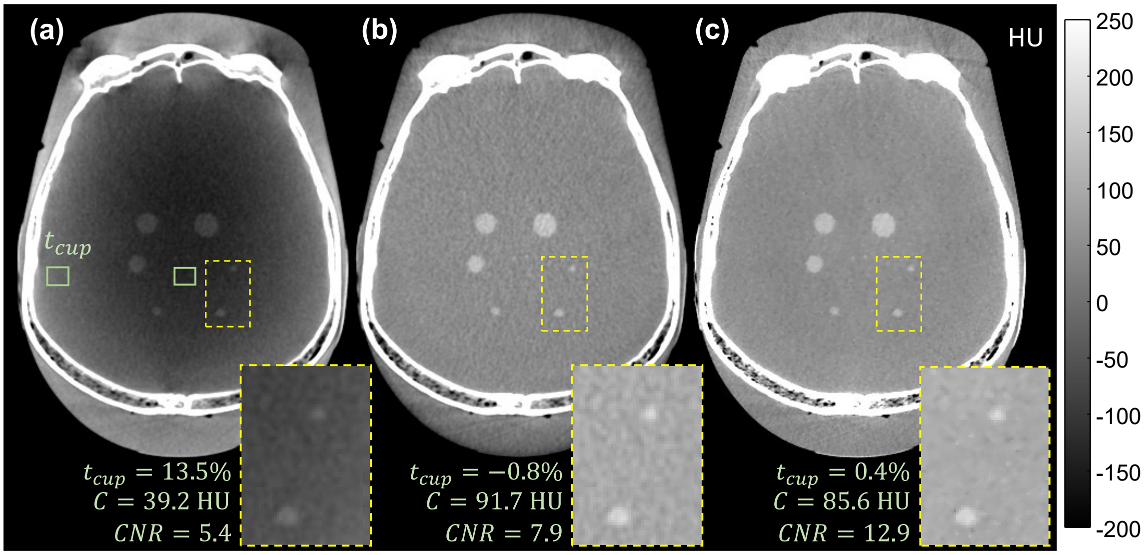

Figure 6.3. Comparison of (a) uncorrected and (b) artifact-corrected FBP image reconstructions. Note the reduction in cupping and restoration of contrast close to the true value (~92 HU for acrylic spheres) despite increase in noise. (c) Reconstruction using PWLS maintains the benefits of artifact correction and reduces noise (at matched spatial resolution).

III.C Contrast, Resolution, and Noise

Figure 6.4a shows the measured FWHM of the wire PSF for FBP (as a function of k_{filt}) and the FWHM associated with the low-contrast ESF for PWLS (as a function of β). The FBP reconstruction at the highest cutoff frequency ($k_{\text{filt}} > 0.8$) achieves slightly better spatial resolution than PWLS (with low regularization, $\log_{10}(\beta) < 1$) and supports the use of FBP for the sharp bone reconstruction protocol. Figure 6.4b shows the MTF for images reconstructed with the nominal FBP high-resolution ($k_{\text{filt}} = 1$, voxel size = 0.3 mm isotropic), FBP soft tissue ($k_{\text{filt}} = 0.5$, voxel size = 0.5 mm isotropic), and PWLS soft tissue ($\beta = 10^{2.6}$) protocols. As expected, the bone reconstruction protocol provides the highest MTF, while the nominal PWLS reconstruction (and soft-tissue FBP reconstruction, roughly spatial-frequency matched) exhibited reduced MTF associated with noise reduction.

Figure 6.4c shows the image noise measured as a function of cutoff frequency and regularization strength. The FBP images exhibit a simple monotonic increase in noise with cutoff frequency as expected. The PWLS images, on the other hand, exhibit a distinctly nonlinear dependence of noise on regularization, with the strongest noise reduction occurring in the range $\log_{10}(\beta) \approx 1.8$–$2.5$ (for δ fixed at 10^{-4} mm^{-1}). Considering Figs. 4a and 4c together, the benefit of PWLS for ICH imaging becomes evident: for example, taking $\log_{10}(\beta) = 2.6$ gives noise ~6.4 HU and FWHM ~1.1 mm; however, achieving the equivalent noise level in FBP via setting $k_{\text{filt}} = 0.5$ gives FWHM ~1.4 mm. The improved noise-resolution tradeoff for PWLS supports its use for the smooth low-contrast ICH reconstruction protocol.

Figure 6.4d shows the effect of detector readout gain mode on CNR and spatial resolution. Analysis of detector readout modes in Chapter 5 showed a ~15–20% increase in CNR from use of DG readout (with FBP reconstruction). At matched spatial resolution (insets showing $\beta = 10^{2.4}$ for DG and $\beta = 10^{2.6}$ for LG), a ~20% improvement in CNR can be observed in DG data compared to LG data using a PWLS reconstruction algorithm as well.

Figure 6.5 shows the effect of dose on spatial resolution and noise in PWLS image reconstructions. Figure 6.5a shows the region of the ICH-gelatin insert at low ($D_0 = 9.6$ mGy), nominal ($D_0 = 24.8$ mGy), and high ($D_0 = 38.2$ mGy) dose reconstructed with regularization ranging $\beta = 10^{1.6}$–$10^{2.8}$. Operation at the nominal dose and reconstruction parameters achieves clear visualization of small, ~50 HU contrast ICH. Figure 6.5b shows the spatial resolution measured as a function of β for the three dose levels. While the spatial resolution at low β is fairly similar among the three dose levels, the degree of smoothing increases more steeply for the lower dose images as β is increased. Similarly, Figure 6.5c shows the image noise as a function of β for the three dose levels, with the lower dose scenario again having a steeper tradeoff between noise and regularization.

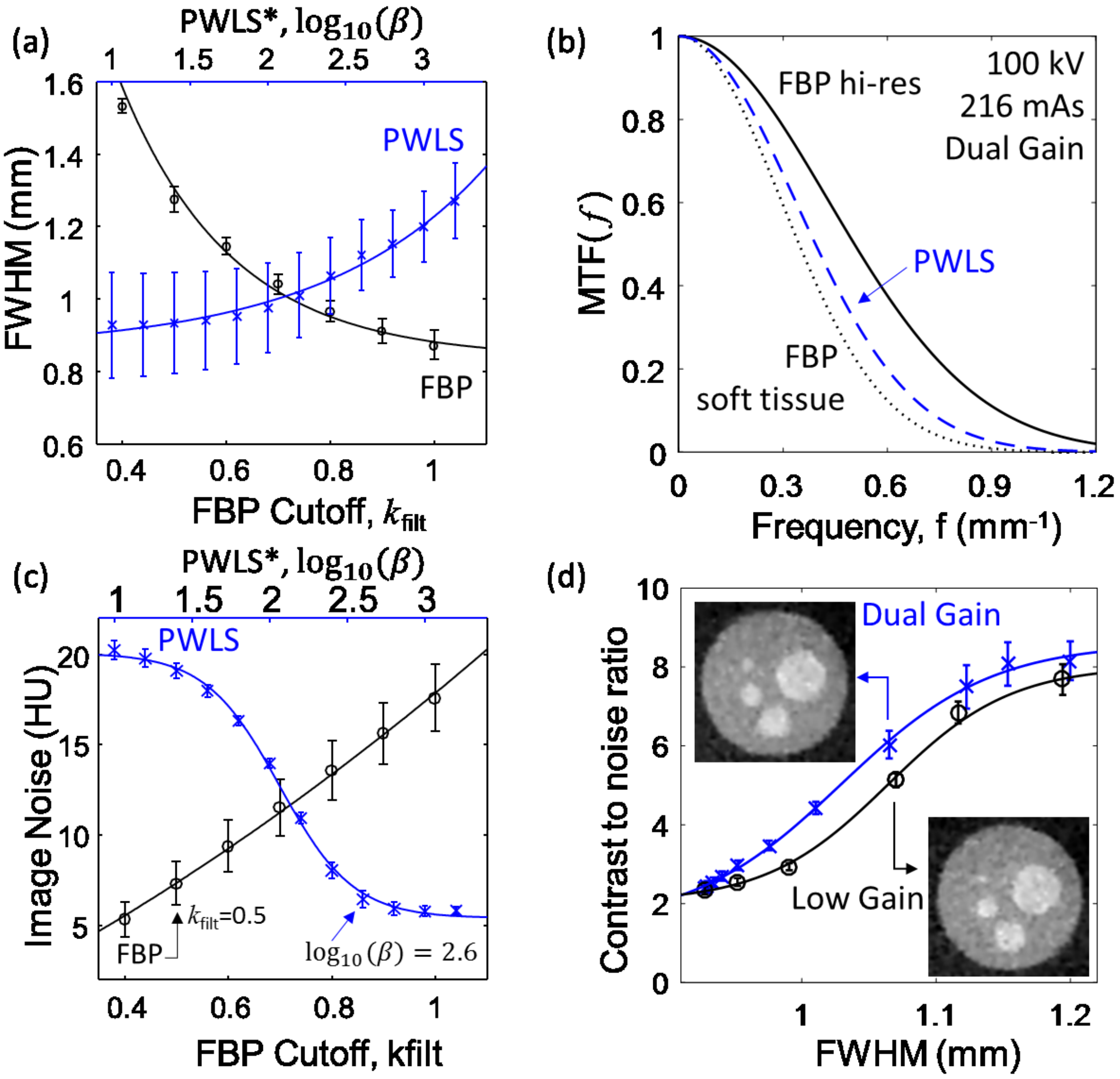

Figure 6.4. (a) Spatial resolution for FBP (FWHM of the wire PSF) and PWLS (FWHM associated with the low-contrast ESF) as a function of filter and regularization strength, respectively. (b) The MTF measured in image reconstructions for the nominal FBP high-resolution, soft tissue, and PWLS reconstruction protocols. (c) Image noise measured as a function of filter and regularization strength, illustrating the distinct noise-resolution tradeoff between the two reconstruction methods. (d) Dual gain readout mode shows up to 20% improved contrast to noise ratio at matched spatial resolution compared to LG readout mode when using PWLS image reconstruction.

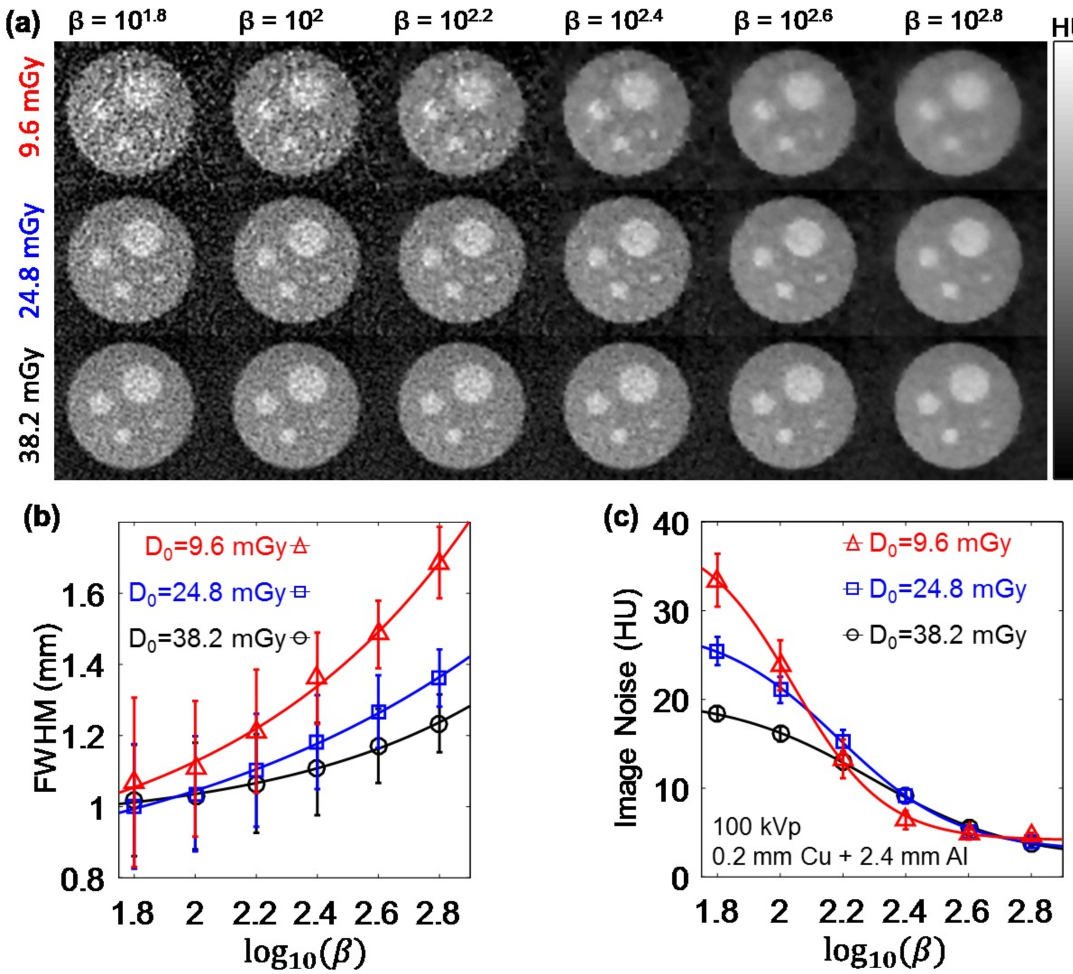

Figure 6.5. Visualization of simulated ICH. (a) PWLS image reconstructions of the gelatin-ICH insert at various levels of dose and regularization. (b) Spatial resolution exhibits a steeper dependence on regularization strength at low dose. (c) Image noise similarly has a stronger dependence on regularization strength at the lower dose level.

III.D Image Quality: Anatomical Features in Cadaver

Assessment of the cadaver images by a neuroradiologist rated performance for task (*i*) (visualization of bone details, cranial sutures, and possible fracture) as "conspicuous," citing clear visualization of sutures and other fine details in bone anatomy. Figure 6.6a shows an axial slice through the petrous bone using the high-resolution FBP reconstruction, demonstrating clear visualization of the stapes and cranial sutures. Figure 6.6b shows a surface rendering of the skull to further illustrate the uniform image quality characteristics supporting visualization of the coronal, lambdoid and sagittal cranial sutures. Overall, the visibility of fine bone details was considered excellent and superior to the MDCT image (recognizing that higher-resolution, higher-dose MDCT head scan protocols could certainly be employed).

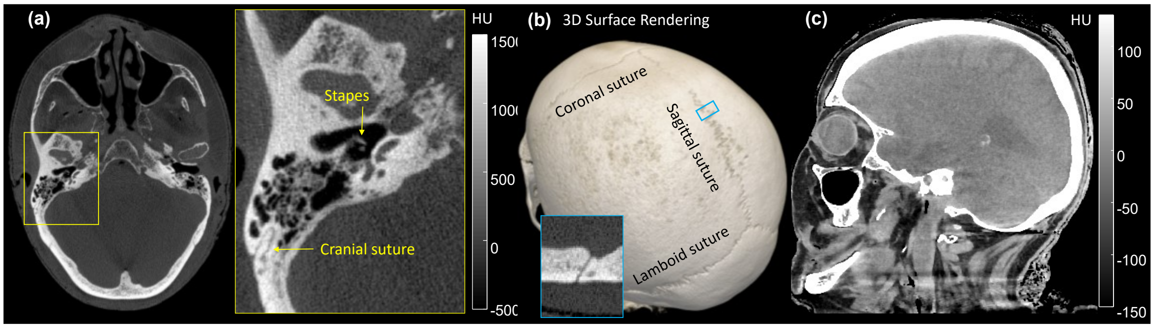

Figure 6.6. High-resolution CBCT reconstruction of the cadaver illustrating bone detail with insets showing (a) stapes and cranial sutures. (b) Surface rendering shows clear visualization of the sagittal and lambdoid sutures and suggests the ability to confidently detect fractures. (c) Soft-tissue visibility in the region of the neck for a PWLS image (muscle-fat window) demonstrating excellent visualization of fat, muscle, and glandular structures.

The images were similarly evaluated with respect to imaging tasks (*ii*)–(*v*) for assessment of low-contrast imaging performance. Figure 6.6c shows a soft-tissue PWLS image reconstruction demonstrating visualization of fat, muscle, and glandular structures that was rated by the neuroradiologist as "well visualized", although cone-beam artifacts arising from the occipital bone, mandible, and cervical vertebrae were potentially confounding in regions of the neck.

Figure 6.7 shows soft tissue reconstructions of the cadaver head (brain window, width = 90 HU). The neuroradiologist assessed the differentiation of CSF and brain [task (*ii*)] and visualization of midline shift [task (*iii*)—e.g., mass effect] as "well visualized." Visualization of the ICH [task (*iv*)—both small and large boluses] was rated as "conspicuous," especially in the PWLS image. Differentiation of gray and white matter [task (*v*)] was rated as "challenging," but was attributed primarily to post-mortem degradation of the tissue (also evident in the MDCT scan). To the extent that gray and white matter were distinguishable, visualization of the internal capsule (white matter surrounded by gray matter) was judged as comparable to the reference MDCT scan. The neuroradiologist noted the presence of cone-beam artifacts (e.g., posterior to the orbits and at the superior-most extent of the cranial vault) which, although visually distracting, did not affect evaluation of the tasks assessed in this study. Additionally, the radiologist remarked on the higher level of image noise in the CBCT images, due in large part to the lower imaging dose (~1/3 the dose of the MDCT images). Overall, task performance was rated superior for the PWLS reconstructions in comparison to FBP, but the slightly unfamiliar texture of the image noise in the PWLS images was noted as potentially distracting.

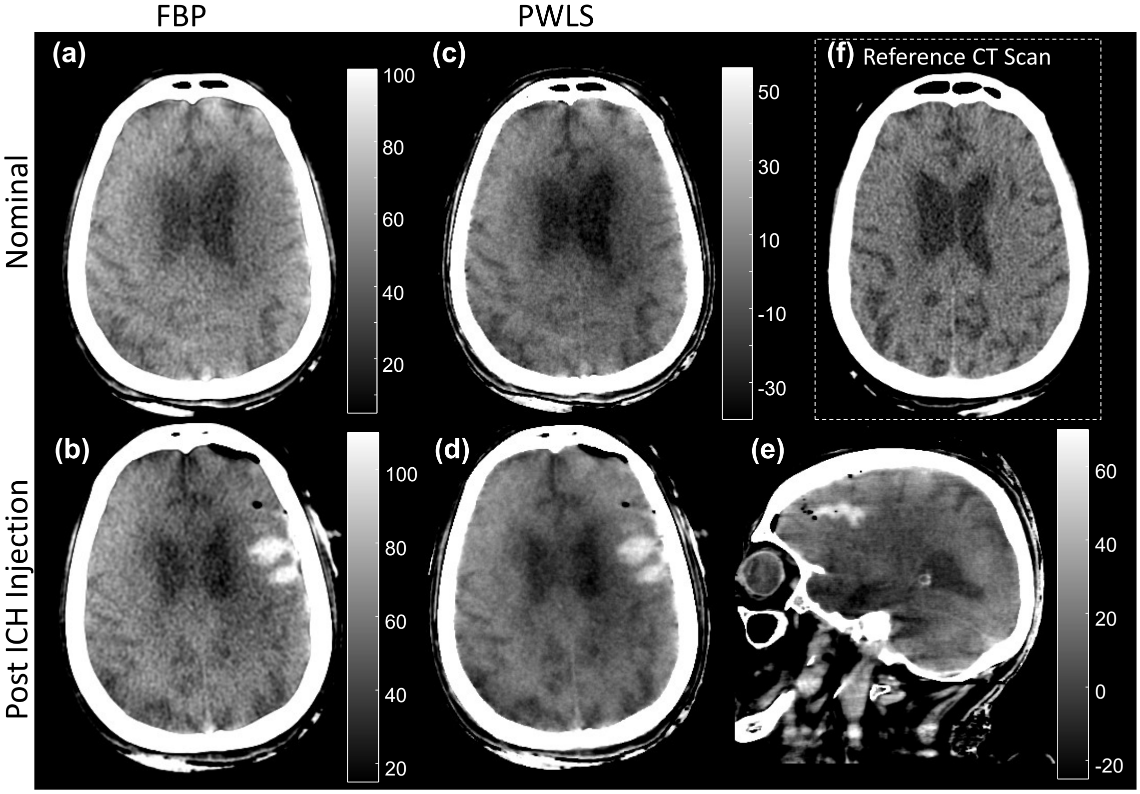

Figure 6.7. Cadaver images from the prototype CBCT head scanner (100 kV, 216 mAs, 22.8 mGy, 0.5×0.5×1.25 mm^3 voxels). (a-b) FBP images before and after injection of simulated ICH. (c-e) PWLS images before and after injection of simulated ICH. (f) MDCT scan acquired as a reference, using a standard clinical head scan protocol (120 kV, 500 mAs, 59.4 mGy dose, 0.42×0.42×1.0 mm^3 voxel size).

IV. Discussion and Conclusions

The imaging performance of a prototype CBCT system for point-of-care imaging of acute ICH was evaluated in terms of spatial resolution, contrast, noise, CNR, image uniformity, and dose, and image acquisition. Reconstruction protocols were identified for high-quality imaging of bone and soft tissue. Nominal scan protocols carried a dose of 22.8 mGy, which is approximately 1/3 the dose of a standard head MDCT scan (59.4 mGy for the standard head CT protocol in this study). The artifact correction methods addressed major factors of x-ray scatter, beam-hardening, image lag, and veiling glare, resulting in 0.4% nonuniformity in images of the head. High-resolution FBP reconstruction demonstrated ~0.9 mm PSF FWHM and excellent delineation of bone features (e.g., cranial sutures), and an edge-preserving PWLS method was shown to provide ICH CNR ~5.7 and conspicuous visualization of simulated ICH. A fresh cadaver imaged with and without simulated ICH demonstrated clear differentiation of CSF from gray-white matter and conspicuous delineation of hemorrhage.

The work reported above enables some level of comparison between the technical performance of the CBCT prototype to that of the current state of the art, taking the CS 9300 evaluated in Chapter 2 as exemplary and recognizing that the work was separated by approximately 4 years and did not employ identical experimental methods or imaging phantoms. Still, the conclusions of Chapter 2 indicated that a state-of-the-art, commercially available CBCT scanner did not provide imaging performance sufficient for reliable detection of ICH (though it was sufficient for its intended use in visualization of high-contrast bone architecture, including the sinuses and temporal bones). It is therefore worthwhile to reflect on the findings of Chapter 2 (for the CS 9300) in comparison to those of Chapter 6 (for the prototype head scanner) to the extent that a fair comparison can be made.

In terms of radiation dose, the nominal CS 9300 imaging protocol (S1 in Chapter 2) gave $D_w = 6.0\ \text{mGy}$. By comparison, the nominal scan protocol for the prototype (Protocol 1 in section II.B) yielded $D_w = 22.8\ \text{mGy}$. Differences in underlying imaging technique are numerous and account for the difference—for the CS-9300 and prototype, respectively: beam energy of 85 kV vs 100 kV; number of projections per scan = 372 vs 720; and 56 mAs vs 216 mAs. While the dose for the prototype is higher, both systems are operating near the upper limit of power (1.5 kW and 5 kW, respectively). In fact, recognizing that more subtle pathologies and better differentiation of gray-white matter would benefit from reduced image noise, the prototype could benefit from the ability to operate at even higher dose for certain indications. Compared to standard diagnostic head CT, these dose levels are still quantifiably low. A typical adult head CT scan protocol at Johns Hopkins Hospital (using the SOMATOM Definition AS, Siemens, Erlangen, Germany) involves the following technique: 120 kV, 380 mAs, 61.8 mGy CTDI_{vol}. It is also pertinent to compare the dose characteristic to that of the standard "Reference Level" for CT dose in the Adult Head. As reported by McNitt-Gray et al. in the AAPM 2011 summit on CT Dose, the standard Reference Level for CT of the Adult Head is 75 mGy.

In terms of spatial resolution, the S1 CS-9300 protocol was found to give a wire phantom MTF f50 (reconstructed using FBP) of 0.7 lp/mm. By comparison, the sharp bone FBP reconstruction protocol of the prototype gave MTF f50 of 0.6 lp/mm. High spatial-frequency and high contrast visualization with the CS 9300 petrous bone protocol and the prototype head scanner are illustrated in Figure 6.8 for similar regions of the anthropomorphic head phantom described in Figure 6.1c. In both scans, high-resolution visualization of bone structures were achieved.

In terms of contrast resolution, the S1 protocol for the CS 9300 yielded the best low-contrast visualization for that scanner. Fair, direct comparison to the noise and CNR is difficult, requiring not only a common test object but also carefully matched dose and spatial resolution. The variance for CT images is inversely proportional to the total dose (D_0) and the fourth power of the isotropic voxel size ($a_{xy}^3 a_z = a_{vox}^4$);[187, 229, 230] the CNR can therefore be roughly normalized by dividing by the square root of the these two factors, recognizing that reconstruction parameters (apodization, k_{filt}) have a further effect that is unaccounted. Coarse comparison as illustrated in Figure 6.8 suggests that the prototype improved the normalized CNR performance by 48% using FBP reconstruction in the largest ICH simulating sphere of the anthropomorphic phantom.

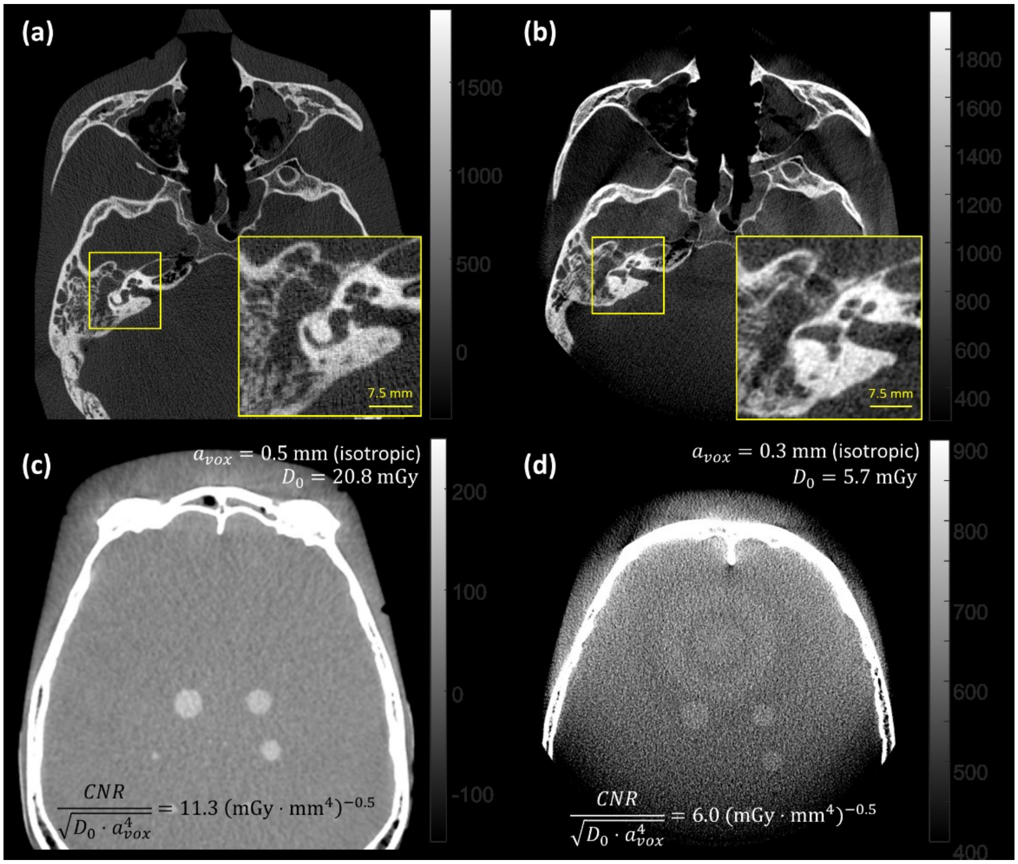

Figure 6.8. Comparison of high-resolution imaging in (a) the head scanner prototype and (b) the CS 9300. Soft tissue visualization is visibly improved for (c) the prototype compared to (d) the CS 9300. Recognizing strong differences in acquisition technique and dose, the CNR normalized by dose and voxel size accounts for the discrepancy to a certain extent and supports the conclusion regarding improved soft-tissue imaging performance for the prototype.

The technical assessment agreed with expectations based on previous modeling and laboratory benchtop experiments[179] as discussed in Chapters 4 & 5 and was a prerequisite to translation of the prototype to clinical studies. The work was also essential to determining key parameters that affect dose and scan speed, which are in turn determined by both the technique factors (kV and mAs) and FPD readout (number of views, frame rate, and readout gain mode). With respect to the latter, the assessment showed that while DG readout can improve CNR by ~15–20% at equivalent dose, the scan time (90 s for the nominal DG technique) is likely prohibitive for clinical use. We therefore worked with the FPD manufacturer to identify an alternative DG scan protocol with hardware binning at 4×4 pixels (cf., 2×2 hardware binning followed by another 2×2 in post-processing) to give a frame rate of 15 fps (cf., 8 fps). Further reduction in scan time was obtained by reducing the number of projections to 450 (cf., 720), since previous work[214] showed negligible increase in noise due to view sampling effects. The mAs per projection was increased to 0.48 mAs, yielding scan time of 30 s and equivalent dose, as shown in the clinical protocol in Table 6.1. Future work will evaluate image quality associated with a half-scan orbit (180° + fan angle) to further increase scan speed. The analysis and resulting scan protocols supported translation of the system to clinical studies.

As discussed in Chapter 1, bringing CT imaging capability to the point of care could offer major benefit to critically ill patients in areas such as the NCCU, ICU, and PACU. Mobile MDCT systems such as the CereTom (Neurologica, Danvers MA, USA) have the potential to address this need as well, and while CBCT offers possible advantages of cost, open geometry, patient access, mechanical simplicity, and capability for radiography / fluoroscopy, both types of system warrant further development and clinical evaluation for this important clinical problem. A fairly early version of the CereTom system (circa 2006) was tested at our institution for application in the NCCU and was judged to have image quality that was insufficient for ICH detection, noting poor spatial resolution associated with thick slices as well as cumbersome setup in the small, closed gantry bore. [Private communication, Dr. Robert Stevens, Department of Anesthesia and Critical Care, Johns Hopkins Hospital.] While other mobile CBCT systems, such as the Vario C-arm (Ziehm Imaging, Nurnberg, Germany) and O-arm (Medtronic, Dublin, Ireland), may also be applicable, the imaging performance for such systems has been conventionally limited to high-contrast (bone) visualization. The system evaluated in this work overcame such conventional limitations through a combination of system design, artifact correction, and MBIR methods developed specifically for high-quality imaging of head injury.

Chapter 7: Summary and Conclusions

I. An Imaging Physics Based Approach to System Design

X-ray imaging of the head is important for a number of clinical diagnostic tasks in otolaryngology and neurology, discussed in Chapter 1. Many of these tasks require high-fidelity visualization of structures with small feature size and/or low contrast. Imaging systems are information transfer systems, and as such, introduce spatial blur, quantum and additive electronics noise, and artifacts (discussed in Chapter 1) that can confound the diagnosis. Careful, quantitative design of such systems—with knowledge of the specific diagnostic task—can optimize the tradeoffs in imaging performance and is especially important for CBCT systems, which typically have higher levels of noise and artifact due to hardware and geometry. Each step of the imaging chain, from x-ray photon interaction to signal readout and digitization, can be modeled as a gain, blur, sampling, additive noise, or thresholding (for PCDs) stage, and the effect of each on imaging performance can be analytically derived or approximated. In this thesis, a point-of-care CBCT system with imaging performance sufficient for high-quality imaging of the head was designed using such a physics-based analytical approach.

II. Landscape of CBCT Head Imaging

A rigorous technical assessment of imaging performance (Chapter 2) was performed for an existing CBCT head scanner, the CS 9300, as a first step towards the design of a new CBCT head imaging system. The assessment of spatial resolution, contrast detail visualization, and dosimetric properties indicated that dedicated OHNS and maxillofacial scanners excelled in high-spatial-resolution imaging performance and identified a number of improvements necessary for soft-tissue visualization in high-quality head imaging. The prevalence, relatively low cost, and compact design of such systems are generally suitable for point-of-care imaging devices, indicating a promising path forward for development of a high-quality CBCT scanner dedicated to imaging of the head.

III. Photon Counting Detectors: Pulse Shaping the Future?

Advances in x-ray detection technology show potential for significant improvements to additive electronics noise and readout speed. In Chapter 3, a new imaging performance model of PCDs was developed and validated with the goal of assessing the general usefulness of such detectors for improving low-contrast visualization. The model is able to predict imaging performance metrics of MTF, NPS, DQE, mean signal gain, charge sharing occurrence, and energy resolution, and is a first step towards quantitative comparison of PCDs with EIDs such as FPDs and CMOS detectors (discussed in Chapter 4 and 5). A hypothetical comparison of a Si-strip PCD to an identical EID (without an energy threshold) indicated advantages for PCDs in low dose and/or high additive noise regimes—for example, at the nominal additive electronics noise level for the PCD ($\sigma_{add} = 200\ \mathrm{e}^{-}$), an exposure per pulse at the detector of < 0.5 μR (behind the object) is needed for PCD operation to be advantageous (at 35 kV). A higher additive electronics noise level ($\sigma_{add} = 2000\ \mathrm{e}^{-}$) more typical of FPD performance indicates that thresholding (for this Si-strip detector) becomes advantageous at exposure < 7 μR per pulse.

For PCDs, Compton interactions can be a major confounding factor, shifting part of the interaction energy spectrum to a lower energy difficult to distinguish from additive noise or charge sharing events by thresholding alone. For the Si-strip PCD, Compton interactions comprised ~20% of all detector interactions at 70 kV and was the main reason that EID performance compared so favorably with thresholding performance. In CdZnTe PCDs, as well as other high-Z PCDs currently under development, Compton interactions may comprise a smaller fraction of the total interactions, allowing better separation of Compton events from additive noise and charge sharing. Additionally, as pixel sizes decrease and pulse pile-up correction methods are developed, charge sharing will start to become a greater limiting factor on PCD performance, corrected in part with coincidence rejection circuitry. A number of technological improvements can be beneficial for the integration of PCDs in CBCT systems: increased FOV (currently limited by wafer size and imperfections in manufacturing), higher detection efficiency (high-Z detector materials are currently under development), lower cost, and smaller size (more efficient on-pixel processing). Of these, perhaps the most important is FOV, which is also a limiting factor for CMOS detectors.

IV. System Optimization Using an Image Quality Model

Many factors beyond detector technology—such as geometric configuration and x-ray source power—are also important considerations for a practical point-of-care CBCT system. As discussed in Chapter 4, the CBCT prototype system was designed with the task-based detectability index as a figure of merit. The model predictions of MTF and NPS as a function of system configuration was combined with Fourier-domain task functions (representing a small ICH and a fracture) and used to optimize tradeoffs between, for example, x-ray focal spot size, geometric magnification, and scatter air gap rejection. Field of view limitations on new detector technologies, such as PCDs and CMOS detectors, motivated the inclusion of a large-area FPD (43×43 cm^2) in the initial prototype.

The prototype CBCT system would, however, benefit from further mechanical optimization for deployment at the point of care. Initial design constraints imposed a large, open bore for ease of patient positioning and adaptability for deployment in various environments during the initial clinical studies. Areas such as the NCCU and ICU are typically fast-paced and limited on space, motivating a more compact, mobile system and specialized patient positioning attachments in the next cycle of design. Of course, as constraints change on size and available power, the design approach presented in Chapter 4 can be repeated as necessary to recompute the optimal configuration of source, detector, etc.

V. Extending the Performance of FPDs

As discussed in Chapter 2, a low-powered (dose limited), portable CBCT system would benefit from inclusion of low-additive-noise detectors. FPDs tend to have relatively high levels of additive electronics noise (compared to PCDs and CMOS detectors), but were chosen for the first prototype due to FOV constraints. Chapter 5 investigated methods to reduce the relative contribution of detector additive electronics noise in FPDs by increasing the readout gain. Image quality measurements in high-gain detector readout mode (at the nominal head scanner protocol identified in Chapter 4) indicated a ~15% improvement in CNR was feasible over typical low-gain readout. HG readout without skin-line saturation was evaluated using both dual-gain readout and a series of pre-patient bowtie filters. Results indicated DG readout as the option providing the best compromise between reduced digitization noise and ease of implementation.

The analysis in Chapter 5 additionally presented several important considerations for the future of low-additive-noise detector design. Digitization noise can become a large contributing factor in 14-bit readout, especially at low gain. As interest in CMOS detectors for use in high-performance CBCT systems increases, the tradeoffs between dynamic range and digitization noise may become an important factor. Single-gain CMOS detectors operating at low well potential (small dynamic range and low additive noise) may find benefit from systems with bowtie filters. However, such filters often impart low-contrast artifacts that may be difficult to completely correct—although an analytical algorithm was presented in Chapter 5 that accomplishes fairly good correction of such “dome” artifacts.

VI. High-Performance CBCT Prototype for Head Imaging

Chapter 6 described the performance assessment of the prototype CBCT head scanner (with design motivated by the work in Chapter 4) in both phantoms and cadaver as a prerequisite for clinical studies. The cadaver was imaged prior to ICH injection in both the prototype system and a MDCT system. The images were assessed by a fellowship-trained neuroradiologist and showed conspicuous visualization of fresh ICH and fractures, with promising ability for gray-white matter differentiation and ventricle/CSF delineation. The assessment also indicated that the imaging dose of the nominal protocol (nearly 1/3 that of standard head protocols) might be a limiting factor for this system. Additionally, for such low-contrast visualization tasks, cone-beam artifacts near the top of the cranium were identified as a large source of residual artifact that lowered diagnostic confidence in the absence of a prior MDCT image.

Further development is underway to address the residual artifacts and increase the power output (and imaging dose) of the system. However, due to the relatively low imaging dose and high noise of the images, model-based image reconstruction techniques (with an edge-preserving penalty) were chosen as the nominal reconstruction algorithm for this prototype. The radiologist assessment of such reconstructions (in comparison to more standard FBP images) was favorable for ICH detection but cited “visually unpleasant” appearance of noise texture. This is an issue of some importance for model based reconstruction techniques, and is largely a result of foreign noise textures with high variability in correlation and appearance between algorithms with different statistical weighting and regularization design. Such variability presents a challenge for moving forward into clinical practice, and a mutual effort—from both engineers and radiologists—can facilitate clinical adoption.

VII. Looking Forward: Future Clinical Applications

The CBCT prototype presented in this thesis was initially designed specifically for ICH and fracture visualization—as indicated by the task functions presented in Chapter 4. However, a combination of system design optimization, artifact correction methods,[158] and advanced reconstruction algorithms[161] have culminated in a CBCT system with excellent imaging performance that may be suitable for a number of clinical tasks. In line with the goal of high-quality head imaging, stroke imaging—with time-sensitive requirements for intervention—would benefit from a CBCT system deployed at the point of care capable of non-contrast ICH imaging as well as perfusion and angiography. Increasing interest in 'one-stop' stroke diagnosis and intervention[231, 232] is motivated by the need for rapid diagnosis and treatment in emergent, ambulatory, and/or critical care units. Another potential area of deployment is in the image-guided surgical suite, with improved soft-tissue visualization benefiting guidance of neurosurgical applications in, for example, hydrocephalus shunt placement, tumor resection, minimally invasive ablative technique, biopsy, and placement of electrodes. In this setting, the prototype system could provide a major advance in surgical precision as the basis for preoperative (MRI or MDCT) registration and 3D-2D guidance and presents a valuable means of validation / QA at the end of the case – allowing visualization of the brain tissues (gray-white matter and ventricles), surgical product (e.g., device placement or region of resection), and possible complication (ICH)—with the ability to revise immediately if necessary.

Appendix A: Photoelectric and Compton Interactions in a Si-Strip PCD

The spectrum at stage 1 (Section II.A of Chapter 3) includes the combined effects of photoelectric absorption and Compton scattering according to the ratio of their cross section to the total cross section. K-fluorescence effects were not considered in the current model, because the effect is negligible for the detector material (Si) used in the PCD in this work. The photoelectric and Compton cross sections and the resulting distributions of interacting photons (q_1) are shown in Figure A.1. For a photoelectric interaction, the spectrum of interacting photons (i.e., the probability of interaction at energy, E) is:

$$q_{1PE}\left(E \mid q_0^{\text{norm}}(E)\right)=q_1\left(E \mid PE, q_0^{\text{norm}}(E)\right)=q_0^{\text{norm}}(E)\left(1-\exp\left[-\mu(E)\,a_z\right]\right) \qquad \text{(A.1)}$$

where $\mu(E)$ is the energy-dependent attenuation coefficient of the detector material, and a_z is the thickness of the detector in the z direction as illustrated in shown in Figure A.2.

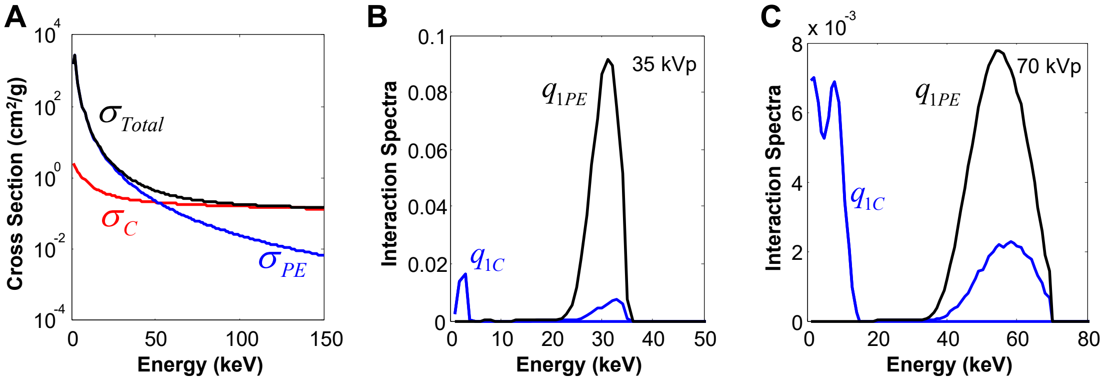

Figure A.1. Photoelectric and Compton interactions. (A) The cross section for photoelectric and Compton interactions was derived from the NIST XCOM database. (B) The spectrum of Compton (q_{1C}) and photoelectric (q_{1PE}) interactions calculated for a 35 kV beam. (C) The same as (B) for a 70 kV beam.

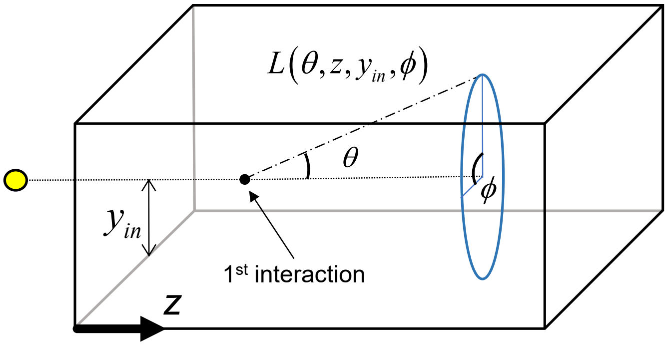

Figure A.2. Illustration of the scattering geometry in an edge-on silicon strip detector. The photon is incident in the z direction. Pixel readout occurs along the x direction. The scatter angle is shown as θ and the azimuthal angle is shown as ϕ. The total pathlength in the material available to the photon after a Compton interaction is given by L, and the incident y position is denoted y_{in}.

For a Compton interaction, there are two scenarios for energy deposition in the detector – one in which the scattered photon escapes the detector and one in which the scattered photon is reabsorbed. In each case, the initial scattering event deposits an amount of energy, E_p, determined by the incident energy E_{in} and the scattering angle θ. The scattered photon has energy $E' = E_{in} - E_p$ and may undergo a second interaction or escape the detector. The spectrum resulting from a Compton interaction can be written as a Bayesian expectation over all incident energies, interaction depths z, and scattering angles:

$$\begin{aligned} q_{1C}(E) &= q_1\left(E \mid C, q_0^{\mathrm{norm}}(E)\right) \\ &= \int_0^{\infty}\int_0^{a_z}\int_0^{\pi} p\left(E \mid \theta, \mathrm{z}, E_{\mathrm{in}}\right) p\left(\theta \mid E_{\mathrm{in}}\right) p\left(z \mid E_{\mathrm{in}}\right) p\left(E_{\mathrm{in}}\right) \mathrm{d}\theta \mathrm{d}z \mathrm{d}E_{\mathrm{in}} \end{aligned} \tag{A.2}$$

with the likelihood of an incident photon having energy E_{in} equal to the normalized spectrum incident on the detector:

$$p\left(E_{\mathrm{in}}\right) = q_0^{\mathrm{norm}}\left(E_{\mathrm{in}}\right) \tag{A.3}$$

The likelihood of interaction at depth z is equal to the marginal probability of interaction (quantum efficiency):

$$p\left(z \mid E_{\mathrm{in}}\right) = \frac{\mathrm{d}}{\mathrm{d}z}\left(1 - \exp\left[-\mu\left(E_{\mathrm{in}}\right) z\right]\right) = \mu\left(E_{\mathrm{in}}\right) \exp\left[-\mu\left(E_{\mathrm{in}}\right) z\right] \tag{A.4}$$

The likelihood of the incident photon scattering at angle θ is computed from the Klein-Nishina equation according to the relative differential cross section, $\frac{\mathrm{d}\sigma_c}{\mathrm{d}\theta}$:

$$\frac{\mathrm{d}\sigma_C}{\mathrm{d}\theta}(\theta)=\pi\alpha^2 r_c^2\sin(\theta)\left(\frac{E'(E_{\mathrm{in}},\theta)}{E_{\mathrm{in}}}\right)^2\left[\frac{E'(E_{\mathrm{in}},\theta)}{E_{\mathrm{in}}}+\frac{E_{\mathrm{in}}}{E'(E_{\mathrm{in}},\theta)}-1+\cos^2\theta\right] \quad \text{(A.5)}$$

with α equal to the fine structure constant, $r_c = \hbar/m_e c$ the reduced Compton wavelength of an electron, and $m_e c^2$ equal to the mass of an electron, and the energy of the scattered photon given by:

$$E'(E_{\mathrm{in}},\theta)=E_{\mathrm{in}}\left[1+\frac{E_A}{m_e c^2}(1-\cos\theta)\right]^{-1} \quad \text{(A.6)}$$

The probability of an x-ray of energy E_{in} scattering at angle θ is therefore:

$$p(\theta\,|\,E_{\mathrm{in}})=\frac{\frac{\mathrm{d}\sigma_C}{\mathrm{d}\theta}(\theta)}{\int_0^{\pi}\frac{\mathrm{d}\sigma_C}{\mathrm{d}\theta}(\theta)\,\mathrm{d}\theta} \quad \text{(A.7)}$$

For a given scattering angle and incident energy, the probability distribution is therefore:

$$p(E\,|\,\theta,\mathrm{z},E_{\mathrm{in}})=\left(1-p_A(\theta,\mathrm{z},E_{\mathrm{in}})\right)\delta\left(E-E_p(\theta,E_{\mathrm{in}})\right)+p_A(\theta,\mathrm{z},E_{\mathrm{in}})\,\delta(E-E_{\mathrm{in}}) \quad \text{(A.8)}$$

where $p_A(\theta,z,E_{\mathrm{in}})$ is the chance that the scattered photon is absorbed before it exits the detector:

$$p_A(\theta,z,E_{\mathrm{in}})=1-\exp\left[-\mu\left(E'(\theta,E_{\mathrm{in}})\right)L(z,\theta)\right] \quad \text{(A.9)}$$

The mean pathlength, $L(z,\theta)$, available to the scattered photon is determined by the scattering angle, θ, and the depth of interaction, z, as:

$$
\begin{aligned}
L(z,\theta) &= \iint \min\left(\frac{y_{in}}{\sin\phi\sin\theta},\frac{z_D(\theta)}{\cos(\theta)}\right) p(y_{\mathrm{in}})\,p(\phi)\,\mathrm{d}y_{\mathrm{in}}\mathrm{d}\phi \\
&= \frac{1}{a_y\pi}\int_0^{\pi}\int_0^{a_y} \min\left(\frac{y_{\mathrm{in}}}{\sin\phi\sin\theta},\frac{z_D(\theta)}{\cos(\theta)}\right)\mathrm{d}y_{\mathrm{in}}\mathrm{d}\phi
\end{aligned}
\tag{A.10}
$$

Note that $L(z,\theta)$ is the pathlength, with the azimuthal angle ϕ uniformly distributed over 2π and incident y position uniformly distributed over $y_{\mathrm{in}} \in [0, a_y]$. The min function selects the shorter pathlength, as L is bounded by the y-dimension of the detector (absorption in septum) or the depth of the detector (exit through distal aspect). Because the pathlength is symmetric in y from either the bottom or the top of the detector, a range of $\phi \in [0, \pi]$ was used and the probability was multiplied by two. The available distance in the z direction (z_D) is determined by the scatter angle:

$$
z_D(\theta) = \begin{cases} a_z - z, & \theta \in \left[0, \pi/2\right) \\ -z, & \theta \in \left(\pi/2, \pi\right) \\ \infty, & \theta = \pi/2 \end{cases}
\tag{A.11}
$$

For a 70 kV beam and the detector used in this work, the fraction of interactions due to Compton scatter is $(\sigma_C/\sigma_{total})$ ~40%, and of those Compton interactions, only 8% are reabsorbed before exiting the detector. Therefore, only a small portion (~3%) of detected photons will have undergone spatial relocation due to Compton scattering. The model can be extended to include a parallel cascade describing the spatial relocation associated with such secondary Compton interactions, as previously done for K-fluorescence.

Since the proportion of such secondary reabsorptions was small for the system considered, we did not include the spatial effect of Compton relocation in the current work, though we did include their contribution to the total energy deposited. This approximation can be considered an upper bound for the contribution of scattered secondary photons over the range of design parameters considered. As the mean energy is reduced, the percent of photons undergoing Compton interactions is reduced compared to those undergoing photoelectric interaction ($\sigma_{PE} >> \sigma_C$). While an increase in the detector thickness (a_z) would reduce the number of scattered photons lost to the distal aspect, in the regime of detector thickness much greater than detector aperture ($a_z >> a_y$), this increase is very small as most of these photons are lost through the *x-z* plane. Finally, a change in detector material (to a material with higher atomic number, such as CdTe detectors) would also reduce the fraction of photons undergoing Compton interactions. For alternative PCD systems or geometries for which the contribution of secondary scattered photons is appreciable, a parallel cascade can be introduced to include the spatial relocation stage (similar to stage 3) with separate branches for photoelectric interaction, single Compton interaction, secondary Compton interaction, etc. This parallel cascade would then be recombined at stage 5.

Appendix B: Effect of Scatter Correction on Contrast, Noise, and Detectability Index

Previous work[158] showed the importance of accurate scatter correction for high-quality CBCT of the head—essential to achieve CT number accuracy, image uniformity, and restore image contrast to the true subject contrast. It is generally recognized that x-ray scatter reduces contrast [viz., by a factor (1/1+SPR)], and its effect on image noise can be complicated, but tends to reduce quantum noise simply in proportion to the total fluence (indiscriminate of primary or scattered photons) as described in Sisniega et al.[162] It is also recognized that scatter correction typically amplifies image noise—e.g., a 2.2-fold increase in quantum noise following MC scatter correction of head CBCT.[158] The Appendix below analyzes these points within the framework of cascaded systems analysis and shows that scatter correction does not affect *d'* within the strict interpretation of local detectability index.

The total mean fluence incident on the detector, $\bar{q}_0^{S+P}$, is composed of the mean primary fluence $\bar{q}_0^P$ and the mean scatter fluence ($\bar{q}_0^S$), each estimated according to the Neitzel air gap model and the spektr implementation[133] of TASMIP[134]. Scatter correction typically involves an estimate of the scatter fluence subtracted from the projection data prior to log normalization, application of the ramp filter, etc. Subtraction of the scatter fluence estimate reduces the mean of the projection signal but does not affect the variance inherent in the measurement. For the log normalization step, previous work[32] showed that the noise in the projection data is reduced by the square of the mean signal; therefore, log normalization gives:

$$S_9\left(f_u, f_v\right) = \frac{1}{\left[\left(\bar{q}_0^P + \bar{q}_0^S\right)\Gamma\right]^2} S_8\left(f_u, f_v\right) \tag{B.1}$$

where S_9 is the NPS of the log-normalized 2D projection image, Γ is the detector gain, and S_8 is the projection image NPS (without scatter correction). Consider scatter correction in which the estimated scatter fluence (to be subtracted) is $\hat{q}_0^S$. The relative error in the scatter fluence estimate can be written:

$$c_s = 1 - \frac{\hat{q}_0^S}{\bar{q}_0^S} \tag{B.2}$$

where $c_S = 0$ corresponds to a perfect estimate of the mean scatter fluence; $c_s < 0$ implies overestimation of the mean scatter fluence; and $c_S = 1$ is equivalent to no scatter correction. The residual scatter fluence in the scatter-corrected data is therefore $c_S \bar{q}_0^S$. The NPS of scatter-corrected, log-normalized projection data is:

$$S_9^C\left(f_u, f_v\right) = \frac{1}{\left[\left(\bar{q}_0^P + c_S \bar{q}_0^S\right)\Gamma\right]^2} S_8\left(f_u, f_v\right) \tag{B.3}$$

The ratio of the 3D NPS of scatter-corrected image data (NPS^C) to that in uncorrected data can then be written:

$$\begin{aligned} \frac{\mathrm{NPS}^C\left(f, f_z\right)}{\mathrm{NPS}\left(f, f_z\right)} &= \frac{\left[S_9{}^C\left(\mathbf{f}\right) T_{11}^2\left(\mathbf{f}\right) T_{12}^2\left(\mathbf{f}\right)\right] *** \mathrm{III}_{15}\left(\mathbf{f}\right)}{\left[S_9\left(\mathbf{f}\right) T_{11}^2\left(\mathbf{f}\right) T_{12}^2\left(\mathbf{f}\right)\right] *** \mathrm{III}_{15}\left(\mathbf{f}\right)} \\ &= \left(\frac{\bar{q}_0{}^P + \bar{q}_0^S}{\bar{q}_0{}^P + c_s \bar{q}_0^S}\right)^2 = \left(\frac{1+\mathrm{SPR}}{1 + c_s \mathrm{SPR}}\right)^2 \end{aligned} \tag{B.4}$$

where S_9^C and S_9 differ only by a scalar, indicating that the NPS (variance) in a perfectly scatter-corrected image is greater than that in the uncorrected image by a factor of $(1+\mathrm{SPR})^2$.

In addition to reducing the mean signal, subtraction of the scatter fluence also recovers contrast in the image; this is reflected in the contrast term (or signal power) of the task function as:

$$C_{\text{task}}^C = \frac{C_{\text{true}}}{1 + c_s \mathrm{SPR}} \tag{B.5}$$

where we see that perfect scatter correction yields image contrast $\left(C_{\text{task}}^C\right)$ equal to the true subject contrast $\left(C_{\text{true}} = \Delta\mu\right)$. The frequency content of the task function is unchanged, so the task function associated with scatter-corrected data is $W_{\text{task}}^C = C_{\text{task}}^C F_{\text{task}}^C = C_{\text{task}}^C F_{\text{task}}$. We furthermore assume that scatter correction does not change the system MTF or the frequency dependence of the NPS, including aliasing effects associated with sampling. The changes in contrast and noise induced by scatter correction can be incorporated in the detectability index for a scatter-corrected image as follows:

$$
\begin{aligned}
d'^2_{\text{corrected}} &= \frac{\left[\iiint \mathrm{MTF}^2 \cdot \left(\mathrm{W}_{\text{task}}^{C}\right)^2 \mathbf{df}\right]^2}{\iiint \mathrm{NPS}^{C} \cdot \mathrm{MTF}^2 \cdot \left(\mathrm{W}_{\text{task}}^{C}\right)^2 \mathbf{df}} \\
&= \frac{\left(C_{\text{task}}^{C}\right)^4}{\left(C_{\text{task}}^{C}\right)^2} \cdot \frac{\left[\iiint \mathrm{MTF}^2 \cdot F_{\text{task}}^2 \mathbf{df}\right]^2}{\iiint \left(\dfrac{1+\mathrm{SPR}}{1+c_s\mathrm{SPR}}\right)^2 \mathrm{NPS} \cdot \mathrm{MTF}^2 \cdot F_{\text{task}}^2 \mathbf{df}} \\
&= \frac{C_{\text{true}}^2}{\left(1+c_s\mathrm{SPR}\right)^2} \cdot \frac{1}{\left(\dfrac{1+\mathrm{SPR}}{1+c_s\mathrm{SPR}}\right)^2} \cdot \frac{\left[\iiint \mathrm{MTF}^2 \cdot F_{\text{task}}^2 \mathbf{df}\right]^2}{\iiint \mathrm{NPS} \cdot \mathrm{MTF}^2 \cdot F_{\text{task}}^2 \mathbf{df}} \\
&= \frac{C_{\text{true}}^2}{\left(1+\mathrm{SPR}\right)^2} \cdot \frac{\left[\iiint \mathrm{MTF}^2 \cdot F_{\text{task}}^2 \mathbf{df}\right]^2}{\iiint \mathrm{NPS} \cdot \mathrm{MTF}^2 \cdot F_{\text{task}}^2 \mathbf{df}} \\
&= C_{\text{task}}^2 \cdot \frac{\left[\iiint \mathrm{MTF}^2 \cdot F_{\text{task}}^2 \mathbf{df}\right]^2}{\iiint \mathrm{NPS} \cdot \mathrm{MTF}^2 \cdot F_{\text{task}}^2 \mathbf{df}} \\
&= \frac{\left(C_{\text{task}}^2\right)^2}{C_{\text{task}}^2} \cdot \frac{\left[\iiint \mathrm{MTF}^2 \cdot F_{\text{task}}^2 \mathbf{df}\right]^2}{\iiint \mathrm{NPS} \cdot \mathrm{MTF}^2 \cdot F_{\text{task}}^2 \mathbf{df}} \\
&= \frac{\left[\iiint \mathrm{MTF}^2 \cdot \mathrm{W}_{\text{task}}^2 \mathbf{df}\right]^2}{\iiint \mathrm{NPS} \cdot \mathrm{MTF}^2 \cdot \mathrm{W}_{\text{task}}^2 \mathbf{df}} = d'^2
\end{aligned}
\tag{B.6}
$$

Therefore, the detectability index in a scatter-corrected image is equivalent to that in the uncorrected image – i.e., scatter correction does not affect local detectability index.

To verify this result, a simulation was performed with a digital phantom consisting of a cylinder of water containing a semicircular adipose disk shown in Figure B.1. Noise-free forward projections were computed over 360°, and a constant scatter fluence equivalent to SPR = 2 behind the cylinder was added to each projection image. Poisson noise was then added according to the mean number of (primary + scatter) photons at each pixel. Reconstruction was performed with the nominal parameters in Table 6.1 to yield the uncorrected image in Figure B.1a. Scatter-corrected images were formed by subtracting the mean scatter fluence from the noisy projections (before log normalization) and reconstructing with the same parameters, yielding the image in Figure B.1b.

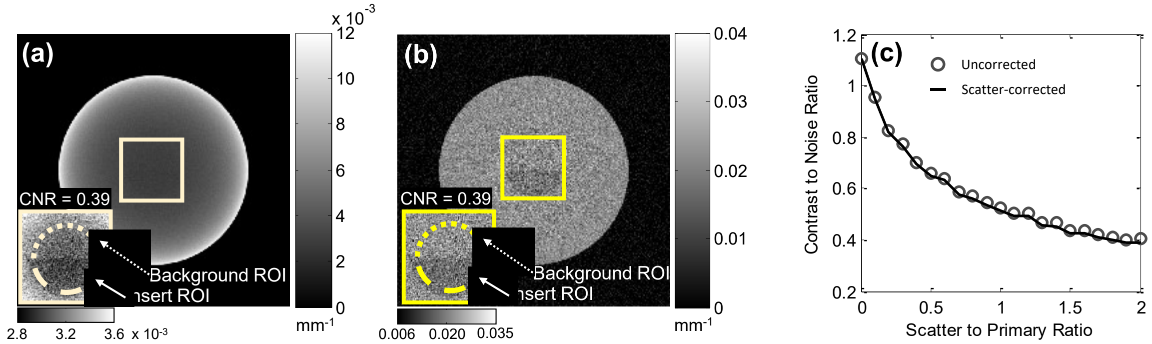

Figure B.1. Simulation / verification of the effect of scatter correction on noise, contrast, and local detectability index. (a) Uncorrected and (b) scatter-corrected axial image reconstructions (SPR = 2). Zoomed inset images were separately windowed (with level equal to the local mean and window width 3 times the local noise) to illustrate visually that the local CNR (adipose-to-water) is the same. (c) CNR measured in corrected and uncorrected images for SPR ranging from 0 to 2.

For a large, low-contrast stimulus such as the semicircular disk in Figure B.1, detection amounts to a low- (essentially zero-) frequency task, so that detectability index [Eq. (B.6)] is simply proportional to CNR (squared), which we take as a surrogate for detectability index in this simulation. As shown in Figure B.1a, the strong image nonuniformity (cupping) and low contrast of the stimulus in the uncorrected image can be mitigated locally simply by window and level adjustment. The local CNR for the two cases – despite strong differences in overall (nonlocal) aspects of image quality, such as uniformity – is the same, and the degradation in contrast due to scatter is compensated by the lower noise associated with higher total fluence. The simulation was repeated for SPR ranging 0 to 2, and the CNR was analyzed as in Figure B.1c, again showing equivalent CNR for corrected and uncorrected images at all levels of scatter magnitude. To the extent that local CNR is a valid surrogate for a low-frequency detection task, scatter correction is seen to have no effect on local detectability, in agreement with the derivation of Eq. (B.6). The analysis in Section 4 therefore is independent of the accuracy (or application) of scatter correction (though scatter correction should be applied to mitigate cupping and streaks), and the optimal system design – in terms of local detectability index – does not depend on aspects of scatter correction.

Bibliography

[1] J.L. Prince and J.M. Links, *Medical imaging signals and systems* (Pearson Prentice Hall, Upper Saddle River N.J., 2006).

[2] Z.-H. Cho, J.P. Jones, and M. Singh, *Foundations of medical imaging* (Wiley-Interscience, 1993).

[3] J.T. Bushberg, J.A. Seibert, E.M. Leidholdt Jr., and J.M. Boone, *The Essential Physics of Medical Imaging* (Lippincott Williams & Wilkins, 2012).

[4] C.R. Crowell, "The Richardson constant for thermionic emission in Schottky barrier diodes," Solid. State. Electron. **8**(4), 395–399 (1965).

[5] M.J. Berger *et al.*, "XCOM: photon cross sections database," NIST Stand. Ref. database **8**, 87–3597 (1998).

[6] N. Grassi, G. Casini, M. Frosini, G. Tobia, and T. Marchi, "PIXE characterization of CsI(Tl) scintillators used for particle detection in nuclear reactions," (2008).

[7] M.J. Weber, "Inorganic scintillators: today and tomorrow," J. Lumin. **100**(1), 35–45 (2002).

[8] M. Nikl, "Scintillation detectors for x-rays," Meas. Sci. Technol **17**, 37–54 (2006).

[9] P.R. Granfors *et al.*, "Performance of a 41×41 cm^2 amorphous silicon flat panel x-ray detector designed for angiographic and R&F imaging applications," Med. Phys. **30**(10), 2715 (2003).

[10] L.E. Antonuk *et al.*, "Strategies to improve the signal and noise performance of active matrix, flat-panel imagers for diagnostic x-ray applications.," Med. Phys. **27**(2), 289–306 (2000).

[11] K. Taguchi and J.S. Iwanczyk, "Vision 20/20: Single photon counting x-ray detectors in medical imaging.," Med. Phys. **40**(10), 100901 (2013).

[12] S. Kappler, A. Henning, B. Kreisler, F. Schoeck, K. Stierstorfer, and T. Flohr, "Photon counting CT at elevated X-ray tube currents: contrast stability, image noise and multi-energy performance," in edited by B.R. Whiting and C. Hoeschen (International Society for Optics and Photonics, 2014), p. 90331C.

[13] A.S. Wang, D. Harrison, V. Lobastov, and J.E. Tkaczyk, "Pulse pileup statistics for energy discriminating photon counting x-ray detectors," Med. Phys. **38**(7), 4265 (2011).

[14] K. Taguchi, E.C. Frey, X. Wang, J.S. Iwanczyk, and W.C. Barber, "An analytical model of the effects of pulse pileup on the energy spectrum recorded by energy resolved photon counting x-ray detectors,"

in *SPIE Med. Imaging*, edited by E. Samei and N.J. Pelc (International Society for Optics and Photonics, 2010), p. 76221C–76221C–8.

[15] K. Taguchi, S. Srivastava, H. Kudo, and W.C. Barber, "Enabling photon counting clinical X-ray CT," in *2009 IEEE Nucl. Sci. Symp. Conf. Rec.*(IEEE, 2009), pp. 3581–3585.

[16] M.J. Tapiovaara and R. Wagner, "SNR and DQE analysis of broad spectrum X-ray imaging," Phys. Med. Biol. **30**(6), 519–529 (1985).

[17] J. Tanguay, S. Yun, H.K. Kim, and I.A. Cunningham, "Extension of cascaded systems analysis to single-photon-counting x-ray detectors," in *SPIE Med. Imaging*, edited by N.J. Pelc, R.M. Nishikawa and B.R. Whiting (International Society for Optics and Photonics, 2012), p. 831310.

[18] X. Wang, D. Meier, K. Taguchi, D.J. Wagenaar, B.E. Patt, and E.C. Frey, "Material separation in x-ray CT with energy resolved photon-counting detectors.," Med. Phys. **38**(3), 1534–46 (2011).

[19] M. Persson *et al.*, "Energy-resolved CT imaging with a photon-counting silicon-strip detector," Phys. Med. Biol. **59**(22), 6709–6727 (2014).

[20] A. El Gamal and H. Eltoukhy, "CMOS image sensors," IEEE Circuits Devices Mag. **21**(3), 6–20 (2005).

[21] A.C. Konstantinidis, M.B. Szafraniec, R.D. Speller, and A. Olivo, "The Dexela 2923 CMOS X-ray detector: A flat panel detector based on CMOS active pixel sensors for medical imaging applications," Nucl. Instruments Methods Phys. Res. Sect. A Accel. Spectrometers, Detect. Assoc. Equip. **689**, 12–21 (2012).

[22] J. Hsieh, *Computed Tomography, Second Edition: Principles, Design, Artifacts, and Recent Advances* (SPIE, 1000 20th Street, Bellingham, WA 98227-0010 USA, 2009).

[23] G.T. Herman, A.V. Lakshminarayanan, and A. Naparstek, "Convolution reconstruction techniques for divergent beams," Comput. Biol. Med. **6**(4), 259–271 (1976).

[24] L.A. Feldkamp, L.C. Davis, and J.W. Kress, "Practical cone-beam algorithm," J. Opt. Soc. Am. A **1**(6), 612 (1984).

[25] I.A. Elbakri and J.A. Fessler, "Statistical image reconstruction for polyenergetic X-ray computed tomography," IEEE Trans. Med. Imaging **21**(2), 89–99 (2002).

[26] S. Tilley, J.H. Siewerdsen, J.W. Stayman, and J.W. Stayman, "Iterative CT Reconstruction using

Models of Source and Detector Blur and Correlated Noise.," Conf. Proc. / Int. Conf. Image Form. X-Ray Comput. Tomogr. Int. Conf. Image Form. X-Ray Comput. Tomogr. **2014**, 363–367 (2014).

[27] J. Nuyts, B. De Man, J.A. Fessler, W. Zbijewski, and F.J. Beekman, "Modelling the physics in the iterative reconstruction for transmission computed tomography," Phys. Med. Biol. **58**(12), R63 (2013).

[28] J.H. Cho and J.A. Fessler, "Regularization Designs for Uniform Spatial Resolution and Noise Properties in Statistical Image Reconstruction for 3-D X-ray CT," IEEE Trans. Med. Imaging **34**(2), 678–689 (2015).

[29] H. Dang *et al.*, "Regularization design for high-quality cone-beam CT of intracranial hemorrhage using statistical reconstruction," in *SPIE Med. Imaging*(2016), p. 97832Y--97832Y.

[30] A.J. Jerri, "The Shannon sampling theorem—Its various extensions and applications: A tutorial review," Proc. IEEE **65**(11), 1565–1596 (1977).

[31] J.H. Siewerdsen, L.E. Antonuk, Y. El-Mohri, J. Yorkston, W. Huang, and I.A. Cunningham, "Signal, noise power spectrum, and detective quantum efficiency of indirect-detection flat-panel imagers for diagnostic radiology," Med. Phys. **25**(5), 614 (1998).

[32] D.J. Tward and J.H. Siewerdsen, "Cascaded systems analysis of the 3D noise transfer characteristics of flat-panel cone-beam CT," Med. Phys. **35**(12), 5510 (2008).

[33] H.H. Barrett, J. Yao, J.P. Rolland, and K.J. Myers, "Model observers for assessment of image quality.," Proc. Natl. Acad. Sci. **90**(21), 9758–9765 (1993).

[34] G.J. Gang *et al.*, "Analysis of Fourier-domain task-based detectability index in tomosynthesis and cone-beam CT in relation to human observer performance.," Med. Phys. **38**(4), 1754–1768 (2011).

[35] J.H. Siewerdsen, D.J. Moseley, B. Bakhtiar, S. Richard, and D.A. Jaffray, "The influence of antiscatter grids on soft-tissue detectability in cone-beam computed tomography with flat-panel detectors," Med. Phys. **31**(12), 3506 (2004).

[36] U. Neitzel, "Grids or air gaps for scatter reduction in digital radiography: A model calculation," Med. Phys. **19**(2), 475 (1992).

[37] E.-P. Rührnschopf and and K. Klingenbeck, "A general framework and review of scatter correction methods in cone beam CT. Part 2: Scatter estimation approaches," Med. Phys. **38**(9), 5186 (2011).

[38] H.K. Tuy, “An Inversion Formula for Cone-Beam Reconstruction,” SIAM J. Appl. Math. **43**(3), 546–552 (1983).

[39] Xiaohui Wang and Ruola Ning, “A cone-beam reconstruction algorithm for circle-plus-arc data-acquisition geometry,” IEEE Trans. Med. Imaging **18**(9), 815–824 (1999).

[40] F. Noo, M. Defrise, R. Clack, E.J. Roney, T.A. White, and S.G. Galbraith, “Stable and efficient shift-variant algorithm for circle-plus-lines orbits in cone-beam CT,” in *Proc. 3rd IEEE Int. Conf. Image Process.*(IEEE, n.d.), pp. 539–542.

[41] J. Hsieh, “A practical cone beam artifact correction algorithm,” in *2000 IEEE Nucl. Sci. Symp. Conf. Rec. (Cat. No.00CH37149)*(IEEE, n.d.), p. 15/71-15/74.

[42] Z. EI, “Computed tomography (CT) of the temporal bone in diagnosis of acquired cholesteatoma of the middle ear,” Vestn. Otorinolaringol. (5), 28–32 (2003).

[43] H.D. Curtin, “Superior Semicircular Canal Dehiscence Syndrome and Multi--Detector Row CT 1,” Radiology **226**(2), 312–314 (2003).

[44] P. Nicolai, C.T. Sasaki, A. Ferlito, and J.A. Kirchner, “Laryngeal Chondrosarcoma: Incidence, Pathology, Biological Behavior, and Treatment,” Ann. Otol. Rhinol. Laryngol. **99**(7), 515–523 (1990).

[45] T.L. Slovis, B. Renfro, F.B. Watts, L.R. Kuhns, W. Belenky, and J. Spoylar, “Choanal atresia: precise CT evaluation.,” http://dx.doi.org/10.1148/radiology.155.2.3983384 (1985).

[46] J.-Y. Lee, K.-J. Shin, J.-N. Kim, J.-Y. Yoo, W.-C. Song, and K.-S. Koh, “A Morphometric Study of the Semicircular Canals Using Micro-CT Images in Three-Dimensional Reconstruction,” Anat. Rec. **296**(5), 834–839 (2013).

[47] C.J. Belden, N. Weg, L.B. Minor, and S.J. Zinreich, “CT Evaluation of Bone Dehiscence of the Superior Semicircular Canal as a Cause of Sound- and/or Pressure-induced Vertigo,” Radiology **226**(2), 337–343 (2003).

[48] M.J. Walden, “Head and Neck Cancer,” Semin. Roentgenol. **48**(1), 75–86 (2013).

[49] S.R. Laker, “Epidemiology of concussion and mild traumatic brain injury.,” PM R **3**(10 Suppl 2), S354-8 (2011).

[50] R.M. Chesnut, “Management of brain and spine injuries,” Crit. Care Clin. **20**(1), 25–55 (2004).

[51] D. Mozaffarian *et al.*, “Heart Disease and Stroke Statistics-2015 Update: A Report From the American Heart Association.,” Circulation **131**(4), e29-322 (2014).

[52] A.B. Dublin, B.N. French, and J.M. Rennlck, “Computed Tomography in Head Trauma 1,” Radiology **122**(2), 365–369 (1977).

[53] J.C. Masdeu and G.R. Gilberto, *Neuroimaging. Part I* (Elsevier, Cambridge, MA, 2016).

[54] R.T. Penninger, T.S. Tavassolie, and J.P. Carey, “Cone-Beam Volumetric Tomography for Applications in the Temporal Bone,” Otol. Neurotol. **32**(3), 453–460 (2011).

[55] T. Rodt *et al.*, “3D visualisation of the middle ear and adjacent structures using reconstructed multi-slice CT datasets, correlating 3D images and virtual endoscopy to the 2D cross-sectional images,” Neuroradiology **44**(9), 783–790 (2002).

[56] M. Wintermark *et al.*, “Imaging Recommendations for Acute Stroke and Transient Ischemic Attack Patients: A Joint Statement by the American Society of Neuroradiology, the American College of Radiology, and the Society of NeuroInterventional Surgery,” Am. J. Neuroradiol. **34**(11), E117–E127 (2013).

[57] M.H. Lev *et al.*, “Utility of Perfusion-Weighted CT Imaging in Acute Middle Cerebral Artery Stroke Treated With Intra-Arterial Thrombolysis:: Prediction of Final Infarct Volume and Clinical Outcome Editorial Comment: Prediction of Final Infarct Volume and Clinical Outcome,” Stroke **32**(9), 2021–2028 (2001).

[58] C. Waydhas, “Equipment review: Intrahospital transport of critically ill patients,” Crit. Care **3**(5), R83 (1999).

[59] I. Smith, S. Fleming, and A. Cernaianu, “Mishaps during transport from the intensive care unit.,” Crit. Care Med. **18**(3), 278–81 (1990).

[60] L.K. Ott, L.A. Hoffman, and M. Hravnak, “Intrahospital Transport to the Radiology Department: Risk for Adverse Events, Nursing Surveillance, Utilization of a MET and Practice Implications.,” J. Radiol. Nurs. **30**(2), 49–52 (2011).

[61] R. Doddamani, S. Gupta, N. Singla, S. Mohindra, and P. Singh, “Role of repeat CT scans in the management of traumatic brain injury,” Indian J. Neurotrauma **9**(1), 33–39 (2012).

[62] M. Blaickner and J. Neuwirth, “Measurements of occupational and patient exposure as well as image

quality for two C-arms," Radiat. Prot. Dosimetry **155**(4), 451–458 (2013).

63 R. Seeberger, M. Buchgeister, A.C. Seethaler, T. Shiozawa, and J. Hoffmann, "Image quality of two different mobile cone beam computed tomographs for maxillofacial surgery.," J. Craniomaxillofac. Surg. **40**(8), 731–4 (2012).

64 W. Zbijewski and J.W. Stayman, "xCAT: A mobile, flat-panel volumetric X-ray CT for head and neck imaging," in *2007 IEEE Nucl. Sci. Symp. Conf. Rec.*(IEEE, 2007), pp. 2985–2986.

65 J. Xu, D.D. Reh, J.P. Carey, M. Mahesh, and J.H. Siewerdsen, "Technical assessment of a cone-beam CT scanner for otolaryngology imaging: image quality, dose, and technique protocols.," Med. Phys. **39**(8), 4932–42 (2012).

66 A.P. Carlson and H. Yonas, "Portable head computed tomography scanner--technology and applications: experience with 3421 scans.," J. Neuroimaging **22**(4), 408–15 (2012).

67 Z. Rumboldt, W. Huda, and J.W. All, "Review of portable CT with assessment of a dedicated head CT scanner.," AJNR. Am. J. Neuroradiol. **30**(9), 1630–6 (2009).

68 R. Gerlach *et al.*, "Feasibility of Polestar N20, an Ultra-Low-Field Intraoperative Magnetic Resonance Imaging System in Resection Control of Pituitary Macroadenomas: Lessons Learned from the First 40 Cases.," Neurosurgery **62**(2), 272–285 (2008).

69 M.J. Daly, J.H. Siewerdsen, D.J. Moseley, D.A. Jaffray, and J.C. Irish, "Intraoperative cone-beam CT for guidance of head and neck surgery: Assessment of dose and image quality using a C-arm prototype," Med. Phys. **33**(10), 3767 (2006).

70 M.J. Wallace, M.D. Kuo, C. Glaiberman, C.A. Binkert, R.C. Orth, and G. Soulez, "Three-dimensional C-arm Cone-beam CT: Applications in the Interventional Suite," J. Vasc. Interv. Radiol. **20**(7), S523–S537 (2009).

71 S. Schafer *et al.*, "Mobile C-arm cone-beam CT for guidance of spine surgery: Image quality, radiation dose, and integration with interventional guidance," Med. Phys. **38**(8), 4563 (2011).

72 P.A. Helm, R. Teichman, S.L. Hartmann, and D. Simon, "Spinal Navigation and Imaging: History, Trends, and Future," IEEE Trans. Med. Imaging **34**(8), 1738–1746 (2015).

73 M. Beck, T. Mittlmeier, P. Gierer, C. Harms, and G. Gradl, "Benefit and accuracy of intraoperative 3D-imaging after pedicle screw placement: a prospective study in stabilizing thoracolumbar

fractures," Eur. Spine J. **18**(10), 1469–1477 (2009).

74 D.A. Jaffray, J.H. Siewerdsen, J.W. Wong, and A.A. Martinez, "Flat-panel cone-beam computed tomography for image-guided radiation therapy," Int. J. Radiat. Oncol. **53**(5), 1337–1349 (2002).

75 Y. Murayama *et al.*, "Robotic Digital Subtraction Angiography Systems within the Hybrid Operating Room," Neurosurgery 1 (2011).

76 J.H. Siewerdsen, "Cone-Beam CT with a Flat-Panel Detector: From Image Science to Image-Guided Surgery.," Nucl. Instrum. Methods Phys. Res. A. **648**(S1), S241–S250 (2011).

77 T.G. Purdie *et al.*, "Cone-beam computed tomography for on-line image guidance of lung stereotactic radiotherapy: localization, verification, and intrafraction tumor position.," Int. J. Radiat. Oncol. Biol. Phys. **68**(1), 243–52 (2007).

78 A.C. Miracle and S.K. Mukherji, "Conebeam CT of the Head and Neck, Part 2: Clinical Applications," Am. J. Neuroradiol. **30**(7), 1285–1292 (2009).

79 D.A. Tyndall and S. Rathore, "Cone-Beam CT Diagnostic Applications: Caries, Periodontal Bone Assessment, and Endodontic Applications," Dent. Clin. North Am. **52**(4), 825–841 (2008).

80 J.A. Carrino *et al.*, "Dedicated cone-beam CT system for extremity imaging.," Radiology **270**(3), 816–24 (2014).

81 J.M. Boone, T.R. Nelson, K.K. Lindfors, and J.A. Seibert, "Dedicated breast CT: radiation dose and image quality evaluation.," Radiology **221**(3), 657–67 (2001).

82 B. Chen and R. Ning, "Cone-beam volume CT breast imaging: feasibility study.," Med. Phys. **29**(5), 755–70 (2002).

83 A.S. Wang *et al.*, "Soft-Tissue Imaging in Low-Dose , C-Arm Cone-Beam CT Using Statistical Image Reconstruction," SPIE Med. Imaging **8668**(February), 86681F (2013).

84 E. King *et al.*, "Intraoperative cone-beam CT for head and neck surgery: feasibility of clinical implementation using a prototype mobile C-arm.," Head Neck **35**(7), 959–67 (2013).

85 W.C. Scarfe and A.G. Farman, "What is cone-beam CT and how does it work?," Dent. Clin. North Am. **52**(4), 707–30 (2008).

86 J.K. Mah, R.A. Danforth, A. Bumann, and D. Hatcher, "Radiation absorbed in maxillofacial imaging with a new dental computed tomography device," Oral Surgery, Oral Med. Oral Pathol. Oral Radiol.

Endodontology **96**(4), 508–513 (2003).

87 P. Mozzo, C. Procacci, A. Tacconi, P. Tinazzi Martini, and I.A. Bergamo Andreis, “A new volumetric CT machine for dental imaging based on the cone-beam technique: preliminary results,” Eur. Radiol. **8**(9), 1558–1564 (1998).

88 S.C. White and M.J. Pharoah, “The Evolution and Application of Dental Maxillofacial Imaging Modalities,” Dent. Clin. North Am. **52**(4), 689–705 (2008).

89 K. Tsiklakis, C. Donta, S. Gavala, K. Karayianni, V. Kamenopoulou, and C.J. Hourdakis, “Dose reduction in maxillofacial imaging using low dose Cone Beam CT,” Eur. J. Radiol. **56**(3), 413–417 (2005).

90 J.A. ROBERTS, N.A. DRAGE, J. DAVIES, and D.W. THOMAS, “Effective dose from cone beam CT examinations in dentistry,” Br. J. Radiol. **82**(973), 35–40 (2009).

91 M. Lamichane, N.K. Anderson, P.H. Rigali, E.B. Seldin, and L.A. Will, “Accuracy of reconstructed images from cone-beam computed tomography scans,” Am. J. Orthod. Dentofac. Orthop. **136**(2), 156.e1-156.e6 (2009).

92 F. Jadu, M. Hill, M. Yaffe, and E. Lam, “Optimization of exposure parameters for cone beam computed tomography sialography,” Dentomaxillofacial Radiol. **40**(6), 362–368 (2011).

93 K. Araki *et al.*, “Characteristics of a newly developed dentomaxillofacial X-ray cone beam CT scanner (CB MercuRay^{TM}): system configuration and physical properties,” Dentomaxillofacial Radiol. **33**(1), 51–59 (2004).

94 W. De Vos, J. Casselman, and G.R.J. Swennen, “Cone-beam computerized tomography (CBCT) imaging of the oral and maxillofacial region: A systematic review of the literature,” Int. J. Oral Maxillofac. Surg. **38**(6), 609–625 (2009).

95 D. Schulze, M. Heiland, H. Thurmann, and G. Adam, “Radiation exposure during midfacial imaging using 4- and 16-slice computed tomography, cone beam computed tomography systems and conventional radiography,” Dentomaxillofacial Radiol. **33**(2), 83–86 (2004).

96 M. Dahmani-Causse, M. Marx, O. Deguine, B. Fraysse, B. Lepage, and B. Escudé, “Morphologic examination of the temporal bone by cone beam computed tomography: Comparison with multislice helical computed tomography,” Eur. Ann. Otorhinolaryngol. Head Neck Dis. **128**(5), 230–235

(2011).

97 W. Zbijewski and J.W. Stayman, “xCAT: A mobile, flat-panel volumetric X-ray CT for head and neck imaging,” in *2007 IEEE Nucl. Sci. Symp. Conf. Rec.*(IEEE, 2007), pp. 2985–2986.

98 W. Zbijewski *et al.*, “A dedicated cone-beam CT system for musculoskeletal extremities imaging: Design, optimization, and initial performance characterization,” Med. Phys. **38**(8), 4700 (2011).

99 D. Ritter, J. Orman, C. Schmidgunst, and R. Graumann, “3D soft tissue imaging with a mobile C-arm,” Comput. Med. Imaging Graph. **31**(2), 91–102 (2007).

100 K.S. Karim, A. Nathan, J.A. Rowlands, and S.O. Kasap, “X-ray detector with on-pixel amplification for large area diagnostic medical imaging,” IEE Proc. - Circuits, Devices Syst. **150**(4), 267 (2003).

101 W. Zhao *et al.*, “Indirect flat-panel detector with avalanche gain: Fundamental feasibility investigation for SHARP-AMFPI (scintillator HARP active matrix flat panel imager),” Med. Phys. **32**(9), 2954 (2005).

102 T. Francke *et al.*, “Dose reduction in medical X-ray imaging using noise free photon counting,” Nucl. Instruments Methods Phys. Res. Sect. A Accel. Spectrometers, Detect. Assoc. Equip. **471**(1–2), 85–87 (2001).

103 S. Weigel, S. Berkemeyer, R. Girnus, A. Sommer, H. Lenzen, and W. Heindel, “Digital Mammography Screening with Photon-counting Technique: Can a High Diagnostic Performance Be Realized at Low Mean Glandular Dose?,” Radiology **271**(2), 345–355 (2014).

104 E.B. Cole, A.Y. Toledano, M. Lundqvist, and E.D. Pisano, “Comparison of radiologist performance with photon-counting full-field digital mammography to conventional full-field digital mammography.,” Acad. Radiol. **19**(8), 916–22 (2012).

105 S.J. Thunberg *et al.*, “Dose reduction in Mammography with Photon Counting Imaging,” in *Med. Imaging 2004*, edited by M.J. Yaffe and M.J. Flynn (International Society for Optics and Photonics, 2004), pp. 457–465.

106 E. Fredenberg, M. Hemmendorff, B. Cederström, M. Åslund, and M. Danielsson, “Contrast-enhanced spectral mammography with a photon-counting detector,” Med. Phys. **37**(5), 2017–2029 (2010).

107 A.D.A. Maidment *et al.*, “Evaluation of a photon-counting breast tomosynthesis imaging system,” in

Med. Imaging, edited by M.J. Flynn and J. Hsieh (International Society for Optics and Photonics, 2006), p. 61420B–61420B–11.

[108] Y. Alivov, P. Baturin, H.Q. Le, J. Ducote, and S. Molloi, "Optimization of K-edge imaging for vulnerable plaques using gold nanoparticles and energy resolved photon counting detectors: a simulation study.," Phys. Med. Biol. **59**(1), 135–52 (2014).

[109] F.F. Schmitzberger *et al.*, "Development of low-dose photon-counting contrast-enhanced tomosynthesis with spectral imaging.," Radiology **259**(2), 558–64 (2011).

[110] J.D. Silkwood, K.L. Matthews, and P.M. Shikhaliev, "Photon counting spectral breast CT: effect of adaptive filtration on CT numbers, noise, and contrast to noise ratio.," Med. Phys. **40**(5), 51905 (2013).

[111] A.M. Alessio and L.R. MacDonald, "Quantitative material characterization from multi-energy photon counting CT.," Med. Phys. **40**(3), 31108 (2013).

[112] T. Takahashi and S. Watanabe, "Recent progress in CdTe and CdZnTe detectors," Nucl. Sci. IEEE Trans. **48**(4), 950–959 (2001).

[113] R.H. Redus, J.A. Pantazis, T.J. Pantazis, A.C. Huber, and B.J. Cross, "Characterization of CdTe detectors for quantitative x-ray spectroscopy," Nucl. Sci. IEEE Trans. **56**(4), 2524–2532 (2009).

[114] J.S. Iwanczyk *et al.*, "Photon Counting Energy Dispersive Detector Arrays for X-ray Imaging.," IEEE Trans. Nucl. Sci. **56**(3), 535–542 (2009).

[115] M. Ruat and C. Ponchut, "Characterization of a Pixelated CdTe X-Ray Detector Using the Timepix Photon-Counting Readout Chip," IEEE Trans. Nucl. Sci. **59**(5), 2392–2401 (2012).

[116] T. Ohsugi, Y. Onno, H.F.-W. Sadrozinski, S. Yoshida, and T. Ohsugi, "Application of silicon strip detectors to X-ray computed tomography," Nucl. Instruments Methods Phys. Res. Sect. A Accel. Spectrometers, Detect. Assoc. Equip. **541**(1), 412–420 (2005).

[117] E. Beuville *et al.*, "High resolution X-ray imaging using a silicon strip detector," IEEE Trans. Nucl. Sci. **45**(6), 3059–3063 (1998).

[118] P.M. Shikhaliev, T. Xu, H. Le, and S. Molloi, "Scanning-slit photon counting x-ray imaging system using a microchannel plate detector," Med. Phys. **31**(5), 1061 (2004).

[119] A. Kuhls-Gilcrist, A. Jain, D.R. Bednarek, and S. Rudin, "The Solid State X-ray Image Intensifier

(SSXII) in Single Photon Counting (SPC) mode.," Proc. SPIE **7622**(76221P), 76221P–76221P–9 (2010).

120 T. Koenig *et al.*, "Imaging properties of small-pixel spectroscopic x-ray detectors based on cadmium telluride sensors.," Phys. Med. Biol. **57**(21), 6743–59 (2012).

121 S. Yun, J. Tanguay, H.K. Kim, and I.A. Cunningham, "Cascaded-systems analyses and the detective quantum efficiency of single-Z x-ray detectors including photoelectric, coherent and incoherent interactions," Med. Phys. **40**, 41916 (2013).

122 M. Lundqvist, B. Cederstrom, V. Chmill, M. Danielsson, and D. Nygren, "Computer simulations and performance measurements on a silicon strip detector for edge-on imaging," in *Nucl. Sci. Symp. 1999. Conf. Rec. 1999 IEEE*(IEEE, 1999), pp. 433–438.

123 J. Tanguay, S. Yun, H.K. Kim, and I.A. Cunningham, "The detective quantum efficiency of photon-counting x-ray detectors using cascaded-systems analyses," Med. Phys. **40**, 41913 (2013).

124 R.J. Acciavatti and A.D.A. Maidment, "An Analytical Model of NPS and DQE Comparing Photon Counting and Energy Integrating Detectors," in *SPIE Med. Imaging*, edited by E. Samei and N.J. Pelc (International Society for Optics and Photonics, 2010), p. 76220I–76220I–12.

125 L.E. Antonuk *et al.*, "Strategies to improve the signal and noise performance of active matrix, flat-panel imagers for diagnostic x-ray applications," Med. Phys. **27**(2), 289 (2000).

126 J.H. Siewerdsen *et al.*, "Empirical and theoretical investigation of the noise performance of indirect detection, active matrix flat-panel imagers (AMFPIs) for diagnostic radiology," Med. Phys. **24**, 71 (1997).

127 W. Zhao, W.G. Ji, A. Debrie, and J.A. Rowlands, "Imaging performance of amorphous selenium based flat-panel detectors for digital mammography: Characterization of a small area prototype detector," Med. Phys. **30**(2), 254 (2003).

128 G. Hajdok, J. Yao, J.J. Battista, and I.A. Cunningham, "Signal and noise transfer properties of photoelectric interactions in diagnostic x-ray imaging detectors," Med. Phys. **33**(10), 3601 (2006).

129 S. Richard and J.H. Siewerdsen, "Cascaded systems analysis of noise reduction algorithms in dual-energy imaging," Med. Phys. **35**(2), 586 (2008).

130 J. Xu *et al.*, "Cascaded systems analysis of photon counting detectors," Med. Phys. **41**(10), 101907

(2014).

131 J. Xu *et al.*, "Cascaded Systems Modeling of Signal, Noise, and DQE for X-Ray Photon Counting Detectors," SPIE Med. Imaging (2014).

132 E. Fredenberg, M. Lundqvist, B. Cederström, M. Åslund, and M. Danielsson, "Energy resolution of a photon-counting silicon strip detector," Nucl. Instruments Methods Phys. Res. Sect. A Accel. Spectrometers, Detect. Assoc. Equip. **613**(1), 156–162 (2010).

133 J.H. Siewerdsen, A.M. Waese, D.J. Moseley, S. Richard, and D.A. Jaffray, "Spektr: a computational tool for x-ray spectral analysis and imaging system optimization.," Med. Phys. **31**(11), 3057–67 (2004).

134 J.M. Boone and J.A. Seibert, "An accurate method for computer-generating tungsten anode x-ray spectra from 30 to 140 kV," Med. Phys. **24**(11), 1661 (1997).

135 G. Hajdok, J.J. Battista, and I.A. Cunningham, "Fundamental x-ray interaction limits in diagnostic imaging detectors: Spatial resolution," Med. Phys. **35**(7), 3180 (2008).

136 R.J. Acciavatti and A.D.A. Maidment, "Optimization of phosphor-based detector design for oblique x-ray incidence in digital breast tomosynthesis.," Med. Phys. **38**(11), 6188 (2011).

137 A. Badano, M. Freed, and Y. Fang, "Oblique incidence effects in direct x-ray detectors: A first-order approximation using a physics-based analytical model," Med. Phys. **38**(4), 2095 (2011).

138 S. Yin *et al.*, "Direct conversion Si and CdZnTe detectors for digital mammography," Nucl. Instruments Methods Phys. Res. Sect. A Accel. Spectrometers, Detect. Assoc. Equip. **448**(3), 591–597 (2000).

139 L.W. Schumann and T.S. Lomheim, "Modulation transfer function and quantum efficiency correlation at long wavelengths (greater than 800 nm) in linear charge coupled imagers.," Appl. Opt. **28**(9), 1701–9 (1989).

140 J.T. Dobbins III, "Effects of undersampling on the proper interpretation of modulation transfer function, noise power spectra, and noise equivalent quanta of digital imaging systems," Med. Phys. **22**, 171 (1995).

141 I.A. Cunningham and B.K. Reid, "Signal and noise in modulation transfer function determinations using the slit, wire, and edge techniques.," Med. Phys. **19**(4), 1037–44 (n.d.).

[142] E. Samei, M.J. Flynn, and D.A. Reimann, “A method for measuring the presampled MTF of digital radiographic systems using an edge test device.,” Med. Phys. **25**(1), 102–13 (1998).

[143] J.H. Siewerdsen, I.A. Cunningham, and D.A. Jaffray, “A framework for noise-power spectrum analysis of multidimensional images.,” Med. Phys. **29**(11), 2655–71 (2002).

[144] E. Fredenberg, M. Lundqvist, M. Åslund, M. Hemmendorff, B. Cederström, and M. Danielsson, “A photon-counting detector for dual-energy breast tomosynthesis,” in *SPIE Med. Imaging*, edited by E. Samei and J. Hsieh (International Society for Optics and Photonics, 2009), p. 72581J–72581J–11.

[145] L.E. Antonuk *et al.*, “Initial performance evaluation of an indirect-detection, active matrix flat-panel imager (AMFPI) prototype for megavoltage imaging,” Int. J. Radiat. Oncol. **42**(2), 437–454 (1998).

[146] R.N. Cahn, B. Cederström, M. Danielsson, A. Hall, M. Lundqvist, and D. Nygren, “Detective quantum efficiency dependence on x-ray energy weighting in mammography.,” Med. Phys. **26**(12), 2680–3 (1999).

[147] J.H. Siewerdsen, L.E. Antonuk, Y. El-Mohri, J. Yorkston, W. Huang, and I.A. Cunningham, “Signal, noise power spectrum, and detective quantum efficiency of indirect-detection flat-panel imagers for diagnostic radiology,” Med. Phys. **25**, 614 (1998).

[148] S. Vedantham *et al.*, “Full breast digital mammography with an amorphous silicon-based flat panel detector: Physical characteristics of a clinical prototype,” Med. Phys. **27**(3), 558 (2000).

[149] A. Ganguly, S. Rudin, D.R. Bednarek, and K.R. Hoffmann, “Micro-angiography for neuro-vascular imaging. II. Cascade model analysis,” Med. Phys. **30**(11), 3029 (2003).

[150] M. Yveborg, M. Danielsson, and H. Bornefalk, “Performance evaluation of a sub-millimetre spectrally resolved CT system on high- and low-frequency imaging tasks: a simulation.,” Phys. Med. Biol. **57**(8), 2373–91 (2012).

[151] J. Yao and I.A. Cunningham, “Parallel cascades: New ways to describe noise transfer in medical imaging systems,” Med. Phys. **28**, 2020 (2001).

[152] S. Richard, J.H. Siewerdsen, D.A. Jaffray, D.J. Moseley, and B. Bakhtiar, “Generalized DQE analysis of radiographic and dual-energy imaging using flat-panel detectors,” Med. Phys. **32**(5), 1397 (2005).

[153] A. Sisniega *et al.*, “Volumetric CT with sparse detector arrays (and application to Si-strip photon

counters)," Phys. Med. Biol. **61**(1), 90 (2015).

154 A.D. Gean and N.J. Fischbein, "Head trauma.," Neuroimaging Clin. N. Am. **20**(4), 527–56 (2010).

155 J.H. Siewerdsen *et al.*, "Volume CT with a flat-panel detector on a mobile, isocentric C-arm: Pre-clinical investigation in guidance of minimally invasive surgery," Med. Phys. **32**(1), 241 (2005).

156 R. Leung, K. Chaung, J.L. Kelly, and R.K. Chandra, "Advancements in computed tomography management of chronic rhinosinusitis.," Am. J. Rhinol. Allergy **25**(5), 299–302 (2011).

157 J.H. Adams, D. Doyle, I. Ford, T.A. Gennarelli, D.I. Graham, and D.R. Mclellan, "Diffuse axonal injury in head injury: Definition, diagnosis and grading," Histopathology **15**(1), 49–59 (1989).

158 A. Sisniega *et al.*, "High-fidelity artifact correction for cone-beam CT imaging of the brain.," Phys. Med. Biol. **60**(4), 1415–39 (2015).

159 D. Prell, Y. Kyriakou, M. Beister, and W.A. Kalender, "A novel forward projection-based metal artifact reduction method for flat-detector computed tomography.," Phys. Med. Biol. **54**(21), 6575–91 (2009).

160 H. Yan *et al.*, "Towards the clinical implementation of iterative low-dose cone-beam CT reconstruction in image-guided radiation therapy: cone/ring artifact correction and multiple GPU implementation.," Med. Phys. **41**(11), 111912 (2014).

161 H. Dang *et al.*, "Statistical reconstruction for cone-beam CT with a post-artifact-correction noise model: application to high-quality head imaging," Phys. Med. Biol. **60**(16), 6153 (2015).

162 J.H. Siewerdsen and D.A. Jaffray, "Optimization of x-ray imaging geometry (with specific application to flat-panel cone-beam computed tomography)," Med. Phys. **27**(8), 1903 (2000).

163 P. Prakash *et al.*, "Task-based modeling and optimization of a cone-beam CT scanner for musculoskeletal imaging," Med. Phys. **38**(10), 5612 (2011).

164 E. Fredenberg, M. Danielsson, J.W. Stayman, J.H. Siewerdsen, and M. Aslund, "Ideal-observer detectability in photon-counting differential phase-contrast imaging using a linear-systems approach.," Med. Phys. **39**(9), 5317–35 (2012).

165 K. Li, N. Bevins, J. Zambelli, and G.-H. Chen, "Fundamental relationship between the noise properties of grating-based differential phase contrast CT and absorption CT: theoretical framework using a cascaded system model and experimental validation.," Med. Phys. **40**(2), 21908 (2013).

[166] B. Zhao and W. Zhao, "Three-dimensional linear system analysis for breast tomosynthesis," Med. Phys. **35**(12), 5219 (2008).

[167] S. Suryanarayanan, A. Karellas, S. Vedantham, and I. Sechopoulos, "Theoretical analysis of high-resolution digital mammography.," Phys. Med. Biol. **51**(12), 3041–55 (2006).

[168] S. Vedantham, A. Karellas, M.M. Emmons, L.J. Moss, S. Hussain, and S.P. Baker, "Dedicated breast CT: geometric design considerations to maximize posterior breast coverage.," Phys. Med. Biol. **58**(12), 4099–118 (2013).

[169] G.J. Gang, J.W. Stayman, W. Zbijewski, and J.H. Siewerdsen, "Task-based detectability in CT image reconstruction by filtered backprojection and penalized likelihood estimation.," Med. Phys. **41**(8), 81902 (2014).

[170] A. Badal, I. Kyprianou, D.P. Banh, A. Badano, and J. Sempau, "penMesh--Monte Carlo radiation transport simulation in a triangle mesh geometry.," IEEE Trans. Med. Imaging **28**(12), 1894–901 (2009).

[171] H.-E. Nilsson, C. Frojdh, and E. Dubaric, "Monte Carlo simulation of charge sharing effects in silicon and GaAs photon-counting X-ray imaging detectors," IEEE Trans. Nucl. Sci. **51**(4), 1636–1640 (2004).

[172] A.A. Vedula, S.J. Glick, and X. Gong, "Computer simulation of CT mammography using a flat-panel imager," in *Med. Imaging 2003*, edited by M.J. Yaffe and L.E. Antonuk (International Society for Optics and Photonics, 2003), pp. 349–360.

[173] A. Sisniega *et al.*, "Monte Carlo study of the effects of system geometry and antiscatter grids on cone-beam CT scatter distributions.," Med. Phys. **40**(5), 51915 (2013).

[174] I. Sechopoulos and C. Ghetti, "Optimization of the acquisition geometry in digital tomosynthesis of the breast," Med. Phys. **36**(4), 1199 (2009).

[175] I. Reiser and R.M. Nishikawa, "Task-based assessment of breast tomosynthesis: Effect of acquisition parameters and quantum noise," Med. Phys. **37**(4), 1591 (2010).

[176] A. Wunderlich and F. Noo, "Estimation of channelized hotelling observer performance with known class means or known difference of class means.," IEEE Trans. Med. Imaging **28**(8), 1198–207 (2009).

[177] L. Yu, S. Leng, L. Chen, J.M. Kofler, R.E. Carter, and C.H. McCollough, "Prediction of human observer performance in a 2-alternative forced choice low-contrast detection task using channelized Hotelling observer: impact of radiation dose and reconstruction algorithms.," Med. Phys. **40**(4), 41908 (2013).

[178] E.C. Frey, K.L. Gilland, and B.M.W. Tsui, "Application of task-based measures of image quality to optimization and evaluation of three-dimensional reconstruction-based compensation methods in myocardial perfusion SPECT.," IEEE Trans. Med. Imaging **21**(9), 1040–50 (2002).

[179] J. Xu *et al.*, "Modeling and Design of a Cone-Beam CT Head Scanner Using Task-Based Imaging Performance Optimization," Phys. Med. Biol. **61**(8), 3180–3207 (2016).

[180] D.J. Tward and J.H. Siewerdsen, "Noise aliasing and the 3D NEQ of flat-panel cone-beam CT: Effect of 2D/3D apertures and sampling," Med. Phys. **36**(8), 3830 (2009).

[181] I.A. Cunningham, "Linear-systems modeling of parallel cascaded stochastic processes: the NPS of radiographic screens with reabsorption of characteristic x-radiation," in *Med. Imaging '98*, edited by J.T. Dobbins III and J.M. Boone (International Society for Optics and Photonics, 1998), pp. 220–230.

[182] M. Albert and A.D.A. Maidment, "Linear response theory for detectors consisting of discrete arrays," Med. Phys. **27**(10), 2417 (2000).

[183] G.J. Day and D.R. Dance, "X-ray transmission formula for antiscatter grids," Phys. Med. Biol. **28**(12), 1429–1433 (1983).

[184] F.A. Miéville, F. Gudinchet, F. Brunelle, F.O. Bochud, and F.R. Verdun, "Iterative reconstruction methods in two different MDCT scanners: physical metrics and 4-alternative forced-choice detectability experiments--a phantom approach.," Phys. Med. **29**(1), 99–110 (2013).

[185] W. Huda, C.C. Chamberlain, A.E. Rosenbaum, and W. Garrisi, "Radiation doses to infants and adults undergoing head CT examinations," Med. Phys. **28**(3), 393 (2001).

[186] Y. Cho, D.J. Moseley, J.H. Siewerdsen, and D.A. Jaffray, "Accurate technique for complete geometric calibration of cone-beam computed tomography systems," Med. Phys. **32**(4), 968 (2005).

[187] A.R. Pineda, D.J. Tward, A. Gonzalez, and J.H. Siewerdsen, "Beyond noise power in 3D computed tomography: the local NPS and off-diagonal elements of the Fourier domain covariance matrix.,"

Med. Phys. **39**(6), 3240–52 (2012).

188 L. Yu *et al.*, “Dose and image quality evaluation of a dedicated cone-beam CT system for high-contrast neurologic applications.,” AJR. Am. J. Roentgenol. **194**(2), W193-201 (2010).

189 J.H. Siewerdsen, “Optimization of 2D and 3D Radiographic Imaging Systems,” in *Handb. Med. Image Percept. Tech.*, 1st ed., edited by E. (Duke U. Samei and E. (University of A. Krupkinski (Cambridge University Press, 2014), pp. 335–355.

190 P.S. Cho, R.H. Johnson, and T.W. Griffin, “Cone-beam CT for radiotherapy applications,” Phys. Med. Biol. **40**(11), 1863–1883 (1995).

191 M.K. Islam *et al.*, “Patient dose from kilovoltage cone beam computed tomography imaging in radiation therapy,” Med. Phys. **33**(6), 1573 (2006).

192 M.-S. Shin *et al.*, “CMOS X-Ray Detector With Column-Parallel 14.3-bit Extended-Counting ADCs,” IEEE Trans. Electron Devices **60**(3), 1169–1177 (2013).

193 D.L. Lee, G. Storti, and K.P. Golden, “New developments in full-field radiography detectors: Direct conversion selenium detector with avalanche gain layer,” in *Opt. Sci. Technol. SPIE 49th Annu. Meet.*, edited by F.P. Doty, R.C. Schirato, H.B. Barber and H. Roehrig (International Society for Optics and Photonics, 2004), pp. 126–132.

194 J.R. Scheuermann *et al.*, “Solid-state flat panel imager with avalanche amorphous selenium,” in *SPIE Med. Imaging*, edited by D. Kontos, T.G. Flohr and J.Y. Lo (International Society for Optics and Photonics, 2016), p. 978317.

195 P.G. Roos *et al.*, “Multiple-gain-ranging readout method to extend the dynamic range of amorphous silicon flat-panel imagers,” in *Med. Imaging 2004*, edited by M.J. Yaffe and M.J. Flynn (International Society for Optics and Photonics, 2004), pp. 139–149.

196 J.H. Siewerdsen *et al.*, “Multimode C-arm fluoroscopy, tomosynthesis, and cone-beam CT for image-guided interventions: from proof of principle to patient protocols,” in *Med. Imaging*, edited by J. Hsieh and M.J. Flynn (International Society for Optics and Photonics, 2007), p. 65101A–65101A–11.

197 K. Yang, S.-Y. Huang, N.J. Packard, and J.M. Boone, “Noise variance analysis using a flat panel x-ray detector: a method for additive noise assessment with application to breast CT applications.,”

Med. Phys. **37**(7), 3527–37 (2010).

198 T.L. Toth, E. Cesmeli, A. Ikhlef, and T. Horiuchi, “Image quality and dose optimization using novel x-ray source filters tailored to patient size,” in *Med. Imaging*, edited by M.J. Flynn (International Society for Optics and Photonics, 2005), pp. 283–291.

199 L. Yu *et al.*, “Radiation dose reduction in computed tomography: techniques and future perspective.,” Imaging Med. **1**(1), 65–84 (2009).

200 S. Bartolac, S. Graham, J. Siewerdsen, and D. Jaffray, “Fluence field optimization for noise and dose objectives in CT.,” Med. Phys. **38 Suppl 1**(S1), S2 (2011).

201 N. Mail, D.J. Moseley, J.H. Siewerdsen, and D.A. Jaffray, “The influence of bowtie filtration on cone-beam CT image quality,” Med. Phys. **36**(1), 22 (2009).

202 K.K. Lindfors, J.M. Boone, T.R. Nelson, K. Yang, A.L.C. Kwan, and D.F. Miller, “Dedicated breast CT: initial clinical experience.,” Radiology **246**(3), 725–33 (2008).

203 J.E. Tkaczyk, Y. Du, D.J. Walter, X. Wu, J. Li, and T. Toth, “Simulation of CT dose and contrast-to-noise as function of bowtie shape,” in *Med. Imaging 2004*, edited by M.J. Yaffe and M.J. Flynn (International Society for Optics and Photonics, 2004), pp. 403–410.

204 S.S. Hsieh and N.J. Pelc, “The feasibility of a piecewise-linear dynamic bowtie filter.,” Med. Phys. **40**(3), 31910 (2013).

205 T.P. Szczykutowicz and C.A. Mistretta, “Experimental realization of fluence field modulated CT using digital beam attenuation.,” Phys. Med. Biol. **59**(5), 1305–26 (2014).

206 J.W. Stayman *et al.*, “Fluence-field modulated x-ray CT using multiple aperture devices,” in *SPIE Med. Imaging*, edited by D. Kontos, T.G. Flohr and J.Y. Lo (International Society for Optics and Photonics, 2016), p. 97830X.

207 J. Xu *et al.*, “Evaluation of detector readout gain mode and bowtie filters for cone-beam CT imaging of the head,” Phys. Med. Biol. **61**(16), 5973–5992 (2016).

208 M. Maolinbay *et al.*, “Additive noise properties of active matrix flat-panel imagers.,” Med. Phys. **27**(8), 1841–54 (2000).

209 J.G. Proakis and D.G. Manolakis, *Introduction to digital signal processing* (Prentice Hall Professional Technical Reference, 1988).

[210] R.H. Walden, “Analog-to-digital converter survey and analysis,” IEEE J. Sel. Areas Commun. **17**(4), 539–550 (1999).

[211] A.M. Hernandez and J.M. Boone, “Tungsten anode spectral model using interpolating cubic splines: unfiltered x-ray spectra from 20 kV to 640 kV.,” Med. Phys. **41**(4), 42101 (2014).

[212] A. Badal and A. Badano, “Accelerating Monte Carlo simulations of photon transport in a voxelized geometry using a massively parallel graphics processing unit,” Med. Phys. **36**(11), 4878 (2009).

[213] P.M. Joseph and R.D. Spital, “A method for correcting bone induced artifacts in computed tomography scanners.,” J. Comput. Assist. Tomogr. **2**(1), 100–108 (1978).

[214] Z. Zhao, G.J. Gang, and J.H. Siewerdsen, “Noise, sampling, and the number of projections in cone-beam CT with a flat-panel detector.,” Med. Phys. **41**(6), 61909 (2014).

[215] H. Dang *et al.*, “Statistical reconstruction for cone-beam CT with a post-artifact-correction noise model: application to high-quality head imaging.,” Phys. Med. Biol. **60**(16), 6153–75 (2015).

[216] Z. Zhuang and B. Bradtmiller, “Head-and-Face Anthropometric Survey of U.S. Respirator Users,” J. Occup. Environ. Hyg. **2**(11), 567–576 (2005).

[217] J. Punnoose, J. Xu, A. Sisniega, W. Zbijewski, and J.H. Siewerdsen, “Technical Note: spektr 3.0—A computational tool for x-ray spectrum modeling and analysis,” Med. Phys. **43**(3057), 4711–41906 (2016).

[218] G. Poludniowski, P.M. Evans, V.N. Hansen, and S. Webb, “An efficient Monte Carlo-based algorithm for scatter correction in keV cone-beam CT,” Phys. Med. Biol. **54**(12), 3847–3864 (2009).

[219] J. Baró, J. Sempau, J.M. Fernández-Varea, and F. Salvat, “PENELOPE: An algorithm for Monte Carlo simulation of the penetration and energy loss of electrons and positrons in matter,” Nucl. Instruments Methods Phys. Res. Sect. B Beam Interact. with Mater. Atoms **100**(1), 31–46 (1995).

[220] A. Sisniega *et al.*, “Monte Carlo study of the effects of system geometry and antiscatter grids on cone-beam CT scatter distributions.,” Med. Phys. **40**(5), 51915 (2013).

[221] W. Zbijewski *et al.*, “A Sparse Monte Carlo Method for High-Speed, High-Accuracy Scatter Correction for Soft-Tissue Imaging in Cone-Beam CT,” in *Proc. CT Meet.*, edited by F. Noo (Salt Lake City, 2014), pp. 401–404.

[222] N. Navab *et al.*, “Dynamic Geometrical Calibration for 3-D Cerebral Angiography,” Med. Imaging

Phys. Med. Imaging **2708**, 361–370 (1996).

223 K. Sauer and C. Bouman, "A local update strategy for iterative reconstruction from projections," IEEE Trans. Signal Process. **41**(2), 534–548 (1993).

224 H. Erdogan and J.A. Fessler, "Ordered subsets algorithms for transmission tomography," Phys. Med. Biol. **44**(11), 2835–2851 (1999).

225 Y. Long, J.A. Fessler, and J.M. Balter, "3D Forward and Back-Projection for X-Ray CT Using Separable Footprints," IEEE Trans. Med. Imaging **29**(11), 1839–1850 (2010).

226 A.S. Wang *et al.*, "Soft-tissue imaging with C-arm cone-beam CT using statistical reconstruction.," Phys. Med. Biol. **59**(4), 1005–26 (2014).

227 J.M. Wilson, O.I. Christianson, S. Richard, and E. Samei, "A methodology for image quality evaluation of advanced CT systems," Med. Phys. **40**(3), 31908 (2013).

228 J. Valentin *et al.*, "The 2007 Recommendations of the International Commission on Radiological Protection," in *Ann. ICRP, Publ. 103*, edited by J. Valentin (Elsevier, Oxford, 2007).

229 H.H. Barrett, S.K. Gordon, and R.S. Hershel, "Statistical limitations in transaxial tomography," Comput. Biol. Med. **6**(4), 307–323 (1976).

230 R.F. Wagner, D.G. Brown, and M.S. Pastel, "Application of information theory to the assessment of computed tomography," Med. Phys. **6**(2), 83 (1999).

231 T. Gross *et al.*, "Impact of a multifunctional image-guided therapy suite on emergency multiple trauma care.," Br. J. Surg. **97**(1), 118–27 (2010).

232 Y. Li *et al.*, "C-arm cone beam CT perfusion imaging using the SMART-RECON algorithm to improve temporal sampling density and temporal resolution," in edited by D. Kontos, T.G. Flohr and J.Y. Lo (International Society for Optics and Photonics, 2016), p. 97830U.

233 J.H. Siewerdsen, W. Zbijewski, and J. Xu, "Cone-Beam CT Image Quality," in *Cone Beam Comput. Tomogr.*, edited by W.R. Hendee and C.C. Shaw (Taylor & Francis Group, Boca Raton, FL, 2014), pp. 37–58.

CURRICULUM VITAE

The Johns Hopkins University School of Medicine

Name: Jennifer Xu Date of this Version: 11/17/2016

Educational History:

Ph.D. Expected 2016 Program in Biomedical Engineering Johns Hopkins School of Medicine

Mentor: Jeffrey Siewerdsen, Ph.D.

M.S. 2009 Biomedical Engineering University of Southern California

B.S. 2008 Biomedical Engineering/Electrical Engineering University of Southern California

Experience:

Johns Hopkins University Baltimore, MD

Graduate Research Assistant, lab of Dr. Jeffrey Siewerdsen 2011–present

University of Baltimore Baltimore, MD

Research Assistant, lab of Dr. Elizabeth Powell 2010–2011

Medtronic MiniMed Northridge, CA

Research and Development Intern, glucose sensor group 2007

University of Southern California Los Angeles, CA

Undergraduate Research Assistant, lab of Dr. Tzung K. Hsieh 2004–2007

Scholarships and fellowships:

1. Recipient of Translational Research in Imaging Training Grant (T32EB010021, 2011-2012)
2. University of Southern California Trustee Merit Scholar (Full tuition scholarship + research grant)

Academic Awards and Honors

1. Moses & Sylvia Greenfield Best Paper Award and Editor's Pick for 2014
2. SPIE Medical Imaging, Physics of Medical Imaging Best Student Paper Award, 2nd place (2014)

Peer-Reviewed Publications

[1] **J. Xu**, A. Sisniega, W. Zbijewski, H. Dang, J. W. Stayman, M. Mow, X. Wang, D. H. Foos, V. E. Koliatsos, N. Aygun, and J. H. Siewerdsen, "Technical assessment of a prototype cone-beam CT system for imaging of acute intracranial hemorrhage," *Med. Phys.*, vol. 43, no. 10, pp. 5745–5757, Oct. 2016.

[2] J. Punnoose, **J. Xu**, A. Sisniega, W. Zbijewski, and J. H. Siewerdsen, "Technical Note: spektr 3.0—A computational tool for x-ray spectrum modeling and analysis," *Med. Phys.*, vol. 43, no. 3057, pp. 4711–41906, 2016.

[3] **J. Xu**, A. Sisniega, W. Zbijewski, H. Dang, J. W. Stayman, X. Wang, D. H. Foos, N. Aygun, V. E. Koliatsos, and J. H. Siewerdsen, "Evaluation of detector readout gain mode and bowtie filters for cone-beam CT imaging of the head," *Phys. Med. Biol.*, vol. 61, no. 16, p. 5973, 2016.

[4] **J. Xu**, A. Sisniega, W. Zbijewski, H. Dang, J. W. Stayman, X. Wang, D. H. Foos, N. Aygun, V. E. Koliatsos, and J. H. Siewerdsen, "Modeling and Design of a Cone-Beam CT Head Scanner Using Task-Based Imaging Performance Optimization," *Phys. Med. Biol.*, vol. 61, no. 8, pp. 3180–3207, 2016.

[5] A. Sisniega, W. Zbijewski, J. W. Stayman, **J. Xu**, K. Taguchi, E. Fredenberg, M. Lundqvist, and J. H. Siewerdsen, "Volumetric CT with sparse detector arrays (and application to Si-strip photon counters)," *Phys. Med. Biol.*, vol. 61, no. 1, p. 90, 2015.

[6] H. Dang, J. W. Stayman, A. Sisniega, **J. Xu**, W. Zbijewski, X. Wang, D. H. Foos, N. Aygun, V. E. Koliatsos, and J. H. Siewerdsen, "Statistical reconstruction for cone-beam CT with a post-artifact-correction noise model: application to high-quality head imaging," *Phys. Med. Biol.*, vol. 60, no. 16, p. 6153, 2015.

[7] A. Sisniega, W. Zbijewski, **J. Xu**, H. Dang, J. W. Stayman, J. Yorkston, N. Aygun, V. Koliatsos, and J. H. Siewerdsen, "High-fidelity artifact correction for cone-beam CT imaging of the brain.," *Phys. Med. Biol.*, vol. 60, no. 4, pp. 1415–39, Feb. 2015.

[8] ***J. Xu**, W. Zbijewski, G. Gang, J. W. Stayman, K. Taguchi, M. Lundqvist, E. Fredenberg, J. A. Carrino, and J. H. Siewerdsen, "Cascaded systems analysis of photon counting detectors," *Med. Phys.*, vol. 41, no. 10, p. 101907, 2014.

[9] J. Cammin, **J. Xu**, W. C. Barber, J. S. Iwanczyk, N. E. Hartsough, and K. Taguchi, "A cascaded model of spectral distortions due to spectral response effects and pulse pileup effects in a photon-counting x-ray detector for CT.," *Med. Phys.*, vol. 41, no. 4, p. 041905, Apr. 2014.

[10] W. Zbijewski, G. J. Gang, **J. Xu**, A. S. Wang, J. W. Stayman, K. Taguchi, J. A. Carrino, and J. H. Siewerdsen, "Dual-energy cone-beam CT with a flat-panel detector: effect of reconstruction algorithm on material classification.," *Med. Phys.*, vol. 41, no. 2, p. 021908, Feb. 2014.

[11] W. Zbijewski, **J. Xu**, S. I. Tilley, J. W. Stayman, K. Taguchi, E. Fredenberg, and J. H. Siewerdsen, "Volumetric imaging with sparse arrays of photon counting silicon strip detectors," *Proc. Fully 3D Image Reconstr.*, pp. 276–279, 2013.

[12] J. M. Smith, **J. Xu**, and E. M. Powell, "Age dependent forebrain structural changes in mice deficient in the autism associated gene Met tyrosine kinase," *NeuroImage Clin.*, vol. 1, no. 1, pp. 66–74, 2012.

[13] **J. Xu**, D. D. Reh, J. P. Carey, M. Mahesh, and J. H. Siewerdsen, "Technical assessment of a cone-beam CT scanner for otolaryngology imaging: image quality, dose, and technique protocols.," *Med. Phys.*, vol. 39, no. 8, pp. 4932–42, Aug. 2012.

Conference Proceedings

[1] H. Dang, J. W. Stayman**, J. Xu**, A. Sisniega, W. Zbijewski, X. Wang, D. H. Foos, N. Aygun, V. E. Koliatsos, and J. H. Siewerdsen, “Regularization design for high-quality cone-beam CT of intracranial hemorrhage using statistical reconstruction,” in *SPIE Medical Imaging*, 2016, p. 97832Y–97832Y.

[2] **J. Xu**, A. Sisniega, W. Zbijewski, H. Dang, J. W. Stayman, X. Wang, D. H. Foos, N. Aygun, V. E. Koliatsos, and J. H. Siewerdsen, “Design and characterization of a dedicated cone-beam CT scanner for detection of acute intracranial hemorrhage,” in *SPIE Medical Imaging*, 2016, p. 97830T.

[3] H. Dang, J. W. Stayman, A. Sisniega, **J. Xu**, W. Zbijewski, J. Yorkston, N. Aygun, V. Koliatsos, and J. H. Siewerdsen, “Cone-beam CT of traumatic brain injury using statistical reconstruction with a post-artifact-correction noise model,” in *SPIE Medical Imaging*, 2015, p. 941207.

[4] A. Sisniega, W. Zbijewski, J. W. Stayman, **J. Xu**, K. Taguchi, and J. H. Siewerdsen, “Spectral CT of the extremities with a silicon strip photon counting detector,” in *SPIE Medical Imaging*, 2015, p. 94120Z–94120Z.

[5] **J. Xu**, W. Zbijewski, G. Gang, J. W. Stayman, K. Taguchi, M. Lundqvist, E. Fredenberg, J. A. Carrino, and J. H. Siewerdsen, “Cascaded systems modeling of signal, noise, and DQE for x-ray photon counting detectors,” in *SPIE Medical Imaging*, 2014, p. 903320.

[6] J. Cammin, **J. Xu**, W. C. Barber, J. S. Iwanczyk, N. E. Hartsough, and K. Taguchi, “Modeling photon-counting detectors for x-ray CT: spectral response and pulse-pileup effects and evaluation using real data,” in *SPIE Medical Imaging*, 2013, p. 86680R–86680R.

Book Chapters

[1] J. H. Siewerdsen, W. Zbijewski, and J. Xu, “Cone-beam CT image quality,” *Cone Beam Computed Tomography*, p. 37, 2014.

Other Media

A Computation Tool for X-Ray Spectrum Modeling and Analysis: spektr 3.0 software toolkit, available for download at istar.jhu.edu/downloads

Presentations

Invited Presentations

[1] **J. Xu**, “X-Ray Imaging Physics: Modeling and System Design,” at GE Global Research, 2016.

Scientific Conferences (Presenting Author)

[1] **J. Xu**, A. Sisniega, W. Zbijewski, H. Dang, J. Stayman, X. Wang, D. Foos, N. Aygun, V. Koliatsos, and J. Siewerdsen, “A Point-of-Care Cone-Beam CT System for Imaging of Intracranial Hemorrhage: Performance Characterization for Translation to Clinical Studies,” in *RSNA Annual Meeting*, 2016 (accepted for oral presentation)

[2] **J. Xu**, A. Sisniega, W. Zbijewski, H. Dang, J. Stayman, X. Wang, D. Foos, N. Aygun, V. Koliatsos, and J. Siewerdsen, “WE-AB-207A-03: A CBCT Head Scanner for Point-Of-Care Imaging of Intracranial Hemorrhage,” in *AAPM Annual Meeting*, 2016. (oral presentation)

[3] **J. Xu**, A. Sisniega, W. Zbijewski, H. Dang, J. Stayman, X. Wang, D. Foos, N. Aygun, V. Koliatsos, and J. Siewerdsen, "Cone-beam CT for point-of-care detection of acute intracranial hemorrhage," in *IJCARS Annual Meeting*, 2016 (poster presentation)

[4] **J. Xu**, A. Sisniega, W. Zbijewski, H. Dang, J. Stayman, X. Wang, D. Foos, N. Aygun, V. Koliatsos, and J. Siewerdsen, "Design and Characterization of a Dedicated Cone-Beam CT Scanner for Detection of Acute Intracranial Hemorrhage," in *SPIE Medical Imaging*, 2015 (oral presentation)

[5] **J. Xu**, A. Sisniega, W. Zbijewski, H. Dang, J. Stayman, X. Wang, D. Foos, N. Aygun, V. Koliatsos, and J. Siewerdsen, "SSK15-04: Development of a dedicated cone-beam CT system for imaging of intracranial hemorrhage," in *RSNA Annual Meeting*, 2015 (oral presentation)

[6] **J. Xu**, A. Sisniega, W. Zbijewski, H. Dang, J. W. Stayman, X. Wang, D. H. Foos, N. Aygun, V. Koliatsos, and J. H. Siewerdsen, "Design and Optimization of a CBCT Head Scanner for Detection of Acute Intracranial Hemorrhage," in *AAPM Annual Meeting*, 2015 (oral presentation)

[7] **J. Xu**, W. Zbijewski, G. Gang, J. W. Stayman, K. Taguchi, M. Lundqvist, E. Fredenberg, J. A. Carrino, and J. H. Siewerdsen, "Imaging Performance of Photon Counting X-Ray Detectors," in *NIBIB Bi-Annual Trainee Meeting*, 2014 (poster presentation)

[8] **J. Xu**, W. Zbijewski, G. Gang, J. W. Stayman, K. Taguchi, M. Lundqvist, E. Fredenberg, J. A. Carrino, and J. H. Siewerdsen, "Cascaded systems modeling of signal, noise, and DQE for x-ray photon counting detectors," in *SPIE Medical Imaging*, 2014 (oral presentation)

[9] **J. Xu**, W. Zbijewski, G. Gang, E. Fredenberg, K. Taguchi, J. Carrino, J. Stayman, and J. Siewerdsen, "TH-A-103-03: Cascaded Systems Analysis of a Silicon-Strip Photon Counting CT System," in *AAPM Annual Meeting*, 2014 (oral presentation)

Scientific Conferences (Contributing Author)

[1] H. Dang, J. W. Stayman, **J. Xu**, A. Sisniega, W. Zbijewski, X. Wang, D. H. Foos, N. Aygun, V. E. Koliatsos, and J. H. Siewerdsen, "Task-Based Regularization Design for Detection of Intracranial Hemorrhage in Cone-Beam CT," in *International Conference on Image Formation in X-Ray Computed Tomography,* 2016 (oral presentation)

[2] H. Dang, J. W. Stayman**, J. Xu**, A. Sisniega, W. Zbijewski, X. Wang, D. H. Foos, N. Aygun, V. E. Koliatsos, and J. H. Siewerdsen, "Regularization design for high-quality cone-beam CT of intracranial hemorrhage using statistical reconstruction," in *SPIE Medical Imaging*, 2016 (poster presentation)

[3] H. Dang, J. Xu, A. Sisniega, W. Zbijewski, J. W. Stayman, X. Wang, D. H. Foos, N. Aygun, V. E. Koliatsos, J. H. Siewerdsen, "A Dedicated Cone-Beam CT System for Detection of Acute Intracranial Hemorrhage at the Point of Care," in *ASNR Symposium,* 2016 (oral presentation)

[4] A. Sisniega, W. Zbijewski, **J. Xu**, H. Dang, J. W. Stayman, N. Aygun, V. E. Koliatsos, X. Wang, D. H. Foos, and J. H. Siewerdsen, "WE-EF-207-05: Monte Carlo Dosimetry for a Dedicated Cone-Beam CT Head Scanner," in *AAPM Annual Meeting*, 2015. (oral presentation)

[5] A. Sisniega, W. Zbijewski, **J. Xu**, H. Dang, J. W. Stayman, N. Aygun, V. E. Koliatsos, X. Wang, D. H. Foos, and J. H. Siewerdsen, "High-Quality Soft-Tissue Imaging with Cone-Beam CT for Point-of-Care Evaluation of Traumatic Brain Injury," in *IJCARS,* 2015 (oral presentation)

[6] H. Dang, J. W. Stayman, A. Sisniega, **J. Xu**, W. Zbijewski, J. Yorkston, N. Aygun, V. Koliatsos, J. H. Siewerdsen, "Cone-Beam CT of Traumatic Brain Injury Using Statistical Reconstruction with a Post-Artifact-Correction Noise Model," in *Division of Medical Imaging Physics Seminar*, 2015 (oral presentation)

[7] A. Sisniega, W. Zbijewski, J. W. Stayman, **J. Xu**, K. Taguchi, E. Fredenberg, M. Lundqvist, J. H. Siewerdsen, "Spectral CT with a Sparsely Sampled Silicon Strip Photon Counting Detector," in *SPIE Medical Imaging,* 2015 (oral presentation)

[8] H. Dang, . W. Stayman, A. Sisniega, **J. Xu**, W. Zbijewski, J. Yorkston, N. Aygun, V. Koliatsos, J. H. Siewerdsen, "Cone-Beam CT of Traumatic Brain Injury Using Statistical Reconstruction with a Post-Artifact-Correction Noise Model," in *SPIE Medical Imaging*, 2015 (oral presentation)

[9] A. Sisniega, W. Zbijewski, H. Dang, **J. Xu**, J. W. Stayman, J. Yorkston, N. Aygun, V. Koliatsos, J. H. Siewerdsen, "High Performance Cone-Beam CT of Acute Traumatic Brain Injury," in *RSNA Annual Meeting,* 2014 (oral presentation)

[10] J. Cammin, **J. Xu**, W. C. Barber, J. S. Iwanczyk, N. E. Hartsough, and K. Taguchi, "Modeling photon-counting detectors for x-ray CT: spectral response and pulse-pileup effects and evaluation using real data," in *SPIE Medical Imaging*, 2013 (oral presentation)

CONFERENCE ABSTRACTS

[1] **J. Xu**, A. Sisniega, W. Zbijewski, H. Dang, J. Stayman, X. Wang, D. Foos, N. Aygun, V. Koliatsos, and J. Siewerdsen, "SSK16-07: A Point-of-Care Cone-Beam CT System for Imaging of Intracranial Hemorrhage: Performance Characterization for Translation to Clinical Studies," in *RSNA Annual Meeting*, 2016

[10] **J. Xu**, A. Sisniega, W. Zbijewski, H. Dang, J. Stayman, X. Wang, D. Foos, N. Aygun, V. Koliatsos, and J. Siewerdsen, "WE-AB-207A-03: A CBCT Head Scanner for Point-Of-Care Imaging of Intracranial Hemorrhage," in *AAPM Annual Meeting*, 2016.

[11] H. Dang, J. W. Stayman, **J. Xu**, A. Sisniega, W. Zbijewski, X. Wang, D. H. Foos, N. Aygun, V. E. Koliatsos, and J. H. Siewerdsen, "Task-Based Regularization Design for Detection of Intracranial Hemorrhage in Cone-Beam CT," in *International Conference on Image Formation in X-Ray Computed Tomography,* 2016

[12] **J. Xu**, A. Sisniega, W. Zbijewski, H. Dang, J. Stayman, X. Wang, D. Foos, N. Aygun, V. Koliatsos, and J. Siewerdsen, "Cone-beam CT for point-of-care detection of acute intracranial hemorrhage," in *IJCARS Annual Meeting*, 2016

[13] **J. Xu**, A. Sisniega, W. Zbijewski, H. Dang, J. Stayman, X. Wang, D. Foos, N. Aygun, V. Koliatsos, and J. Siewerdsen, "Design and Characterization of a Dedicated Cone-Beam CT Scanner for Detection of Acute Intracranial Hemorrhage," in *SPIE Medical Imaging*, 2015

[14] H. Dang, J. W. Stayman, **J. Xu**, A. Sisniega, W. Zbijewski, X. Wang, D. H. Foos, N. Aygun, V. E. Koliatsos, and J. H. Siewerdsen, "Regularization design for high-quality cone-beam CT of intracranial hemorrhage using statistical reconstruction," in *SPIE Medical Imaging*, 2016

[15] H. Dang, J. Xu, A. Sisniega, W. Zbijewski, J. W. Stayman, X. Wang, D. H. Foos, N. Aygun, V. E. Koliatsos, J. H. Siewerdsen, "A Dedicated Cone-Beam CT System for Detection of Acute Intracranial Hemorrhage at the Point of Care," in *ASNR Symposium,* 2016

[16] **J. Xu**, A. Sisniega, W. Zbijewski, H. Dang, J. Stayman, X. Wang, D. Foos, N. Aygun, V. Koliatsos, and J. Siewerdsen, "SSK15-04: Development of a dedicated cone-beam CT system for imaging of intracranial hemorrhage," in *RSNA Annual Meeting*, 2015

[17] **J. Xu**, A. Sisniega, W. Zbijewski, H. Dang, J. W. Stayman, X. Wang, D. H. Foos, N. Aygun, V. Koliatsos, and J. H. Siewerdsen, "Design and Optimization of a CBCT Head Scanner for Detection of Acute Intracranial Hemorrhage," in *AAPM Annual Meeting*, 2015

[18] A. Sisniega, W. Zbijewski, **J. Xu**, H. Dang, J. W. Stayman, N. Aygun, V. E. Koliatsos, X. Wang, D. H. Foos, and J. H. Siewerdsen, "WE-EF-207-05: Monte Carlo Dosimetry for a Dedicated Cone-Beam CT Head Scanner," in *AAPM Annual Meeting*, 2015

[19] A. Sisniega, W. Zbijewski, J. W. Stayman, **J. Xu**, K. Taguchi, E. Fredenberg, M. Lundqvist, J. H. Siewerdsen, "Spectral CT with a Sparsely Sampled Silicon Strip Photon Counting Detector," in *SPIE Medical Imaging,* 2015

[20] H. Dang, . W. Stayman, A. Sisniega, **J. Xu**, W. Zbijewski, J. Yorkston, N. Aygun, V. Koliatsos, J. H. Siewerdsen, "Cone-Beam CT of Traumatic Brain Injury Using Statistical Reconstruction with a Post-Artifact-Correction Noise Model," in *SPIE Medical Imaging*, 2015

[21] A. Sisniega, W. Zbijewski, **J. Xu**, H. Dang, J. W. Stayman, N. Aygun, V. E. Koliatsos, X. Wang, D. H. Foos, and J. H. Siewerdsen, "High-Quality Soft-Tissue Imaging with Cone-Beam CT for Point-of-Care Evaluation of Traumatic Brain Injury," in *IJCARS,* 2015 (oral presentation)

[22] A. Sisniega, W. Zbijewski, H. Dang, **J. Xu**, J. W. Stayman, J. Yorkston, N. Aygun, V. Koliatsos, J. H. Siewerdsen, "High Performance Cone-Beam CT of Acute Traumatic Brain Injury," in *RSNA Annual Meeting,* 2014

[23] **J. Xu**, W. Zbijewski, G. Gang, J. W. Stayman, K. Taguchi, M. Lundqvist, E. Fredenberg, J. A. Carrino, and J. H. Siewerdsen, "Imaging Performance of Photon Counting X-Ray Detectors," in *NIBIB Bi-Annual Trainee Meeting*, 2014

[24] **J. Xu**, W. Zbijewski, G. Gang, J. W. Stayman, K. Taguchi, M. Lundqvist, E. Fredenberg, J. A. Carrino, and J. H. Siewerdsen, "Cascaded systems modeling of signal, noise, and DQE for x-ray photon counting detectors," in *SPIE Medical Imaging*, 2014

[25] **J. Xu**, W. Zbijewski, G. Gang, E. Fredenberg, K. Taguchi, J. Carrino, J. Stayman, and J. Siewerdsen, "TH-A-103-03: Cascaded Systems Analysis of a Silicon-Strip Photon Counting CT System," in *AAPM Annual Meeting*, 2014

[26] J. Cammin, **J. Xu**, W. C. Barber, J. S. Iwanczyk, N. E. Hartsough, and K. Taguchi, "Modeling photon-counting detectors for x-ray CT: spectral response and pulse-pileup effects and evaluation using real data," in *SPIE Medical Imaging*, 2013

Service and Leadership

2013-2016	Mentored an undergraduate research assistant for development of new x-ray spectral simulation software toolkit, spektr 3.0.
2014-2015	Conducted weekly small-session discussion section and office hours as a graduate teaching assistant.
	Developed lesson plans and delivered lectures for senior-level signals and systems, controls, and thermodynamic courses.